Mechanical
Engineering Advances

https://ojs.acad-pub.com/index.php/mea

ACADEMIC
ACADEMIC PUBLISHING PTE LTD

2024 VOLUME 2 ISSUE 2
ISSN: 3029-1232 (Online)

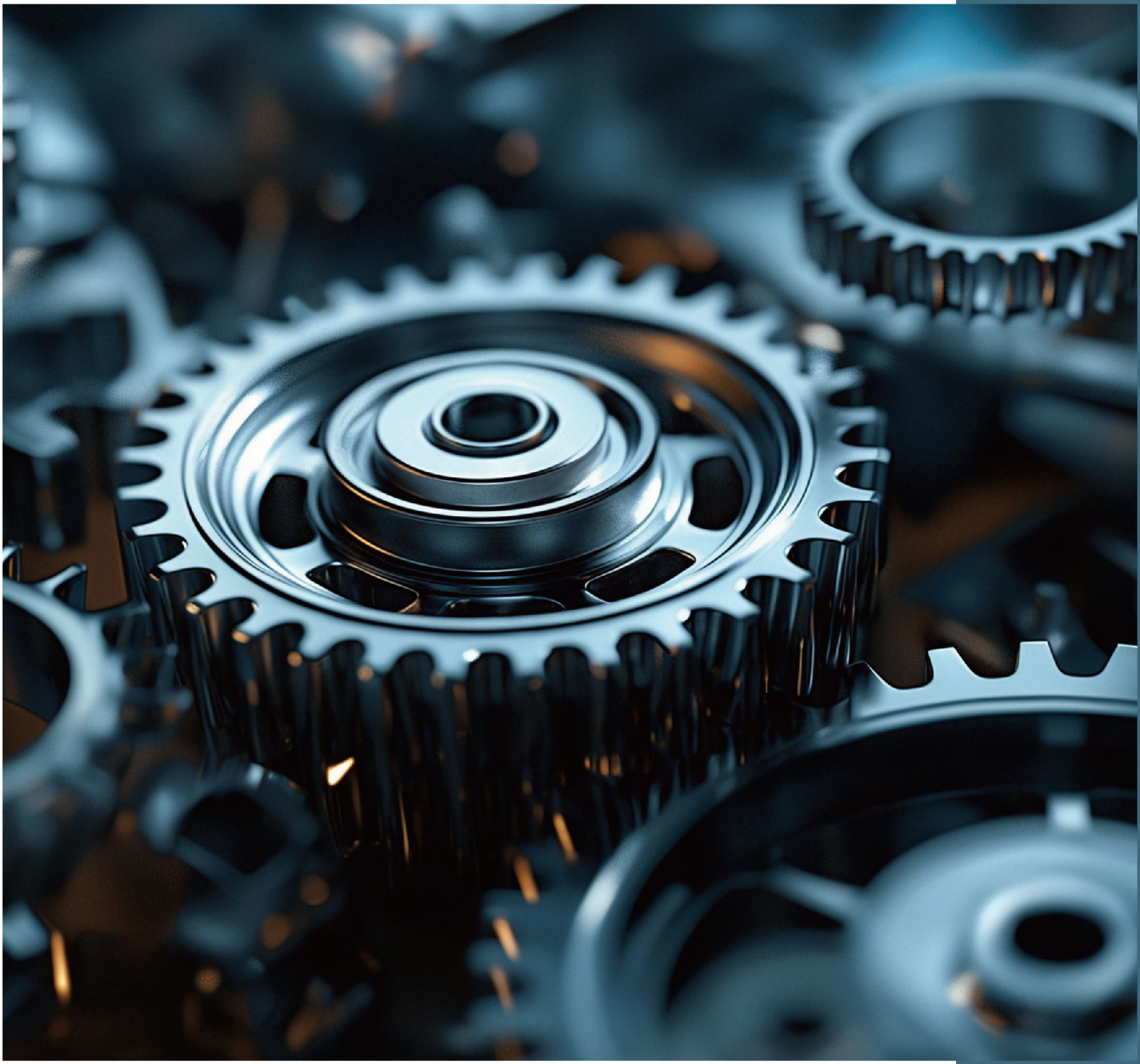

2

ACADEMIC
ACADEMIC PUBLISHING PTE LTD

Editorial Board

Editor-in-Chief

Associate Editor

Editorial Board Members

Dr. Marian Grigoras
National Institute of Research and Development for Technical Physics (NIRDTP)
Romania

Prof. Stan Chirita
Alexandru Ioan Cuza University of Iasi
Romania

Dr. Araliya Mosleh
University of Porto
Portugal

Dr. Tianzhu Sun
University of Warwick
United Kingdom

Prof. Serguei Murzin
Samara National Research University
Russia

Prof. Rosario Sinatra
Università degli Studi di Catania
Italy

Prof. Hitesh Panchal
Government Engineering College
India

Prof. Mohsen Sheikholeslami Kandelousi
Babol Noshirvani University of Technology
Iran

Assoc. Prof. Emilian Florin Mosnegutu
"Vasile Alecsandri" University of Bacau
Romania

Dr. Ahmad Serjouei
Nottingham Trent University
United Kingdom

Prof. Van-Tu Nguyen
Pusan National University
Korea

Prof. Mohammad Zaman Kabir
Department of Civil and Environmental Engineering
Iran

Prof. José Manoel Balthazar
Universidade Tecnológica Federal do Paraná
Brazil

Prof. Sohail Ahmad Khan
Quaid-i-Azam University
Pakistan

Prof. Freddie Liswaniso Inambao
University of KwaZulu-Natal
South Africa

Dr. Sajad Saraygord Afshari
University of Manitoba
Canada

Prof. Eurico Augusto Rodrigues de Seabra
University of Minho
Portugal

Prof. K.K. Viswanathan
Samarkand State University
Uzbekistan

Prof. Angelo Aloisio
Università degli Studi dell'Aquila
Italy

Prof. Hosein Naderpour
Toronto Metropolitan University
Canada

Prof. Vinícius Piccirillo
Federal Technological University of Parana
Brazil

Prof. Ali Nikkhoo
University of Science and Culture
Iran

Prof. Hassaine Daouadji Tahar
University of Tiaret Algeria
Algeria

Prof. Gilberto Santos
Polytechnic Institute Cavado Ave
Portugal

Dr. Mohammad Molla-Alipour
University of Mazandaran
Iran

Volume 2 Issue 2 • 2024

Mechanical Engineering Advances

Editor-in-Chief

Prof. Chunsheng Lu

Curtin University, Australia

ACADEMIC
ACADEMIC PUBLISHING PTE LTD

2024 | Volume 2 | Issue 2

Mechanical Engineering Advances

https://ojs.acad-pub.com/index.php/mea

Contents

Articles

Review

Mechanical Engineering Advances 2024, 2(2), 463.
https://doi.org/10.59400/mea.v2i2.463

Article

Performance-based optimization of active-passive hybrid mass damper based on virtual TMD algorithm

Yu Yang[1], Qi Wang[2,*], Qingshan Yang[1], Tao Long[1], Guandong Qiao[2], Tian Li[1]

[1] School of Civil Engineering, Chongqing University, Chongqing 400044, People's Republic of China
[2] School of Civil and Architectural Engineering, Hainan University, Haikou 570228, People's Republic of China
*** Corresponding author:** Qi Wang, dkw57@hainanu.edu.cn

CITATION

Yang Y, Wang Q, Yang Q, et al. Performance-based optimization of active-passive hybrid mass damper based on virtual TMD algorithm. Mechanical Engineering Advances. 2024; 2(2): 463. https://doi.org/10.59400/mea.v2i2.463

ARTICLE INFO

Received: 14 May 2024
Accepted: 4 July 2024
Available online: 2 August 2024

Abstract: Subjecting structures to external forces inevitably leads to the generation of vibrations. For high-rise and flexible structures, excessive vibrations can significantly impact their normal operation and structural integrity. To mitigate these undesirable vibrations, structural vibration control is essential. Among various passive control methods, the tuned mass damper (TMD) is widely used for its ability to reduce vibrations through resonance with the structure. Meanwhile, the active mass damper (AMD) can also achieve an excellent control efficiency by exerting active control force on structures. Hybrid control integrates the benefits of multiple control strategies and applies the control forces on the same structure simultaneously. Hybrid mass damper (HMD) combines the passive characteristics of TMD and the active features of AMD, overcoming the limitations associated with using either system in isolation. This paper proposes a novel hybrid control method based on virtual TMD algorithm and optimizes the parameters of HMD by weighting the structural response and stroke of HMD to improve the comprehensive control performance. The effectiveness of this optimization is substantiated in the frequency domain. Additionally, numerical simulations are conducted to compare the optimized HMD with the traditional TMD and the unoptimized HMD, demonstrating both the effectiveness of the optimization and the superior control performance of the optimized HMD. The numerical results indicate that the optimized HMD reduces stroke by 15.6% compared to the unoptimized HMD on the premise that the control effect only loses 2.4%. Overall, the optimized HMD demonstrates superior comprehensive control performance relative to the unoptimized HMD.

Keywords: vibration control; active-passive hybrid mass damper; virtual tuned mass damper; weighted function; performance-based optimization; comprehensive control performance

1. Introduction

Actual engineering structures are located in complex environments and subjected to various loads. The excessive vibrations caused by the external loads may affect the normal service and safety of structures, especially for the high rise and flexible structures. Therefore, it is essential to control the structure's vibration to avoid excessive vibrational deformation that could impair its functionality. Structural vibration control is an effective measure to reduce the undesired vibrations of structures, and can be divided into passive, active, semi-active, and hybrid control [1] according to whether external energy output is required.

Tuned mass damper (TMD) is one of the most commonly used passive control methods in engineering, originating from a vibration device called dynamic vibration absorber (DVA) invented by Frahm in 1909 [2]. The TMD device consists of a mass block, spring and viscous damping. Owing to its straightforward structure and economical cost, the TMD is extensively employed in practical engineering structures. For example, Tsai et al. and Rana et al. studied the optimal design parameters of TMD under harmonic and seismic excitations respectively [3,4]. TMD has a good control performance in the responses dominated by the fundamental frequency of structure and widely used in the vibration of high rise and flexible structures. For example, Murtagh et al. researched the control performance of TMD for vibration control of wind turbines under random wind loads [5]. Kim et al. studied the passive control of along wind response of tall building using TMD [6]. Dinh and Basu studied the application of TMD in vibration control of floating wind turbines [7]. When the natural frequency of TMD is tuned with the structure, it rapidly attenuates the dynamic response of the structure by resonating with the structure and dissipating energy through damping. Generally, when tuned with the structures, TMD has a good control performance in the fundamental frequency of structures.

Active mass damper (AMD) or active tuned mass damper (ATMD) can achieve an excellent control efficiency by exerting active control force on the structures [8–10]. When AMD or ATMD is integrated with suitable active control algorithms, the control effectiveness can surpass that of TMD, thus it is also extensively applied in practical engineering. For example, You et al. researched the along wind-induced vibration control using ATMD [8]. Fitzgerald et al. studied the vibration control of wind turbine towers using ATMD and demonstrated the improvements in structural reliability of the ATMD equipped wind turbine towers [9]. Cong adopted ATMD to simultaneously control the vibrations in wind turbine blades and tower and demonstrated that the ATMD has good control effect on blades and tower [10]. The main components of an active control system include controllers, sensors, and actuators. The controller is the key of the active control and AMD/ATMD combined with effective and reasonable controllers can achieve excellent control performance.

Semi-active control can reduce the vibrations of structures and maintain the tuning state by changing the stiffness or damping of control devices [11–17]. Compared to passive control, semi-active control is tunable and reduces the risk of detuning. When combined with suitable semi-active control algorithms, its effectiveness can rival that of active control. Consequently, numerous scholars have investigated different semi-active control devices and algorithms to achieve high-performance control. For example, Hrovat et al. studied the semi-active control of civil engineering structures and proposed rules for semi-active control systems to achieve the active control performance as much as possible [11]. Nagarajaiah and Varadarajan proposed a mechanical semi-active variable stiffness tuned mass damper to realize the semi-active control of high-rise buildings under wind loads [12]. Sun et al. applied magnetorheological elastomer in TMD to achieve the semi-active control and conducted an experiment under earthquake excitation [13]. Yang et al. also utilized the semi-active control characteristic of magnetorheological elastomer TMD to control the wind induced vibrations of constructing bridge towers [14]. Wang et al. utilized the variable stiffness and damping characteristics of semi-active control to reduce the earthquake and human induced vibrations [15–17]. Generally, semi-active control can change its own dynamic parameters to avoid the risk of detuning and can achieve excellent control performance with appropriate semi-active control algorithms.

Hybrid control contains the characteristics of two or more control measures, and applies the control forces on the same structure simultaneously. The hybrid mass damper (HMD) combines the advantages of both TMD and AMD, and has attracted the attention of many scholars [18–20]. Li and Cao studied the application of HMD to attenuate the undesirable vibrations of structures under the ground acceleration [18]. Collette and Chesne proposed that adding an active control force between TMD and structure to make the TMD device a hybrid mass damper with active-passive characteristics [19]. Hsieh et al. combined TMD tuned to the fundamental frequency and tuned liquid damper (TLD) tuned to the forced frequency to form HMD and researched the control performance for offshore wind turbines [20]. HMD combines the advantages of TMD and AMD, and reduces the limitations of using TMD or AMD systems alone. Moreover, and the control effect of HMD is similar to that of active control and with lower energy consumption and power output requirements.

While TMD devices offer effective narrowband control, their performance is significantly compromised if detuning occurs due to changes in the structure's fundamental frequency. Although AMD and ATMD can deliver excellent control results, they necessitate substantial external energy input. Semi-active control techniques can provide continuous real-time tuning, but their range of tuning capability is also limited. The HMD combines the characteristics of both TMD and AMD, thereby minimizing the risk of detuning while maintaining robust control efficiency. Therefore, it is valuable to research the HMD in the structural vibration control.

This paper introduces an HMD device utilizing a virtual TMD control algorithm based on the vibration reduction principles of TMD and ATMD, and optimizes the design of the HMD by weighting the control effect and actuation stroke. Compared to existing HMD devices, the HMD device in this article aims to achieve the control effect of TMD devices with high mass ratios (≥5%) through the passive and active parts of the HMD without increasing the actual physical mass, where the passive part is the restoring force provided by stiffness and damping, and the active part is the active control force based on actuators. This paper first studied the hybrid control based on virtual TMD and validated the feasibility by frequency domain analysis. Then, this paper optimized the design parameters of HMD by considering the responses of structure and the stroke of control device in a weighted manner. Subsequently, the feasibility of the optimized design parameters was verified through numerical example. The results showed that the optimized HMD almost has the same control effect of the unoptimized HMD, while the stroke of the optimized HMD is much lower than that of the unoptimized HMD.

2. Hybrid control based on virtual TMD

TMD has good control performance in the responses of the fundamental frequency of structure and the control effect increases as the mass of TMD increases. While in actual engineering, the mass of TMD will be limited by the economy and installation space, which limits the control performance of TMD. This paper applies the control force of TMD with large mass onto structure to form AMD to improve the control effect without increasing the actual mass of control device. Afterwards, by replacing part of the control force with stiffness and damping, AMD is transformed into HMD without changing the control effect to possess both active and passive control characteristics. The schematic diagram of SDOF structure with HMD is shown in **Figure 1**.

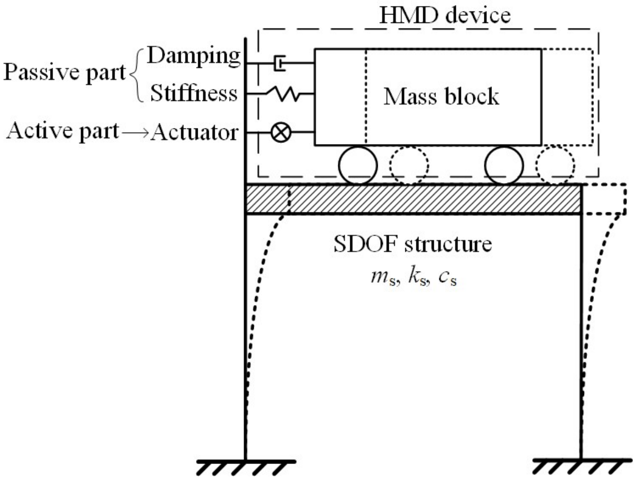

Figure 1. Schematic diagram of SDOF structure with HMD.

Assuming the mass of the single degree of freedom (SDOF) structure is m_s, the stiffness is k_s, and the damping is c_s. The total mass of the control device is m_t, the virtual mass of TMD is m_{vs}, the virtual stiffness is k_{vs}, and the virtual damping is c_{vs}.

The dynamic equation of the controlled SDOF structure is:

$$\begin{cases} m_s\ddot{x}_s + c_s\dot{x}_s + k_s x_s - f = p \\ m_t(\ddot{x}_s + \ddot{x}_t) + f = 0 \\ f = k_{vs}x_{vs} + c_{vs}\dot{x}_{vs} \end{cases} \tag{1}$$

The control equation of virtual TMD is:

$$\begin{cases} m_s\ddot{x}_s + c_s\dot{x}_s + k_s x_s - c_{vs}\dot{x}_{vs} - k_{vs}x_{vs} = p \\ m_{vs}(\ddot{x}_s + \ddot{x}_{vs}) + c_{vs}\dot{x}_{vs} + k_{vs}x_{vs} = 0 \end{cases} \tag{2}$$

Combining Equations (1) and (2), the expression of the control force can be obtained as:

$$f = \frac{k_{vs}m_t}{m_{vs}}x_t + \frac{c_{vs}m_t}{m_{vs}}\dot{x}_t - \left(k_{vs}\frac{m_{vs} - m_t}{m_{vs}}x_s + c_{vs}\frac{m_{vs} - m_t}{m_{vs}}\dot{x}_s\right) \tag{3}$$

From the expression of control force based on virtual TMD, the active control force based on the positive feedback of the relative state of the control device is similar to the control equation of TMD. Therefore, the control force can be replaced by stiffness and damping elements. The parameters of the stiffness and damping components for the replacement part are as follows.

$$k_t = \frac{k_{vs}m_t}{m_{vs}}; c_t = \frac{c_{vs}m_t}{m_{vs}} \tag{4}$$

The expression of the active force after replacement is:

$$f_{ac} = k_{vs}\frac{m_{vs} - m_t}{m_{vs}}x_s + c_{vs}\frac{m_{vs} - m_t}{m_{vs}}\dot{x}_s = ax_s + b\dot{x}_s \tag{5}$$

Then, the dynamic equation of SDOF structure controlled by HMD based virtual TMD is:

$$\begin{cases} m_s\ddot{x}_s + c_s\dot{x}_s + k_s x_s - k_t x_t - c_t\dot{x}_t + ax_s + b\dot{x}_s = p \\ m_t(\ddot{x}_s + \ddot{x}_t) + k_t x_t + c_t\dot{x}_t - ax_s - b\dot{x}_s = 0 \end{cases} \tag{6}$$

Denoting that $k_\mathrm{s}/m_\mathrm{s} = \omega_\mathrm{s}^2$, $c_\mathrm{s}/m_\mathrm{s} = 2\xi_\mathrm{s}\omega_\mathrm{s}$, $a/m_\mathrm{s} = \omega_\mathrm{eq}^2$, $b/m_\mathrm{s} = 2\xi_\mathrm{eq}\omega_\mathrm{eq}$, $k_\mathrm{t}/m_\mathrm{t} = \omega_\mathrm{t}^2$, $c_\mathrm{t}/m_\mathrm{t} = 2\xi_\mathrm{t}\omega_\mathrm{t}$, $m_\mathrm{t}/m_\mathrm{s} = \mu$, $\omega_\mathrm{t}/\omega_\mathrm{s} = \upsilon$, $\omega/\omega_\mathrm{s} = \lambda$, $\omega_\mathrm{eq}/\omega_\mathrm{s} = \gamma$, the transfer function of SDOF structural response controlled by HMD based virtual TMD can be obtained.

$$|H_\mathrm{s}(i\omega)| = \frac{1}{k_\mathrm{s}}\sqrt{\frac{(\upsilon^2-\lambda^2)^2+(2\xi_\mathrm{t}\upsilon\lambda)^2}{\left\{\begin{bmatrix}(1+\gamma^2-\lambda^2)(\upsilon^2-\lambda^2)-4\xi_\mathrm{t}\upsilon\lambda^2(\xi_\mathrm{s}+\xi_\mathrm{eq}\gamma)\\+\upsilon^2(-\gamma^2-\mu\lambda^2)+4\xi_\mathrm{t}\xi_\mathrm{eq}\upsilon\gamma\lambda^2\end{bmatrix}^2+\begin{bmatrix}2\xi_\mathrm{t}\upsilon\lambda(1+\gamma^2-\lambda^2)+2\lambda(\xi_\mathrm{s}+\xi_\mathrm{eq}\gamma)(\upsilon^2-\lambda^2)\\-2\xi_\mathrm{eq}\gamma\upsilon^2\lambda+2\xi_\mathrm{t}\upsilon\lambda(-\gamma^2-\mu\lambda^2)\end{bmatrix}^2\right\}}} \tag{7}$$

The transfer function of HMD stroke is:

$$|H_\mathrm{t}(i\omega)| = \sqrt{\frac{(\gamma^2/\mu+\lambda^2)^2+(2\xi_\mathrm{eq}\gamma\lambda/\mu)^2}{(\upsilon^2-\lambda^2)^2+(2\xi_\mathrm{t}\upsilon\lambda)^2}}|H_\mathrm{s}(i\omega)| \tag{8}$$

The design parameters of TMD are set as follows:

$$\upsilon_\mathrm{TMD} = \frac{1}{1+\mu}, \xi_\mathrm{TMD} = \sqrt{\frac{3\mu}{8(1+\mu)^3}} \tag{9}$$

The design parameters of HMD based on virtual TMD are set as follows:

$$\upsilon = \frac{1}{1+\mu}, \xi_\mathrm{t} = \sqrt{\frac{3\mu}{8(1+\mu)^3}}, \gamma = \frac{\sqrt{\mu_\mathrm{vs}-\mu}}{1+\mu_\mathrm{vs}}, \xi_\mathrm{eq} = \sqrt{\frac{3\mu_\mathrm{vs}(\mu_\mathrm{vs}-\mu)}{8(1+\mu_\mathrm{vs})^3}} \tag{10}$$

It can been that when $\mu = \mu_\mathrm{vs}$, $\gamma = \xi_\mathrm{eq} = 0$ and Equation (7) is the transfer function of TMD controlled SDOF structure. When $\mu = 0.01$, $\mu_\mathrm{vs} = 0.05$ or 0.1, the amplitude of transfer functions of TMD and HMD controlled SDOF structural responses are displayed in **Figure 2**. The amplitude of transfer functions of TMD and HMD strokes are shown in **Figure 3**.

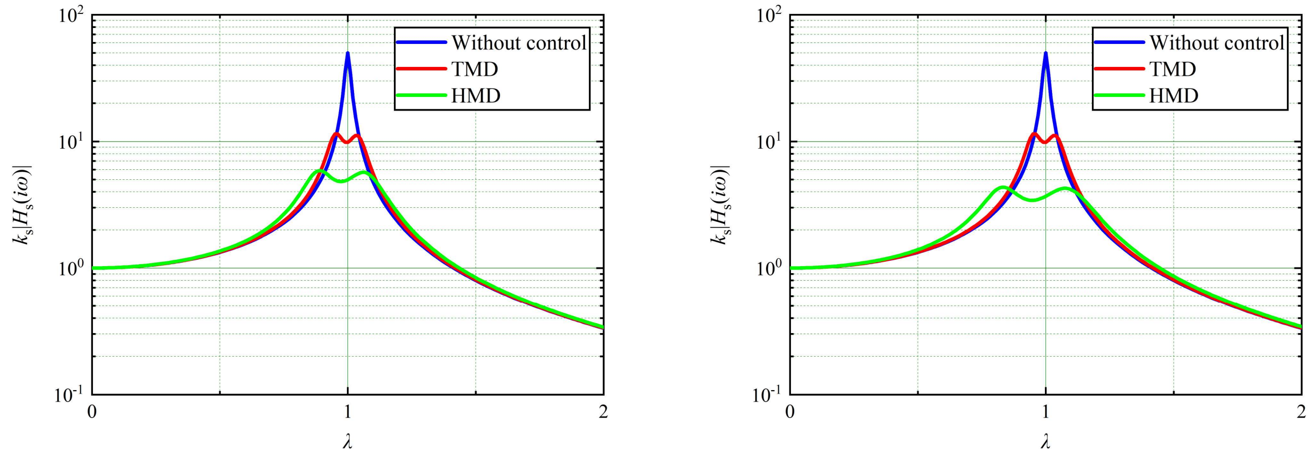

(a) $\mu = 0.01$, $\mu_\mathrm{vs} = 0.05$.

(b) $\mu = 0.01$, $\mu_\mathrm{vs} = 0.1$.

Figure 2. Amplitudes of TMD and HMD controlled SDOF structural responses. **(a)** $k_\mathrm{s}|H_\mathrm{s}(i\omega)|$ with $\mu = 0.01$, $\mu_\mathrm{vs} = 0.05$; **(b)** $k_\mathrm{s}|H_\mathrm{s}(i\omega)|$ with $\mu = 0.01$, $\mu_\mathrm{vs} = 0.1$.

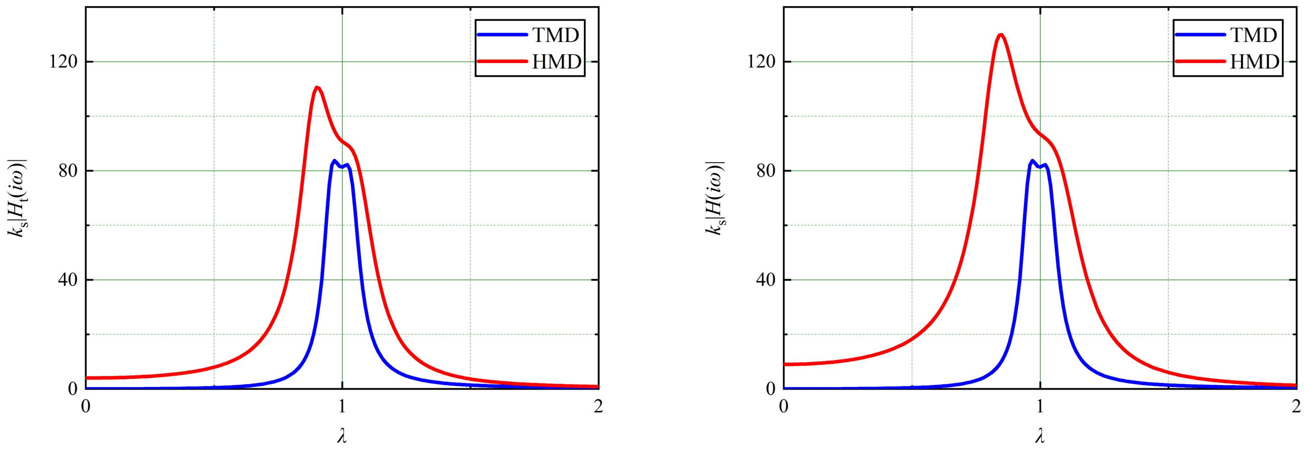

(a) $\mu = 0.01$, $\mu_{vs} = 0.05$.

(b) $\mu = 0.01$, $\mu_{vs} = 0.1$.

Figure 3. Amplitudes of TMD and HMD strokes. **(a)** $k_s|H_t(i\omega)|$ with $\mu = 0.01$, $\mu_{vs} = 0.05$; **(b)** $k_s|H_t(i\omega)|$ with $\mu = 0.01$, $\mu_{vs} = 0.1$.

The results show that the HMD based on virtual TMD does not change the mass of device and realizes the improvement in control effect. The control performance of HMD based on virtual TMD increases with the increase of virtual mass ratio μ_{vs}, while the stroke will also increase. From Equations (7) and (8), it can be seen that the control performance and stroke of HMD are influenced by parameters γ, ξ_{eq}, υ and ξ_t. In order to balance the control performance and the stroke of HMD, the next chapter will optimize those parameters of HMD considering the structural response and the stroke in a weighted manner.

3. Optimization of hybrid mass damper

From the previous section, it can be seen that when μ and μ_{vs} are ascertained, the control effect of HMD is influenced by four parameters, i.e., active parameters (γ and ξ_{eq}) and passive parameters (υ and ξ_t). **Figures 4** and **5** give the influences of active parameters on the structural response and stroke of HMD. **Figures 6** and **7** give the influences of passive parameters on the structural response and stroke of HMD.

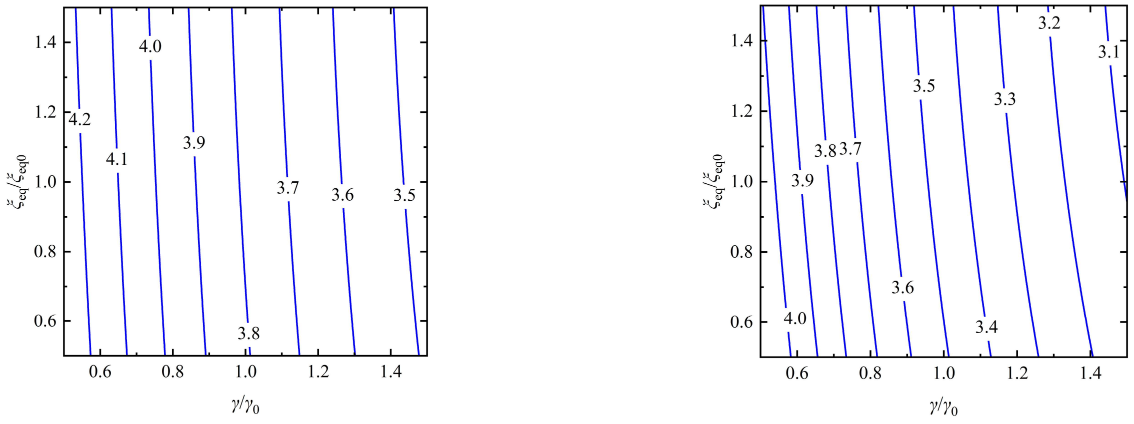

(a) $\mu = 0.01$, $\mu_{vs} = 0.05$.

(b) $\mu = 0.01$, $\mu_{vs} = 0.1$.

Figure 4. Influences of active parameters on the structural response. **(a)** ξ_{eq}/ξ_{eq0} with $\mu = 0.01$, $\mu_{vs} = 0.05$; **(b)** ξ_{eq}/ξ_{eq0} with $\mu = 0.01$, $\mu_{vs} = 0.1$.

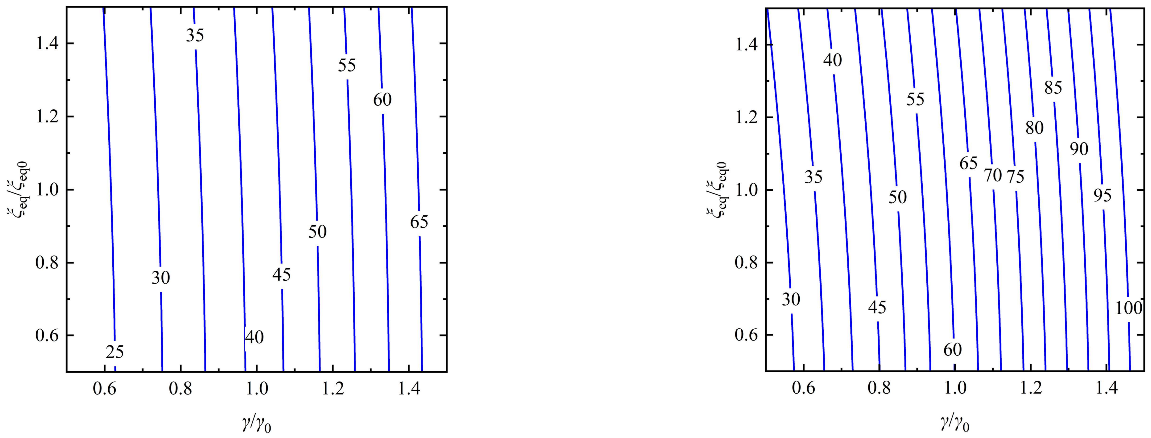

(a) $\mu = 0.01$, $\mu_{vs} = 0.05$. **(b)** $\mu = 0.01$, $\mu_{vs} = 0.1$.

Figure 5. Influences of active parameters on the stroke of HMD. **(a)** ξ_{eq}/ξ_{eq0} with $\mu = 0.01$, $\mu_{vs} = 0.05$; **(b)** ξ_{eq}/ξ_{eq0} with $\mu = 0.01$, $\mu_{vs} = 0.1$.

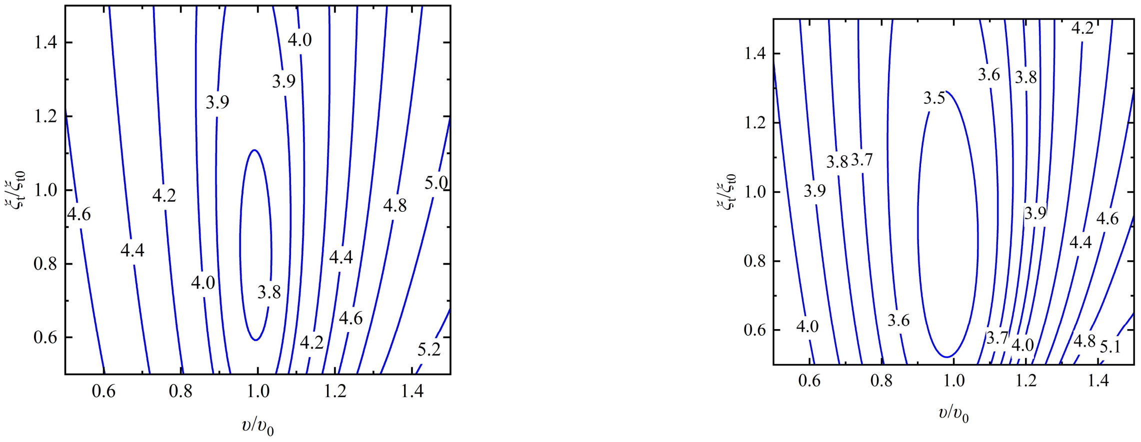

(a) $\mu = 0.01$, $\mu_{vs} = 0.05$. **(b)** $\mu = 0.01$, $\mu_{vs} = 0.1$.

Figure 6. Influences of passive parameters on the structural response. **(a)** ξ_t/ξ_{t0} with $\mu = 0.01$, $\mu_{vs} = 0.05$; **(b)** ξ_t/ξ_{t0} with $\mu = 0.01$, $\mu_{vs} = 0.1$.

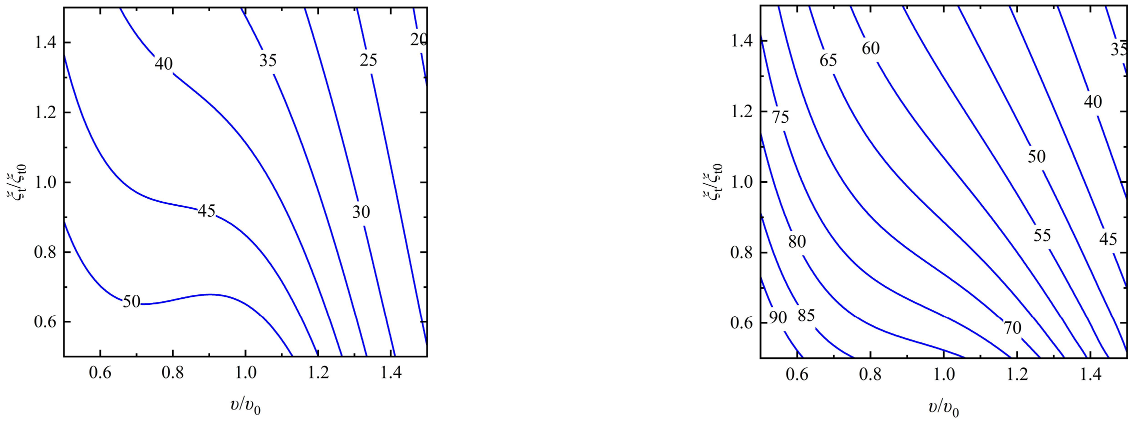

(a) $\mu = 0.01$, $\mu_{vs} = 0.05$. **(b)** $\mu = 0.01$, $\mu_{vs} = 0.1$.

Figure 7. Influences of passive parameters on the stroke of HMD. **(a)** ξ_t/ξ_{t0} with $\mu = 0.01$, $\mu_{vs} = 0.05$; **(b)** ξ_t/ξ_{t0} with $\mu = 0.01$, $\mu_{vs} = 0.1$.

The values on the contour lines in **Figures 4–7** represent k_s times the area of the transfer function, and the parameters on the coordinate axis are as follows.

$$\upsilon_0 = \frac{1}{1+\mu}, \xi_{t0} = \sqrt{\frac{3\mu}{8(1+\mu)^3}}, \gamma_0 = \frac{\sqrt{\mu_{vs}-\mu}}{1+\mu_{vs}}, \xi_{eq0} = \sqrt{\frac{3\mu_{vs}(\mu_{vs}-\mu)}{8(1+\mu_{vs})^3}} \tag{11}$$

It can be seen in **Figures 4** and **5** that the structural response and HMD stroke basically do not change with the variation of ξ_{eq}, while almost linear variation with γ. As **Figures 6** and **7** shown, the structural response has an optimal value and the structural response changes little near the optimal value, while the HMD stroke changes a lot with the variation of υ and ξ_t. It is worth noting that near the optimal value of structural response, the structural response almost keeps unchanged, while the HMD stroke changes a lot. Therefore, it can be achieved by weighting and optimizing the structural response and HMD stroke without significantly changing the control effect in structural response.

In order to weight the structural response and HMD stroke, this article normalized the structural response and HMD stroke, and then weighted them in the performance index function as follows.

$$J_{ij} = C_s \frac{A_{s,ij}}{\sum A_{s,ij}} + C_t \frac{A_{t,ij}}{\sum A_{t,ij}}, C_s + C_t = 1 \tag{12}$$

where, C_s and C_t are the weighted coefficients of structural response and HMD stroke respectively, $A_{s,ij}$ and $A_{t,ij}$ are the k_s times the area of the transfer function of structural response and HMD stroke respectively when $\upsilon = \upsilon_i$, $\xi_t = \xi_{t,i}$.

When the weighted coefficients of structural response and HMD stroke are 0.9 and 0.1 respectively, the optimized results after weighting are displayed in **Figures 8–10**. **Figure 8** is the optimized results of performance index function with different passive parameters, the optimal parameters for HMD are the parameters corresponding to the minimum value in **Figures 8–10** give the amplitudes of structural responses and strokes with TMD control, unoptimized HMD (UHMD) control and optimized HMD (OHMD) control under the optimal situation considering the balance of structural response and stroke of HMD. The parameters of UHMD are calculated using Equation (11).

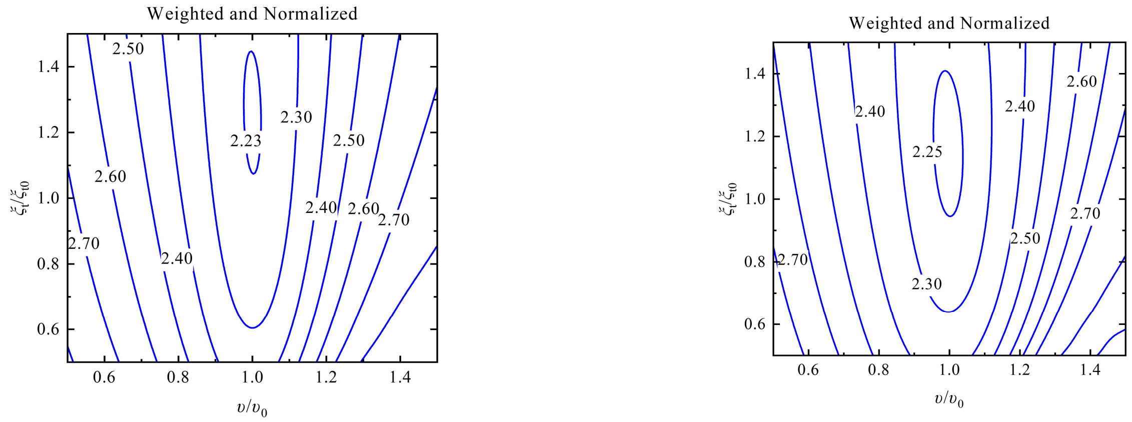

(a) $\mu = 0.01$, $\mu_{vs} = 0.05$. **(b)** $\mu = 0.01$, $\mu_{vs} = 0.1$.

Figure 8. Influences of passive parameters on performance index function (×10^{-5}). **(a)** ξ_t/ξ_{t0} with $\mu = 0.01$, $\mu_{vs} = 0.05$; **(b)** ξ_t/ξ_{t0} with $\mu = 0.01$, $\mu_{vs} = 0.1$.

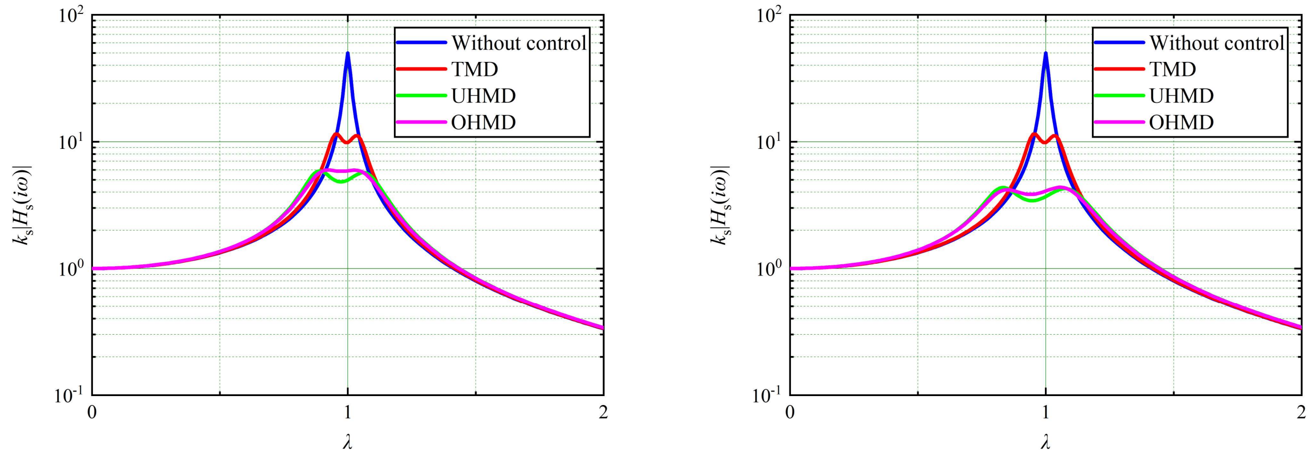

(a) $\mu = 0.01$, $\mu_{vs} = 0.05$.

(b) $\mu = 0.01$, $\mu_{vs} = 0.1$.

Figure 9. Amplitudes of TMD, UHMD and OHMD controlled SDOF structural responses. **(a)** $k_s|H_s(i\omega)|$ with $\mu = 0.01$, $\mu_{vs} = 0.05$; **(b)** $k_s|H_s(i\omega)|$ with $\mu = 0.01$, $\mu_{vs} = 0.1$.

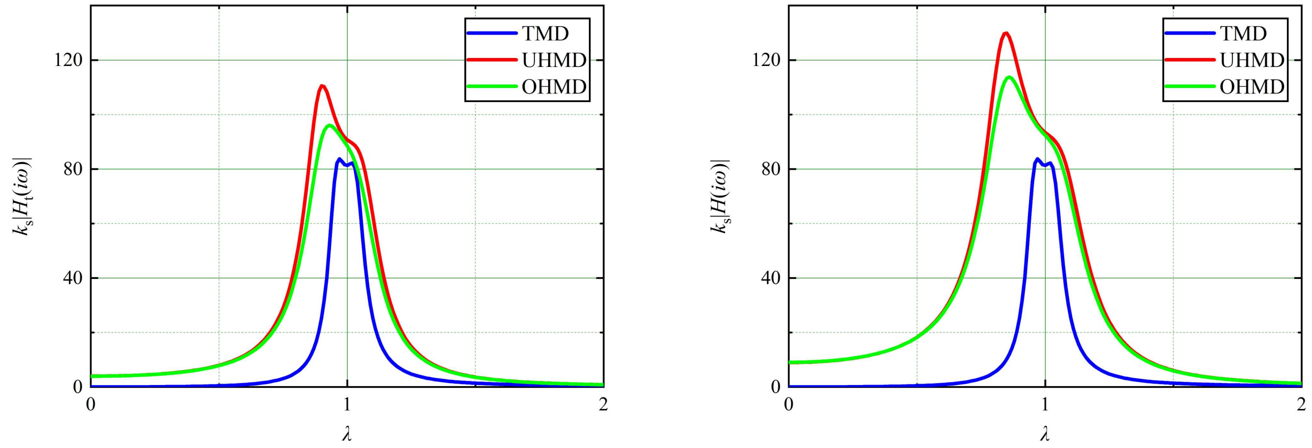

(a) $\mu = 0.01$, $\mu_{vs} = 0.05$.

(b) $\mu = 0.01$, $\mu_{vs} = 0.1$.

Figure 10. Amplitudes of TMD, UHMD and OHMD strokes. **(a)** $k_s|H_t(i\omega)|$ with $\mu = 0.01$, $\mu_{vs} = 0.05$; **(b)** $k_s|H_t(i\omega)|$ with $\mu = 0.01$, $\mu_{vs} = 0.1$.

From the optimized results in **Figures 9** and **10**, it can be seen that the control effect of OHMD is slightly decreased but not significantly decreased compared UHMD, while the stroke of OHMD is lower than that of UHMD. When $\mu = 0.01$, $\mu_{vs} = 0.05$ or 0.1, the control effect of OHMD decreased by 1.0% and 0.6% compared to UHMD, while the stroke of HMD decreased by 9.6% and 5.8%. That is to say, weighting and optimizing the structural response and HMD stroke is a feasible optimization method for HMD based on virtual TMD without sacrificing too much control performance.

4. Numerical example

The previous chapter optimized the HMD by weighting the structural response and HMD stroke, reducing the stroke of the HMD without significantly changing the control effect, and verified the feasibility of the optimization in the frequency domain.

This chapter uses the optimization method from the previous section to optimize the HMD and verifies its control performance in the time domain.

Considering a SDOF structure with fundamental frequency $f_s = 0.2$ Hz and with damping ratio $\xi_s = 1\%$. The load for SDOF structure is the Gaussian white-noise load with a standard deviation of 0.1 and a mean value of 0. The load time-history and its power spectral density (PSD) are displayed in **Figure 11**. The dynamic equation of the SDOF structure is:

$$\ddot{x} + 2\xi_s\omega_s\dot{x} + \omega_s^2 x = p \tag{13}$$

where, $\omega_s = 2\pi f_s$, p represents the random load.

Rewriting Equation (13) into state space equation.

$$\dot{Z} = AZ + Dp, Z = \{x \quad \dot{x}\}^T, A = \begin{bmatrix} 0 & 1 \\ -\omega_s^2 & -2\xi\omega_s \end{bmatrix}, D = \begin{Bmatrix} 0 \\ 1 \end{Bmatrix} \tag{14}$$

The state space equation of the controlled SDOF structure is:

$$\dot{Z} = AZ + Bu + Dp, B = \{0 \quad 1\}^T \tag{15}$$

where, u is the control force of control device acting on the SDOF structure.

The weighted coefficients of structural response and HMD stroke are 0.9 and 0.1 respectively. In addition, in order to reduce the random errors in the calculation process, this paper simulated the responses of SDOF structure under 10 different random loads, as well as the control performance and stroke of HMD devices. the simulation results are given in **Figures 12–18** and **Table 1**.

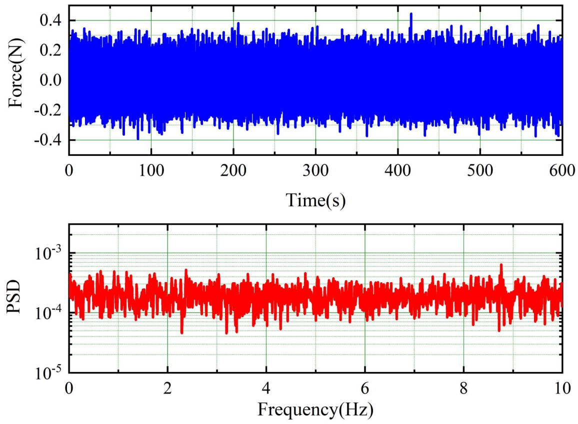

Figure 11. Load time-history and its PSD.

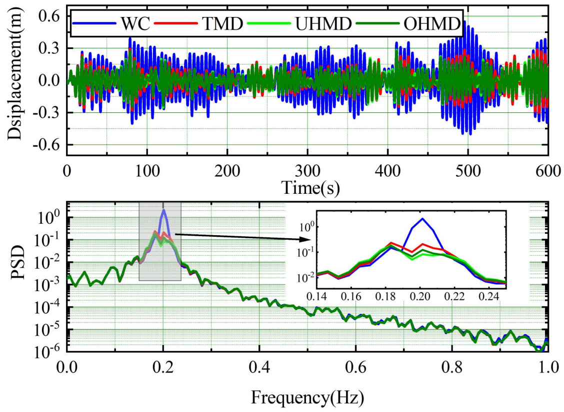

Figure 12. Displacement time-history and its PSD.

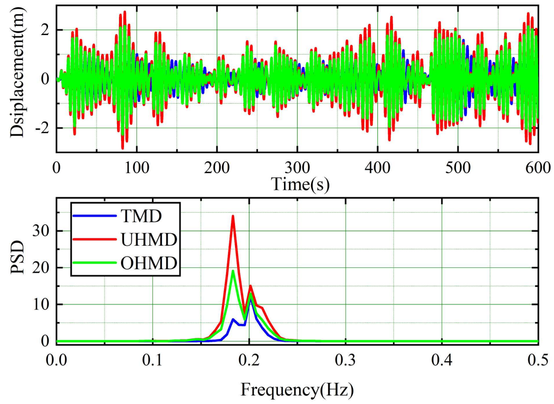

Figure 13. Stroke time-history and its PSD.

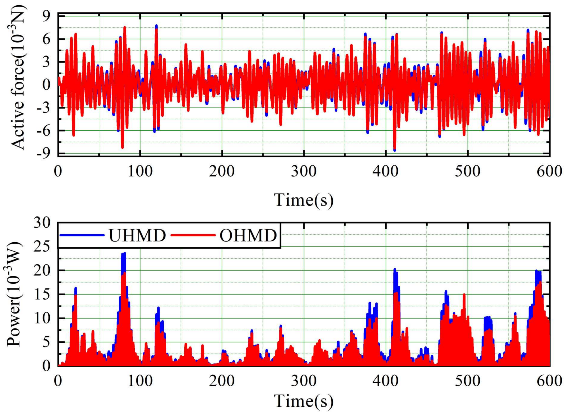

Figure 14. Active control force and power.

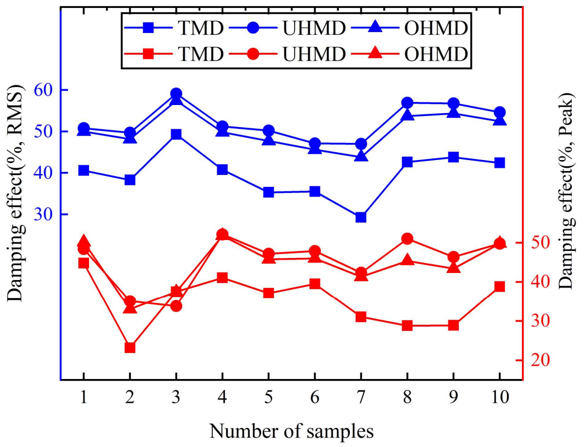

Figure 15. Displacement damping effects.

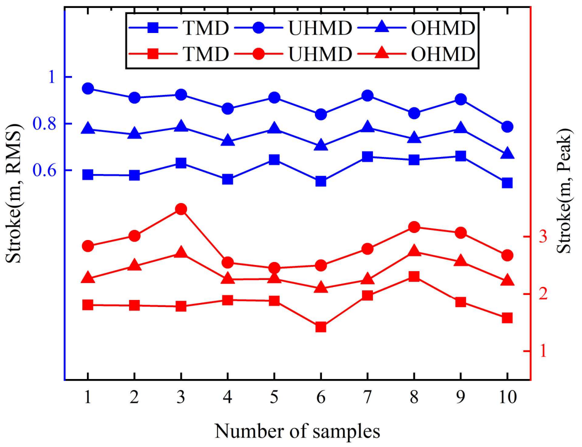

Figure 16. Strokes of control devices.

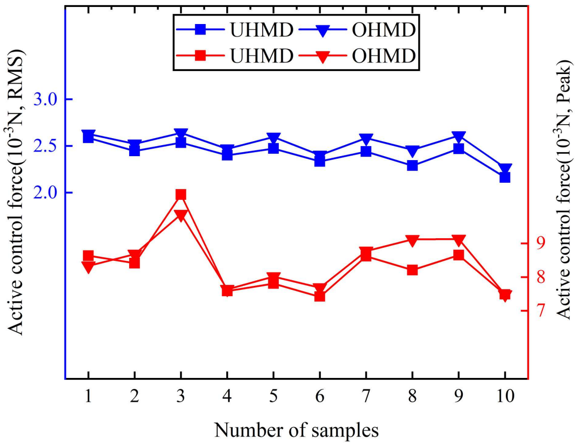

Figure 17. Active control force of UHMD and OHMD.

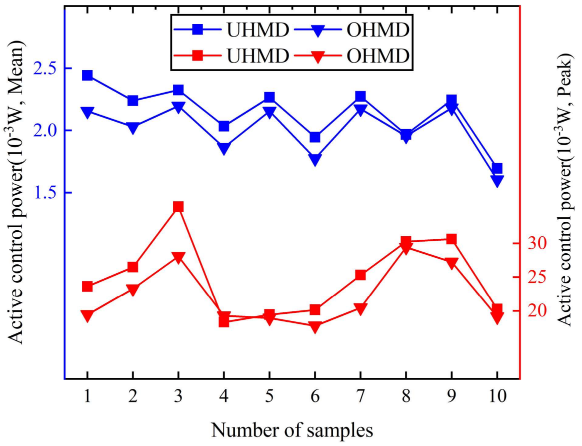

Figure 18. Active control power of UHMD and OHMD.

Table 1. Control performances of TMD, UHMD and OHMD.

	Displacement (m)		**Stroke (m)**		**Active control force (10^{-3} N)**		**Active control power (10^{-2} W)**	
	Average RMS	**Average Peak**	**Average RMS**	**Average Peak**	**Average RMS**	**Average Peak**	**Average Mean**	**Average Peak**
WC	0.168	0.502	-	-	-	-	-	-
TMD	0.100	0.329	0.606	1.826	-	-	-	-
UHMD	0.079	0.273	0.886	2.854	2.413	8.329	0.214	2.499
OHMD	0.083	0.278	0.748	2.385	2.518	8.473	0.201	2.231

Figures 12 and **13** display the structural displacement time-history and stroke time-history of without-controlled (WC), TMD controlled, UHMD controlled and OHMD controlled SDOF structures under one sample load. **Figures 15** and **16** summarize the root mean square (RMS) and peak values of structural displacement and stroke under 10 sample loads. From the results, it can be seen that the control effect of OHMD is better than TMD and almost the same as UHMD, while the stroke of OHMD is much lower than UHMD. The average control effects in RMS values of UHMD and OHMD controlled structural displacements are 53.0% and 50.6% respectively, and average control effects in peak values of UHMD and OHMD

controlled structural displacements are 45.6% and 44.6% respectively. **Figure 14** gives the active control force and power time-histories of UHMD and OHMD. **Figure 17** shows the RMS and peak values of active control forces of UHMD and OHMD and **Figure 18** exhibits the mean and peak values of active control powers of UHMD and OHMD. The active control force of OHMD is much higher than UHMD, while the active control power of OHMD is much lower than UHMD.

Generally speaking, the control effect of OHMD loses 2.4% in RMS value and 0.8% in peak value compared to UHMD, while the stroke of OHMD reduces 15.6% in RMS value and 16.4% in peak value compared to UHMD. The active control force of OHMD increases 4.4% in RMS value and 1.7% in peak value compared to UHMD, while the active control power of OHMD decreases 6.1% in mean value and 10.7% in peak value compared to UHMD. The comprehensive control performance of OHMD is better than UHMD. That is to say, the optimization of HMD through weighting the structural response and stroke is feasible. This optimization method can improve the comprehensive control performance of HMD without significantly reducing the control effect.

5. Conclusion

This paper proposed a hybrid control algorithm based on virtual TMD and verified its feasibility through frequency domain analysis, and then optimized the parameters of HMD by weighting the structural response and stroke to improve the comprehensive control performance. In order to further demonstrate the comprehensive control performance of the optimized HMD, this paper conducted time history analysis under 10 different white noise random loads. The simulation results demonstrated that the optimized HMD has a better comprehensive control performance than the unoptimized HMD. The main conclusions are as follows.

1) HMD based on virtual TMD control algorithm can achieve excellent control effect than passive TMD with large mass ratio (≥5%) in the premise of unchanging the actual physical mass of the control device.

2) Without changing the original control effect, by replacing some of the active control force with stiffness and damping, the active control force of HMD can be further reduced.

3) After weighting and optimizing the structural response and HMD stroke, although the control effect of HMD is slightly reduced, the HMD stroke is also significantly reduced. Overall, the comprehensive control performance of the optimized HMD has been improved.

Author contributions: Conceptualization, YY and QW; methodology, YY; software, YY; validation, YY, QW and QY; formal analysis, YY; investigation, YY, QW and TL (Tao Long); resources, QW; data curation, YY; writing—original draft preparation, YY and QW; writing—review and editing, YY, QW, QY, TL (Tian Li) and GQ; visualization, YY; supervision, QW, QY, TL (Tian Li) and GQ; project administration, QW; funding acquisition, QW, QY, TL (Tian Li) and GQ. All authors have read and agreed to the published version of the manuscript.

Funding: This research was funded by the National Natural Science Foundation of

China, Grant No. (52008061, 567890 and 42002293), Hainan Provincial Key R&D Program, Grant No. (ZDYF2022SHFZ353-06) and the China Postdoctoral Science Foundation, Grant No. (2020M673138).

Conflict of interest: The authors declare no conflict of interest.

References

1. Pourzeynali S, Lavasani HH, Modarayi AH. Active control of high rise building structures using fuzzy logic and genetic algorithms. Engineering Structures. 2007; 29(3): 346–357. doi: 10.1016/j.engstruct.2006.04.015
2. Frahm H. Device for damping vibrations of bodies. U.S. Patent 0989958, 18 April 1911.
3. Tsai H, Lin G. Optimum tuned-mass dampers for minimizing steady-state response of support-excited and damped systems. Earthquake Engineering & Structural Dynamics. 1993; 22(11): 957–973. doi: 10.1002/eqe.4290221104
4. Rana R, Soong TT. Parametric study and simplified design of tuned mass dampers. Engineering structures. 1998; 20(3): 193–204. doi: 10.1016/S0141-0296(97)00078-3
5. Murtagh PJ, Ghosh A, Basu B, et al. Passive control of wind turbine vibrations including blade/tower interaction and rotationally sampled turbulence. Wind Energy. 2007; 11(4): 305–317. doi: 10.1002/we.249
6. Kim Y, You K, You J. Passive control of along-wind response of tall building. Journal of Central South University. 2014; 21(10): 4002–4006. doi: 10.1007/s11771-014-2388-3
7. Dinh VN, Basu B. Passive control of floating offshore wind turbine nacelle and spar vibrations by multiple tuned mass dampers. Structural Control and Health Monitoring. 2014; 22(1): 152–176. doi: 10.1002/stc.1666
8. You KP, You JY, Kim YM. LQG Control of Along-Wind Response of a Tall Building with an ATMD. Mathematical Problems in Engineering. 2014; 2014: 1–7. doi: 10.1155/2014/206786
9. Fitzgerald B, Sarkar S, Staino A. Improved reliability of wind turbine towers with active tuned mass dampers (ATMDs). Journal of Sound and Vibration. 2018; 419: 103–122. doi: 10.1016/j.jsv.2017.12.026
10. Cong C. Using active tuned mass dampers with constrained stroke to simultaneously control vibrations in wind turbine blades and tower. Advances in Structural Engineering. 2018; 22(7): 1544–1553. doi: 10.1177/1369433218817892
11. Hrovat D, Barak P, Rabins M. Semi-active versus passive or active tuned mass dampers for structural control. Journal of Engineering Mechanics. 1983; 109(3): 691–705. doi: 10.1061/(ASCE)0733-9399(1983)109:3(691)
12. Nagarajaiah S, Varadarajan N. Short time Fourier transform algorithm for wind response control of buildings with variable stiffness TMD. Engineering Structures. 2005; 27(3): 431–441. doi: 10.1016/j.engstruct.2004.10.015
13. Sun S, Yang J, Du H, et al. Development of magnetorheological elastomers–based tuned mass damper for building protection from seismic events. Journal of Intelligent Material Systems and Structures. 2018; 29(8): 1777–1789. doi: 10.1177/1045389x17754265
14. Yang Q, Yang Y, Wang Q, et al. Study on the fluctuating wind responses of constructing bridge towers with magnetorheological elastomer variable stiffness tuned mass damper. Journal of Intelligent Material Systems and Structures. 2021; 33(2): 290–308. doi: 10.1177/1045389x211014574
15. Wang L, Zhou Y, Shi W. Seismic Response Control of a Nonlinear Tall Building Under Mainshock–Aftershock Sequences Using Semi-Active Tuned Mass Damper. International Journal of Structural Stability and Dynamics. 2023; 23(16n18). doi: 10.1142/s0219455423400278
16. Wang L, Nagarajaiah S, Zhou Y, et al. Experimental study on adaptive-passive tuned mass damper with variable stiffness for vertical human-induced vibration control. Engineering Structures. 2023; 280: 115714. doi: 10.1016/j.engstruct.2023.115714
17. Wang L, Zhou Y, Shi W. Random crowd-induced vibration in footbridge and adaptive control using semi-active TMD including crowd-structure interaction. Engineering Structures. 2024; 306: 117839. doi: 10.1016/j.engstruct.2024.117839
18. Li C, Cao B. Hybrid active tuned mass dampers for structures under the ground acceleration. Structural Control and Health Monitoring. 2014; 22(4): 757–773. doi: 10.1002/stc.1716
19. Collette C, Chesné S. Robust hybrid mass damper. Journal of Sound and Vibration. 2016; 375: 19–27. doi: 10.1016/j.jsv.2016.04.030
20. Hsieh MC, Huang GL, Liu H, et al. A numerical study of hybrid tuned mass damper and tuned liquid damper system on structure motion control. Ocean Engineering. 2021; 242: 110129. doi: 10.1016/j.oceaneng.2021.110129

Mechanical Engineering Advances 2024, 2(2), 1633.
https://doi.org/10.59400/mea.v2i2.1633

Article

Reliability, sustainability, resiliency, and performance investigation of an embedded splice-sleeve connector at high velocity semi-trailer impact

Suman Roy

Department of Civil and Environmental Engineering, Utah State University, Logan, UT 84322, USA; sumanroy74@gmail.com

CITATION

Roy S. Reliability, sustainability, resiliency, and performance investigation of an embedded splice-sleeve connector at high velocity semi-trailer impact. Mechanical Engineering Advances. 2024; 2(2): 1633. https://doi.org/10.59400/mea.v2i2.1633

ARTICLE INFO

Received: 22 April 2024
Accepted: 25 June 2024
Available online: 20 July 2024

Abstract: Presently, dynamic impacts occurrences caused by car crashes have been frequently reported. Statistical results from different articles indicate that vehicle crashworthiness of bridge pier supersedes the other events. However, majority of the published articles focusses on sustainability and finding severity of distressed pier due to impact correlating faster construction methods, like accelerated bridge construction (ABC). This article is an attempt to examine post impacted behavior of a commonly used connector in ABC for resisting short duration shock. Static and dynamic performance analyses of a connector embedded within a coupler system has been examined. A representative ABC pier with the standardized and selected material properties collected from manufacturer's data has been utilized. Coupler composite materials consisting of a hollow uniform cross-section cast iron cylinder filled up with specified concrete grout conforms higher strength. The performance examination has been conducted by numerical modeling using finite element method (FEM). A commercially used software ANSYS has been utilized for carrying out the simulations. To investigate the post impact dynamic behavior, mesh-independent studies seems inevitable and hence are executed to evaluate dynamic impact factor (DIF). Sensitivity studies are carried out for validating results in precision. The DIF of the main reinforcing tensile steel embedded into the grout placed inside the connector has been determined. Results captured from simulations to identify material properties at plastic stage in sustaining such load have been conducted. The results provide significant information that aids opting for selecting suitable connectors for attaining help the design offices.

Keywords: non-traditional bridge pier; semi-trailer impact; connector; FEM and its validity

1. Introduction

Increased occurrences of dynamic impact caused by high strain rate loading warrants structural viability that intimidates serviceability, resilience, and reliability. Reinforced concrete (RC) bridge piers primarily receive various short duration impact loads caused by earthquake, blast, and car crash. All these loads being short duration impact may cause performance degradation from less severe to pier dislocation. High seismicity being considered in the western United States of America (USA) has received adequate attention to examine structural feasibility [1]. Traditional RC bridge piers responding at higher seismic loads has been the subject of interests by many researchers from years. To improve the post impact behavior of such piers by resisting damage during medium to devastating earthquakes, adequate research was carried out to assess various damage levels. Blast resistant design of structures has been carried out by many researchers as well [2]. On the other hand, high strain rate impact loads exerted by vehicular collision creates quite complex mechanisms comprising uncertainty caused by relatively unknown vehicle bridge-pier interaction and failure mechanism. However, this area of structural investigations has received limited attention. So, an additional insightful study is required for RC bridge pier performance at short duration high strain rate load. High velocity vehicle crash as exerts higher strain rate force at high-speed hit on bridge pier, frontal overpressure due to contact for collision can result certain damage levels from concrete spalling to cracking [3]. Recently published articles in various journals corroborated that the car crashes with bridge elements most likely to be occurred with the rising number of vehicles [4]. The post-crash behavior of the coupler composite incurred by high velocity vehicle impact has been investigated. Results in terms of stresses are captured at the highly possible susceptible region to estimate plastic deformation. Different high strain rates dynamic loads instilled at tensile steel bar of traditional RC pier were analyzed, and the evaluated results were published for both flexure and combined stresses [5]. Different studies corroborate that damage characterization experienced by impact load is not only the function of reinforcing steel but highly dependent on the strength of concrete. Combination of different parameters controlling post impact pier behavior endorses a fairly good agreement between withstanding the transverse load resisting capacity as a primary mechanism followed by the flexural capacity that governs principal serviceability to resist post impact distresses in bridge pier [6].

Dynamic load exhibited on connectors used in the non-traditional ABC bridge pier also warrants an insightful investigation and hence demand rigorous estimation of performance at dynamic load. This present context will help to precisely scrutinize the material behavior and the post impact response of such connectors at high velocity crash load incurred by semi-trailer hit by using uncertainty variables controlling performance level. Adequate investigation due to a high frequency of occurrence of vehicle impact on ABC pier warrants precise attention [7]. This has been recently observed that crashworthiness of pier direly reduces the health, and hence calls for serviceability. The prevalence of the present research studies is carried out to identify various damage levels or increasing survivability [8,9]. On the other hand, connectors such as splice sleeves and high strength grout used in ABC system are commonly used as connectors assembling different bridge components such as beam elements and piers along with the foundations needs additional inspection. Permanent hinges due to large plastic deformation are predicted to be formed in the fragile part of the structural element, envisaging substantial amount of energy dissipation [10]. The introduction of new materials used as connectors in terms of splice sleeves and grouted couplers in withstanding the dynamic load differs from traditional RC pier in a manner that they are expected to behave like higher stiffness's than a single reinforcing bar although the discontinuities of the bar at 'Rebar Stop' takes place to change the energy dissipation path at connector [10,11]. In addition, connectors in order to facilitate the construction method of bridge, formation of the plastic hinge at short duration impact requires rigorous scrutinization. However, this is restricted with the consideration of seismic as specified in the bridge design codes by [12]. Additionally, investigating newer construction methods using connectors, various performance at impacts and their damage levels needs to be assessed under multi-hazard load effects. The combination of sequential loads by virtue of blast and car crash have already been discussed for traditional RC pier using resistance reduction method (RRM).

In performing an explicit evaluation of the post impact behavior of coupler system utilized in ABC needs to be scrutinized. In this present study, geometries of pier proposed by Utah Department of Transportation (UDOT) [12] has been considered and examined for studies. The connectors' details were extracted from manufacturer's data furnished by NMB splice sleeve needs an additional attention. To precisely depict the crash performance of connector, it is placed in the pier- foundation junction. Connectors are embedded in the foundation to understand the complex mechanism as predicted by the composite material's interactive action [13] has further been studied and the report was published by 'Idaho Transportation Department'. In addition, particularly at pier-foundation junction, the most vulnerable part has been predicted and envisaged, as specified in the article [14]. The recommendations help to provide an outline that an increased stiffness of the pier could possibly be utilized in such a way in withstanding dynamic events in an improved manner. Coupler sections consisting of higher stiffness's are scrutinized as a means of increasing resilience of the ABC pier by manifesting enhanced performance at seismic event to overcome plastic hinge formation at the highly expected vulnerable zones [15]. As such, failure mechanism of individual connector necessitates scrupulous examination before recommending it for widespread use [16]. The present study is an attempt to scrutinize depiction of the individual connector in a connector-system inserted in a foundation for examining the apportioned axial and transversal loads transmitted through main reinforcing steel bar. In short, this study aims to discuss the followings:

- Impact behavior along with serviceability criterion of the connectors placed within the foundation of ABC bridge pier at semi-trailer crash has been scrutinized using analytical method through introducing DIF corresponding to reinforcing steel bar.
- To ascertain the impact behavior, numerical analyses have been intensely taken place through finite element analyses (FEA).
- Manufacturer's supplied material data were utilized to conform the FE model, and experimental testing results were utilized to validate the model.
- Investigation of material resilience of connectors behaving as a composite and their endurance level at high velocity dynamic impact warrants accurate calibration before its widespread practical implementation.

2. Specimen's geometry

A splice-sleeve and grouted coupler data extracted from manufacturer's data has been extracted. As specified, connectors are embedded in a foundation cap. The specific sleeve has been investigated for # 8 ASTM 706 steel bar used as main (longitudinal) reinforcement as specified. By using high strength grout, the steel bars are embedded and aligned in place within coupler. Details of prototyped pier geometries and reinforcements are shown in **Figure 1**.

The reinforcement is aligned in such a way to hold in position by high strength grout. Reinforcing steel bars passing all the through pier has been disconnected within connector to dissipate energy as a post impact phenomenon. The prototyped half-sized representative RC pier has been designed in such a way to utilize a recommended characteristic compressive concrete strength of 3 ksi. The main reinforcing steel bar comprises of grade 60 steel (60 ksi yield strength) and has been designed as recommended by [17,18]. Grade 36 steel (36 ksi) has been considered to be used for shear reinforcement (transverse), forming helix as shown in **Figure 1**. Sectional elevation and detailed cross-section (c/sec) of the representative pier are also shown in **Figure 1**.

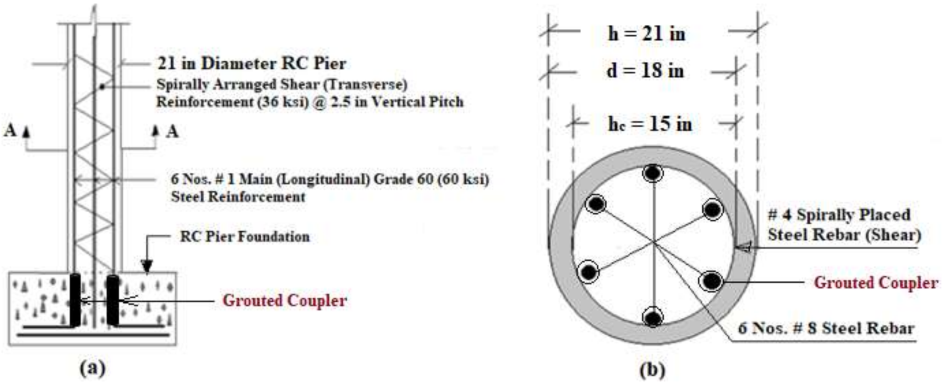

Figure 1. (a) Connector position in the representative pier; **(b)** section A-A.

The pier specimen length is considered as 8.5 feet with a circular c/sec throughout the length. Main reinforcement of six (6) numbers # 8 steel bars all the way to the pier length, followed by a spirally placed transverse reinforcement comprising of # 4 steel (36 ksi) bar @ 2.5 inches (62.50 mm) pitches throughout are kept in the pier specimen. Transverse reinforcement due to withstanding shear limit in a pier specimen provided conforms to the minimum reinforcing shear bar criteria in terms of diameter and pitch as specified in ACI 2011 [19].

3. Methodology

High strain rate dynamic loading incurred from high velocity semi-trailer crash has been considered to investigate for the performance of connectors. The impact performance of the half-sized prototyped representative ABC pier with specified reinforcing steel strength has been utilized as recommended to precisely evaluate deformation at the coupler-steel bar region along with recommended concrete strength while experiencing vehicle hit [8]. The impact subject to concrete strength has been considered as a primary criteria due to its exposed surface is susceptible to car crashes. The impact as primarily experienced by concrete can result significant damage. However, in short, this present study quantifies the distress behavior of the connector embedded at concrete foundation receiving impact from high velocity semi-trailer.

To keep connectors at position, connectors are placed as shown in **Figure 1**. Post impact behavior load transmittance via predicting material properties of the connector is determined by apportioning the load as modelled. The post impact coupler performance has been investigated by carrying out FEA. Material properties are collected from manufacturer's data and used to carry out simulations. Short duration impact performances are considered to examine failure patterns through conducting static and dynamic numerical simulations via FEA. The results captured from FEA has been validated with experimental data to determine DIF's. The respective simulations are conducted by using ANSYS WORKBENCH. The respective DIFs's determined from FEA and damage index (DI) method are correlated followed by validating with the results published in the research article [8]. The results are further corroborated by carrying out the reliability analysis by estimating reliability index (β).

Properties of connector

Connectors using sleeve and grout as a composite section have been investigated using standardized geometries and material properties as shown in **Figure 1** [20,21]. To put together the precast components of the connector in place needs special detail to behave as a composite section. This type of connection is expected to predict improved performance to withstand short duration, high strain rate dynamic load exerted by high velocity vehicular impact.

Geometrical details of coupler have been considered in this study followed by the standardized specification as recommended. The typically used in ABC connector specified as sleeve number 8U-X that has been shown in the **Figure 2** and **Table 1**. 'Rebar Stop' is shown within the sleeve where reinforcing steel bar has been discontinued. Splice-sleeves made up of cast iron has been used for grouted coupler composite inserted within in the pier along with reinforcing steel bar is embedded, placed, and aligned as shown in **Figure 2**. This arrangement has been made to predict enhanced performance in dynamic response via energy dissipation [12]. The sleeve is filled up by high strength cement grout to hold the steel bar in place with a discontinuation at 'Rebar Stop' as shown in **Figure 2**.

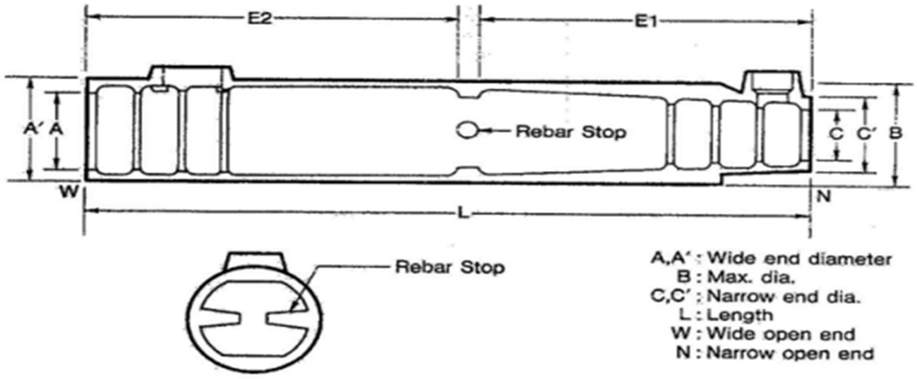

Figure 2. Details of connector [20].

Table 1. Geometry of sleeve number 8U-X [21].

Sleeve zone	Sleeve type	Internal dia. (inch) (mm)	External dia. (inch) (mm)
W = Larger end	8U-X	1.89 (48.01)	2.52 (64.01)
N = Smaller end	8U-X	1.3 (33.02)	2.52 (64.01)

To determine the post impact performance and ascertain the expected plastic deformation, connectors are inserted in stratagem in the region where high stress zones are expected to be formed due to impacting force incurred by high velocity vehicle crash. In addition, with the placing of connector into the foundation has been recommended and as followed by [14]. The connector (grouted coupler) is positioned within the pier section as described in **Figure 1**. Sleeve data has been extracted from manufacturers catalogue has been described in **Table 1** and is as shown in **Figure 3**. Boundary conditions of the prototyped per specimen has been modeled as the upper and lower ends are restricted from rotation and deflection while upper end is positioned under the axial compression as shown in **Figure 3**. The impact point of pier specimen has been taken at 3 feet (0.914 m) from the foundation top as also shown in **Figure 3**.

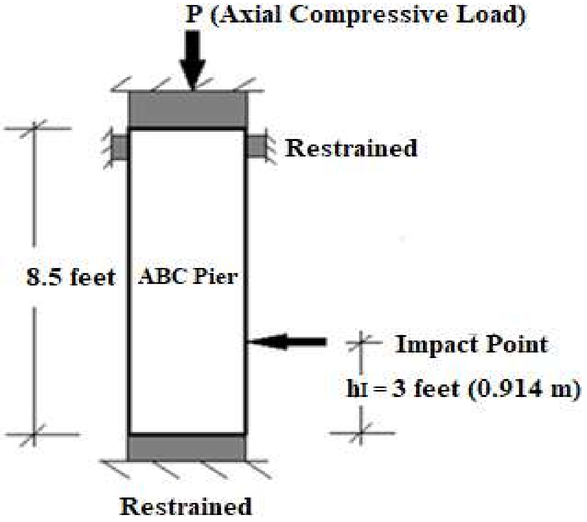

Figure 3. Impact location and boundary conditions.

4. Post-crash behavior of representative bridge pier at dynamic load

Present study investigates that the high velocity impact damage of connector placed within the ABC pier by vehicular. This type of collisions and formation of localized damage along with concrete spalling has been a significant trend. Frequency of occurrence of vehicular crash causing damage seems surpassing the other high strain rate loads like earthquakes and blasts [16]. Furthermore, this can trigger not only deterioration of the pier from cosmetic to collapse but involves overall infrastructural degradation as stated in different studies [22]. High velocity impact from larger vehicles and its severity has received adequate attention. However, specific performance of connectors at high velocity impact experienced from semi-trailer has not yet been fully examined. The connector and steel bar junction region are expected to evince pertinent stress limit over the stress resulted by impact for ensuring serviceability criteria. Expected plastic hinge is likely to be formed at 150% of the yield strength as specified of inserted reinforcing steel bar as recommended by [15]. Stresses are estimated using FEM to examine the connector and steel bar at post performances. The mobile dislocating velocity increases at a higher rate to accommodate the required plasticity has already been discussed [22]. Results captured from post deformed models are considered for analyzing performance behavior. This leads to accomplish rate sensitivity analyses through high stresses induced resulting large deformation taken place.

4.1. Flexural properties of connector

Flexural properties have been determined from withstanding axially compression static load (P_n) of the specimen and shall be determined by using Equation (1).

$$P_n = 0.85 \times f_c'(A_g - A_s) + A_s f_y \qquad (1)$$

where: A_g and A_s indicate c/sec areas of pier and the area of longitudinal steel, and f'_c and f_y conforms the concrete strength in compression at 28 days and reinforcing steel bar in tension.

Post impact performances of the coupler model hit by fractioned transmitted has been studied for flexure and shear. Determination of transmitted loads passing through the longitudinal axis of column specimen and via respective main reinforcing steel bar are included in respective **Tables 1** and **2**. The evaluated results comprising axial compressive force carried out by the pier specimen has been shown in **Table 2**.

Table 2. Pier geometry and material properties.

f'_c (ksi) (MPa)	f_y (ksi)(MPa)	A_g (in^2) (mm^2)	A_s (in^2) (cm^2)	P_n (kips) (kN)
3 (20.68)	60 (413.68)	346.50 (2235.48)	4.70 (30.32)	1310 (5827.17)

Apportioned axial load transmitted by the column specimen has been incurred by each connector pier has been evaluated via each elements considering a composite sectional phenomenon. Axial compression governed by each connector conforming material properties and geometries obtained from the literature can be determined through Equation (2).

$$P_{n,s} = (P_n) \times \left[\frac{A_{CI} \times E_{CI} + A_{Grout} \times E_{Grout}}{A_{net} \times E_{Concrete} + A_s \times E_s}\right] \times \eta \qquad (2)$$

where: P_n and $P_{n,s}$ express the design axial loads (compression) of the specimen and fractioned each reinforcing steel bar respectively; A_{CI}, A_s, and A_{Grout} express overall cross-sectional area (c/sec) of cast iron component of the splice sleeve, c/sec area of main reinforcement, and c/sec area of filled and compacted grout; E_{CI}, E_{Grout}, $E_{Concrete}$, and E_s indicate respective material moduli of the hollow splice sleeve made up with cast iron, high strength grout, peripheral concrete, and main reinforcing steel bar; and η is the energy dissipation factor. To analyze the coupler behavior, $E_{Concrete}$ is considered as 2.65 psi, and the respective values of E_{CI}, E_{Grout}, and E_s are considered.

The apportioned axial compressive force transmitted into each connector has been evaluated by Equation (2) yielding 3.01 kips (13.38 kN).

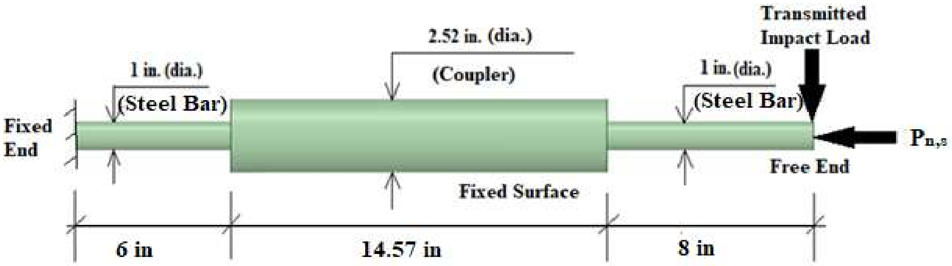

Figure 4. Load model of coupler and main steel bar.

$A_{connector}$ indicates the simple scaler addition of hollow cylindrical splice sleeve (cast iron) c/sec and c/sec of high strength cement grout. From geometry, $A_{connector}$ can be deduced by summing up A_{CI} and A_{Grout} using **Figures 4** and **5** and is shown in Equation (3).

$$A_{connector} = A_{CI} + A_{Grout} \tag{3}$$

where: $A_{connector}$ is the gross c/sec area of connector filled up with high strength cement grout; and A_{CI} and A_{Grout} are already explained as shown in **Table 3**.

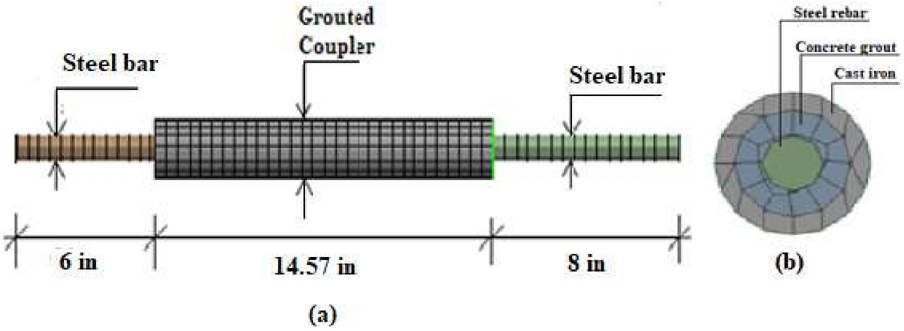

Figure 5. Mesh of grouted coupler for **(a)** longitudinal view; **(b)** top view.

Using **Table 1**, and **Figures 4** and **5**, $A_{coupler}$ can be evaluated as 2.20 in^2 (14.20 cm^2).

The transmittance of impact force into pier specimen under axially transferred preload and the inter-materialistic interaction of the composite connector needs an insight to inspect the complex mechanism during and after high strain rate vehicle crash. However, initially shear force administers the post impact behavior and is followed by the force due to flexure which brings about an intricate phenomenon. Axial force being a secondary controlling factor for which the vehicle crash is governed, an imperceptible amount of apportioned axially compressive force (η is approximately considered as 0.2% due to energy dissipation effect) has been transmitted to the connector composite after being dissipated a considerable amount of energy. To alleviate the effect of modulus of individual composite material in controlling the impact mechanism, Equation (2) has been simplified and approximated. This results a close proximity following same outcome within a minimal of 2.9% variation can be precisely estimated by using Equation (4).

$$P_{n,s} = P_n \times \left[\frac{A_{connector}}{A_{net}}\right] \tag{4}$$

where: P_n, $P_{n,s}$ and $A_{connector}$ are already explained; A_{net} expresses net c/sec area of the connector.

The fractioned design loads resulted from Equation (1) through Equation (4) are given in **Table 3**.

Table 3. Design values of respective axial loads.

P_n (kips) (kN)	$P_{n,d}$ (kips) (kN)	$P_{n,s}$ (kips) (kN)
1308.20 (5819.16)	1310 (5827.17)	3.01 (13.38)

4.2. Estimation of DIFs

The DIFs in reinforcing steel (dynamic increase factor) has been evaluated by the ratio of the dynamic over static counterpart forces incurred by high strain rate loading of the specific element as recommended [23]. Longitudinal steel bar used as main reinforcement in the pier being considered as an isotropic and homogeneous material can be most likely to dissipate higher percentage of energy and carries out relevant amount of impact load. Determination of DIF for main reinforcing steel bar needs to be essentially evaluated the static counterpart of shock exerted by high velocity semi-trailer crash. This has been put together and shown in **Table 4**.

Table 4. Determination of dynamic coupler moment.

I_S (kips) (kN)	h' (feet) (m)	M_s (kip-ft) (kN-m)	DIF	M_{dyn} (kip-ft) (kN-m)
3271.89 (14,554.12)	3 (0.91)	22.26 (30.16)	1.053	23.44 (31.78)

Impacting vehicular weight (W) along with the crashing velocity (V) of the semi-trailer are considered as 42.11 kips (187.30 kN) and 100 ft/s (30.48 m/s) respectively conforming standardized specifications. Permissible vehicular speed has been considered as recommended in the standardized specification [24]. Determination of DIF as a pertinent criterion of vehicular impact needs to be evaluated. Dynamic flow stress (σ_{dyn}) of main reinforcement during high strain rate vehicle crash has been estimated by using Equation (5), as recommended by [3].

$$\sigma_{dyn} = (\sigma_y) \times \left[1 + \left(\frac{\acute{\varepsilon}}{C}\right)^{1/p}\right] \tag{5}$$

where: σ_y is a static flow stress of for ASTM A 706 (ASTM 2015) using Grade 60 steel bar and is considered as 60 ksi (420 MPa); C addresses as material coefficient and p indicates the strain rate parameters which are considered as 40 and 5 respectively [9]. Rate of change of strain with the time of main reinforcing steel bar ($\acute{\varepsilon}$) has been utilized as 0.16 s^{-1} for specific vehicle crashing high velocity speed at 100 ft/s (30.48 mtr/s). Severity of damage level during high-speed vehicle collision considering non-linear trend of transverse loading incurred from horizontal impact has been estimated [25]. Using Equation (5), σ_{dyn} (Dynamic flow stress) has been determined that yields the result as 79.80 ksi (550.2016 MPa).

Using Equations (3) through 5, the dynamic parameter 'ψ' can be determined by utilizing the Equation (6) as recommended by [26,27].

$$\psi = 0.019 - (0.009) \times \left[\frac{\sigma_{dyn}}{60}\right] \tag{6}$$

where: ψ is termed as dynamic parameter which is a function of yield stress at the strain hardening zone, and σ_{dyn} is the dynamic flow stress at uniaxial plastic strain rate of steel.

Equations (6) results ψ as 0.0172 after inserting σ_{dyn} using Equation (4) as 79.80 ksi.

Dynamic Impact factor of the main reinforcement (DIFs) can be estimated from Equation (7) by using ψ correspondingly evaluated from Equation (7) [27].

$$\text{DIFs} = \left(\frac{\acute{\varepsilon}}{10^{-4}}\right)^{\psi} \tag{7}$$

where: DIFs and ψ are already explained; and $\acute{\varepsilon}$ expresses as strain rate of main reinforcing steel.

Analytical estimation of DIF using Equation (7) has been evaluated as 1.053.

4.3. Computation of analytical static and dynamic forces of coupler

Static impact force (I_S) due to vehicular collision can be estimated by using Equation (8).

$$I_S = \frac{W \times V}{\tau} \tag{8}$$

where: I_S addresses impact force at static condition, W indicates the weight of semi-trailer (42.11 kips or 19099.87 kg-wt); V is expressed as the maximum permissible crashing speed being considered as 100 ft/s (30.48 m/s) [3], τ is crashing time from impact till post impact deformation being considered as 40 ms (milli-second) [3], and h_I has been considered as the height of impact as shown in **Figure 3**.

Inserting the values in Equation (8), yields I_S as 105270 kip-ft/s^2 or 142,114.50 kN-m/s^2 (corresponding equivalent load is 3271.896 kips or 14,554.12 kN) [28,29].

Pier experiencing equivalent static moment (M_s) can be estimated from Equation (9) using I_s and h_I.

$$M_s = I_S \times h_I \tag{9}$$

where: I_s and h_I have already been expressed.

Approximated load apportioning has been executed in a simplified way after multiplying M_s as shown in Equation (8) with area ratio expressed as $A_{connector}/A_{net}$. This leads to estimating the static moment incurred by a single connector ($M_{s,c}$) as furnished in Equation (10).

$$M_{s,c} = M_s \times \left[\frac{A_{connector}}{A_{net}}\right] \tag{10}$$

The corresponding dynamic moment exerted by single connector ($M_{dyn,c}$) can be estimated via DIF multiplied with $M_{s,c}$ as shown in Equation (11).

$$M_{dyn,c} = \text{DIF} \times M_{s,c} \tag{11}$$

where: $M_{s,c}$, $M_{dyn,c}$, and DIFs are already addressed.

Equation (10) yields $M_{s,c}$ as 22.26 kip-ft (30.17 kN-mtr). The corresponding $M_{dyn,c}$ has been determined by Equation (11), resulting as 23.44 kip-ft, (30.18 kN-mtr). The resulting moments at connector and steel bar junction are as shown in **Table 4**. As the dynamic properties cannot be estimated directly due to short duration collision strike, it can be indirectly determined by using the DIFs [10]. Semi-trailer vehicle weight [30] has been considered for evaluating impact force and utilized from the data given and as shown in **Table 4**.

The apportioned loads transmitted to the single coupler composite via reinforcing steel of the connector system has been determined for axial compression ($P_{n,s}$) evaluated as 3.01 kips (13.40 kN) that has been already discussed in Section 3.1. The fractioned transverse load as modelled at the free end of individual reinforcing steel bar (longer edge as shown in **Figure 4**) are developed from the static moment (M_s) as a result of the vehicle crash, which additionally incurs moment at connector and steel bar junction comprising of conservative analyses. Using Equation (10), M_s has been evaluated as 22.26 kip-ft. (31.54 kN-m) which results high stress in the coupler-steel bar junction depicting large deformation for both static and dynamic analyses. Energy dissipation is expected to be taken place considerably during and immediate after the impact expecting large plastic deformation to be occurred as the stiffness's of the members warranting flexural resilience being reached at elastic-plastic state [30].

5. Numerical modeling (FEM) of grouted coupler

Numerical simulations are conducted by using FEM which has been used to assess the individual connector performance. Commercially available 'ANSYS' has been extensively used to evaluate static and explicit dynamic performances. To develop the FE model, hollow cylindrical cast iron splice-sleeve conforming strength of 36 ksi (248 MPa) is used along with 6 ksi (41.36 MPa) cement grouting and # 8 reinforcing steel bar embedded into the grout, as shown in **Figure 2**. For all different material's connections, composite coupler system has been considered for developing the FE model. The mesh size considered for the simulations by going through mesh-independence studies and is considered as 0.01 in. (0.254 mm). Reinforcing steel bar conforms specified yield strength (60 ksi or 420 MPa) are embedded and extended from coupler in both sides are 8 in. (20.32 cm) and 6 in. (15.24 cm) respectively, as shown in **Figure 4**. The external peripheral surface of the splice-sleeve is considered as fixed as it is embedded and placed within the foundation concrete. The free end of the 6 in. side is also considered as fixed (as shown in **Figure 4**) as it is extended within the foundation receiving adequate development length.

FEA models are generated in such a way where the apportioned axially compressive load and moments are transmitted via incorporating area ratio described as ($A_{coupler}/A_{net}$). To compare and validate the DIF's computed from FEM and the analytical formulations, stress ratio ($\sigma_{dyn}/\sigma_{static}$) is considered via using $\acute{\varepsilon}$ as shown in Equation (4). Apportioned horizontal (shear due to impact) and axial (flexure due to axial bending) forces are exerted on the model from the respective forces force of pier deployed at the free end (8 in. edge of steel bar from pier base and foundation top within pier) and is shown in the **Tables 3** and **4**. Boundary conditions of the FE model are elaborately furnished in **Figure 4**.

Table 5. Manufacturers supplied material properties [15].

SL. No.	Properties	Cast iron	Grout	Steel bar
1	Density (pci) (kN/m^3)	0.284 (77)	0.083 (22.53)	0.284 (77)
2	Modulus of Elasticity (psi) (MPa)	29×10^6 (2×10^5)	43.51 (0.3)	29×10^6 (2×10^5)
3	Poisson's ratio	0.3	0.3	0.3
4	Bulk modulus (psi) (MPa)	2.42×10^7 (1.6×10^5)	2.26×10^6 (1.6×10^4)	2.42×10^7 (1.6×10^5)
5	Shear modulus (psi) (MPa)	1.12×10^7 (7.7×10^4)	1.84×10^6 (1.26×10^4)	1.12×10^7 (7.7×10^4)
6	Tensile yield strength (psi) (MPa)	3.62×10^4 (249.6)	0	3.62×10^4 (249.6)
7	Tensile ultimate strength (psi) (MPa)	3.62×10^4 (249.6)	0	6.67×10^4 (459.8)
8	Compressive ultimate strength (psi) (MPa)	0	5.95×10^3 (41.02)	0

Material properties are extracted from manufacturer's (NMB Splice Sleeve Inc., North America) data to develop composite FE model. Using this, FE model has been developed to carry out simulations under high velocity vehicle impact. In addition, **Table 5** illustrates the manufacturer's supplied material properties that have been collected and utilized to develop FEM.

5.1. Connector composite meshing system

The connector along with the embedded reinforcing bars are meshed for the analyses and is considered as 0.01 in. as shown in **Figure 5**. All elements conforming square mesh has been considered. Mesh sizes are further reiterated from 0.1 in., and 0.05 in. respectively to carry out the sensitivity analyses showing if any variation in the results can be apprehended. For all three different materials, a composite system has been modelled to be incorporated and acting as a monolithic composite behavior under the specific load as shown in **Figure 4**. However, **Figure 5** shows FE model represents mesh independence with its size converges at 0.01 in^2 (0.254 mm^2).

5.2. Mesh sensitivity (refinement) study of FEM

Mesh independence studies are performed for respective mesh sizes of 0.1 in., 0.05 in. and 0.01 in, where results from Von-mises stress, strain and total deformation are considered. Simulations are carried out for both static and dynamic impacts. Different mesh sizes are considered for examining mesh convergence and thus the optimization via mesh refinement has been obtained. Mesh sizes utilized for pursuing the simulations show the results are within permissible range. To conduct static and explicit dynamics analyses, mesh sizes are conformed to 0.01 in^2 (0.254 mm^2) through performing sensitivity analysis. Results captured from static and explicit dynamic are plotted in **Figures 6–8** respectively considering mesh sizes comprising deformation and strain. Static analyses show the linear trends while dynamic analyses contemplate non-linear trends to come up with the optimal mesh size.

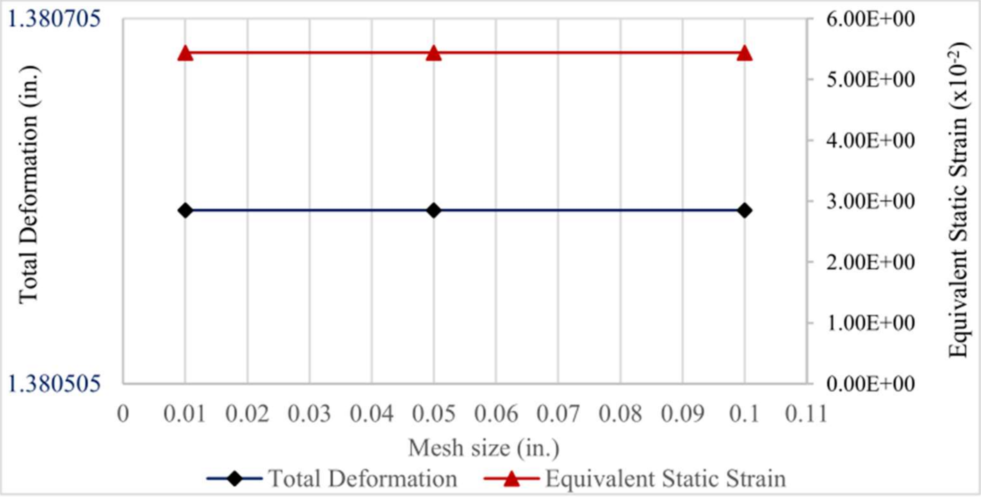

Figure 6. Results for mesh independence for static deformation and strain.

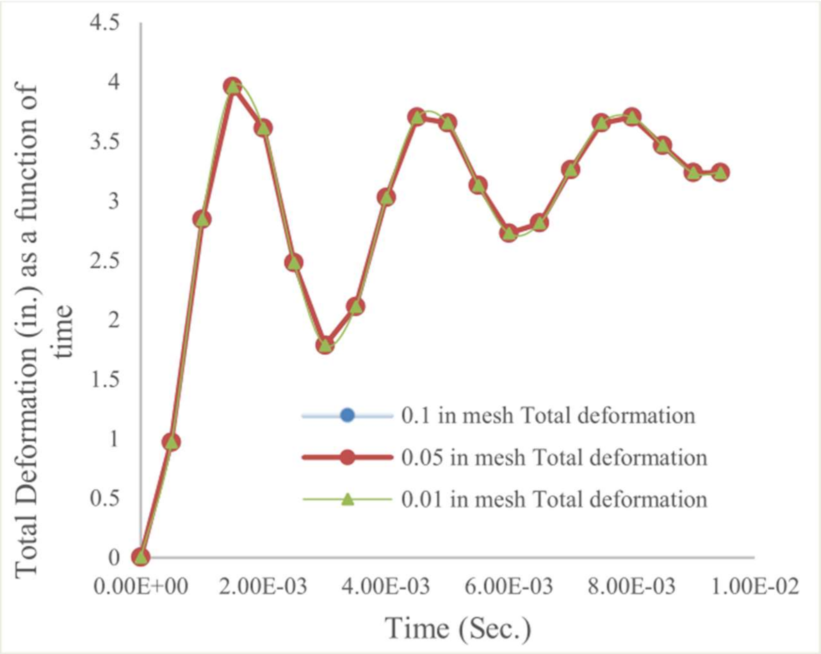

Figure 7. Dynamic mesh independent results for deformation.

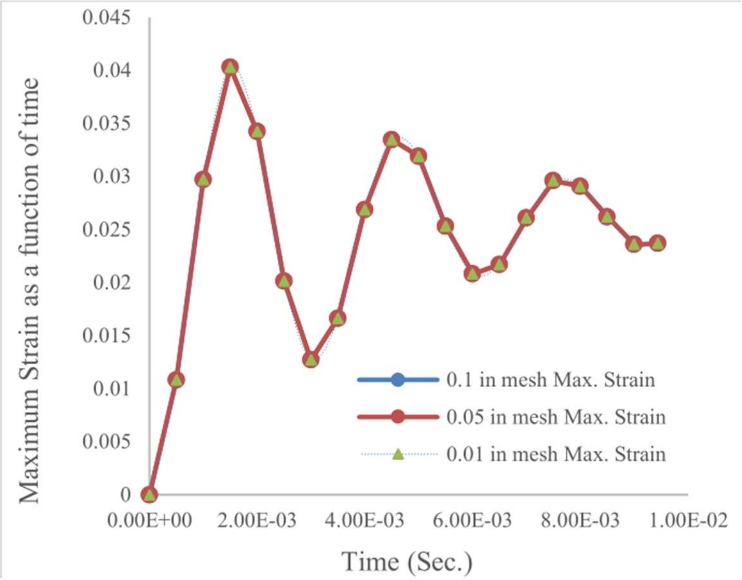

Figure 8. Dynamic mesh independent results for maximum strain.

5.3. Uncertainty assessment using confidence interval (CI)

Confidence Interval (CI) has been utilized to capture the degree of uncertainty for assessing the numerical results evaluated from dynamic simulation using normal distribution. CI is also able to evaluate the probability that a parameter falls between a pair of values around the mean. Thus, the confidence interval (CI) is utilized to assess uncertainty, and determined via using mean (μ), standard deviation (SD), confidence level (z) and sample size (N) (as shown in **Table 5**), and is as shown in the Equation (12). CI helps provide to assess the role of uncertainty parameters during car crashes.

$$\mathrm{CI} = \mu \pm z \times \left[\frac{SD}{\sqrt{N}}\right] \tag{12}$$

where: μ is the mean of sample size, SD is the standard deviation, N is the sample size considered as one thousand data, and z is the confidence or significance level considered as 98%.

CI data to capture the uncertainty is shown in **Table 6**.

Table 6. Input data for CI.

Input variables	σ_D (psi)	εD	E_D (psi)
Significance Level (z)	0.02	0.02	0.02
Mean (μ)	668,798.4	0.023975	32,417,194
Standard Deviation (SD)	628,000	0.008989	628,000
Sample size (N)	1000	1000	1000

5.4. Reliability analysis

Monte Carlo simulations being expensive and requiring millions of simulations, moment-based methods such as the Hasofer-Lind reliability index (β) method is one of these methods that was developed as an alternative to the simulations and has been recognized as an effective and precise method to estimate structural safety. This method is considered in this study for its advantage over other moment-based methods including its invariance to the specific form and not requiring prior knowledge of the distributions of the variables.

5.4.1. Integrity analysis

To estimate β via integrity analyses using factor of safety (F) from using results extracted from FE results as shown in **Table 4**, Equation (13) can be fairly used [31,32]. The Hasofer-Lind reliability index [33] is computed using an iterative procedure involving reduced variates, using factor of Safety (F) from the materials integrity, capturing data from FEA and variables as computed in [34,35].

$$\beta = \frac{E(F) - 1}{SD \times (F)} \tag{13}$$

where: β is the reliability index, F (moduli of dynamic over static using numerical simulation) is the factor of safety computed from dynamic simulation results, E is the modulus of elasticity and SD is the standard deviation.

5.4.2. Direct reliability index

Performance reliability *(β)* of the individual coupler is further determined directly by using the probability of failures (P_f) resulted from dynamic simulation [32]. Results from the dynamic analysis is utilized as modulus of maximum elasticity (E) in demand utilizing dynamic DIF resulted from simulation (shown in Equation (10), E as 30×10^6 psi), as it exceeds the material E-modulus (29×10^6 psi). Maximum resulted stresses and strains from dynamic numerical simulations in terms of E-modulus in demand due to post impact behavior are captured to evaluate dynamic amplification effect (DIF) as 1.07 through the ratio of dynamic moduli (dynamic modulus/static modulus) draw an insightful correlation between DIF's computed analytically as 1.053. This result triggers to evaluate failures and corresponding reliabilities of coupler. Performance reliability (β) of the individual coupler can also be computed directly from probability of failure (P_f) is evaluated from the DIF's with a difference of 1.6% which results as 0.0021 by using the inverse of the standard normal cumulative distribution functions of probability of failures (P_f) resulted from direct approximation method and is as shown in Equation (14) [33].

$$\beta = -\Phi^{-1}(P_f) \tag{14}$$

where: P_f is the probability of failure and Φ^{-1} is the inverse of the standard normal cumulative distribution function.

6. Results

6.1. Results using FEM

Results captured from using FE models shows substantial deformations along with high stress and strain are also observed. Large deformation at the free end of bar where loads are applied depicts failure occurring at the junction of steel bar and connector.

6.1.1. Static analysis

Results from static analysis present considerable deformation at the main reinforcing steel bar. Deformations in both X and Y directions seem uniform, as 0.12 in. (0.004 mm.) and as shown in **Figure 8**. High strain concentrations and significant stress are observed in the contact of grouted coupler and steel bar as shown in **Figure 9** through 11. Maximum permissible material modulus instilling material modulus (Maximum stress/Maximum strain) requirements are observed from the simulation results subjected to static strain yields as 1.38 (as shown in **Figure 10**) and static stress (as shown in **Figure 11**) comprises 8.51×10^5 psi (5.8×10^3 MPa). The deformations are observed in both the directions and estimated as 1.375 in. (34.925 mm) and 0.12 in. (3.02 mm) for static (**Figure 12**), and 2.38 in. (60.45 mm) and 0.11 in. (2.80 mm). The material modulus in demands depict as 6.17×10^5 psi (7.57×10^5 MPa) for steel bar at the coupler junction. This endorses material property can be safe enough as modulus of elasticity incorporating reinforcing steel bar has been commonly considered as 29×10^6 psi.

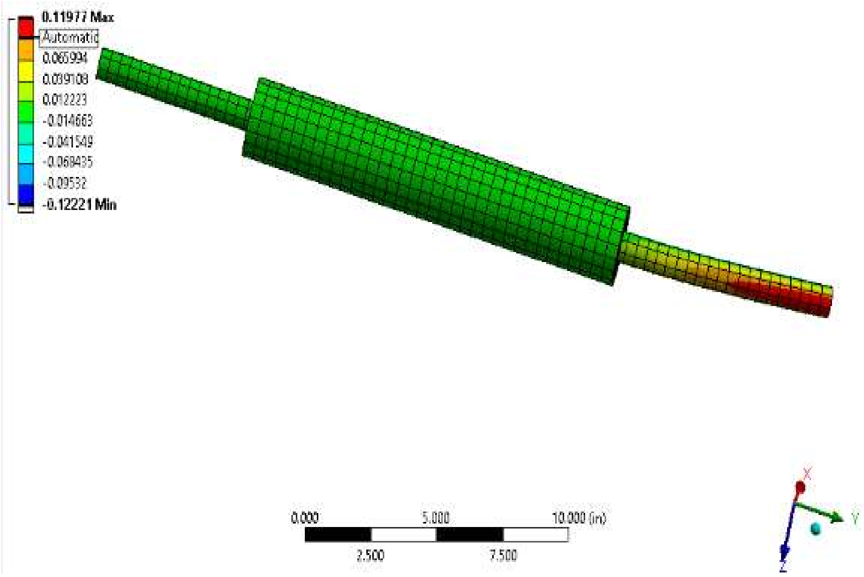

Figure 9. Directional deformation.

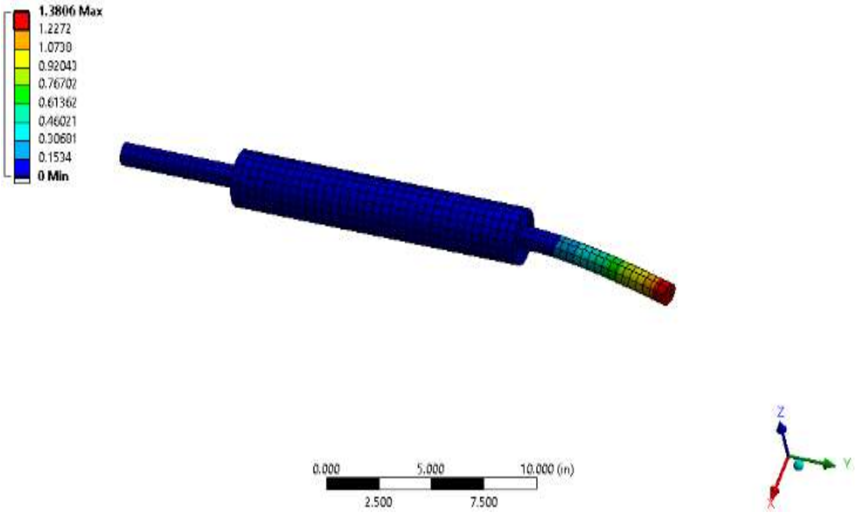

Figure 10. Static strain.

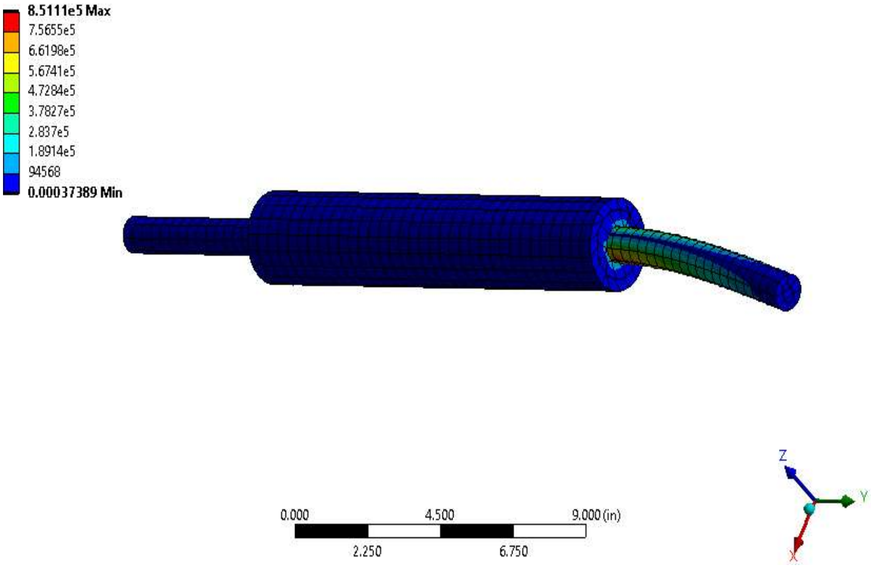

Figure 11. Static stress.

Dynamic results incorporating time-dependent studies are shown in **Figure 12**. This also observes directional deformations and provide quite different results in the respective directions (3.15 in. and 0.12 in.) along *X* and *Y* as shown in **Figure 12a,b** respectively with tight R^2 values of 0.999 and 0.996 which conform optimistic trend of static strain and stress.

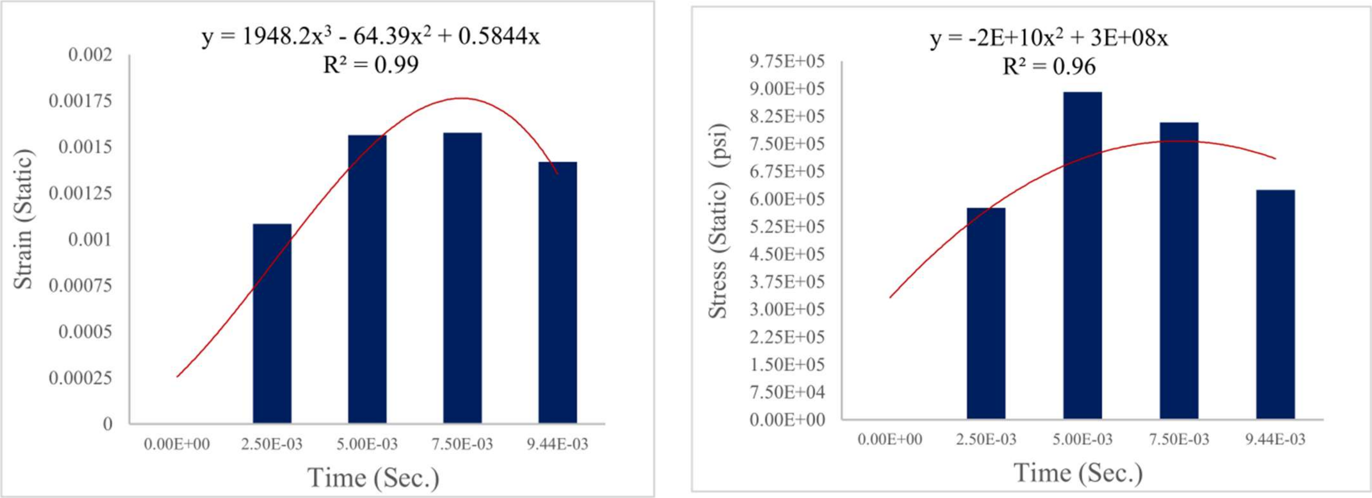

(a) **(b)**

Figure 12. (a) Time-dependent static strain; **(b)** time-dependent static stress.

6.1.2. Dynamic analysis

Results from explicit dynamic analyses show significant deformation at steel bar as high stress and strain have resulted at the junction as shown in **Figures 13–15**. Maximum permissible material modulus (Maximum Dynamic Modulus = Maximum dynamic stress/Max. dynamic strain) at dynamic load requirements from simulations subjected to dynamic stress and strain are 6.25×10^5 psi (1.82×10^5 MPa) and 0.2 which are exceeded by the material E-modulus. Using maximum dynamic stress (**Figure 14**) over dynamic strain, modulus in demand (maximum dynamic stress/maximum dynamic strain) is computed as 31.25×10^6 psi (2.15×10^5 MPa), whereas material E-modulus is commonly considered as 29×10^6 psi (2.1×10^5 MPa). However, demand of material modulus for dynamic over material from FE analysis is computed as 1.07, whereas the numerical DIFs is computed as 1.053. For dynamic analyses, results captured for parallel and perpendicular to the application of load have been shown in **Figure 16**. Time-dependent dynamic strain and stress are captured and are shown in **Figure 16**.

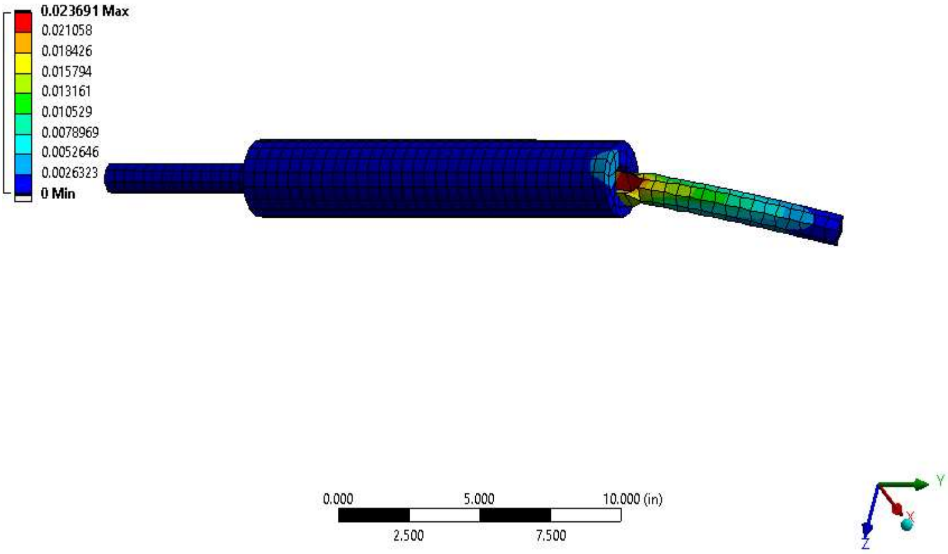

Figure 13. Directional deformation.

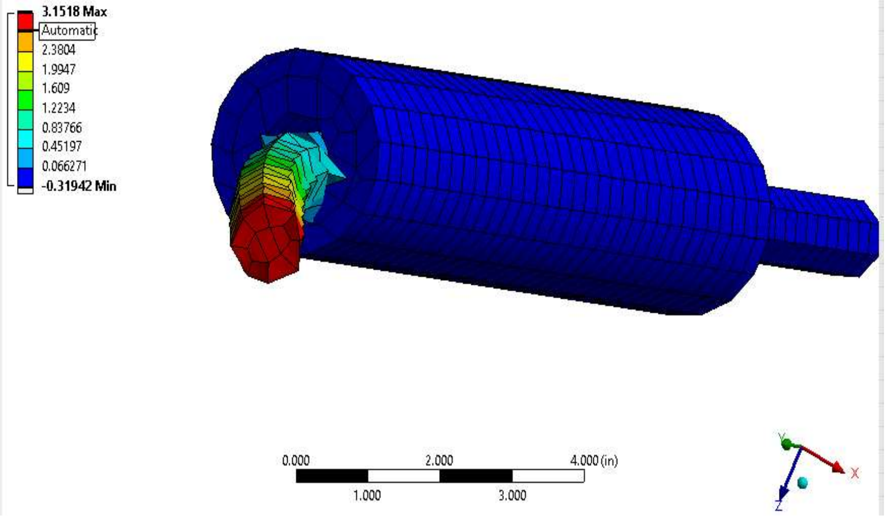

Figure 14. Dynamic strain.

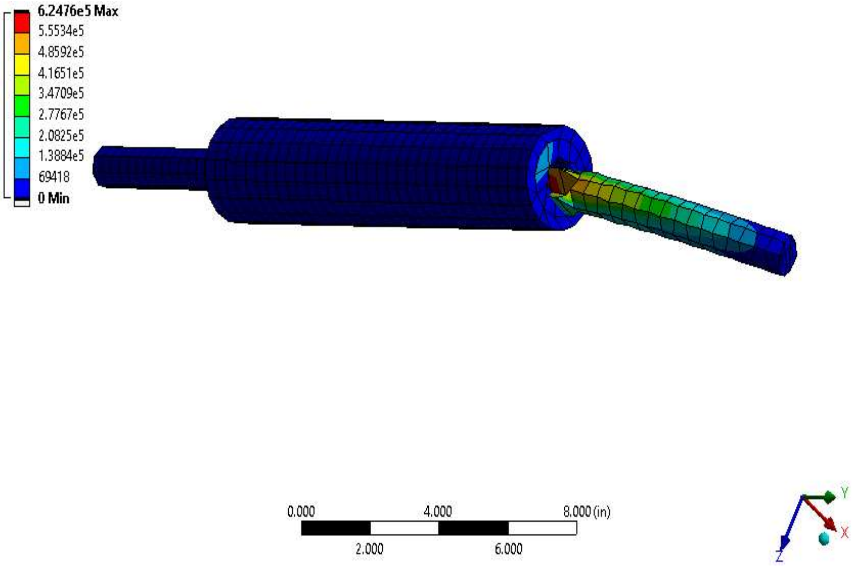

Figure 15. Dynamic stress.

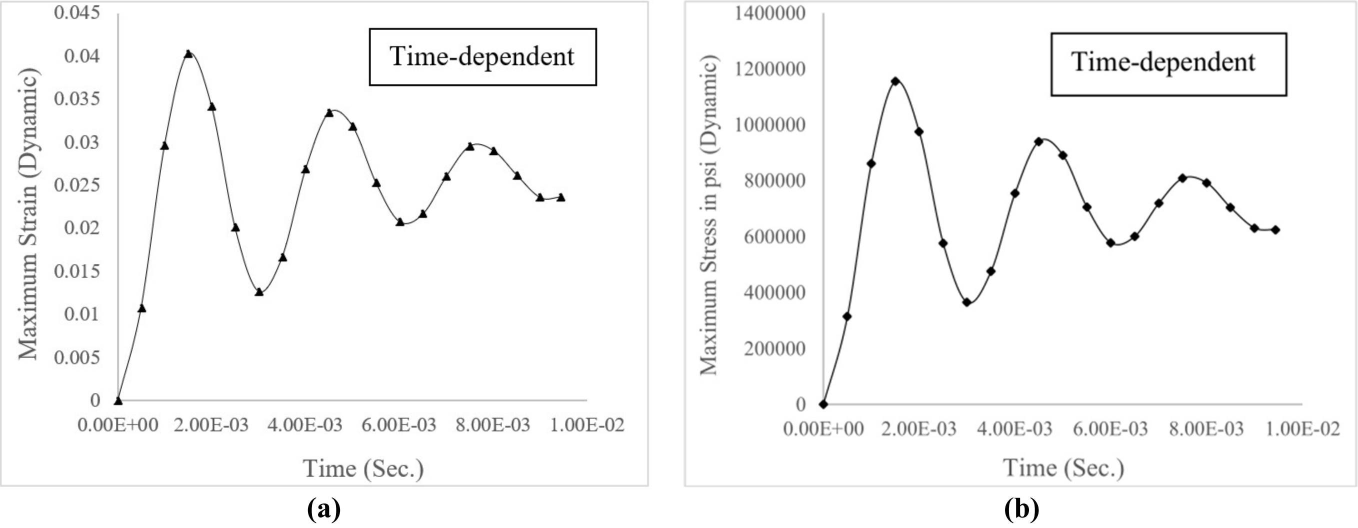

Figure 16. (a) Dynamic strain; **(b)** dynamic stress.

Transmitted dynamic impact load parallel and normal to the external applied loads resulting large deformations are captured are shown respectively in **Figure 17a,b**. Resulted deformation that takes place parallel to the load seems significantly higher than that of the normal. To avoid the discrepancies in capturing deformations at different directions as a function of time, dynamic simulation has been carried out to determine maximum plastic deformation. **Figure 17** shows the deflection behavior at the post impacted distress.

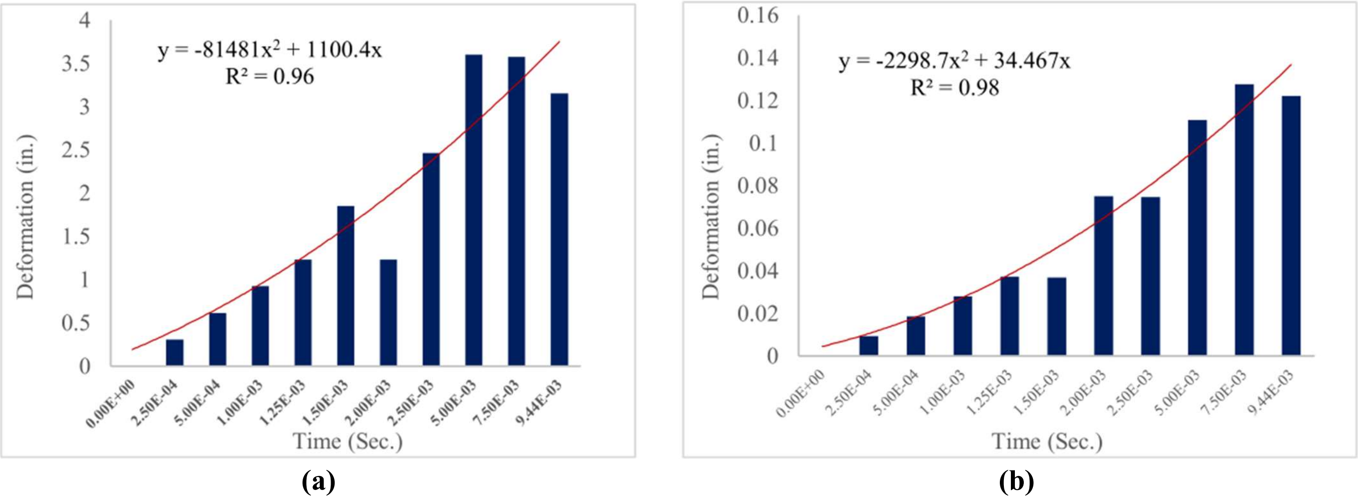

Figure 17. (a) Deformation parallel to load; **(b)** deformation normal to load.

In **Figure 17a,b**, the respective captured deformations from FE simulations confirm the trend patterns are proximately justifiable as the respective R^2 values are shown as 0.96 and 0.98.

6.2. Regression results of dynamic analysis

Resulted stress corresponding to plastic strain captured and plotted from dynamic simulations can well estimate the non-linear trend of material performance via regression analysis. To come up with the non-linear trend via evaluating of performance function (*g*), the resulted dynamic stress and strain at plastic zone are plotted as shown in **Figure 18**.

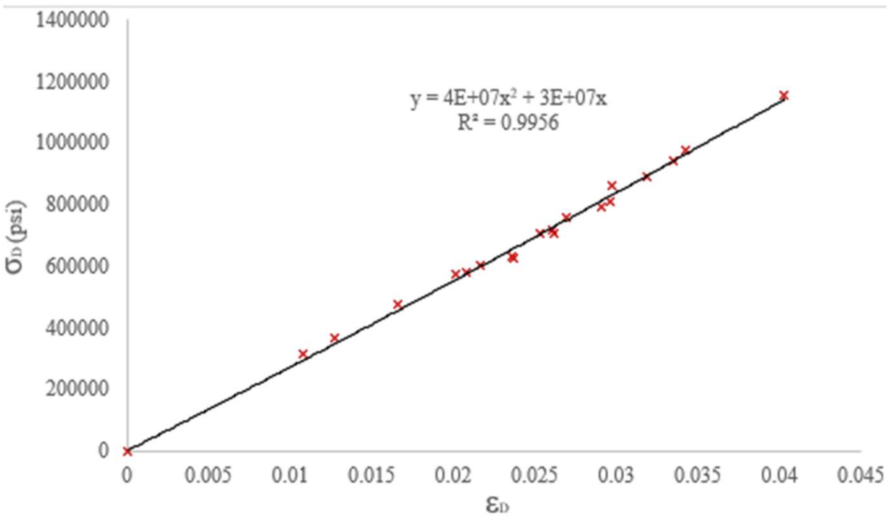

Figure 18. Result of dynamic stress and strain.

As shown in **Figure 18**, regression results are plotted with the observed R^2 yield as 0.99.

$$g(\sigma_D, \varepsilon_D) = \sigma_D - 4.10^7 \times (\sigma_D^2) - 3.10^7 \times (\varepsilon) \tag{15}$$

where: σ_D expresses dynamic stress concentration, ε_D is the dynamic strain, and g is the post impact performance function.

6.3. Model integrity analysis

Anomalies in the results captured from static and dynamic simulations and complexities involved to control material behavior at post impact performance. Exceeding dynamic over static material modulus at plastic zone, and dynamic results for material modulus in demand are governed to carry out integrity analysis of the model. Integrity analysis includes statistical parameters of mean (μ), covariance (V) and standard deviation (SD) resulted from dynamic simulations and is given in **Table 7**. To carry out simulations, one thousand data comprising of dynamic stress and strain were developed by using random variables depicting dynamic stress (σ_D), dynamic strain (ε_D), and material modulus considered between yield to plastic zone (E_D). The computations have been conducted using EXCEL by generating RAND function. This has been inculcated from random variables to run the regression analysis (**Figure 19**). Integrity analysis has been conducted from using the dynamic simulation results utilizing **Table 4**.

Table 7. Variables μ, V and SD.

Variables	μ	V	SD
σ_D	6.74×10^5 psi (4647.06 MPa)	0.383	2.58×10^5 psi (1778.84 MPa)
ε_D	0.024	0.38	0.0091
E_D	2.65×10^5 psi (1827.11 MPa)	0.237	6.28×10^5 psi (4329.91 MPa)

The respective statistical parameters μ, *V* and *SD* are utilized for obtaining the respective dynamic parameters σ_D, ε_D and E_D. The dynamic parameters are also extracted from the simulation results executed from the simulated results captured from FE analyses.

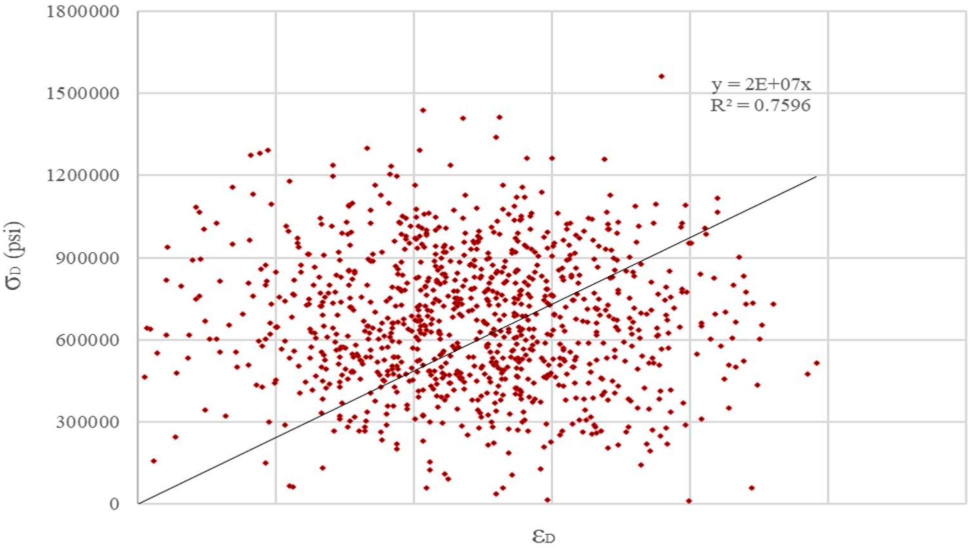

Figure 19. Dynamic stress and strain results using integrity analysis.

With the virtue of regression analysis, results from explicit dynamic undergoing FEA are captured and plotted, and as shown in **Figure 19** in terms of performance function (*g*) which is given Equation (14). This equation will help to provide higher precision via linearizing results with a relatively flexible R^2 value of 0.76.

$$g(\sigma_D, \varepsilon_D) = \sigma_D - (2 \times 10^7) \times (\sigma_D^2) \tag{16}$$

where: *g*, σ_D and ε_D are already explained.

6.4. Performance reliability of coupler

The results comprising reliability indices based on vehicle impact performance for RC ABC pier is determined and as shown in **Figure 20**. This study has been carried out using FE model incorporating static and dynamic analyses. Performance of coupler-embedded (ABC) RC pier is determined from the stress developed at coupler using the conservative results from dynamic simulation in experiencing high velocity vehicle impact.

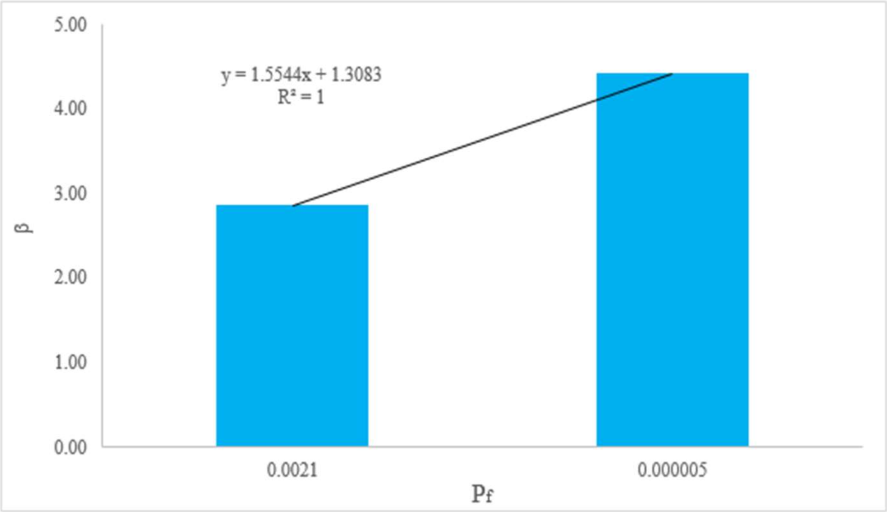

Figure 20. Determination of β from P_f.

6.4.1. Performance reliability using integrity analysis

Using Equation (14) and **Table 4**, β is evaluated from integrity analysis utilizing F results (F as 5.16×10^{-3}) yields 4.4 with a corresponding approximate P_f of 5×10^{-5}.

6.4.2. Performance reliability using direct reliability method

Post impact performance as a reliability index (β) is also directly evaluated from probability of failure (P_f) as a function of DIF. Result from the dynamic analysis is utilized as dynamic modulus of material in demand using DIF resulted from simulation exceeding the material E-modulus. This result leads to evaluate failures and corresponding reliabilities of coupler. The performances are evaluated by determining probability of failures (P_f) and corresponding performance reliability through integrity analyses (IA) from resulting stress and strain from conservative dynamic impact. The IA of the impacted pier is conducted using resulted stresses and strains from FEA. Stresses resulted due to impact and the dynamic amplification effect (DIF) draw an insightful correlation between DIF's computed analytically (1.053) and numerically using the FE simulation (1.07) through the ratio of moduli. Probability of failure (P_f) is evaluated from the DIF's with a difference of 1.6% which results as 0.0021. Performance reliability (β) has been directly computed using Equation (13), yields as 2.86.

6.4.3. Determination of reliability index

Reliability Index (β) of the coupler can be determined using Sec. 3.2.1 and 3.2.2 from the corresponding probability of failures (P_f). The comparative results are put together and is as shown in **Figure 20**.

Using **Figure 20**, overall β of the coupler undergoing high velocity vehicle impact can be determined using the results of the regression analysis with R^2 value of 1 as shown in Equation (14).

$$\beta = 1.6.P_f + 1.31 \tag{17}$$

where: P_f and β are already explained.

6.4.4. Uncertainty assessment using confidence interval (CI)

To ascertain integrity, confidence Interval (CI) has been further utilized to estimate the degree of uncertainty for assessing non-linear results comprising of σ_D, ε_D, and E_D. The uncertainty in the results has been determined using the CI has been already exhibited in **Table 6** which is, in addition, precisely presented in **Table 8**.

Table 8. CI results.

Variables	Confidence value (CV)	Confidence interval (CI)
σ_D (psi)	46,199.18	(7.15×10^5, 6.22×10^5)
ε_D	0.000661	(0.0246, 0.0233)
E_D (psi)	46,199.18	(3.24×10^7, 3.23×10^7)

6.5. Model validation

The model shows a good tradeoff between the experimental results extracted from the published journals and simulation results captured using [12]. The correlation of FEA and experimental models are plotted and are as shown in **Figure 21** conforming the validation of the model.

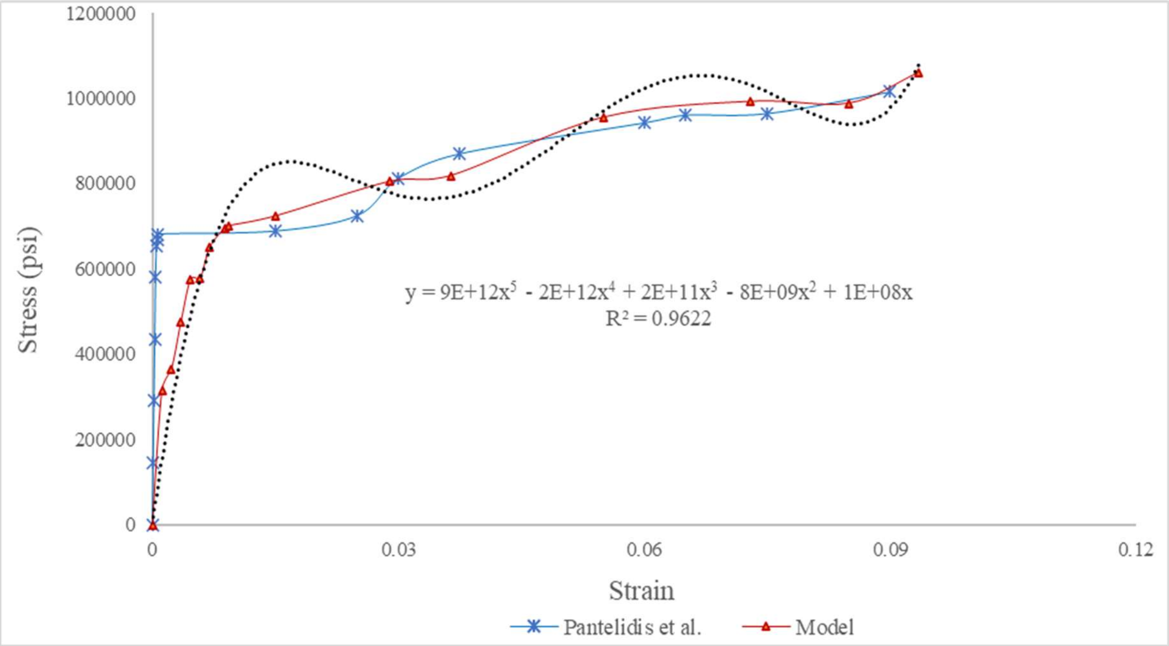

Figure 21. Model verification [12].

Figure 20 can decently provide a compatible and acceptable normalized stress and strain results data of the coupler composite at specific high strain rate load and high deformation incurred by semi-trailer impact via utilizing experimental and numerical results corresponding to the best fit curve with tight R^2 value of 0.96 as shown in Equation (14).

$$\sigma = 9 \times 10^{12} \times (\varepsilon^5) - 2 \times 10^{12} \times (\varepsilon^4) + 2 \times 10^{11} \times (\varepsilon^3) - 8 \times 10^9 \times (\varepsilon^2) + 10^8 \times (\varepsilon) \qquad (18)$$

where: σ and ε indicate stress (in psi) and strain at coupler composite due to specific high strain rate loading to designate the overall material properties to safely withstand failure.

7. Discussions of results

Post impact performance of a coupler composite embedded in ABC bridge pier considering flexural response has been examined. Connectors consisting of splice-sleeve along with grouted coupler have been investigated for post impact performances. Stresses resulted due to impact and the amplification effect draw significant correlation between DIF$_s$ computed analytically (1.053) and FEA (1.07) using the ratio of material properties at failure zones. In addition, results depicting from the mesh sensitivity studies are executed and results are shown in the respective **Figures 6–8** incorporating deformations and corresponding equivalent strain. Mesh sensitivity studies to incorporate static results are precisely shown in **Figure 6**, whereas the results from dynamic performance comprising deformation and strain for different mesh sizes are shown in **Figures 7** and **8** respectively. FEM analyses present a little conservative result as observed. To sum up the results, the following observations are drawn from this study:

1) Analytical results showing from the exaction solution comprises a DIF of 1.053 (i.e., increased by 5.3%). Using FEA, a DIF$_s$ of 1.07 (i.e., 7% increment) has been estimated with an outcome of 1.6% increment. FEA results are used to determine and validate analytically computed DIF$_s$ Provides a good agreement with a minimal difference in results (1.6%). This indicates high stress concentration in steel bar-coupler junction.
2) Due to the deployed boundary conditions for FEA, a little conservative result has been observed, and hence seems more realistic conforming design criteria. Results shown from the analytical solution provides a DIF$_s$ of 1.053 (i.e., 5.3%), whereas material properties result a DIF$_s$ of 1.07 (i.e., 7%) using dynamic properties of material.
3) This is observed from the results that maximum stress has developed at the contact of steel bar and coupler zone that leads high deformation. This is also observed that coupler and steel bar junction has been. Significant damage along with the bend and twist of steel bar has been observed in the junction as well.
4) Dynamic performances of the steel and concrete composite system and its post impact behavior are further assessed to precisely obtain stress and strain via developing linearized model and executing time dependent analyses.
5) Integrity analysis followed by reliability analysis using dynamic stress-strain resulted from simulations has been further carried out and the results are plotted through regression method. This can scrupulously capture material property at large post deformation state.
6) Model validation has been conducted using the results captured from static counterparts of stress and strain with the extracted experimental data. and is as shown in **Figure 20**.

8. Conclusions and future works

Bridge piers are usually contemplated as the most susceptible members to vehicle crash due to their exposed face and slender behavior. The characteristics and the associated severity of damage of the connectors used in ABC pier due to a high velocity and weight of semi-trailer collision were not well defined. Therefore, there has been a dire need to verify the accountability of such existing structures against such collisions, and proffer solutions to limit such susceptibility to enhance its performance level. Based on the comparison of analytical studies and simulation results using FEA, and its validation with the experimental results published in the journals, the following conclusions can be drawn:

1) A reasonable enhancement in 7% to 10% strength of material modulus is recommended for the cast-iron and steel bar.
2) To precisely detect high variations of results due non-linearity, adequately accurate results are obtained through utilizing the integrity study.
3) By using CI, risk analysis has been conducted to provide a clear understanding to scrupulously using the uncertainty parameters.
4) High precision experimental studies are recommended before extensive use.

Table 9. US customary to the equivalent SI units.

US customary	SI unit
1 ksi 1 ksi	6.89 MPa (kN/mm^2) 6894.76 kN/m^2
1 kip-in	0.113 kN-m
1 kip	4.45 kN
1 lbs	0.00445 kN
1 mph	1.61 km/hr
1 ft-lb/s	0.00136 kN-m/s (1.36 N-m/s)
1 in	0.0254 m (25.4 mm)
1 foot	0.3048 m (304.80 mm)
1 pci	271.447 kN/m^3
1 psi	6894.76 N/m^2

The data conversions from US Customary to SI are shown in **Table 9**.

Funding: NMB Splice Sleeve Inc. North America and Utah State University, Logan, Utah 84322, United States.

Availability of data and material: Some or all data, models, or code that support the findings of this study are available from the corresponding author upon reasonable request.

Conflict of interest: The author declares no conflict of interest.

Abbreviations

f'_c	Concrete strength
A_g	Gross cross-sectional area of pier specimen
A_s	Cross-sectional area of reinforcing steel bar
A_{net}	Net cross-sectional area of pier
$A_{n,s}$	Cross-sectional area of each steel rebar
A_{CI}	Cross-sectional area of splice sleeve (cast iron)
A_{Grout}	Cross-sectional area of grout

$A_{connector}$	Cross-sectional area of hollow splice-sleeve
E_{CI}	Material modulus of cast iron
E_{Grout}	Material modulus of grout, concrete
$E_{Concrete}$	Material modulus of concrete
E_s	Material modulus of reinforcing steel rebar
η	Energy dissipation
f_y	Yield strength of steel
P_n	Axial load of RC pier
$P_{n,s}$	Axial load of reinforcing steel bar
$P_{n,s}$	Scaled-down design axial bar load
σ_{dyn}	Dynamic flow stress
σ_y	Static flow stress
$\dot{\varepsilon}$	Quasi-static strain rate of steel bar
h	Pier diameter
h_I	Height of impact from pier base
σ	Stress
ε	Strain
E	Modulus of elasticity of coupler
σ_D	Stress
ε_D	Strain
E_D	Modulus demand of coupler at dynamic impact
ψ	Dynamic parameter
C and p	Material constants
I_S	Static impact force
W	Vehicle weight
M_s	Static moment for each coupler
$M_{s,c}$	Static moment incurred by each coupler
$M_{dyn,c}$	Dynamic moment incurred by each coupler
M_{dyn}	Dynamic moment for each coupler
t	Impact duration (sec)
DIFs	Dynamic increase factor
CI	Confidence interval
μ	Mean
SD	Standard deviation
Z	Significance level
N	Sample size

References

1. Hauksson E, Kanamori H, Stock J, et al. Active Pacific North America Plate boundary tectonics as evidenced by seismicity in the oceanic lithosphere offshore Baja California, Mexico. Geophysical Journal International. 2013; 196(3): 1619-1630. doi: 10.1093/gji/ggt467
2. Thomas RJ, Steel K, Sorensen AD. Reliability analysis of circular reinforced concrete columns subject to sequential vehicular impact and blast loading. Engineering Structures. 2018; 168: 838-851. doi: 10.1016/j.engstruct.2018.04.099
3. Feyerabend M. Hard transverse impacts on steel beams and reinforced concrete beams. University of Karlsruhe (TH),

Germany; 1988.

4. Sharma H, Gardoni P, Hurlebaus S. Performance-Based Probabilistic Capacity Models and Fragility Estimates for RC Columns Subject to Vehicle Collision. Computer-Aided Civil and Infrastructure.
5. Roy S, Unobe I, Sorensen AD. Vehicle-Impact Damage of Reinforced Concrete Bridge Piers: A State-of-the Art Review. Journal of Performance of Constructed Facilities. 2021; 35(5): 03121001. doi: 10.1061/(ASCE)CF.1943-5509.0001613
6. Roy S, Unobe ID, Sorensen AD. Investigation of the performance of grouted couplers in vehicle impacted reinforced concrete ABC bridge piers. Advances in Bridge Engineering. 2022; 3(1). doi: 10.1186/s43251-022-00065-y
7. Sanders, David H. Evaluation of the Seismic Performance of Circular and Interlocking RC Bridge Columns under Bidirectional Shake Table Loading. In: Proceedings of the 15th World Conference on Earthquake Engineering (15WCEE); September 2018.
8. Pantelides CP, Ameli MJ, Parks JE, Brown DN. Seismic evaluation of grouted splice sleeve connections for precast RC bridge piers in ABC. Utah Department of Transportation; 2014.
9. Sharma H, Hurlebaus S, Gardoni P. Performance-based response evaluation of reinforced concrete columns subject to vehicle impact. International Journal of Impact Engineering. 2012; 43: 52-62. doi: 10.1016/j.ijimpeng.2011.11.007
10. Kowalsky MJ. Deformation limit states for circular reinforced concrete bridge columns. Journal of Structural Engineering, American Society of Civil Engineers. 126(8); 869-878. doi: 10.1061/(ASCE)0733-9445(2000)126:8(869)
11. Roy S, Unobe ID, Sorensen A. Damage characterization and resilience optimization of reinforced concrete bridge piers under vehicle impact. Advances in Bridge Engineering. 2022; 3(1). doi: 10.1186/s43251-022-00067-w
12. Ameli MJ, Brown DN, Parks JE, et al. Seismic Column-to-Footing Connections Using Grouted Splice Sleeves. ACI Structural Journal. 2016; 113(5). doi: 10.14359/51688755.
13. Jacob GC, Fellers JF, Starbuck JM, et al. Crashworthiness of automotive composite material systems. Journal of Applied Polymer Science. 2004; 92(5): 3218-3225. doi: 10.1002/app.20336
14. Ebrahimpour A, Earles B. Seismic Performance of Columns with Grouted Couplers in Idaho Bridges. IABSE Symposium, Vancouver 2017: Engineering the Future. 2017; 109: 1817-1823. doi: 10.2749/vancouver.2017.1817
15. Tazarv M, Saiidi MS. Seismic design of bridge columns incorporating mechanical bar splices in plastic hinge regions. Engineering Structures. 2016; 124: 507-520. doi: 10.1016/j.engstruct.2016.06.041
16. Zhao X, Wu YF, Leung AY, et al. Plastic Hinge Length in Reinforced Concrete Flexural Members. Procedia Engineering. 2011; 14: 1266-1274. doi: 10.1016/j.proeng.2011.07.159
17. Roy S, Sorensen A. Energy Based Model of Vehicle Impacted Reinforced Bridge Piers Accounting for Concrete Contribution to Resilience. In: Proceedings of the 18th International Probabilistic Workshop: IPW 2020. p. 301.
18. Roy S, Sorensen A. A Reliability Based Crack Propagation Model for Reinforced Concrete Bridge Piers Subject to Vehicle Impact. In: Proceedings of the 18th International Probabilistic Workshop: IPW 2020. p. 95.
19. ACI. ACI 318-11: Building Code Requirements for Structural Concrete. American Concrete Institute; 2011.
20. ICC-ES Evaluation Report ESR-3433. Available online: https://icc-es.org/report-listing/esr-3433/ (accessed on 2 March 2024).
21. ICC-ES Report. Available online: https://www.pwcva.gov/assets/2021-05/PA1201Att (accessed on 2 March 2024).
22. Gray GT. High-Strain-Rate Deformation: Mechanical Behavior and Deformation Substructures Induced. Annual Review of Materials Research. 2012; 42(1): 285-303. doi: 10.1146/annurev-matsci-070511-155034
23. Chopra AK. Dynamics of Structures, Theory and Applications to Earthquake Engineering. Upper Saddle River: Pearson-Prentice Hall; 2001.
24. Wikipedia. Speed limits in the United States. Available online: https://en.wikipedia.org/wiki/Speed_limits_in_the_United_States (accessed on 2 June 2024).
25. Tavio T, Tata A. Predicting Nonlinear Behavior and Stress-Strain Relationship of Rectangular Confined Reinforced Concrete Columns with ANSYS. Civil Engineering. 2009; 11(1): 23-31.
26. Malvar LJ. Review of static and dynamic properties of steel reinforcing bars. ACI Materials Journal.
27. Malvar LJ, Crawford JE. (1998). Dynamic increase factors for steel reinforcing bars. 28th DDESB Seminar.
28. Buth CE, Brackin MS, Williams WF, Fry GT. Collision Loads on Bridge Piers: Phase 2 Report of Guidelines for Designing Bridge Piers and Abutments for Vehicle Collisions. Austin, Texas. 2011; p. 100.
29. Cowper GR, Symonds PS. Strain-hardening and strain-rate effects in the impact loading of cantilever beams. Defense Technical Information Center; 1957. doi: 10.21236/ad0144762

30. AFDC. Vehicle Weight Classes & Categories. Alternative Fuels Data Centre, U.S. Department of Energy; 2018.
31. Roy S. Sustainability and Resiliency Investigation of Grouted Coupler Embedded in RC ABC Bridge Pier at Vehicle Impact. Engineering and Applied Sciences. 2024; 9(1): 14-33. https://doi.org/10.11648/j.eas.20240901.12
32. Ameli MJ, Pantelides CP. Seismic analysis of precast concrete bridge columns connected with grouted splice sleeve connectors. Journal of Structural Engineering, American Society of Civil Engineers. 2017; 143(2): 4016176. doi: 10.1061/(ASCE)ST.1943-541X.0001678
33. Andrzej S, Nowak KR, Collins. Reliability of Structures, 2nd ed. CRC Press; 2012.
34. El-Tawil S, Severino E, Fonseca P. Vehicle collision with bridge piers. Journal of Bridge Engineering. 2005; 10(3): 345-353.
35. Matos JC, Lourenço PB, Oliveira DV, et al. 18th International Probabilistic Workshop. Springer International Publishing; 2021.

Mechanical Engineering Advances 2024, 2(2), 1495.
https://doi.org/10.59400/mea.v2i2.1495

Article

Research on tire internal defect identification method based on deep learning

Jiaqi Chen, Aijuan Li[*]**, Te Wang, Xibo Wang**

School of Automotive Engineering, Shan Dong Jiaotong University, Jinan 250357, China
*** Corresponding author:** Aijuan Li, liaijuan@sdjtu.edu.cn

CITATION

Chen J, Li A, Wang T, Wang X. Research on tire internal defect identification method based on deep learning. Mechanical Engineering Advances. 2024; 2(2): 1495. https://doi.org/10.59400/mea.v2i2.1495

ARTICLE INFO

Received: 2 July 2024
Accepted: 10 September 2024
Available online: 25 October 2024

Abstract: As an important part of automobile, the safety and durability of tire have attracted more and more attention. Tire defect detection is an important link to ensure tire quality, while traditional detection methods have problems such as low efficiency, high false detection rate and high labor intensity. Therefore, this study aims to develop an efficient and accurate tire defect identification and classification technique to improve the efficiency and accuracy of tire inspection. In this paper, based on YOLO (You Only Look Once) v5 algorithm, tire defect recognition and classification are studied. Firstly, the data sets containing various types of tire defects were collected and sorted out, and the data sets were preprocessed. Then, by constructing, training and optimizing the YOLOv5 tire defect recognition model, the fast and accurate recognition of tire defects was realized. Finally, the performance of the model was evaluated through experiments and compared with the existing methods. The experimental results show that the tire defect recognition and classification method based on YOLOv5 proposed in this study has high accuracy. Compared with traditional methods, this method has a significant improvement in detection speed and accuracy.

Keywords: tire; internal defect; deep learning; dataset training; YOLOv5

1 Introduction

Tire is one of the key components of automobile, and its quality directly affects the driving safety. In the manufacturing process of tires, it is easy to produce various types of defects, these defects will not only affect the normal use of tires, but also may pose a serious threat to people's life safety. Therefore, in order to ensure the safety performance of tires in the process of driving, strict and comprehensive quality inspection must be carried out before leaving the factory. Traditional detection methods often rely on artificial naked eyes for defect identification [1]. Although this method is intuitive and easy to understand, it is relatively inefficient and easy to cause visual fatigue for long hours, which affects the accuracy of detection. With the continuous development of machine learning technology, the methods based on machine learning have gradually become a research hotspot. Based on YOLOv5 algorithm, this paper does further research on the recognition and classification of tire defects. By using the advantages of YOLOv5 algorithm, we expect to realize the automatic, fast and accurate recognition and classification of tire defects, so as to improve the efficiency and accuracy of tire quality detection.

At present, the target detection algorithm can realize the location and classification of the target at the same time, which provides new possibilities for defect detection. Cui et al. [2] developed a tire texture depth detection method based on machine vision technology. This method can identify the small defects inside the tire, but the stability is poor, and the measurement accuracy is greatly affected by the measurement time. Li and Jiang used Faster R-CNN (Region-based Convolutional Network) model to detect tire defects [3]. Although certain results have been achieved, there are still defects in the application of detecting real tires. Wang et al. built an automatic detection system for the tread wear degree of automobile tires by using a camera [4]. Although the automation level is high, the detection success rate still needs to be improved. Therefore, although the existing tire defect detection technology has made some progress, it still faces many challenges in practical applications, and it still faces the problems of low detection success rate and easy to be interfered by external factors. On this basis, YOLOv5 network is used to construct an automobile tire defect recognition and classification model based on deep convolutional neural network, and the test results are predicted and analyzed.

2. Tire defect analysis and dataset construction

As an important part of the car, the tire has a decisive impact on the driving performance of the car. A qualified tire needs to have good handling, stability, comfort and safety. However, in the production process, tires may have various defects, which may affect the performance of tires and even endanger the life safety of drivers and passengers [5–9]. Therefore, the identification and classification of tire defects is particularly important.

2.1. Common types of tire defects

In the production process, the quality of radial tires is sometimes unqualified due to improper production equipment, technological process and operation [10]. According to the nature of tire defects, these defects can be roughly divided into two types: structural type defects and gray type defects [11]. This article will introduce some of the most common defects, including tire cord cracking, uneven distribution of cord, impurities, and wrong edges [12–15].

(1) Tire cord cracking

Tread cord cracking is a common tire defect. The X-ray picture of tread cord cracking is shown in **Figure 1**. As the key supporting structure of the tire, the cord inside the tire plays a vital role in coping with external forces and maintaining the shape and stability of the tire [16]. Cord cracking will lead to a significant decrease in the load-bearing capacity and deformation resistance of the tire, thus increasing the risk of tire burst during high-speed rotation.

(2) Uneven distribution of cord lines

The X-ray image of uneven distribution of cord is shown in **Figure 2**. Uneven distribution of cord will increase the risk of shoulder empty and bulging of tires, and in severe cases, it may even cause tire burst failure, resulting in premature tire damage [17].

(3) Impurities

In the manufacturing process of tires, sometimes foreign objects such as screws, rubber fragments or iron filings may be accidentally mixed into the interior of tires. The X-ray image of tire impurities is shown in **Figure 3**. The presence of these foreign substances will significantly thickensome areas of the tire, forming various shapes and prominent black block shadows on the X-ray detection image of the tire [18].

(4) wrong side of the cord

The X-ray image of the wrong edge of the cord is shown in **Figure 4**. In the cord layer of the tire, the cord is not arranged in the predetermined position or direction, and it is offset or misplaced. When driving at high speeds or bearing heavy loads, this structural weakness may cause deformation or damage of the tire, and even cause safety accidents [19].

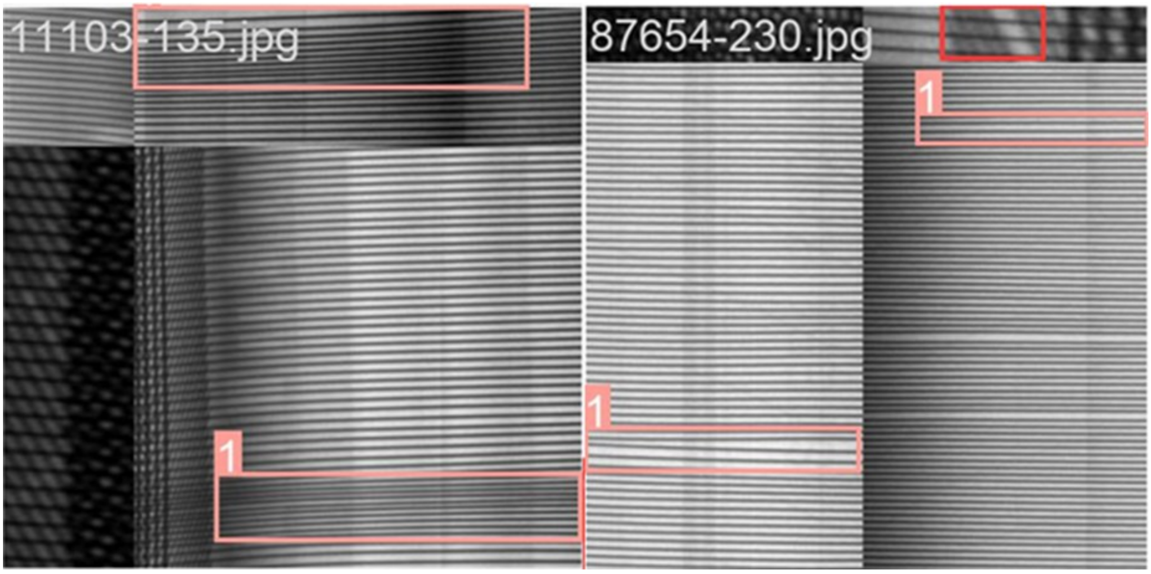

Figure 1. X-ray picture of tread cord cracking.

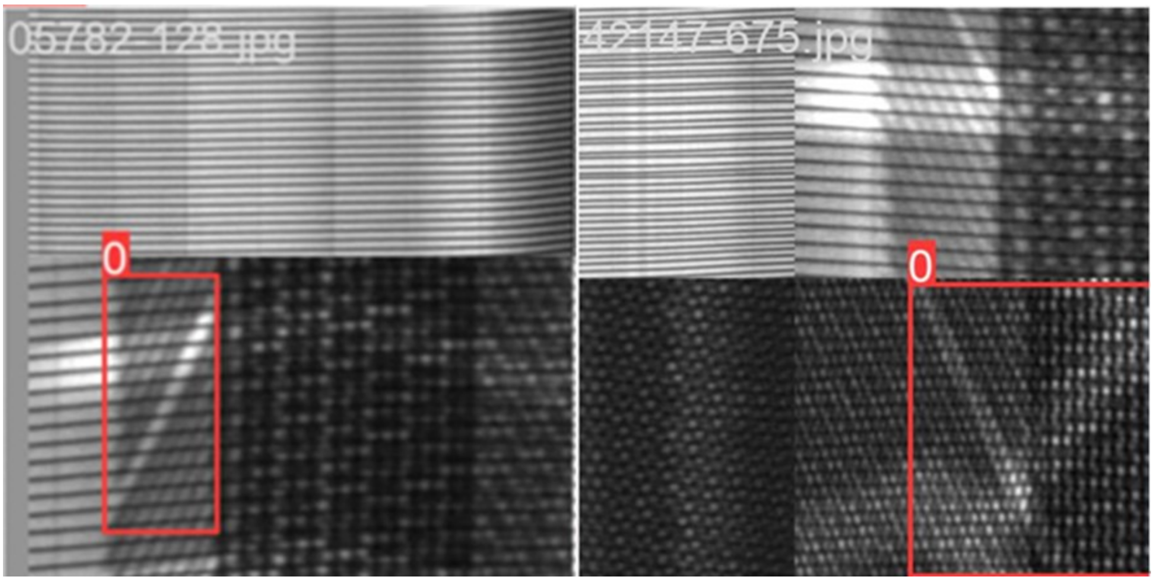

Figure 2. X-ray picture of unevenly distributed cord.

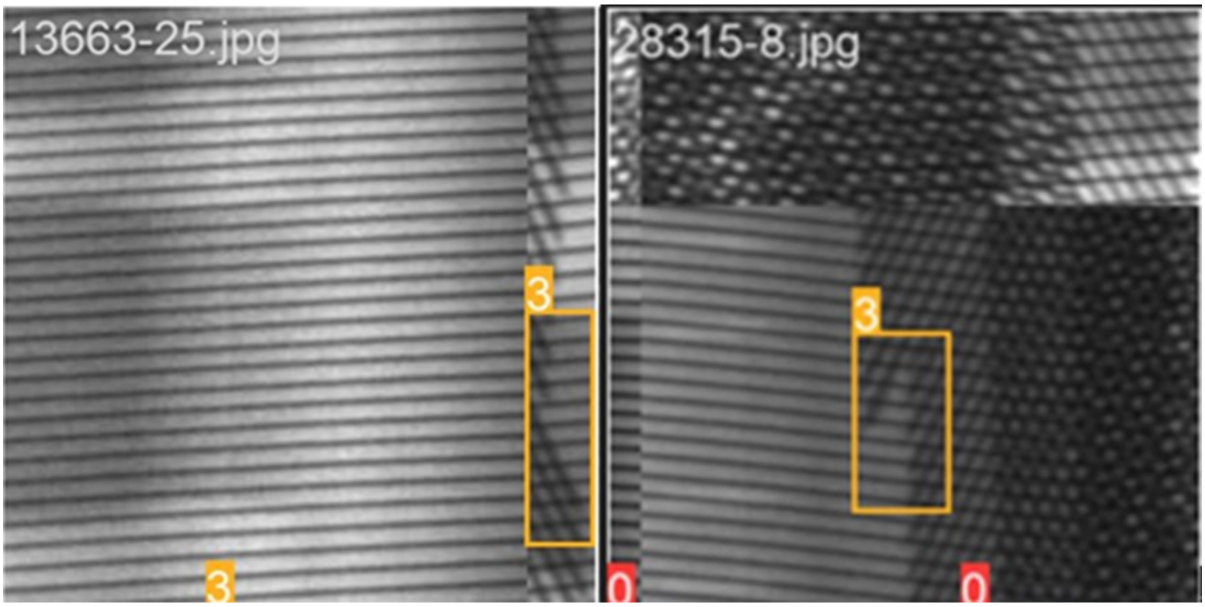

Figure 3. Tire impurity X-ray picture.

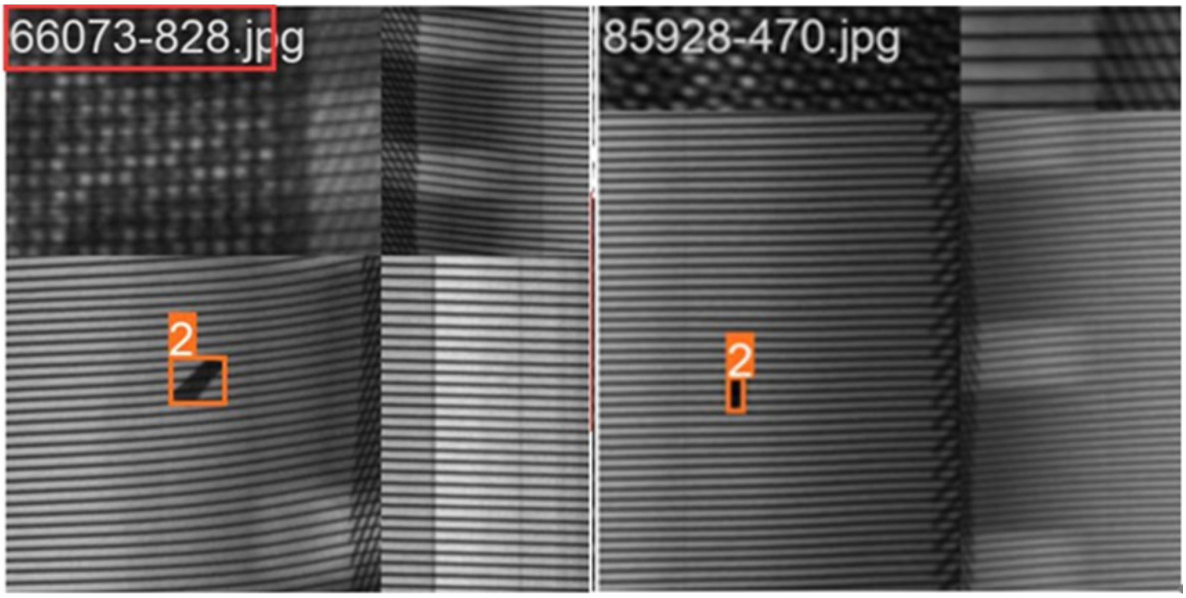

Figure 4. X-ray picture of tire cord misalignment.

2.2. Dataset construction

In order to train an efficient YOLOv5 model, the selection and annotation of the dataset is crucial, as it will directly affect the performance of the model. The data used in the experiment comes from 1905 X-ray images of radial tire defect detection provided by the Network Control Center of Shanghai University, which are 480 × 480 pixels in size and contain 4 categories in total. They are tire cord cracking (2#-open), uneven distribution of cord (cords_defects), impurity (impurity) and wrong edge of cord (belt_cuobian). The Labelimg tool is used for image annotation, and the file after annotation takes.txt as the suffix, and the file name is consistent with the image name. The Labelimg annotation interface is shown in **Figure 5**. First, select the YOLO dataset format, then press the W key to enter the annotation mode, and drag the box to completely cover the defect part. Finally, input the defect category in the pop-up window, and click the OK option to divide the dataset, and finally obtain 1142 images in the training set, 382 images in the validation set and 381 images in the test set.

The test set and validation set tire X-rays are shown in **Figure 6**, where **Figure 6 a–d** are the test set tire X-rays, and **Figure 6e–h** are the validation set tire X-rays. The confusion matrix, shown in **Figure 7**, quickly helps to analyze the misclassification of each class, so that the analysis can be adjusted in turn.

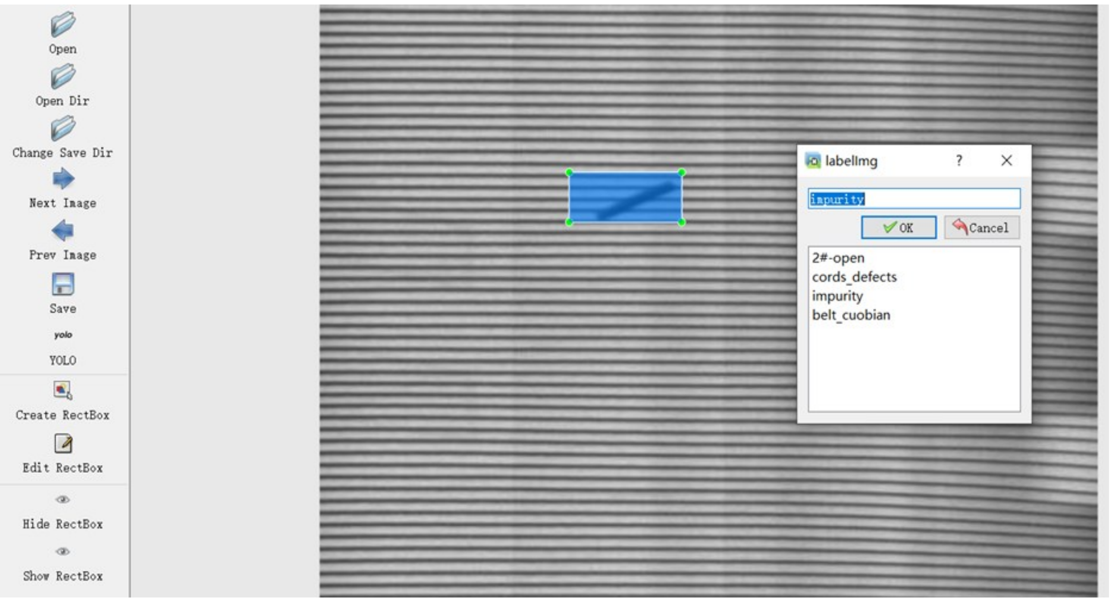

impurity

2#-open
cords_defects
impurity
belt_cuobian

Figure 5. Labelimg annotation interface.

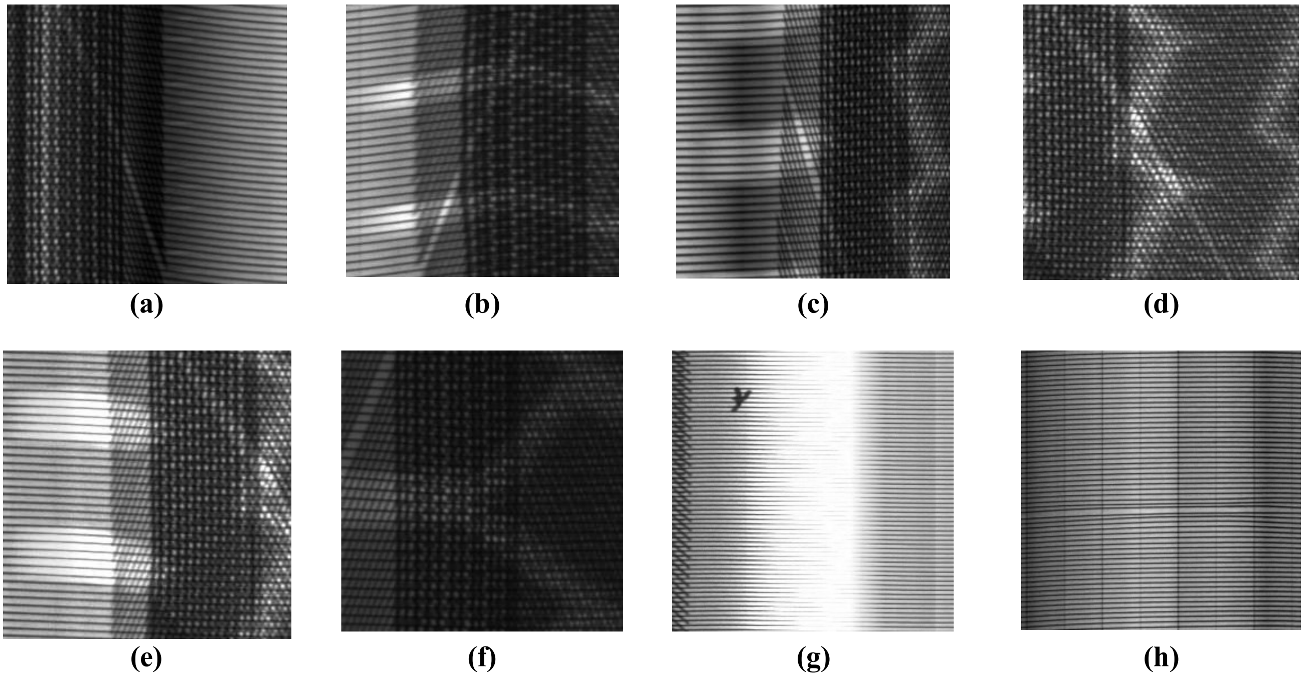
(a) (b) (c) (d)
(e) (f) (g) (h)

Figure 6. Labeling annotation interface. **(a)** unevenly distributed cord; **(b)** unevenly distributed cord; **(c)** tire impurity; **(d)** unevenly distributed cord; **(e)** unevenly distributed cord; **(f)** tread cord cracking; **(g)** cord misalignment; **(h)** tread cord cracking.

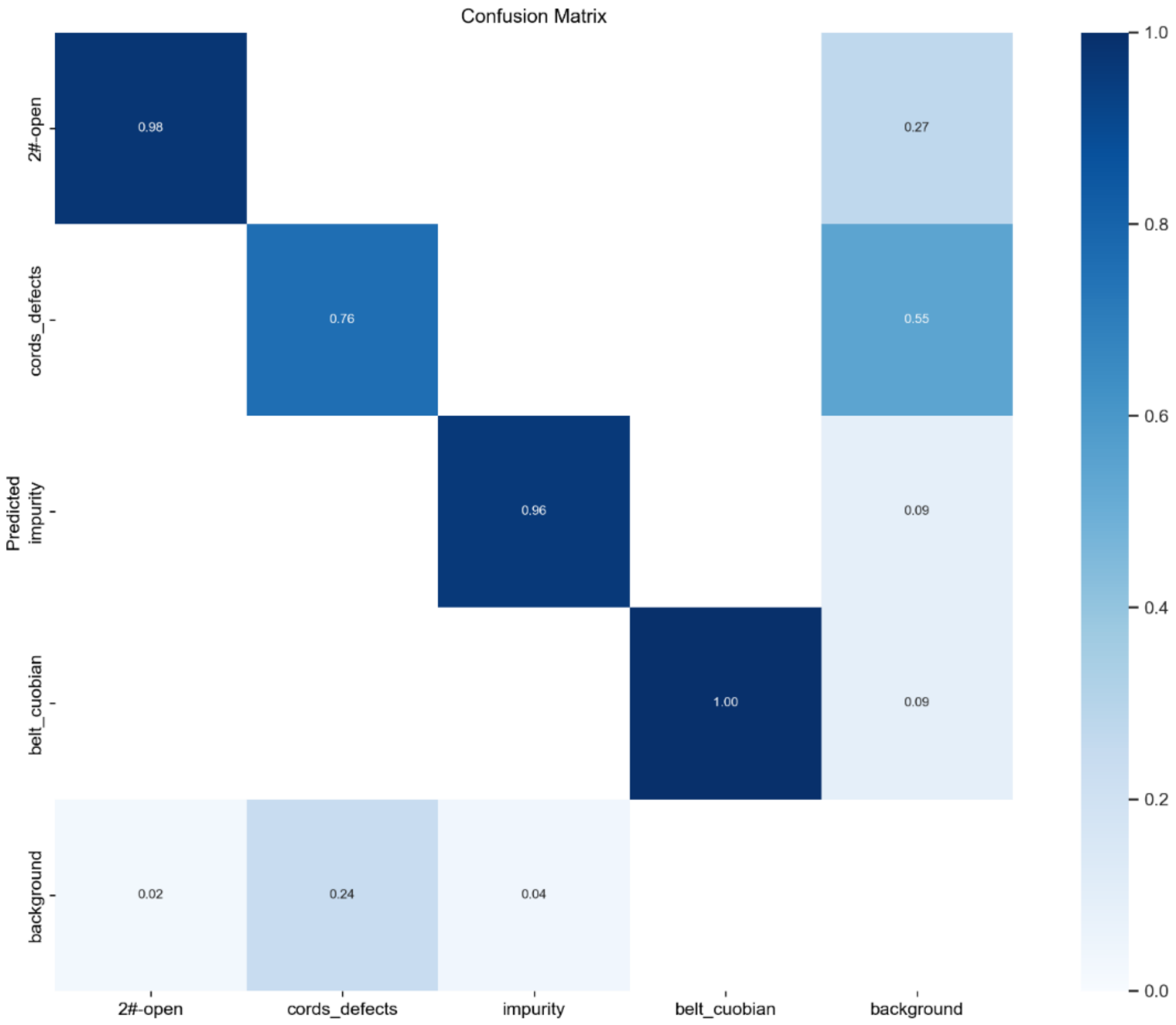

Figure 7. Confusion matrix of dataset.

3. Design of tire defect recognition method based on YOLOv5

You Only Look Once (YOLO) family of algorithms is a single-stage object detection algorithm designed for end-to-end training and real-time detection. Suitable for running in resource-constrained environments such as mobile devices and embedded systems. Its small model size and fast inference speed make it very popular in practical applications. During training, the input image is cleverly divided into $C \times C$ grids, each of which constitutes a prediction box and matches with the actual target box, so as to complete the target prediction efficiently.

3.1. Algorithm model and experimental environment

YOLOv5 uses Cross Stage Partial (CSP) and Focus slicing module on the backbone network [19,20]. The model cleverly uses the similarities existing between different levels to construct a global network structure and is trained through a deep learning process to obtain the final classification results. This design idea enables the model to make full use of the multi-scale information in the image and improve the accuracy and robustness of classification. PyTorch framework was used in the experiment environment, and Intel(R) Core (TM) i9-13900HX CPU (Central Processing Unit) and NVIDIA (An artificial intelligence computing company) GeForce RTX4050 GPU (Graphics) were used Processing Unit, using Windows11 operating system, acceleration environment is CUDA (Compute Unified Device Architecture) 11.7.

3.2. Loss function

The reason why YOLOv5 algorithm performs well in object detection tasks is inseparable from its carefully designed loss function. Specifically, the loss function of YOLOv5 consists of three key parts. These are Classification Loss, Confidence Loss, and localization loss. These three functions together make the model achieve high accuracy in identifying the target, evaluating the probability of the existence of the target, and accurately locating the target.

In YOLOv5, the classification loss and confidence loss are calculated by a binary cross-entropy loss function. The classification loss is used to evaluate the accuracy of the model in predicting the target class, and can well reflect the difference between the probability distribution predicted by the model and the true distribution. Confidence loss, which evaluates the accuracy of the model's prediction of the presence of an object, can help the model better determine whether a particular object is present in the image. Localization loss is used to measure the prediction accuracy of the model on the position of the target bounding box, and CIOU_LOSS is usually used as its loss function. In the loss calculation, CIOU_LOSS simultaneously considers the overlap area between the predicted box and the real box, the distance between the center point, and the aspect ratio, so as to measure the accuracy and precision of the predicted box more comprehensively [21]. The formula is as follows:

$$V = \frac{4}{\pi^2}(arctan\frac{w^{gt}}{h^{gt}} - arctan\frac{w}{h})^2 \tag{1}$$

$$IoU = \frac{|A \cap B|}{|A \cup B|} \tag{2}$$

$$\alpha = \frac{V}{(1 - IoU) + V} \tag{3}$$

$$\mathscr{L}_{CIoU} = 1 - IoU + \frac{\rho^2(k, k^{gt})}{c^2} + \alpha V \tag{4}$$

where w, h, w^{gt}, h^{gt} are the width and height of the predicted and true box respectively, k, k^{gt} are the center points of the predicted and true box respectively, and ρ is the Euclidean distance between the two center points. c represents the diagonal distance of the smallest closure region capable of containing both the predicted and true boxes.

3.3. Target detection evaluation index

In the field of object detection, Precision (*P*), Recall (*R*) and Average Precision (*AP*) are often used as evaluation metrics. In general, the higher the *AP* value, the better the accuracy of the model.

The formula is as follows:

$$P = \frac{TP}{TP + FP} \tag{5}$$

$$R = \frac{TP}{TP + FN} \tag{6}$$

$$AP = \int_0^1 PdR \tag{7}$$

In Equations (5) and (6), *TP* (True Positive) represents a Positive sample predicted by the model as a positive class, *FP* (False Positive) represents a Negative sample predicted by the model as a positive class, and *FN* (False Negative) represents a positive sample predicted by the model as a negative class.

By setting different thresholds, we can obtain different *TP*, *FP* and *FN* values, and thus calculate multiple sets of *P* and *R* values. Using these data points of *P* and *R*, a P-R curve can be plotted. This curve provides a visual representation of the trade-off between precision and recall, which helps us to better evaluate the performance of the model.

In object detection tasks, it is also common to compute the Mean Average Precision (mAP) to fully evaluate the performance of the model on the entire dataset. The higher the mAP value, the better the model performs in the object detection task.

4. Experimental results and analysis

In this experiment, we used the dataset mentioned above to train the YOLOv5 model. During the training process, we recorded the localization loss value, confidence loss value, and classification loss value, and plotted the loss curve as shown in **Figure 8**. By observing the plotted loss curve, we can find that with the increase of the number of iterations, the three loss values of the training set and the validation set show a decreasing trend and eventually become stable. This indicates that our model gradually learns the effective information in the dataset during the training process, and the parameter Settings are reasonable.

In order to more comprehensively show the performance of YOLOv5 algorithm on tire defect detection task, we randomly selected a certain number of tire images from the test set to detect them. Part of the inspection results are shown in **Figure 9,** showing the inspection effects of different defect types respectively. Among them, 2#-open represents the cracked tire cord, cords_defects represents the uneven distribution of the cord, impurity represents the presence of impurities, belt_cuobian represents the wrong edge of the cord, and the number after the category label is the confidence degree. From **Figure 9**, it can be found that YOLOv5 has a better recognition effect on large-size targets such as tire cord cracking and wrong edge, and a slightly worse recognition effect on small-size targets such as uneven distribution of cord.

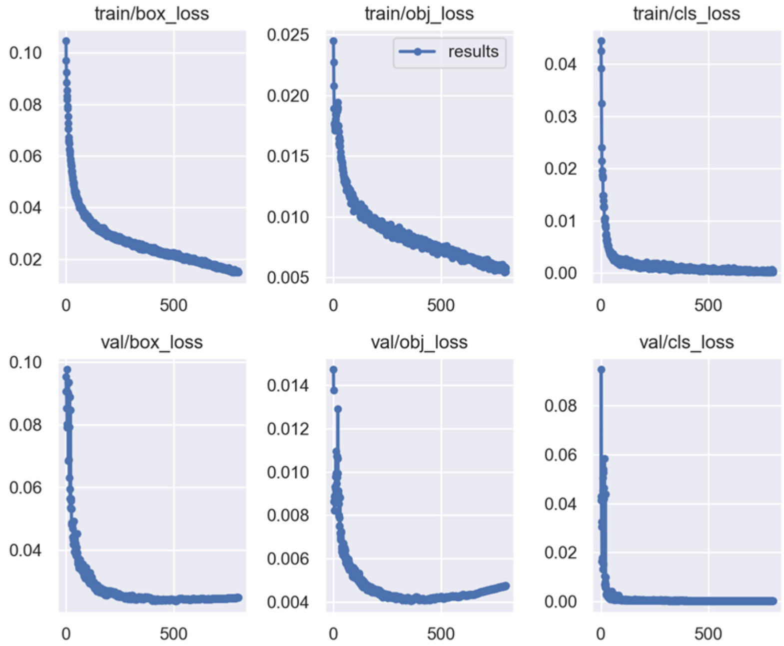

Figure 8. Loss plot.

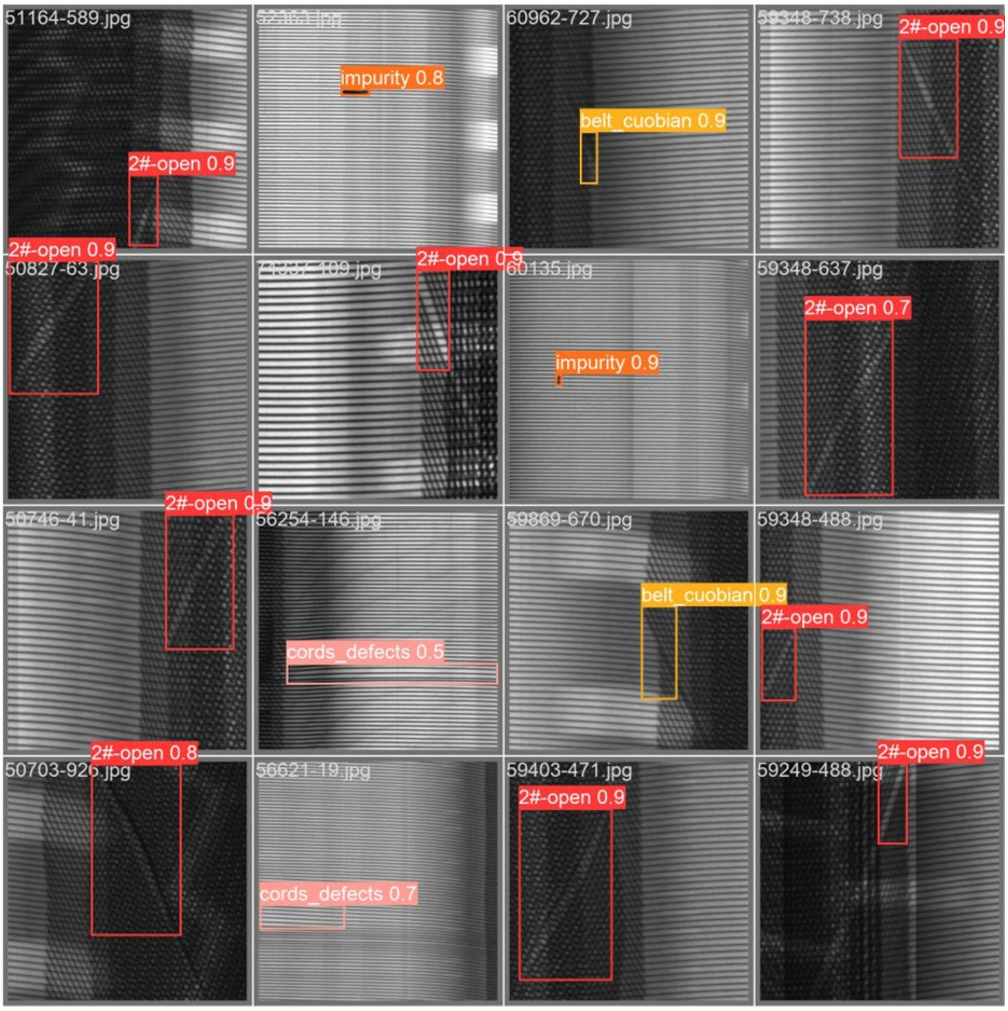

Figure 9. Partial test result.

The P-R curve of YOLOv5 model is shown in **Figure 10**. It can be intuitively seen from **Figure 10** that the area enclosed by the P-R curve with uneven distribution of the curtain line (orange line) and the coordinate axis is slightly smaller than the area enclosed by other P-R curves and the coordinate axis, that is, the *AP* value of the uneven distribution of the curtain line is slightly smaller than that of the other defects, which is also verified in **Figure 10**. The mAP curve is shown in **Figure 11**. It can be seen from the mAP curve that with the increase of the number of iterations of the model, the mean average precision gradually tends to about 95%, which proves that the YOLOv5 model can identify the location and category of the target very accurately. And compared with the traditional object detection algorithms (such as the Faster R-CNN algorithm used in literature [22], whose mAP value is 0.88, and the YOLOv3 algorithm used in literature [23], whose mAP value is 0.825), the YOLOv5 algorithm has higher detection accuracy. As shown in **Table 1**, the training speed and testing speed of the algorithm in this chapter are greatly improved compared with R-CNN, SPP (Spatial Pyramid Pooling) and Fast R-CNN, but the training time and testing time of the algorithm in this chapter are slightly higher than that of the algorithm in Faster R-CNN. And the mAP value of YOLOv5 model is significantly higher than that of other algorithms.

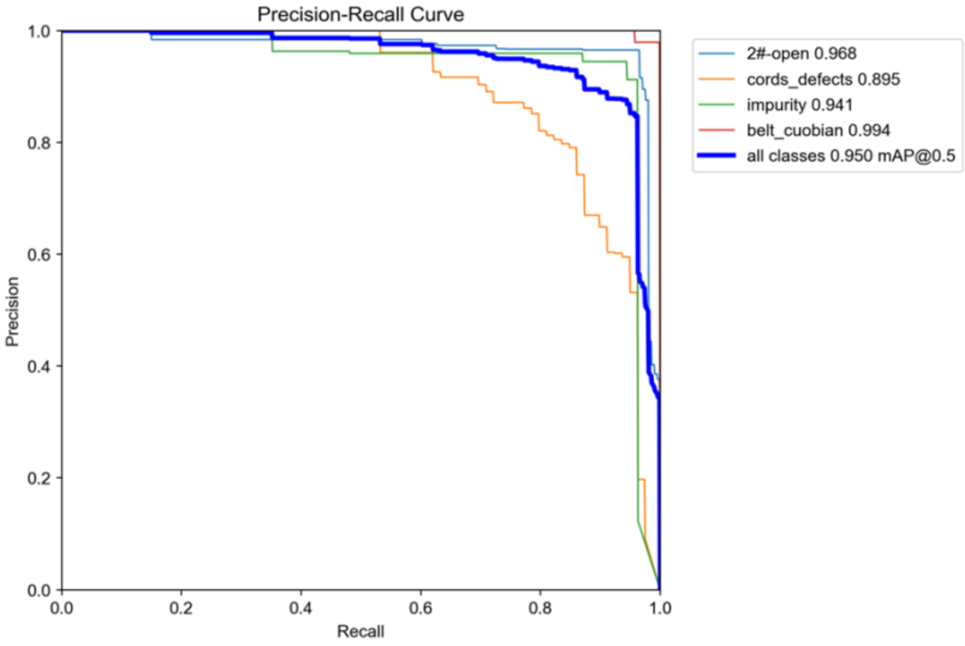

Figure 10. P-R curve.

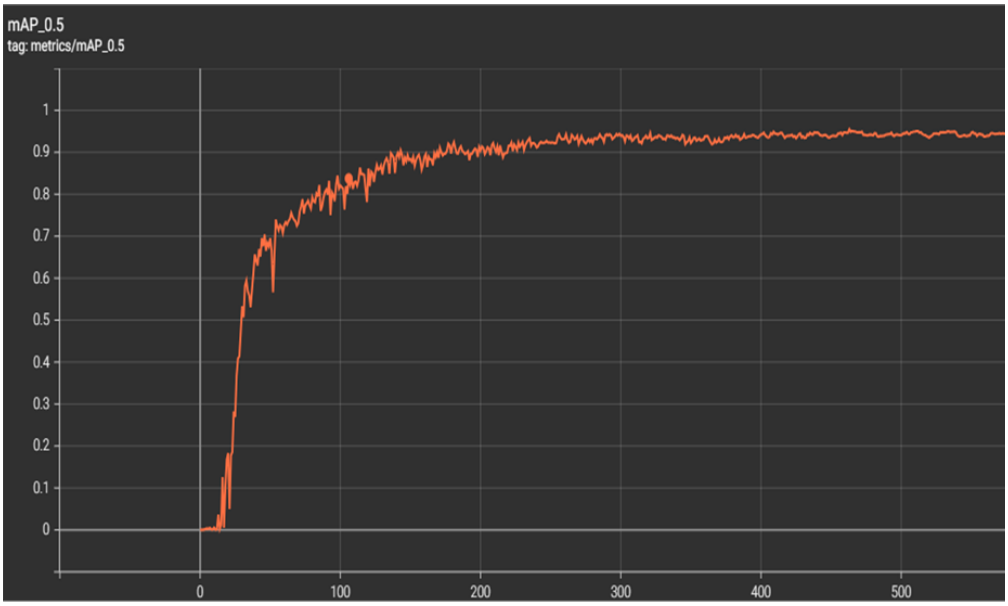

Figure 11. mAP curve.

Table 1. Performance comparison of advanced algorithms.

Algorithm	**Training Time (h)**	**Testing Time (s)**	**mAP Value**
R-CNN	27	49	0.792
SPP	4.8	2.8	0.803
Fast R-CNN	4.5	2.3	0.821
Faster R-CNN	3.7	0.26	0.884
YOLOv3	3.6	0.29	0.825
YOLOv5	4.1	0.27	0.952

5. Summary and prospect

Aiming at the problem of tire defect recognition and classification, this paper proposes the research of tire defect recognition and classification based on YOLOv5, aiming to solve the shortcomings of traditional tire defect detection methods in accuracy and efficiency. The main research of this paper consists of the following aspects:

(1) In the model construction part, this paper introduces the YOLOv5 algorithm, and introduces the basic principle and structure of the YOLOv5 algorithm. Then, by carefully building the experimental environment, this paper trains and verifies the model in detail, in order to achieve the best detection effect.

(2) Experimental design and result analysis show the performance of the proposed model in practical applications. By using the object detection evaluation index, the performance of the model is comprehensively evaluated. Through experimental verification, this method shows high accuracy and generalization ability in tire defect recognition task, and has obvious advantages compared with traditional methods.

However, this study still has some limitations, and future work will focus on the following aspects:

(1) Dataset expansion: Although this study has collected a certain number of tire

defect samples, it is still necessary to further expand the dataset scale and add more types of tire defect samples to improve the robustness and applicability of the model.

(2) Model optimization: Future work will continue to focus on the optimization of the model structure and try to introduce new modules or techniques, such as attention mechanism and multi-scale feature fusion, to improve the recognition speed and accuracy of the model.

Author contributions: Writing—original draft preparation, JC; methodology, AL; software, TW; validation, XW. All authors have read and agreed to the published version of the manuscript.

Conflict of interest: The authors declare no conflict of interest.

References

1. Qin Z, Song Y, Li M, et al. Research on Quality Problems and Countermeasures of Automobile Tire. Theory and Research. 2012; 48(9): 25-27.
2. Cui M, Yang H, Xie S, et al. Design of Automobile Tire Wear Detection System Based on Machine Vision. Manufacturing Automation. 2020; 42(01): 10-14.
3. Li M, Jiang J. Tire Defect Detection Algorithm Based on Deep Learning. Information Technology and Informatization. 2021; (2): 52-53.
4. Wang Z, Ren A, Li S. Detection System of Tire Tread Wear Degree. Computer System Application. 2021; 30(06): 88-93.
5. Yang H, Wang Q, Xue M. Selection and Use Effect Analysis of Construction Machinery Tires. Rubber & Plastic Technology & Equipment. 2018; 44(11): 19-23.
6. Huang Z, Zhang Y. A Survey of Object Detection Based on Deep Learning. Science and Technology Information. 2023; 21(24): 13-16.
7. Zeng Z. Application Progress of Deep Learning in the field of Computer Vision. Computer Products and Circulation. 2020; (01): 230.
8. Duan X, Zhou Y, Tian D. et al. Applications of Deep Learning in the field of autonomous driving. Unmanned System Technology. 2021; 4(06): 1-27.
9. Zhang Y, Dong Z, Meng X. Research on Personalized Advertisement recommendation System and its application. Journal of Computer Science. 2021; 44(03): 531-563.
10. Liu J, Jiang X, Ding Y, et al. Application of Face recognition Technology Based on Deep Learning in Computer Room Monitoring. Information Technology and Informatization. 2023; (11): 213-216.
11. Wu S, Xu Y, Zhao D. A Survey of Object Detection Based on Deep Convolutional Networks. Pattern Recognition and Artificial Intelligence. 2018; 31(04): 335-346.
12. Krizhevsky A, Sutskever I, Hinton GE. ImageNet classification with deep convolutional neural networks. Communications of the ACM. 2017; 60(6): 84-90. doi: 10.1145/3065386
13. Abhronil S, Yuting Y, Robert W et al. Going Deeper in Spiking Neural Networks: VGG and Residual Architectures. Frontiers in neuroscience. 2019: 1395.
14. He K, Zhang X, Ren S, et al. Deep Residual Learning for Image Recognition. In: Proceedings of the 2016 IEEE Conference on Computer Vision and Pattern Recognition (CVPR). doi: 10.1109/cvpr.2016.90
15. Zhou F, Jin L, Dong J. A Survey on Convolutional Neural Networks. Journal of Computer Science. 2017; 40(06): 1229-1251.
16. Li B, Liu K, Gu Z, et al. A Survey on Convolutional Neural Networks. Computer Times. 2021; (04): 8-12, 17.
17. Liu Y, Wang Y, Wang Y, et al. Image recognition based on deep learning convolutional neural network. Information and Communication. 2019; (07): 7-8.
18. Zheng X. Tire Band Layer Defect Detection Based on X-ray Imaging and Texture Analysis. Jinan University; 2019.
19. Wang CY, Mark Liao HY, Wu YH, et al. CSPNet: A New Backbone that can Enhance Learning Capability of CNN. In: Proceedings of the 2020 IEEE/CVF Conference on Computer Vision and Pattern Recognition Workshops (CVPRW). doi:

10.1109/cvprw50498.2020.00203

20. Zhang Y, Guo W, Cai Z, et al. Remote sensing image object detection based on joint multi-scale and attention mechanism. Journal of Zhejiang University: Engineering Science Edition. 2022; 56(11): 2215–223.
21. Zheng Z, Wang P, Liu W, et al. Distance-IoU Loss: Faster and Better Learning for Bounding Box Regression. In: Proceedings of the AAAI Conference on Artificial Intelligence. doi: 10.1609/aaai.v34i07.6999
22. Ai X. Research on Automatic Defect Detection Algorithm Based on Tire X-ray Image. Harbin Engineering University; 2019.
23. Chen M. Research on Tire Defect detection Algorithm Based on X-ray Image. Shanghai Jiaotong University; 2020.

Mechanical Engineering Advances 2024, 2(2), 1470.
https://doi.org/10.59400/mea.v2i2.1470

Article

Hydrogel 3D printing with direct and indirect extruder

Thanh Tan Nguyen[1], **Ngoc Hieu Pham**[1], **Hoang Son Tran**[1], **Le Nguyen Cao**[1], **Thi Hong Nga Pham**[1], **Quoc Bao Phan**[2], **Van Tron Tran**[1,*]

[1] Faculty of Mechanical Engineering, Ho Chi Minh City University of Technology and Education, Ho Chi Minh City 71307, Vietnam
[2] Advanced Manufacturing Center, Binh Duong University, Binh Duong province 75000, Vietnam
*** Corresponding author:** Van Tron Tran, trontv@hcmute.edu.vn

CITATION

Nguyen TT, Pham NH, Tran HS, et al. Hydrogel 3D printing with direct and indirect extruder. Mechanical Engineering Advances. 2024; 2(2): 1470. https://doi.org/10.59400/mea.v2i2.1470

ARTICLE INFO

Received: 24 June 2024
Accepted: 6 September 2024
Available online: 29 October 2024

Abstract: The advancement of additive manufacturing technology or 3-Dimesion printing (3D printing) allows for the creation of parts with intricate designs, resulting in less material waste compared to conventional manufacturing methods. Although current 3D printers primarily use plastic or metal materials, there is a growing interest in using biomaterials for 3D printing. To facilitate this trend, developing and designing 3D printers capable of using hydrogel materials is crucial. In this research, the 3D printer with direct and indirect extruders for hydrogel material is designed, calculated, and manufactured. Then, the 3D printer is tested with conductive sodium alginate 5% + 5% activated carbon by weight. In addition, the electrical conductivity of the material is measured. Through meticulous research and development, a 3D printer capable of printing hydrogel materials has been successfully manufactured, setting the stage for further exploration and the creation of environmentally friendly 3D biomedical printing materials.

Keywords: hydrogel; additive manufacturing; biomaterial; design; manufacture; direct and indirect extruder

1. Introduction

Hydrogels are three-dimensional networks of hydrophilic polymers that can rapidly absorb and retain substantial amounts of water or other liquids [1-2]. These versatile materials are highly flexible and responsive to their environment, making them valuable across various biomedical industries including drug delivery, wound healing, valve and tissue engineering, and sensor applications Hydrogels have gained popularity due to their unique properties, such as high-water retention, softness, flexibility, biocompatibility, responsiveness to temperature, and cost-effectiveness [3–4].

Hydrogel material plays a crucial role in tissue engineering, and the development of hybrid hydrogels using different polymers is a research focus [4]. Their applications range from regenerative medicine to tissue engineering, including bone regeneration, cartilage and vascular tissue engineering, heart-related applications, wound healing, and artificial cornea development. Their biocompatibility, adjustable viscosity, physical and mechanical properties, ability to provide a framework for various tissues, high water content, and oxygen permeability make them highly suitable for these applications [5–7]. There are many ways to synthesize hydrogels such as shear forces, magnetic and electric fields, compression and stretching forces, directional crystallization, ion diffusion, photolithography, and 3D printing [8].

Furthermore, additive manufacturing is an innovative manufacturing technique that creates three-dimensional objects by adding successive layers of material based on a digital blueprint. Using 3D printing technology with hydrogel materials presents an opportunity to manufacture flexible designs and other complex structures. This advancement may introduce a shift from traditional plastic materials in 3D printing and pave the way for flexible materials to replace plastics, representing a significant breakthrough in 3D printing technology (**Figure 1**).

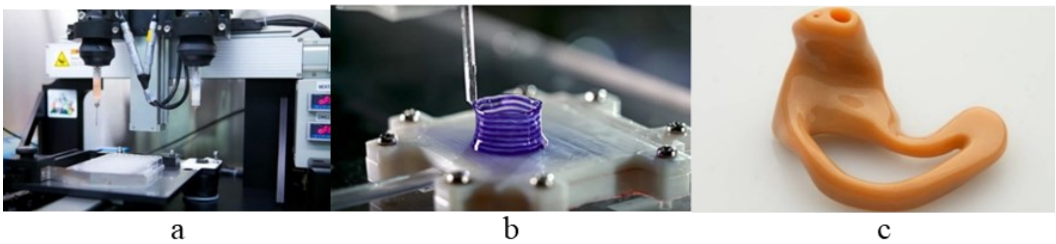

Figure 1. (a) 3D printing technology using hydrogel materials; **(b)** 3D printing hydrogel to create human body tissues; **(c)** 3D printed artificial ears using flexible materials.

The growth of the additive manufacturing industry is attributed to the opportunities it presents in producing supportive medical items such as artificial organs, implants, surgical guides, and assistive devices. Hydrogel materials, particularly in the production of coronary stents, are widely used in the medical field. Looking ahead, the research and development of 3D printers for hydrogel materials are expected to be a strategic focus. As the manufacturing industry continues to seek innovative and creative directions, 3D printing technology is seen as a transformative tool in the era of Industry 4.0. Exploring various 3D printing technologies and materials, hydrogel biomaterials show promise for producing flexible components. Hence, the development of a liquid material 3D printer and the preparation of hydrogel materials for liquid 3D printing are crucial. Experimental manufacturing and thorough evaluation of printed products will be essential for future research. In this research, the design and manufacture of the 3D printer with direct and indirect extruders was implemented. In addition, conductive sodium alginate 5% + 5% activated carbon by weight material was evaluated in this 3D printer.

2. Material and methods

2.1. Material

Hydrogel: conductive sodium alginate 5% by weight + 5% activated carbon by weight.

Sodium alginate (Na-alginate, viscosity 80–120 cP) was purchased from FUJIFILM Wako Pure Chemical Corporation, Japan. Charcoal (Steam-activated) was purchased from Duchefa Biochemie (Netherlands). Food coloring was bought from KUPKACE SHOP Ltd., Vietnam. All chemicals were used as received without further purification. Distilled water was used for gel preparation

2.2. Sample preparation procedure

Prepare sodium alginate solution using sodium alginate, distilled water, activated carbon and food coloring (**Figure 2**).

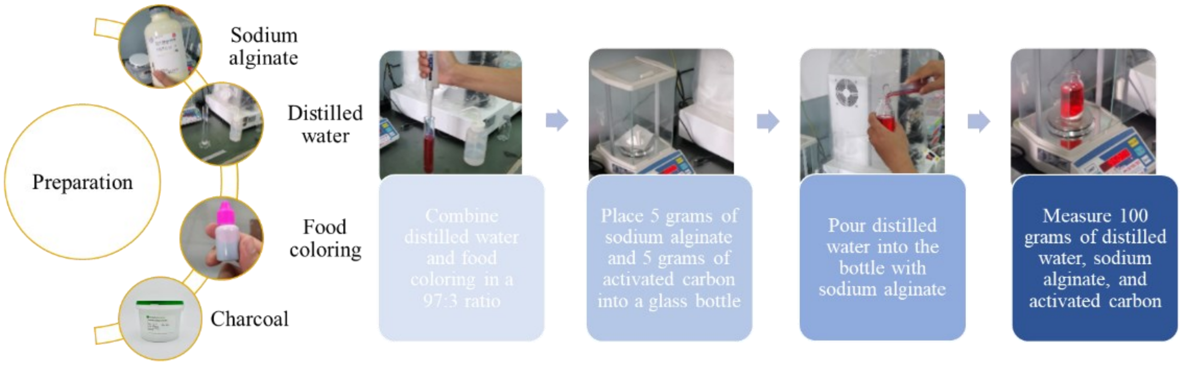

a) b)

Figure 2. Preparation of materials for making hydrogel.

First, combine distilled water and food coloring in a 97:3 ratio. Second, place 5 grams of sodium alginate and 5 grams of activated carbon into a glass bottle. Next, pour distilled water into the bottle with sodium alginate. Then, measure 100 grams of distilled water, sodium alginate, and activated carbon. Subsequently, stir the solution containing water, charcoal, and alginate twice a day for 3–4 days.

3. Design and calculation

3D printers are often built with 3-axis Cartesian *X*, *Y*, *Z*, Delta, and Polar coordinates. Cartesian structures have the primary benefit of being less expensive than other structure types that have comparable accuracy and repeatability in additive manufacturing [9]. For this project, the Cartesian structure is chosen and managed by the Arduino Mega 2560 circuit, which controls the stepper motor driver of the extruder and the three axes *X*, *Y*, and *Z*. The driver regulates the stepper motor of each axis using lead screw transmission mechanisms-nuts, guide belts, and slide rails to facilitate the movement of the three axes to the desired positions. The machine's hardware is composed of *X*, *Y*, and *Z* axes and dual print heads actuated by stepper motors. Individual axis movements are controlled by drivers, with overall operation managed by an Arduino Mega 2560. Printer settings are displayed on a 2004 LCD panel. The printer communicates with a computer via a USB interface (see **Figure 3**) [10–14].

The process of extrusion in 3D printing technology is facilitated by two primary components: the printer, which regulates the position of the print head, and the extruder, which controls the flow of material. The extrusion system encompasses three main types: a drive screw motor that propels the piston, compressed air that propels the piston, and a drive-through screw that extracts material from an external source. In the drive screw motor system, where the piston is propelled, direct contact is established between the material and the piston. This mechanism effectively governs the extrusion speed due to consistent volume displacement. However, one drawback of this approach is the requisite time to compensate for material loss in the needle tip, potentially leading to imprecise printing.

Alternatively, the pneumatic extrusion system harnesses compressed air as the driving force for extrusion. While compressed air is the more commonly employed medium, nitrogen may be utilized when sterility is necessary, particularly in bio-ink printing applications. Pneumatic extrusion demonstrates proficiency in extruding a diverse array of viscoelastic objects while boasting rapid response times facilitated by the swift pressurization and depressurization of the tank. Notwithstanding its efficacious performance, this system is comparatively intricate to construct and operate relative to motor control-based systems due to its reliance on compressed air.

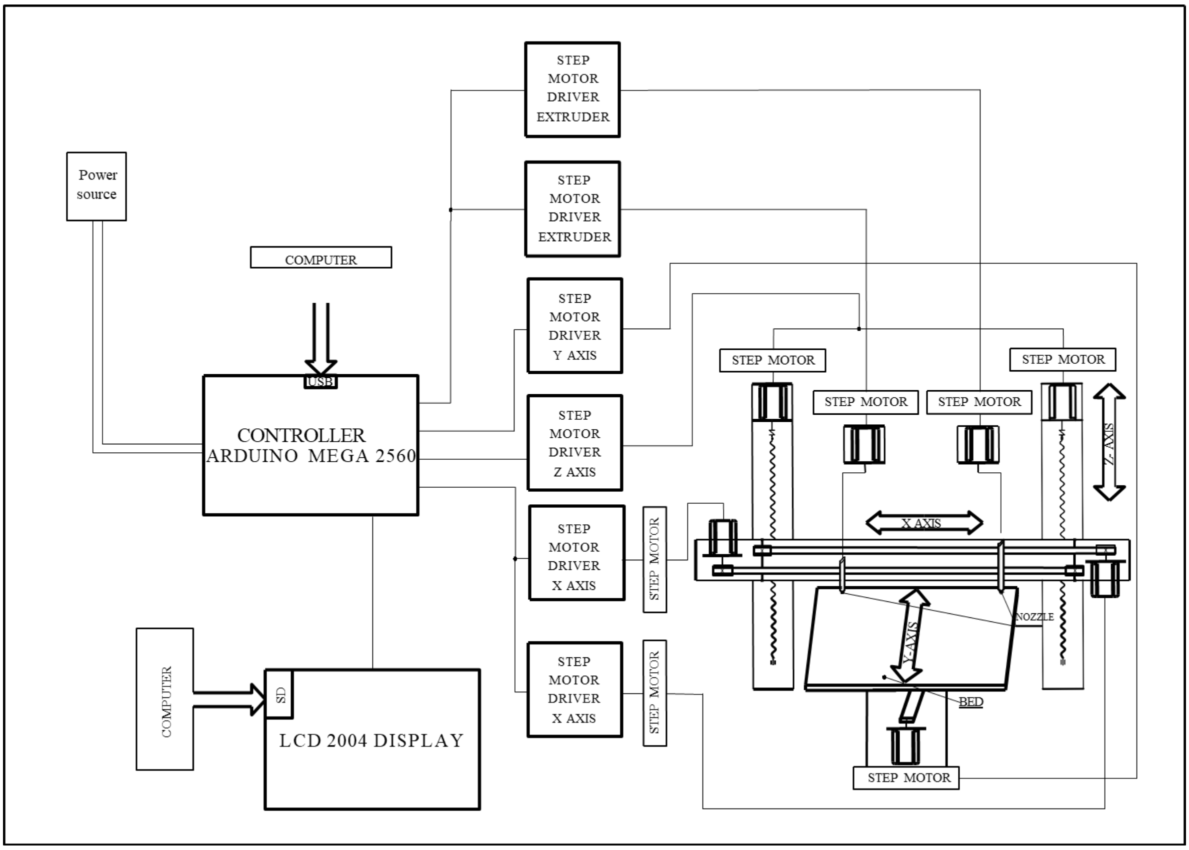

Figure 3. Diagram illustrating the operating principle of a 3D printer.

Lastly, the screw extrusion system engages a singular screw extruder to convey material from the hopper to the nozzle. A notable advantage of this design is its ability to facilitate continuous printing, as material can be loaded on demand. Furthermore, the rotating screw aids in homogenizing the material during the printing process, promoting uniformity and mitigating phase separation. Nevertheless, this design presents potential challenges, such as the risk of cross-contamination, as materials necessitate separate storage containers. Furthermore, delicate materials, such as cells, are unsuitable for screw extrusion transport, as the shear force incurred may compromise the integrity of the cell membrane. Moreover, the extruder design provides two options: direct and indirect extrusion, each accompanied by distinct advantages and disadvantages, as depicted in **Figure 4** and **Table 1**, respectively.

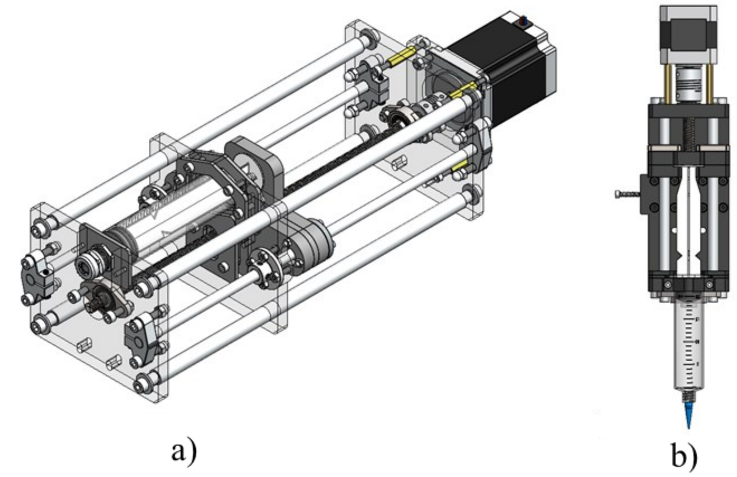

Figure 4. Design option. **(a)** Indirect extruder; **(b)** direct extruder.

Table 1. Advantages and disadvantages of Direct and indirect extruders [15–19].

Design method	Advantages	Disadvantages
Indirect extruder	• Large capacity • Does not limit the operating space of the machine • Movement is smoother because the *X*-axis does not have an extruder attached, and only the extruder head is attached.	• Need a motor with high torque. • Slow response time due to friction of the material in the tube. • Extrusion is unstable due to the impact of a large shear force.
Direct extruder	• Stable extrusion • Better material withdrawal • The engine has less power • Less affected by shear stress	• Increasing the *X*-axis mass leads to a limitation in printing speed. • Small storage capacity. • Limit the machine's working space.

This study designed and calculated a combination of direct and indirect extrusion as follows:

Calculate the *X*-axis:

X-axis parameters:

+ Load mass mounted on the *Y* axis: $m_1 = 1.5(\text{kg})$

+ Working length: L=100 (mm)

+ Maximum speed: $v_{max} = 120 \text{ mm/s}$

+ Printing speed: $v_{in} = 60 \text{ mm/s}$

+ Working time: t = 2 h

Calculate and select the stepper motor:

Pulley attached to the engine with parameters:

+ Number of teeth: $z = 20$

+ Pitch: $p = 2(\text{mm})$

The achievable maximum speed: v_{max}

→ Pulley's angular speed:

$$\omega_{in} = \frac{v_{in}}{d/2} = \frac{120}{4.75} \approx 25(\text{r/s}) \tag{1}$$

→ Time to rotates 1 round: $t = \frac{1}{25}(\text{s})$.

Distance traveled by the belt when Pulley rotates 1 round:

$$s = z \times p = 20 \times 2 = 40(\mathrm{mm}) \tag{2}$$

Maximum speed of stepper motor:

$$V = \frac{s}{t} = \frac{40(\mathrm{mm})}{\frac{1}{25}(\mathrm{s})} = \frac{40(\mathrm{mm})}{\frac{1}{25} \times \frac{1}{60}(\min())(mm/\min())} \tag{3}$$

$$V = \frac{60000}{40}\left(\mathrm{r}/\min()(\mathrm{r}/\min())\right) \tag{4}$$

The selected stepper motor is Nema 17 (model KH4238–B90201) with a rated current of 1.2A and voltage of 24V. Maximum rotation speed of the engine is $V = 1500(\mathrm{r}/\min())$. The torque of the stepper motor is $M = 125(\mathrm{mN.m})$.

The motor power:

$$P = V.M = 125 \times 10^{-3}.\frac{1500}{60} = 3.125(\mathrm{W}) \tag{5}$$

with: V–motor rotation speed (r/s); M–torque (N. m).

The overall performance of the drive system: $\eta = 0.95$.

Motor working capacity:

$$P_{lv} = \frac{P}{\eta} = \frac{3.125}{0.95} = 3.29(\mathrm{W}) \tag{6}$$

Using the same calculation method, the calculation parameters for the Y and Z axes are respectively $P_{lv} = 3.28(\mathrm{W})$, $P_{lv} = 1.89(\mathrm{W})$, extruder motor is $P_{lv} = 3.15(\mathrm{W})$.

Figure 3 illustrates the printer's operating principle in detail. **Figure 5** presents a detailed block diagram of the hardware components. The mechanical design for the indirect and direct extruder options is shown in **Figure 6**.

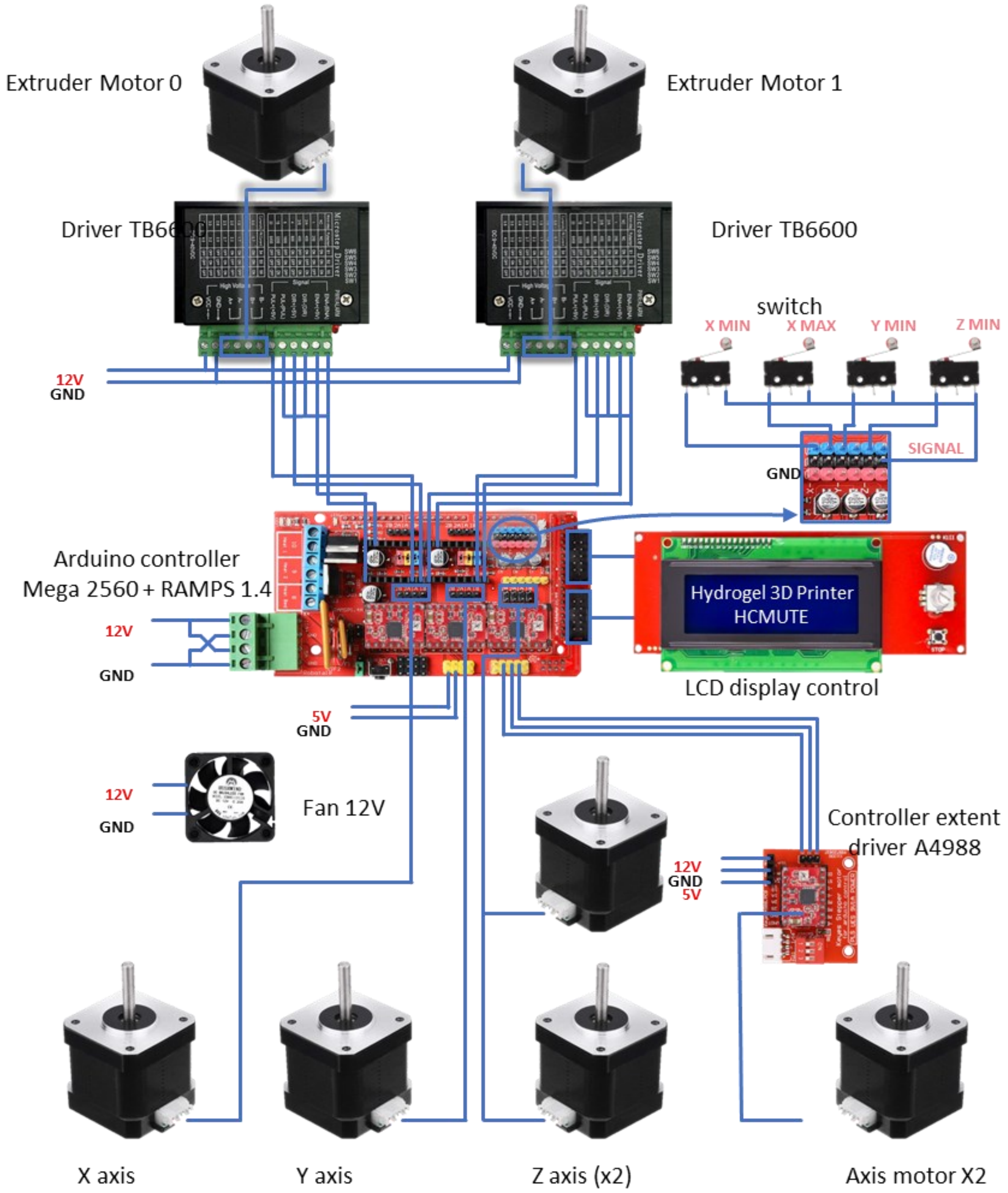

Figure 5. Control block wiring diagram.

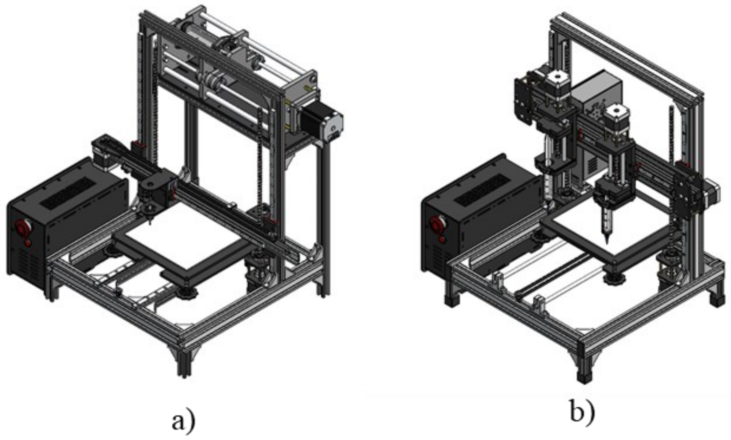

Figure 6. Designed of the 3D printer with. **(a)** Indirect extrusion; **(b)** direct extrusion.

Calculate the hydrogel extruder

Calculate and select screws and nuts:

Input parameters:

+ Volume of cylinder: $V = 20(ml) = 0.02(dm^3)$

+ Specific gravity of gel: $d = 625000(N/m^3)$

+ Average axial force:

$$F_a = Vd = 0.02 \times 10^{-3} \times 625000 = 12.5(N) \tag{7}$$

+ Travel route: L = 150 (mm)

Calculate the average diameter according to the formula:

$$d_2 \geq \sqrt{\frac{F_a}{\pi \psi_H \psi_h [q]}} \tag{8}$$

With $\psi_H = 2.0$ (raw nut); square thread height coefficient $\psi_h = 0.5$; The allowable pressure depends on the material of the screw and nut, we have the material of the screw - nut being steel - brass, choose $[q] = 10(\text{MPa})$.

$$d_2 \geq \sqrt{\frac{12.5}{3.14 \times 2 \times 0.5 \times 10}} \rightarrow d_2 \geq 0.63(\text{mm}) \tag{9}$$

Select $d_2 \approx 7(\text{mm})$, screw pitch $p = 2(\text{mm})$

Select thread parameters:

Thread profile height: $h = 0.1.\, d_2 = 0.1 \times 7 = 0.7(\text{mm})$

Outer diameter: $d = d_2 + h = 7 + 0.7 = 7.7(\text{mm})$

Inner diameter: $d_1 = d_2 - h = 7 - 0.7 = 6.3(\text{mm})$

Thread step: $p = 2h = 2 \times 0.7 = 1.4(\text{mm})$

Screw step: $p_h = Z_h p = 4 \times 1.4 = 5.6(\text{mm})$

Screw angle: $\gamma = arctg[p_h/(\pi d_2)] = arctg\left[\frac{5.6}{\pi \times 7}\right] = 0.25°$

The friction coefficient of the poorly lubricated steel-brass material pair is *f* = 0.1, so $\varphi = \text{arctg}(0{,}1) = 3.64°$.

Through the calculated parameters of the thread, we choose the T8 lead screw with the following parameters:

+ Outside diameter: $d = 8(\text{mm})$

+ Thread profile height: $h = 1(\text{mm})$

+ Average diameter: $d_2 = d - h = 8 - 1 = 7(\text{mm})$

+ Inner diameter: $d_1 = d_2 - h = 7 - 1 = 6(\text{mm})$

+ Thread step: $p = 2(\text{mm})$

+ Number of contacts: $Z_h = 4$

+ Screw step: $p_h = Z_h \times p = 4 \times 2 = 8(\text{mm})$

Test durability:

$$\sigma_{td} = \sqrt{\left(\frac{4F_a}{\pi d_1^2}\right)^2 + 3\left(\frac{T}{0.2 d_1^3}\right)^2} \tag{10}$$

where F_a-axial force (N); T—dangerous torque on the dangerous cross-section of the screw.

The dangerous torque on the dangerous front is determined according to the formula:

$$T = \frac{F_a tg(\gamma + \varphi) d_2}{2} = 12.5 \times tg(0.25^\circ + 3.64^\circ) \times \frac{7}{2} = 2.97(\text{Nmm}) \tag{11}$$

$$\sigma_{td} = \sqrt{\left(\frac{4 \times 12.5}{3.14 \times 6^2}\right)^2 + 3 \times \left(\frac{2.97}{0.2 \times 6^3}\right)^2} = 0.46(\text{MPa}) \tag{12}$$

With stainless steel, $\sigma_{ch} = 205(\text{MPa})$, therefore,

$$[\sigma] = \frac{\sigma_{ch}}{3} = \frac{205}{3} = 68.33(\text{MPa}) \tag{13}$$

$\sigma_{td} < [\sigma]$ →Durable conditions are guaranteed.

Test stability:

To determine the softness of the screw, it is necessary to calculate the moment of inertia *J* and radius of inertia *i*:

$$J = \frac{\pi d_1^2}{4}\left(0.4 + 0.6\frac{d}{d_1}\right) = \frac{3.14 \times 7^2}{4} \times \left(0.4 + 0.6 \times \frac{8}{7}\right) = 41.762(\text{mm}^2) \tag{14}$$

$$i = \sqrt{\frac{J}{\pi d_1^2/4}} = \sqrt{\frac{41.762}{3.14 \times 7^2/4}} = 1.04 \tag{15}$$

Softness of screw:

$$\lambda = \frac{\mu L}{i} = \frac{2 \times 150}{1.04} = 288.46 \tag{16}$$

in which: $\mu = 2$ (screw is screwed in fixed-free style).

Using $\lambda > 100$the Euler formula to calculate the limit load, according to the Euler formula:

$$F_{th} = \pi^2 EJ/(\mu L)^2 \tag{17}$$

where *E* is the elastic modulus, for steel $E = 2.1.10^5(MPa)$; J—moment of inertia of the screw cross section.

$$F_{th} = \frac{3.14^2 \times 2.1 \times 10^5 \times 41.762}{(2 \times 150)^2} = 960.77(N) \tag{18}$$

Stable safety factor:

$$S_o = \frac{F_{th}}{F_a} = \frac{960.77}{10} = 96.077 > [S_o] = 2.5\ to\ 4 \tag{19}$$

Stable conditions are guaranteed.

Size of nut:

+ Height of nut: $H = \psi_H \times d_2 = 2 \times 7 = 14(mm)$

+ Number of thread turns of the nut $z = \frac{H}{p} = \frac{14}{2} = 7 < z_{max}$

+ Outside diameter of nut:

$$D \geq \sqrt{4F_a/(\pi[\sigma_K]) + d^2} = \sqrt{4 \times 12.5/(3.14 \times 40) + 8^2} = 8(mm) \tag{20}$$

select$D = 8(mm)$

+ Outside diameter of nut flange:

$$D_1 \geq \sqrt{4F_a/(\pi[\sigma_d]) + D^2} = \sqrt{4 \times 12.5/(3.14 \times 80) + 8^2} = 8(mm) \tag{21}$$

select $D_1 = 8(mm)$

Calculate and select the stepper motor:

Screw diameter: $d = 8(mm)$

Length of screw:$L = 150(mm)$

Thread step:$p = 2(mm)$

Distance traveled when the screw rotates once:

$$s = Z_h.p = 4.2 = 8(mm) \tag{22}$$

with Z_h—number of leads; p—screw thread pitch.

Maximum speed achieved by the structure: $v_{max} = 160\ (mm/s)$

→Angular velocity of Pulley when printing:

$$\omega_{in} = \frac{v_{max}}{R\frac{v_{max}}{d/2\frac{160}{4}(r/s)}} \tag{23}$$

→Time to complete 1 round of Pulley: $t = \frac{1}{40}(s)$.

Maximum speed of stepper motor:

$$V = \frac{s}{t} = \frac{8(mm)}{\frac{1}{40}(s)} = \frac{8(mm)}{\frac{1}{40} \times \frac{1}{60}(min())\left(mm/min()\frac{19200}{8}\left(r/min()(r/min())\right)\right)} \tag{24}$$

The stepper motor chosen is Nema 17 (model KH4238-B90201) with a rated current of 1.2 A, and a voltage of 24 V.

Based on the graph of Figure 5 and the maximum rotation speed of the motor, $V = 2400(r/min)$. The torque of the stepper motor can determine $M = 75(mN.m)$.

The engine's capacity is:

$$P = V.M = 75 \times 10^{-3}.\frac{2400}{60} = 3(W) \tag{25}$$

where: V—engine rotation speed (r/s); M—torque (Nm).

The overall efficiency of the drive system is: $\eta = 0.95$.

Engine capacity:

$$P_{lv} = \frac{P}{\eta} = \frac{3}{0.95} = 3.15(W) \tag{26}$$

The 3D printer hydrogel with parameters follows in **Table 2**.

Table 2. 3D printer hydrogel parameter.

Parameter	**Value**
Print size	180 mm × 180 mm × 150 mm
Print head	2
Material volume/print head	20 mL
Print head diameter	0.6 mm
Speed extrusion	20–80 mm/s
Printing speed	10–90 mm/s

4. Fabrication and experiment

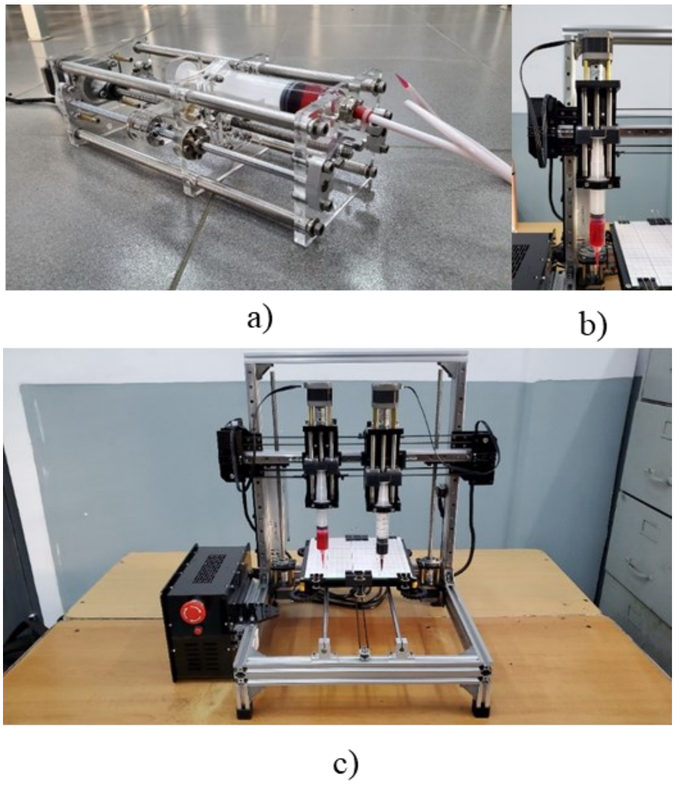

Figure 7. (a) Indirect extruder; **(b)** direct extruder; **(c)** dual direct extruder 3D printer.

After the design and manufacture of the 3D hydrogel material printer machine based on design and calculation results, it underwent evaluation for stability criteria (**Figure 7**). The machine frame ensures strong bearing capacity for the moving mechanisms of the *X*, *Y*, and *Z* clusters. The results demonstrate that the manufactured products meet the specified requirements (as **Table 2**). Following the verification of stable machine hardware operation, the machine is loaded with gel into the extruder and subjected to testing using both the direct and indirect extrusion methods, as shown in **Figure 8**. Test results show that hydrogel material can be completely printed on a 3D printer. Both direct and indirect extrusion heads provide good results. However, to evaluate the efficiency and optimal parameters of direct and indirect extruders, more in-depth research is needed.

Figure 8. Test results with indirect extruder and indirect extruder.

Assessment of the electrical conductivity of the hydrogel material 5% by weight of sodium alginate + 5% by weight of activated carbon through 3 test samples with different lengths (**Figure 9**). The result is shown in **Table 3**.

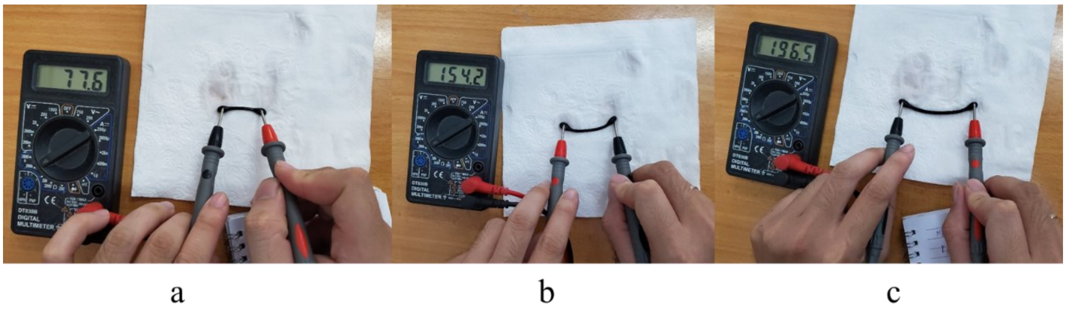

a b c

Figure 9. Conductivity measurement. **(a)** Sample 1; **(b)** sample 2; **(c)** sample 3.

Table 3. The result of the conductivity sample.

Item	Sample 1	Sample 2	Sample 3
Resistor R (kΩ)	77.6	154.2	196.5
Length l (mm)	34	50	67
Diameter d (mm)	2	2.3	2.7
Section A (mm^2)	3.14	4.16	5.73
Conductivity σ (s/m)	1.375×10^{-3}	1.347×10^{-3}	1.950×10^{-3}

Average conductivity:

$$\overline{\sigma} = \frac{\sigma_1 + \sigma_2 + \sigma_3}{3} = \frac{1{,}375 + 1{,}347 + 1{,}950}{3} \times 10^{-3} = 1{,}559 \times 10^{-3} (s/m)$$

Error:

$$a = |\overline{\sigma} - \sigma_1| = |1{,}558 - 1{,}375| \times 10^{-3} = 0{,}000183$$

$$b = |\overline{\sigma} - \sigma_2| = |1{,}558 - 1{,}347| \times 10^{-3} = 0{,}000211$$

$$c = |\overline{\sigma} - \sigma_3| = |1{,}559 - 1{,}950| \times 10^{-3} = 0{,}000394$$

$$d = \frac{a + b + c}{3} = \frac{0.000183 + 0.000211 + 0.000394}{3} = 0.000263$$

Conductivity:

$$\sigma = \overline{\sigma} \pm d = 1{,}558 \times 10^{-3} \pm 0{,}000263 (S/m)$$

Factors such as the type of hydrogel, the composition ratio, and the shaping method can significantly influence the conductivity of hydrogels. Previous studies have supported this. By changing the concentration of PAA, the ionic conductivity (up to $35.36 \pm 7.72 \times 10^{-3}$ S.cm^{-1}). A PPy-based microfluidic hollow hydrogel fiber, which combines sodium alginate and polyacrylamide, has a conductivity of 0.32 S m^{-1}, based on the Fe^{3+} triggered simultaneous polymerization of pyrrole and bio adhesive dopamine on hyperbranched polymer chains, a paintable hydrogel with conductivity ($6.51 \pm 0.12 \times 10^{-4}$ S.cm^{-1} [20]. The hydrogels' extremely high apparent electrical conductivity is a result of their heterogeneous structure's thoughtful construction of 1.66×10^{-4} S.m^{-1} [21].

5. Conclusions

The 3D printer is capable of fully accommodating the 3D printing of hydrogel materials while meeting the parameters set in the original design. It has been tested for both indirect and direct extrusion methods, with the results demonstrating the printer's ability to work with hydrogel materials. The 3D printer is manufactured with parameters: 180 × 180 × 150mm working space, dual print head, 20 mL material volume, 0.6 mm nozzle diameter, 20–80mm/s in speed extrusion, and 10–90mm/s in printing speed.

The printer's ability to produce high-quality conductive hydrogel prints paves the way for further exploration of 3D-printed hydrogel-based materials. Conductive hydrogels offer a promising avenue for ongoing research, particularly in the development of biomedical sensors and electrically conductive biomaterials

Additionally, future studies should focus on further evaluating the optimal parameters for direct and indirect extrusion. The successful development of a 3D printer for hydrogel materials establishes a solid foundation for future research and can be extended to similar materials.

Author contributions: Conceptualization, TTN and VTT; methodology, NHP; software, HST and LNC; validation, TTN; formal analysis, NHP, HST and LNC; investigation, HST and LNC; resources, VTT; data curation, HST and LNC; writing—original draft preparation, NHP and TTN; writing—review and editing, THNP; visualization, THNP; supervision, VTT and QBP; project administration, TTN and VTT; funding acquisition, QBP. All authors have read and agreed to the published version of the manuscript.

Funding: This work belongs to project grant No: T2023-105 funded by Ho Chi Minh City University of Technology and Education, Vietnam. We extend our gratitude to the materials testing laboratory, Faculty of Mechanical Engineering, Ho Chi Minh City University of Technology and Education for their provision of the necessary equipment and machinery for the successful execution of this project. Additionally, we would like to thank the reviewers and editors for their constructive comments and suggestions for improving our work.

Conflict of interest: The authors declare no conflict of interest.

References

1. Tran VT, Mredha MdTI, Na JY, et al. Multifunctional poly(disulfide) hydrogels with extremely fast self-healing ability and

degradability. Chemical Engineering Journal. 2020; 394: 124941. doi: 10.1016/j.cej.2020.124941

2. Tran VT, Mredha MdTI, Jeon I. High-water-content hydrogels exhibiting superior stiffness, strength, and toughness. Extreme Mechanics Letters. 2020; 37: 100691. doi: 10.1016/j.eml.2020.100691
3. Nguyen TT, Tran VT. Long Nhut-Phi Nguyen, et al. A study on mechanical properties of Ca-alginate hydrogels. In: Proceeding of the 6th International Conference on Green Technology and Sustainable Development (GTSD); 2022.
4. Tran VT, Xu X, Mredha MdTI, et al. Hydrogel bowls for cleaning oil spills on water. Water Research. 2018; 145: 640-649. doi: 10.1016/j.watres.2018.09.012
5. J Wang J, Liu Y, Zhang X, et al. 3D printed agar/ calcium alginate hydrogels with high shape fidelity and tailorable mechanical properties. Polymer. 2021; 214: 123238. doi: 10.1016/j.polymer.2020.123238
6. Thien NC, Phuoc VV, Trinh PTD. Hydrogel materials—Properties and potential applications. Vietnam Science and Technology. 2019; 1-2.
7. Pham DTM, Hoang HT, Dang VD, et al. Preparation of bio - adhesive hydrogel based on chitosan for wound sealant. Science and Technology Development Journal. 2015; 18(2): 88-95. doi: 10.32508/stdj.v18i2.1136
8. Sano K, Ishida Y, Aida T. Synthesis of Anisotropic Hydrogels and Their Applications. Angewandte Chemie International Edition. 2018; 57(10): 2532-2543. doi: 10.1002/anie.201708196
9. Kopets E, Karimov A, Scalera L, et al. Estimating Natural Frequencies of Cartesian 3D Printer Based on Kinematic Scheme. Applied Sciences. 2022; 12(9): 4514. doi: 10.3390/app12094514
10. Huang CY. Extrusion-based 3D Printing and Characterization of Edible Materials. Elsevier. 2018.
11. Shahrubudin N, Lee TC, Ramlan R. An Overview on 3D Printing Technology: Technological, Materials, and Applications. Procedia Manufacturing. 2019; 35: 1286-1296. doi: 10.1016/j.promfg.2019.06.089
12. Jakus AE. An Introduction to 3D Printing—Past, Present, and Future Promise. 3D Printing in Orthopaedic Surgery. Published online 2019: 1-15. doi: 10.1016/b978-0-323-58118-9.00001-4
13. Jadhav A, Jadhav VS. A review on 3D printing: An additive manufacturing technology. Materials Today: Proceedings. 2022; 62: 2094-2099. doi: 10.1016/j.matpr.2022.02.558
14. Liu C, Xu N, Zong Q, et al. Hydrogel prepared by 3D printing technology and its applications in the medical field. Colloid and Interface Science Communications. 2021; 44: 100498. doi: 10.1016/j.colcom.2021.100498
15. Goyanes A, Allahham N, Trenfield SJ, et al. Direct powder extrusion 3D printing: Fabrication of drug products using a novel single-step process. International Journal of Pharmaceutics. 2019; 567: 118471. doi: 10.1016/j.ijpharm.2019.118471
16. Singamneni S, Behera MP, Truong D, et al. Direct extrusion 3D printing for a softer PLA-based bio-polymer composite in pellet form. Journal of Materials Research and Technology. 2021; 15: 936-949. doi: 10.1016/j.jmrt.2021.08.044
17. Van Damme L, Briant E, Blondeel P, et al. Indirect versus direct 3D printing of hydrogel scaffolds for adipose tissue regeneration Lana Van Damme, Emilie Briant, Phillip Blondeel, Sandra Van Vlierberghe. MRS Advances. 2020; 5(17): 855-864. doi: 10.1557/adv.2020.117
18. Cai J, Zhang B, Zhang M, et al. Indirect 3D printed ceramic: A literature review. Journal of Central South University. 2021; 28(4): 983-1002. doi: 10.1007/s11771-021-4674-1
19. Naghieh S, Sarker M, Sharma NK, et al. Printability of 3D Printed Hydrogel Scaffolds: Influence of Hydrogel Composition and Printing Parameters. Applied Sciences. 2019; 10(1): 292. doi: 10.3390/app10010292
20. Liang Y, Qiao L, Qiao B, et al. Conductive hydrogels for tissue repair. Chemical Science. 2023; 14(12): 3091-3116. doi: 10.1039/d3sc00145h
21. Zhou Q, Lyu J, Wang G, et al. Mechanically Strong and Multifunctional Hybrid Hydrogels with Ultrahigh Electrical Conductivity. Advanced Functional Materials. 2021; 31(40). doi: 10.1002/adfm.202104536

Mechanical Engineering Advances 2024, 2(2), 421.
https://doi.org/10.59400/mea.v2i2.421

Article

Traction drive simulations when starting an electric locomotive series ŽS 444 on the railway tracks of Serbia

Branislav Gavrilovic[1,*], **Vladimir Aleksandrovich Baboshin**[2]

[1] Railway College, Academy of Technical and Art Applied Studies Belgrade, 11000 Belgrade, Serbia
[2] Department of Reconstruction of Automation, Telemechanics and Communication Devices on Railways, The Ulyanovsk Higher Military Command School of Communications, Sankt. Peterburg 198206, Russia
* **Corresponding author:** Branislav Gavrilovic, gavrilovic branislav5@gmail.com

CITATION

Gavrilovic B, Baboshin VA. Traction drive simulations when starting an electric locomotive series ŽS 444 on the railway tracks of Serbia. Mechanical Engineering Advances. 2024; 2(2): 421. https://doi.org/10.59400/mea.v2i2.421

ARTICLE INFO

Received: 5 July 2024
Accepted: 30 September 2024
Available online: 31 October 2024

Abstract: The manuscript presents and describes the Model in Matlab-simulink, which allows to display the time change of the firing angle of the thyristor of the single-phase rectifier, the mean value of the voltage, the armature current and the speed of the electric motor during the start-up of the electric locomotive ŽS 444 series for different given mechanically loaded and reference speeds of traction electric motors. The model makes it possible to establish the desired reference speed change ramps for different reference speeds and mechanical loads from +250 rpm, i.e., the maximum current of the electric motor armature up to 1250 A.

Keywords: railways of Serbia; electric locomotive ŽS 444 series; direct current electric motor

1. Introduction

Electric locomotives of the 444 series, known as "Severine", were obtained by improving 30 electric locomotives of the 441 series. Improvements are reflected in the application of thyristor converters, which enabled the continuous regulation of traction motor current. The drive is divided into two independent twin-engine units. Certain improvements have also been made in the functioning of the electrodynamic (electro resistive) brake. The new system of regulation of the locomotive's electric motor drive was realized with the help of a microprocessor. In general, there was not much modernization in the mechanical part. After the reconstruction and modernization of 30 locomotives, the 441 series was renumbered to 444 (from 001 to 030) and was put into traffic during the following years (2004–2007).

The designer of this type is ASEA from Sweden, and the license for the production of these locomotives was taken over by the Croatian factory "Rade Končar" in 1970 in cooperation with "MIN" from Niš, Serbia [1–3].

Figure 1 shows the layout, and **Figure 2** shows a simplified diagram of the ŽS 444 series electric locomotive.

Figure 1. Appearance of the ŽS 444 series electric locomotive [4].

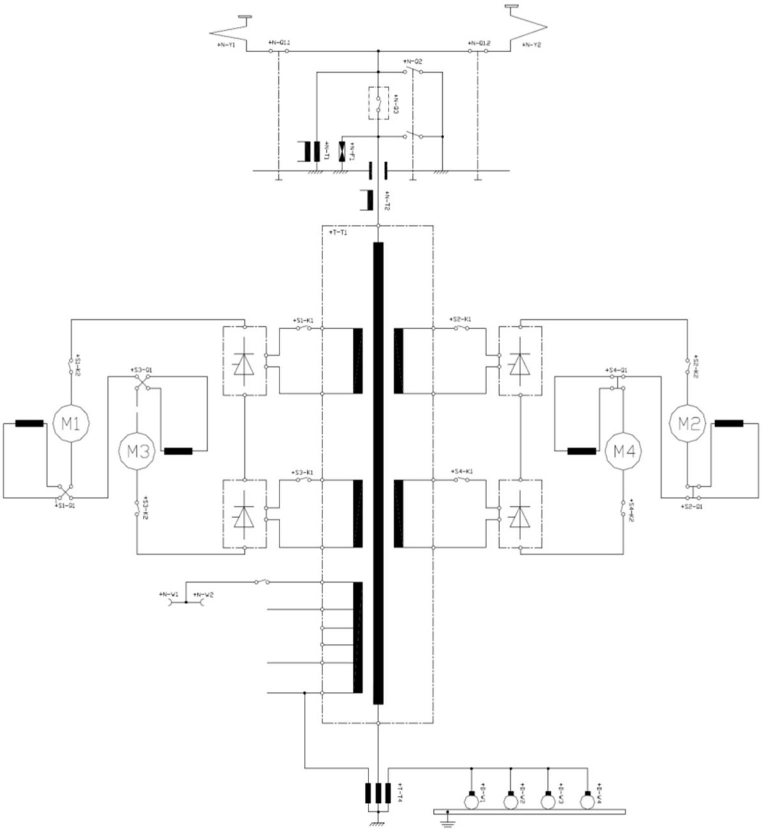

Figure 2. Simplified diagram of the main circuit in traction [4].

Table 1 shows the basic data of the ŽS 444 series electric locomotive [4].

Table 1. Technical data of the electric locomotive series ŽS 444 [4].

Parameter	**The data**
Axle arrangement	Bo’ Bo’
Track width	1.435 mm
The distance between the axles in the stand	2.700 mm
Pedestal spacing	7.700 mm
Total mass of locomotives	78 t ± 2 %
Axle pressure	19.5 t ± 2%

Table 1. (*Continued*).

Parameter	The data
Top speed	120 km/h
Transmission ratio of the axle gear	1 : 3, 65
Lasting power	3.860 kW
Maximum traction	276 kN
One-hour traction	188 kN
Permanent traction	175 kN
Power for electric heating	800 kVA
Contact network voltage	25 kV
The highest height of the contact line	6.500 mm
Temperature range of locomotive operation	−25–+40 °C

2. Locomotive model in Matlab-Simulink

2.1. Modeling and simulation methodology

In general, the simulation of complex systems such as electric locomotives of the ŽS 444 series helps to understand those systems and has an indispensable role, considering that experimenting with this system is often impossible, impractical, too expensive, time-consuming and too dangerous.

Modeling and simulation of the ŽS 444 series electric locomotive (which are often considered together, as compatible techniques that have the same goal), were carried out in the following three stages.

- Task setting

Before starting the act of modeling and simulation, the tasks and goals of the research are clearly defined. These findings were reflected in the need for a clear understanding of the dynamic state of operation of the devices and equipment of the main circuit immediately when the locomotive of the ŽS 444 series was started. In doing so, it was insisted on understanding first of all: temporal changes in the firing angle of the thyristor of the single-phase rectifier, the mean value of the voltage, the armature current and movement speed. of the electric motor when starting the electric locomotive for different mechanical loads of the locomotive. In view of the need for the smallest possible degree of idealization (approximation) of locomotive operation, the simulation model in Matlab-Simulink was chosen, this is because Matlab-Simulink offers three options for describing the ŽS 444 series locomotive that can be combined: locomotive description using higher programming languages, locomotive description using Matlab functions and graphical representation of the model using blocks. At the same time, using blocks is the most convenient and fastest way to edit the model until the desired results are achieved [4].

- Studying the system and forming a structural scheme

After setting the task and defining the stated goals, we started identifying and determining the limits of the System (technical characteristics of the locomotive), as well as its components and the way they interact. The variable quantities, their arrangement and mutual relations, as well as the inputs and outputs of the system, are defined. At the same time, the change in contact network voltage was defined as a possible external influence on the proper operation of the locomotive. The ranges of possible changes in this voltage are determined within the limits of 19 kV to 27.5 kV.

- Model development

The simulation of electric locomotives of the ŽS 444 series in principle boils down to determining the behavior of the model based on the set input values (voltage of the contact network, set limit speed of movement and mechanical load of the locomotive). With this simulation, the accuracy of the model was evaluated by comparing the values of individual variables in the process and the corresponding values of the variables in the model. The results of the simulations were continuously analyzed during the creation of the model with the necessary evaluation of the model until the results were not satisfactory with the experimental results that were available.

2.2. Structural scheme of the model

Figure 3 shows the model of the 444 series electric locomotive in Matlab-Simulink during speed control. The model illustrates a single-phase thyristor converter drive used to power an 850 kW DC motor. The locomotive's thyristor converters are fed to the 25 kV, 50Hz catenary via the main transformer to step down the voltage to 1265V (no-load). The technical characteristics of the main transformer are given in **Table 2** [4].

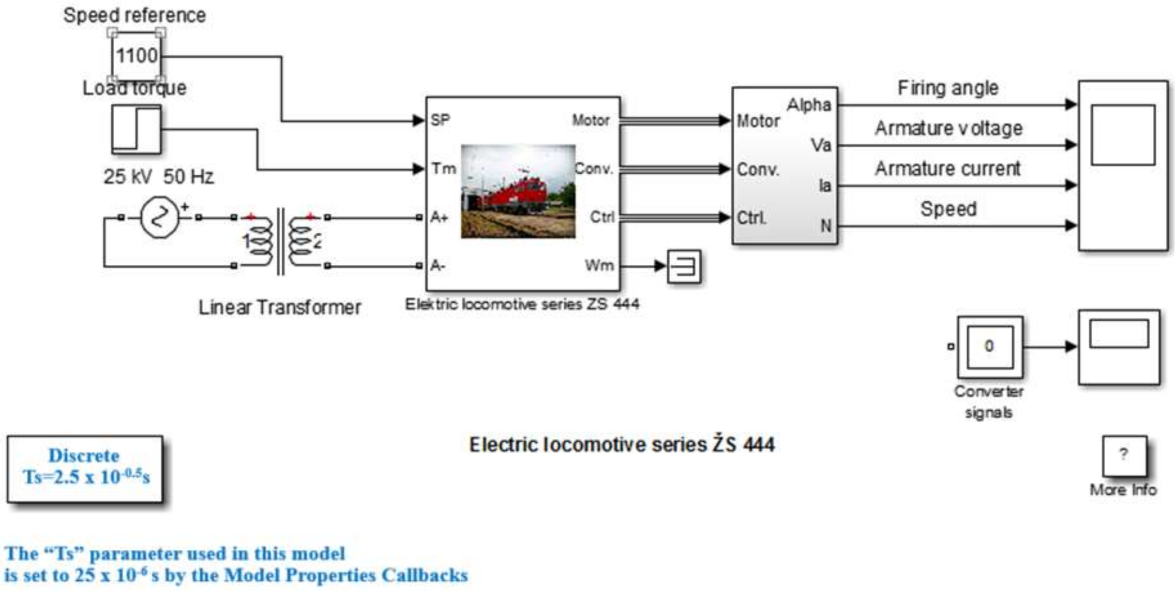

Figure 3. Structural scheme of the model of the 444 series electric locomotive in Matlab-Simulink during speed control.

The locomotive model is built from five main blocks. The DC drive electric motor, single-phase thyristor rectifier and thyristor bridge firing unit blocks are provided from the SimPowerSystems™ library while the speed controller and traction motor current controller blocks are specific and modeled separately. The armature voltage of the motor is provided by a two-square thyristor rectifier controlled by PI current and speed regulators through the main choke of inductance 4.5 mH. The speed controller provides the armature current reference (in pu) through the speed sensor, which is used by the current controller to obtain the electromagnetic torque required to achieve the desired speed. The rate of change of the speed reference follows the acceleration and deceleration ramps to avoid sudden reference changes that could cause excessive armature current and destabilize the system. The current regulator controls the armature current by calculating the appropriate firing angle of the thyristor. This generates the rectifier output voltage required to obtain the desired armature current. The block "regulation switch" allows switching from one type of regulation to another. During current (torque) regulation, the speed controller is disabled. **Figure 4** shows the model of the locomotive at speed regulation with the above blocks.

Table 2. Technical characteristics of the main electrical transformer series 444 [4].

Nominal primary voltage	**25 kV, 50 Hz**
The highest voltage of the traction secondary (no load)	1265 V
Voltage for electrodynamic braking in end position	115 V
Train heating voltage (idle)	1525 V
Permanent train heating current	335 A (max 400A)
Voltages on the outputs of the secondary for the auxiliary drive	403 V, 482 V (546V), 718 V, 892 V (1009 V)
Secondary traction power	4 × 1265 kVA
Secondary power for auxiliary drive	115 kVA
Cooling	OFAF (forced oil, forced air)

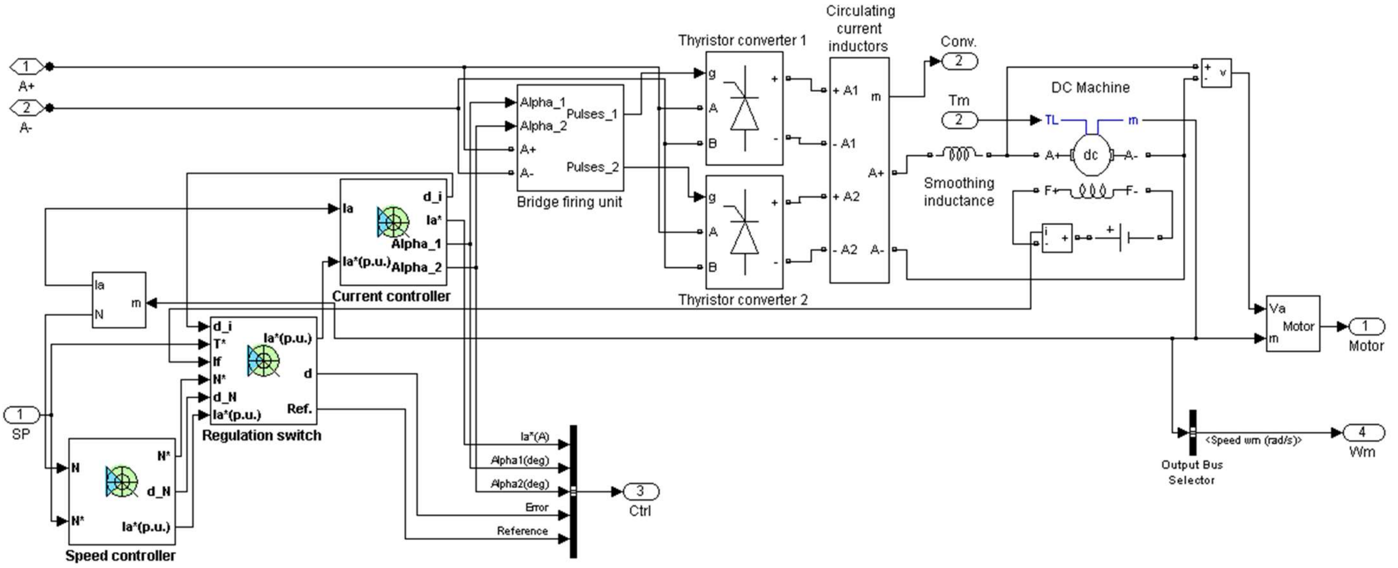

Figure 4. Blocks as integral parts of the ŽS 444 series electric locomotive.

2.3. Speed regulator block

The speed controller is shown in **Figure 5** and uses a PI controller. The controller provides an armature current reference (in pu) that is used by the current regulator to obtain the electromagnetic torque required to achieve the desired speed. During torque regulation, the speed controller is disabled [5–7].

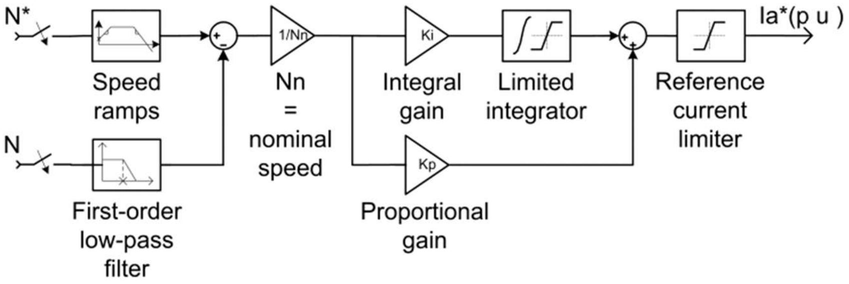

Figure 5. Traction electric motor speed regulator block.

The speed controller takes the speed reference (in rpm) and the rotor speed of the DC traction electric motor as input parameters. The rate of change of the reference speed will follow the acceleration and deceleration ramps that are predefined to avoid sudden reference changes that could cause excessive armature current and destabilize the system. The velocity measurement is filtered using a first-order low-pass filter. The current reference output is limited between 0 pu and a predefined upper limit.

2.4. Current regulator block

The armature current regulator is shown in **Figure 6** and uses a second PI controller. The regulator controls the armature current by calculating the appropriate firing angle of the thyristor. This generates the rectifier output voltage required to obtain the desired armature current and thus the desired electromagnetic torque. The controller takes the current reference (in pu) and the armature current flowing through the motor as input parameters. The current reference is either provided by the speed controller during speed control or is calculated from the torque reference that is preset during torque control. This is controlled by means of a block: “control switch” [5,8,9].

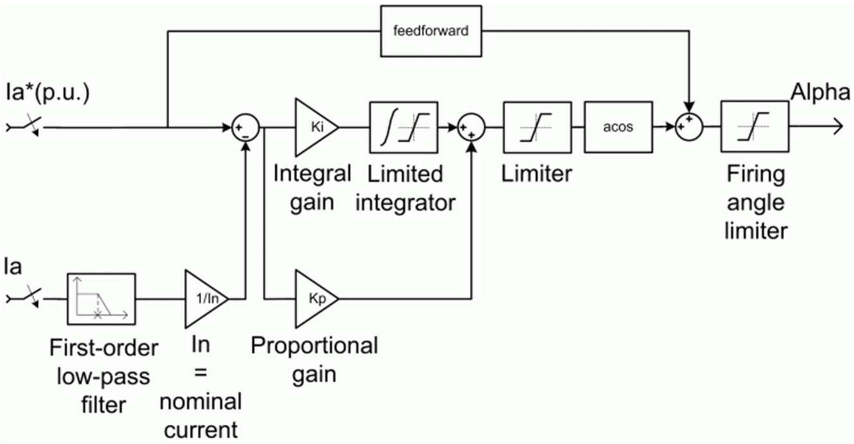

Figure 6. Traction electric motor armature current regulator block.

The armature current input is filtered using a first-order low-pass filter. The arcsin function is used to linearize the control system during continuous execution. To compensate for the nonlinearities that appear during discontinuous conduction, the firing angle is added in advance. This improves system response time. The shooting angle can vary between 0 and 180 degrees.

2.5. Single-phase thyristor rectifier block

The thyristor rectifier block consists of one controlled current source on the AC side and one controlled voltage source on the DC side (**Figure 7**) [5,10–26].

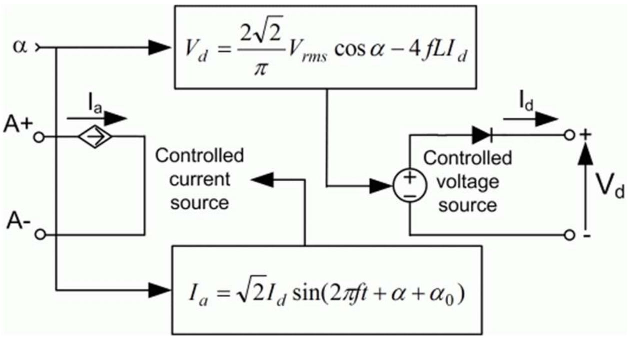

Figure 7. Single-phase thyristor rectifier block.

The input, alternating current of the rectifier is given by the following equation:

$$I_a = \sqrt{2} I_d \, sin(2\pi f t + \alpha + \alpha_0) \tag{1}$$

where are they:

α—ignition angle value,

α_0—phase angle on the alternating current side,

f—alternating current frequency *i*,

I_d—value of the rectified output current.

The DC output voltage of the rectifier represents the average value of the rectified voltage waveform for the continuous armature current according to the following equation:

$$V_a = \frac{2\sqrt{2}}{\pi} V_{rms} \, cos\, \alpha - 4fLI_d \tag{2}$$

where are they:

V_{rms}—input rms voltage value, and

L—source inductance.

2.6. The pulse generator block for starting the thyristor rectifier

The discrete synchronized pulse generator block generates pulses for firing the rectifier thyristors. The Synchronized 6-Pulse Generator block is configured to operate in double-pulse mode. In this mode, two pulses are sent to each thyristor: the first pulse when the alpha angle is reached, then the second pulse 60 degrees later, when the next thyristor is activated.

Figure 8 shows six-pulse synchronization for an alpha angle of 30 degrees and with a dual-pulse mode. It is easy to see that the pulses are generated 30 degrees after the zero crossing between line to line [12–14].

The sequence of pulses at the output of the block corresponds to the natural sequence of commutation of the three-phase thyristor bridge. When a 6-pulse synchronized generator block is connected to the pulse input of a universal bridge block (with thyristors as a power electronic device), the pulses are sent to the thyristors in the following order [12,15–26]:

- Input alpha 1 is an alpha signal in degrees and is connected to the controller system for controlling the pulse of the generator, a
- Inputs alpha 1, A+ and A−AB are the inputs to which the synchronization voltage is supplied, which is in phase with the input AC voltage of the single-phase thyristor rectifier.
- Input 5 allows the operation of the generator to be blocked. The output contains two pulse signals.

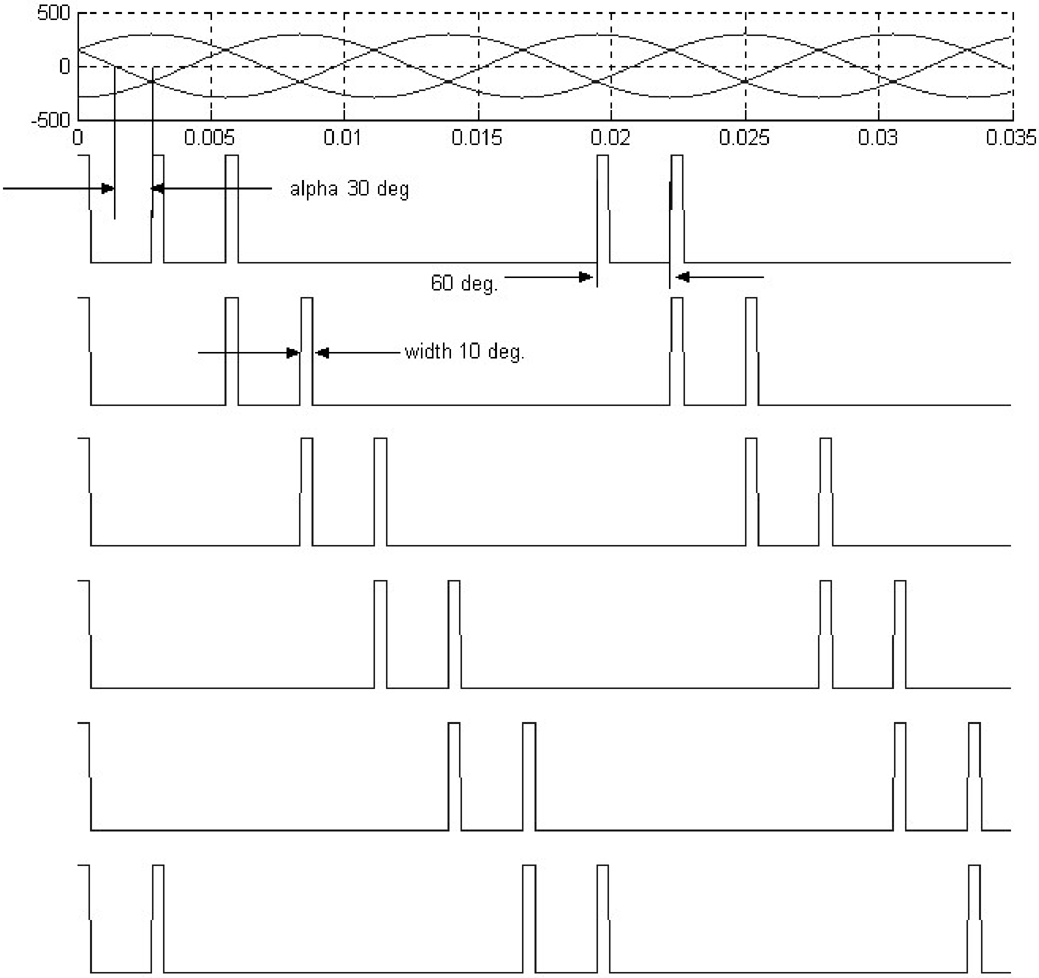

Figure 8. Synchronized 6-pulse generator block configured in dual-pulse mode.

3. Locomotive table dialog

The dialogue box of the locomotive consists of: the dialogue table of the drive electric motor, thyristor rectifier and controller.

3.1. Drive electric motor table dialog

Traction electric motors of locomotives are unidirectional wave machines of different types LJE 108-2 (ASEA, ELIN, ELECTROPUTERE) and ISVK 644-8 (KONĆAR), but of exactly the same construction, identical parameters and characteristics. The technical characteristics of the electric motor are given in **Table 3** [2–4].

Table 3. Nominal data of traction motors of the ŽS 444 series locomotive.

	Permanently	**One hour**	**Maximum**
Voltage (V)	770	770	870
Current (A)	1180	1250	1715
Rotation speed (rpm)	1100	1185	1715
Power (kW)	850	900	
Full Excitation (%)	87		
Min. Excitation (%)	45		

The drive electric motor dialog table is shown in **Figure 9** and provides the electrical parameters and mechanical parameters of the motor. The electrical parameters of the motor refer to the ohmic and inductive resistance of the windings of the stator and rotor of the motor. Given that a speed of 1100 (rpm) was chosen as the mechanical input when modeling the mechanical system of the engine, the electromagnetic torque as an output quantity was obtained based on the expression:

$$T_e = J\frac{d}{dt}\omega_r + F\omega_r + T_m \tag{3}$$

where are they:

J—coefficient of inertia of all rotating masses of the engine (J = 0.25 kg m^2),

F—coefficient of viscous friction.

T_m—coefficient of torsional friction.

During the conducted simulations, it was assumed that: $J = 0.25$ kg m^2, $F = 0.01$ Nms, $T_m = 0.01$ Nm [2–4].

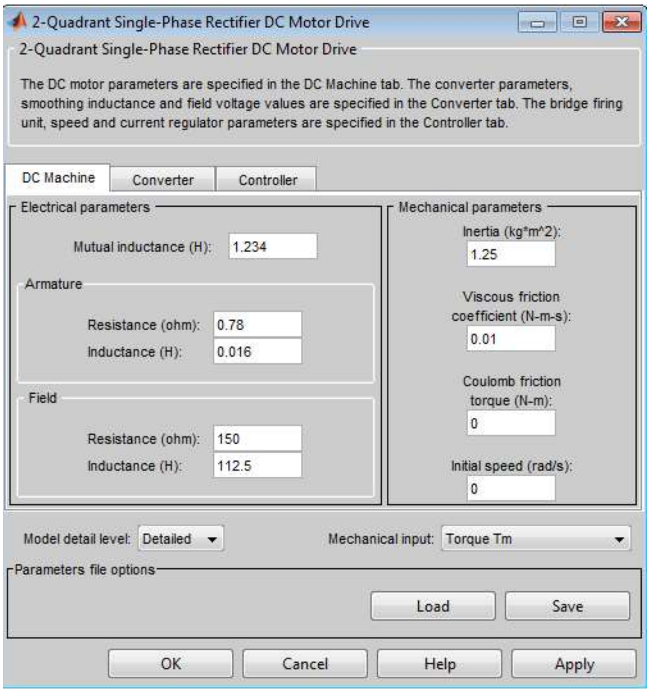

2-Quadrant Single-Phase Rectifier DC Motor Drive

The DC motor parameters are specified in the DC Machine tab. The converter parameters, smoothing inductance and field voltage values are specified in the Converter tab. The bridge firing unit, speed and current regulator parameters are specified in the Controller tab.

Mutual inductance (H): 1.234

Armature Resistance (ohm): 0.78

Armature Inductance (H): 0.016

Field Resistance (ohm): 150

Field Inductance (H): 112.5

Inertia (kg*m^2): 1.25

Viscous friction coefficient (N-m-s): 0.01

Coulomb friction torque (N-m): 0

Initial speed (rad/s): 0

Model detail level: Detailed

Mechanical input: Torque Tm

Figure 9. Layout of the dialog table of the drive electric motor of direct current.

3.2. Thyristor rectifier table dialog

Value of voltage and inductance of the excitation winding of the motor, value of single-phase voltage and inductance of the source connected to the A+, A− block of the pulse generator for firing the thyristor rectifier are shown in **Figure 10**.

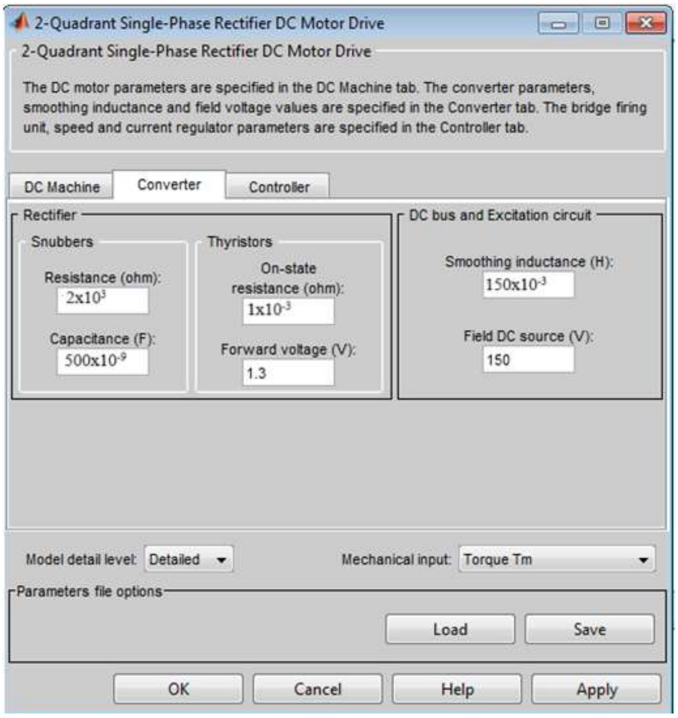

2-Quadrant Single-Phase Rectifier DC Motor Drive

2-Quadrant Single-Phase Rectifier DC Motor Drive

The DC motor parameters are specified in the DC Machine tab. The converter parameters, smoothing inductance and field voltage values are specified in the Converter tab. The bridge firing unit, speed and current regulator parameters are specified in the Controller tab.

Rectifier

Snubbers

Resistance (ohm): $2x10^3$

Capacitance (F): $500x10^{-9}$

Thyristors

On-state resistance (ohm): $1x10^{-3}$

Forward voltage (V): 1.3

DC bus and Excitation circuit

Smoothing inductance (H): $150x10^{-3}$

Field DC source (V): 150

Model detail level: Detailed

Mechanical input: Torque Tm

Figure 10. Layout of the thyristor rectifier table dialog.

3.3. Controller table dialog

The controller table dialog gives the possibility to select the parameters of the speed controller, the current controller and the thyristor bridge firing unit.

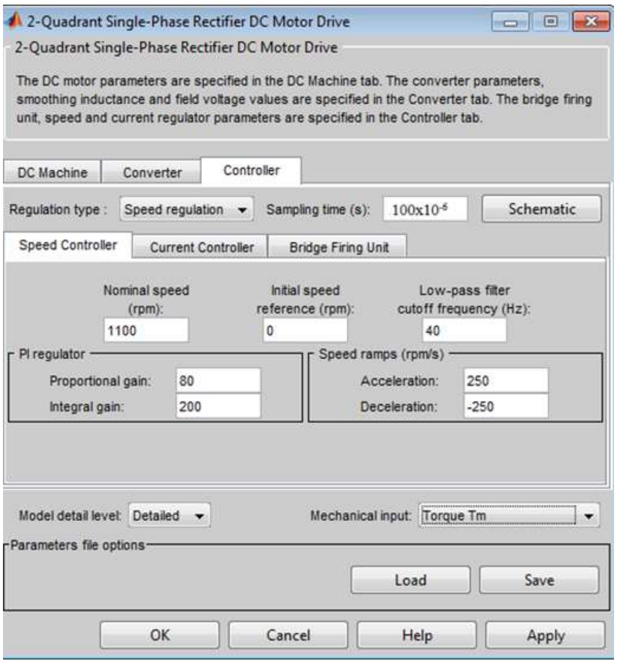

2-Quadrant Single-Phase Rectifier DC Motor Drive

2-Quadrant Single-Phase Rectifier DC Motor Drive

The DC motor parameters are specified in the DC Machine tab. The converter parameters, smoothing inductance and field voltage values are specified in the Converter tab. The bridge firing unit, speed and current regulator parameters are specified in the Controller tab.

Regulation type : Speed regulation

Sampling time (s): $100x10^{-6}$

Nominal speed (rpm): 1100

Initial speed reference (rpm): 0

Low-pass filter cutoff frequency (Hz): 40

PI regulator

Proportional gain: 80

Integral gain: 200

Speed ramps (rpm/s)

Acceleration: 250

Deceleration: -250

Model detail level: Detailed

Mechanical input: Torque Tm

Figure 11. Layout of the speed controller table dialog.

A dialog of the table and relevant values of the speed controller parameters is given in **Figure 11**.

The current controller table and parameters dialog is given in **Figure 12**.

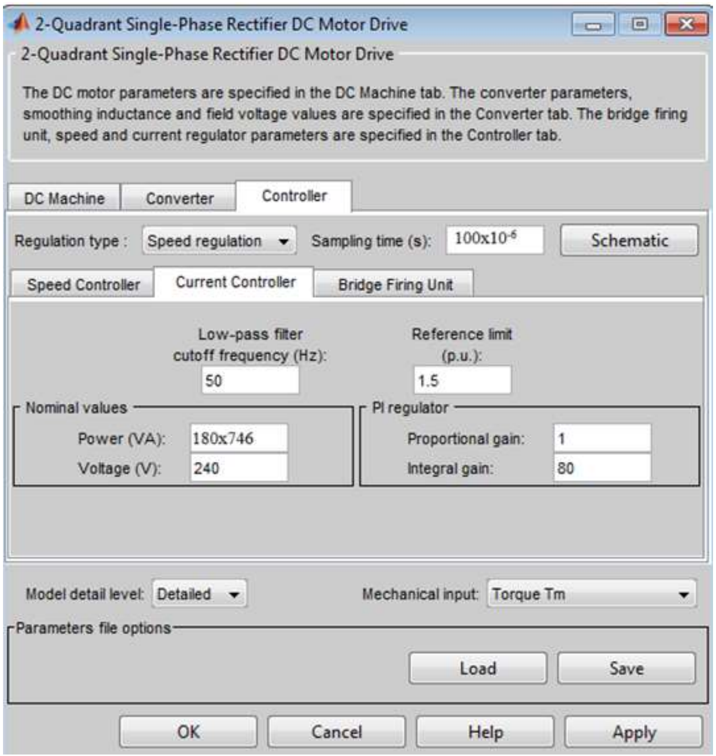

2-Quadrant Single-Phase Rectifier DC Motor Drive

2-Quadrant Single-Phase Rectifier DC Motor Drive

The DC motor parameters are specified in the DC Machine tab. The converter parameters, smoothing inductance and field voltage values are specified in the Converter tab. The bridge firing unit, speed and current regulator parameters are specified in the Controller tab.

Regulation type : Speed regulation

Sampling time (s): 100x10⁻⁶

Low-pass filter cutoff frequency (Hz): 50

Reference limit (p.u.): 1.5

Nominal values

Power (VA): 180x746

Voltage (V): 240

PI regulator

Proportional gain: 1

Integral gain: 80

Model detail level: Detailed

Mechanical input: Torque Tm

Figure 12. Layout of the current controller table dialog.

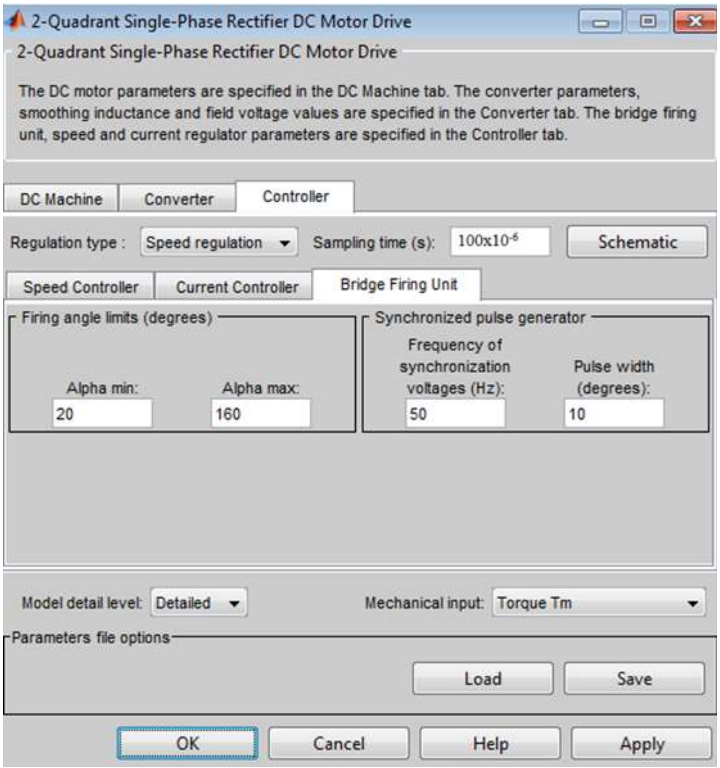

2-Quadrant Single-Phase Rectifier DC Motor Drive

2-Quadrant Single-Phase Rectifier DC Motor Drive

The DC motor parameters are specified in the DC Machine tab. The converter parameters, smoothing inductance and field voltage values are specified in the Converter tab. The bridge firing unit, speed and current regulator parameters are specified in the Controller tab.

Regulation type : Speed regulation

Sampling time (s): 100x10⁻⁶

Firing angle limits (degrees)

Alpha min: 20

Alpha max: 160

Synchronized pulse generator

Frequency of synchronization voltages (Hz): 50

Pulse width (degrees): 10

Model detail level: Detailed

Mechanical input: Torque Tm

Figure 13. Layout of the thyristor bridge ignition unit dialog.

The layout of the dialog table and relevant parameters of the thyristor bridge firing unit controller is given in **Figure 13**.

4. Results of simulations

Figures 14 and **15** show the results of simulations of the change in firing angle of the rectifier thyristor, voltage and armature current, and at the set reference speed of 1100 rpm at the moment *t* = 0 s of the electric motor. In both simulations, an initial torque on the electric motor shaft of 15 N m was assumed.

The speed of the electric motor in both cases follows the reference ramp (+250 rpm) and reaches a stable state around *t* = 8.75 s when the load moment in the first case goes from 15 N.m. to 20 N.m. (light passenger trains), and in the second case from 15 N.m. to 100 N.m. (heavy freight trains).

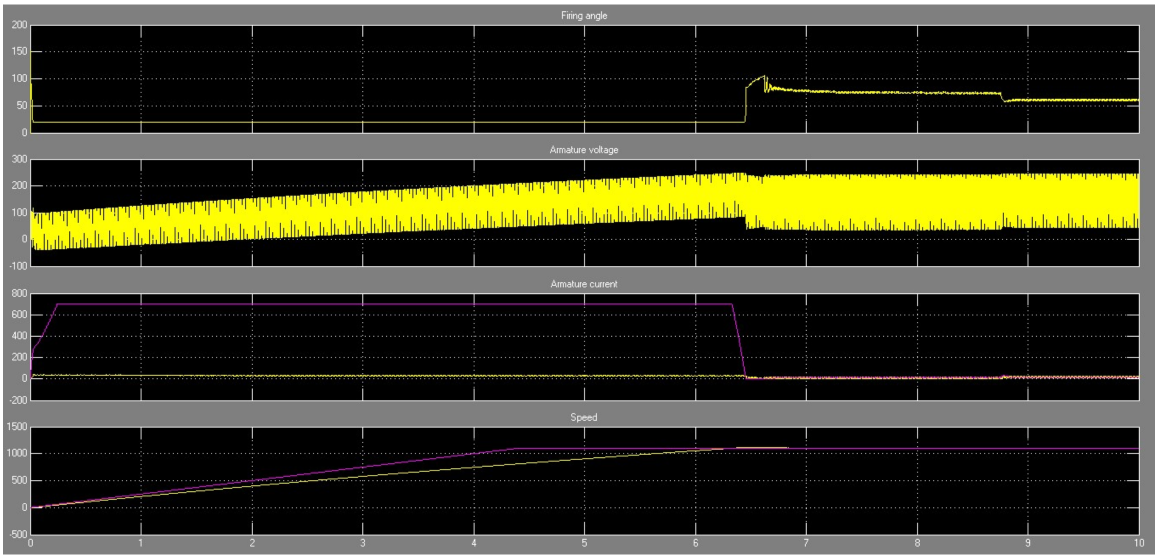

Figure 14. Temporal changes of the ignition angle of the rectifier thyristor, voltage and armature current of the ŽS 444 series locomotive electric motor in light passenger trains.

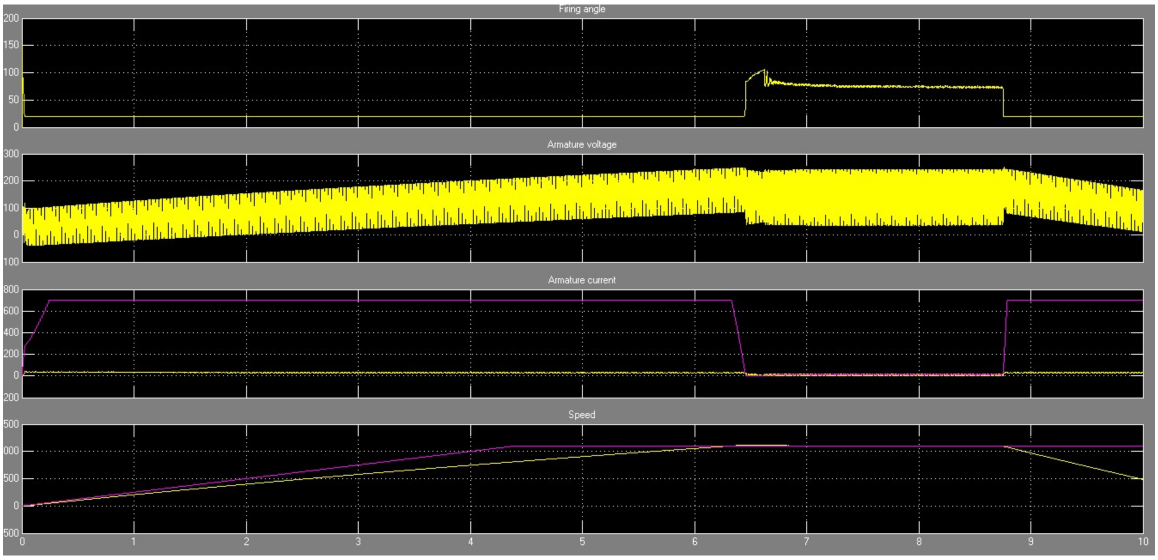

Figure 15. Temporal changes of the ignition angle of the rectifier thyristor, voltage and armature current of the ŽS 444 locomotive electric motor in heavy freight trains.

The armature current follows the reference current very well in both cases, and the firing angle remains at the lower limit of 20 degrees until *t* = 6.35 s after which it takes on higher values, still below 90 degrees to keep the converter in rectifier mode (first mode quadrant). The mean value of the armature voltage of 240V was reached in *t* > 6.35 s.

In both analyzed cases, the engine speed increases rapidly and recovers to 1100 rpm at *t* = 10 s. When the engine starts (starting the locomotive), the armature current in both cases increases to 720 A, but at the moment *t* = 6.35 s and reaches the nominal speed, the current in both cases drops to a significantly lower value of 10A. In the first case, such a low value of the armature current remains unchanged for *t* > 8.75 s, while in the second case, it rises again to 720A at that moment due to a significantly higher load on the electric motor and the need for a higher electromagnetic torque to maintain the required speed. The armature current perfectly follows its reference value, which in this case is set to 730 A.

5. Discussion

The simulation model of the locomotive ŽS 444 series иn Matlab-Simulink, described in chapter 2 of this manuscript, enables a clear visualization of the following output values: temporal changes in the firing angle of the single-phase rectifier thyristor, mean voltage values, armature current and movement speed. traction electric motors when starting an electric locomotive for different mechanical loads of the locomotive. This possibility was achieved by taking into account the technical characteristics, arrangement and mutual influence of all devices in the main circuit of the locomotive as described in chapter 3 of this manuscript. Two physical quantities appear as input to the realized system: the contact network voltage and the mechanical load of traction electric motors. Therefore, it can be said that the realized model allows not only to see the sensitivity of the above-mentioned output values, but also their dependence for different mechanical loads of traction electric motors.

The following results were obtained when the locomotive was started from rest and at a set nominal voltage of the contact network of 25 kV and a mechanical load of the traction electric motors of 15 N.m. (light passenger trains) or 100 N.m. (heavy freight trains):

- The armature current follows very well the reference current of 730 A in both cases, and the firing angle remains at the lower limit of 20 degrees until *t* = 6.35 s after which it takes on higher values, still below 90 degrees to keep the converter in mode rectifier (first mode quadrant). The mean value of the armature voltage of 240 V was reached for *t* > 6.35 s.
- At the set reference speed of 1100 rpm at the moment *t* = 0 s, the speed of the electric motor in both cases follows the reference ramp (+250 rpm) and reaches a steady state around *t* = 8.75 s.
- \- In both analyzed cases, the engine speed increases rapidly and returns to the set reference speed of 1100 rpm at *t* = 10 s. When starting the engine (starting the locomotive), the armature current in both cases increases to 720 A, but at the moment *t* = 6.35 s and reaching the rated speed, the current in both cases drops to a significantly lower value of 10 A. In the first case, such a low value of the

armature current remains unchanged t >8.75 s, while in the second case it increases again to 720 A at that moment due to a significantly higher load on the electric motor and the need for a higher electromagnetic torque to maintain the required speed. The armature current perfectly follows its reference value, which in this case is set to 730 A.

The above results indicate a fast and efficient automatic regulation of the locomotive speed and traction electric motor current when starting light (passenger) and heavy (freight) trains.

In addition to the observed examples, it is also possible to observe the time change of the specified output values for other values of the resistance moment and voltage of the contact network. In the simulations that were carried out at different contact network voltages from 19 kV to 27.5 kV. and at the same mechanical loads of 15 Nm and 100 Nm they show almost the same results as at a voltage of 25 kV. This fact indicates an important characteristic of the locomotive, i.e., that the locomotive drive is not sensitive to permitted changes in the contact network voltage.

The above simulation results were experimentally confirmed based on numerous measurements carried out on these locomotives [4].

6. Conclusion

For different mechanically loaded and reference rotation speeds of the traction electric motors of the electric locomotive ŽS 444 series, the model provides a clear picture of the time change of the thyristor firing angle of the single-phase rectifier, the mean value of the voltage, the armature current and the rotation speed of the electric motor when the locomotive starts up.

When starting the locomotive, the mean value of the armature current of the electric motor does not exceed the set value (720 A). This value can be adjusted up to 1250 A (one-hour permissible value of the electric motor) if adhesion conditions between the wheel and the rail of the locomotive allow it. At higher mechanical loads, this value is retained longer due to the need for higher electromagnetic torques at higher speeds. Regardless of the value of the set reference armature current, the armature current during the starting of the electric motor always follows it perfectly.

In addition to the set speed reference value of 1100 rpm and the initial mechanical load of 15 Nm, i.e., the load of 20 Nm and 100 Nm after t = 8.75s, other speed reference values and the mechanical load of the electric motor can be set, which indicates the important possibility of the model to different operating characteristics of the locomotive when pulling different trains are analyzed.

In the simulations that were carried out at different contact network voltages from 19 kV to 27.5 kV. and at mechanical loads of 15 Nm and 100 Nm, almost the same results were obtained as at a voltage of 25 kV. This fact indicates an important characteristic that the locomotive drive is not sensitive to the permitted changes in the catenary voltage.

Given that the research was carried out on a model that requires input of a resisting torque on the electric motor shaft when starting the locomotive, future research will look at the influence of variable traction resistance on the traction force of the rail wheels. With additional modeling of the power transmission and axle assembly of the locomotive, it will be possible to clearly see the output values (time changes of the firing angle of the thyristor of the single-phase rectifier, the mean voltage and current of the electric motor armature and the speed of the locomotive) at different traction resistances between the wheel and the rail.

Author contributions: Conceptualization, BG and VAB; methodology, BG; software, BG; validation, BG and VAB; formal analysis, BG; investigation, BG; resources, BG; data curation, BG; writing—original draft preparation, BG; writing—review and editing, BG; visualization, BG; supervision, BG; project administration, BG; funding acquisition, VAB. All authors have read and agreed to the published version of the manuscript.

Conflict of interest: The authors declare no conflict of interest.

References

1. Milićević Z, Aranđelović D, Marjanović V, Pejčić D. Electric locomotives JŽ 441 series. Želnid, Belgrade; 1997.
2. Dragan B. Rajković: Contribution to the analysis of axle breakage on locomotives series 441, 461 and 444. In: Proceedings of the XIV ŽELKON '10 Niš; 2010.
3. Vabić V, Grašković I. Course for service personnel of locomotive series JŽ 444 and JŽ 461-200 sedries, Končar-električne lokomotive dd., document number GO5926, archive location 211-0103. Zagreb; 2005.
4. Branislav G. Research and Analysis in the Electric Traction System of the Serbian Railways. Eliva Press; 2023.
5. Boldea I, Nasar SA. Electric Drives. CRC Press; 2016. doi: 10.1201/9781315368573
6. Nondahl, Thomas A. Microprocessor Control of Motor Drives and Power Converters, tutorial course. IEEE Industry Application Society; 1993,
7. Bolton W. Mechatronics: Electronic Control Systems in Mechanical and Electrical Engineering, 3rd ed. Pearson Education; 2004.
8. Harpreet Kaur. Electric drives and their controlling techniques. Scholar's press London; 2019.
9. Mohan N, Raju S. Analysis and Control of Electric Drives: Simulations and Laboratory Implementation. John Wiley & Sons, Inc; 2021.
10. Merabet A. Advanced Control Systems for Electric Drives. Electronics; 2021. doi: 10.3390/books978-3-03943-700-9
11. Dorji C. Review Of Electric Motor Drives. Machine Drives and control; 2015. doi: 10.13140/RG.2.1.1198.6408
12. Golnaraghi F, Kuo BC. Automatic Control Systems, 9th ed. John Wiley & Sons, Inc; 2010.
13. Kryukov OV, Blagodarov DA, Dulnev NN, et al. Intelligent Control of Electric Machine Drive Systems. In: Proceedings of the 2018 X International Conference on Electrical Power Drive Systems (ICEPDS); 2018.
14. Hughes A. Electric Motors and Drives—Fundamentals, Types and Applications, 3rd ed. Elsevier, Oxford, UK; 2006.
15. Schröder D. Elektrische Antriebe—Grundlagen, 3rd ed. Springer Berlin Heidelberg; 2007.
16. Jauch C, Tamilarasan S, Bovee K, et al. Modeling for drivability and drivability improving control of HEV. Control Engineering Practice. 2018; 70: 50-62. doi: 10.1016/j.conengprac.2017.09.014
17. Ramachandran N, Sivasubramanian R, Palanivel R, et al. Design and Fabrication of Hybrid Mobility Scooter. Advances in Materials Research; 2021.
18. Omar AMS, Samat AAA, Isa SSM, et al. New model of inverting substation for DC traction with regenerative braking system. AIP Conference Proceedings. 2017; 1875: 030016. doi: 10.1063/1.4998387
19. Barna G. Simulation model of a series DC motor for traction rail vehicles. In: Proceedings of the 21st International Conference on Methods and Models in Automation and Robotics (MMAR); 2016.
20. Wang X, Peng T, Wu P, et al. Influence of electrical part of traction transmission on dynamic characteristics of railway vehicles based on electromechanical coupling model. Scientific Reports. 2021; 11(1). doi: 10.1038/s41598-021-97650-4
21. Goolak S, Tkachenko V, Bureika G, et al. Method Of Spectral Analysis Of Traction Current Of Ac Electric Locomotives. Transport. 2021; 35(6): 658-668. doi: 10.3846/transport.2020.14242

22. Litovchenko VV, Nazarov DV, Sharov VA. Simulation Model of a Direct-Current Electric Locomotive with Commutator Traction Motors. Russian Electrical Engineering. 2020; 91(1): 69-76. doi: 10.3103/s1068371220010071
23. Goolak S, Sapronova S, Tkachenko V, et al. Improvement of the model of power losses in the pulsed current traction motor in an electric locomotive. Eastern-European Journal of Enterprise Technologies. 2020; 6(5 (108)): 38-46. doi: 10.15587/1729-4061.2020.218542
24. Chiriac G, Nituca C, Sticea D. Electric Locomotive Laboratory Test Bench for Research and Educational Purposes. 2019 8th International Conference on Modern Power Systems (MPS). Published online May 2019: 1-4. doi: 10.1109/mps.2019.8759652
25. Goolak S, Yermolenko E, Tkachenko V, et al. Determination of voltage at the rectifier installation of the electric locomotive VL-80K for each position of the controller driver’s. Technology audit and production reserves. 2022; 1(1(63)). doi: 10.15587/2706-5448.2022.251947
26. Goolak S, Riabov I, Tkachenko V, Yeritsyan B. Simulation model of traction electric drive of AC electric locomotive equipped with collector electric motors. Przegląd Elektrotechniczny. 2023; 1(4): 120-129. doi: 10.15199/48.2023.04.21

Mechanical Engineering Advances 2024, 2(2), 1578.
https://doi.org/10.59400/mea.v2i2.1578

Article

Design of optimum spacecraft reorientation control with a combined criteria of quality based on the quaternions

Mikhail Levskii

Maksimov Research Institute of Space systems as branch of Khrunichev State Space research-and-production Center, Korolev, 141091 Moscow region, Russia; levskii1966@mail.ru

CITATION

Levskii M. Design of optimum spacecraft reorientation control with a combined criteria of quality based on the quaternions. Mechanical Engineering Advances. 2024; 2(2): 1578. https://doi.org/10.59400/mea.v2i2.1578

ARTICLE INFO

Received: 31 July 2024
Accepted: 12 October 2024
Available online: 11 November 2024

Abstract: Specifical original problem of attitude controlling for spacecraft was proposed in this paper. Problem of optimal rotation from a known initial state in a prescribed spatial orientation was studied in detail (turnaround time is not fixed). Design of optimal program of reorientation is based on new indicator of quality that combines energy costs including the contribution of controlling torques and integral of rotary energy (in a known proportion) and reorientation time; presence of duration factor bounds time of rotation finish. To construct an optimal control of angular momentum changing, quaternionic method and the maximum principle were applied. Differential equation that relates spacecraft angular momentum and quaternion of spacecraft orientation is a base to obtain analytic solution to a problem. We reveal the properties of optimum control program analytically, and study key features of optimum motion in details. Also, we write the formalized equations, mathematical formulas to design optimal law for change of spacecraft's angular momentum. Analytic relations and equations are given for finding the optimal solution. Control law (in as explicit dependence between phase variables and con-trolling variables has been formulated. Main relations determining optimum values of parameters for rotation control algorithm were given. The closed-form law for rotation was obtained for dynamically symmetric solids. Numerical example as well as results of mathematical modeling of spacecraft motion that formed using optimum control are presented. This data as addition to the made theoretic descriptions shows reorientation process (in virtual form) and demonstrates practical feasibility of the developed control method. A designed algorithm for optimal control of rotation improves an efficiency of attitude system, and originates more economical performing of space vehicle during its flight along orbit.

Keywords: quaternion; spatial attitude; optimal control; angular momentum; maximum principle; combined criterion of quality; boundary value problem

1. Introduction

Spacecraft transfer problem from its initial spatial position into a given angular position has been solved. Spatial reorientation consists in moving of spacecraft axis from the known attitude in another given position within finite time *T*. Spacecraft attitude is specified with respect to the chosen frame of reference. A case when inertial frame was reference basis has been considered. Use of new quality indicator (without any constraint for the control variables) is principial difference in solution proposed.

Problem of controlling the angular position of a solid is known very well [1–28]. It was considered in various formulations and studied by different methods in wide range, including analytic design of optimum controllers [1], or basing on inverse dynamics problem [2] and others, as well as issues of optimum control [1,3–

26]. Methods for optimizations are very different, for example, optimization based on the maximum principle [9–26], where classical criteria for estimate control process (a speed-optimal [4–12], energy costs [11,13,14,19], minimum fuel consumption [14], etc.) have been used, or kinematic problems on turning [15–18]. Optimum control problem in dynamic statements is of special interest; in particular case (when process end time is fixed) method of variables separation was applied [14]. Analytic solution of optimum turn controlling in a closed form remain practically important because this solution allow a finished law of program control to be applied onboard (as well as variation of optimal rotation trajectory of spacecraft). But extremely difficult to solve problem and find optimum law for solids when moments of inertia are arbitrary. Consequently, approximate numeric methods can be used only for solving the problem of a turn. Some special cases of control were known in case of spherically symmetric [12,19] or solids with dynamical symmetry [8–11,16,20–22]. Specifical features of control for the spacecrafts equipped with inertial actuators (for example, the gyrodins) were investigated earlier [29–31]. Attitude system based on control using the gyrodins (or other control moment gyroscopes) can use the patented method [31].

Personal contribution of authors of papers published earlier is: Sinitsin and Kramlikh [1] advanced the method of analytical construction of optimal regulators for problems of spacecraft attitude. Velishchanskii and Krishchenko [2] successfully adapted the method of inverse problems of dynamics well-known in the theory of dynamic systems to the problems of angular motion control. Branets and Shmyglevskii [12] have developed theory of quaternion application to is-sues of description of solid rotations kinematics and control of a spacecraft (in other domains of sciences, quaternionic approach was used also). Zelepukina et al. [16] investigated in detail the construction of optimal laws of variation in the angular momentum vector during spatial turn (including for axisymmetric rigid space-craft). Huge range of problems of optimal control with application of maximum principle basing on the quaternions were solved by Molodenkov and Sapunkov [10] in different years (approximate solutions or numerical solutions are given); analytical solutions were obtained for axisymmetric spacecraft and spherically symmetric spacecrafts, moreover, different criteria of quality was used. Lastly, Aipanov and Zhakypov [14] proposed the method of separation of variables for solving the problems of optimal turn control.

Below, we will solve a problem of optimum spacecraft rotation with new indicator of quality that combines (in an assigned proportion) the contribution of control for performing a maneuver (in energy consumption sense) and an integral of rotary energy; a presence of such integral leads to limitation of energy of rotation during a turn). Phase variables are orientation quaternion and spacecraft angular momentum. This problem statement differs significantly from earlier research with the complex functional by type of optimality index which includes both control variables and phase variables, as well as time of maneuver [21–26]. In our paper, the adopted functional characterizes complex combination of the energy costs and time, necessary for a turning. Minimization of such functional is important issue for spaceflight practice. Currently, cost-efficiency control remains very relevant for space engineering. Defining and studying an optimum rotation control from one attitude to other attitude (with minimum of a selected optimality index) is topic and subject of research.

2. Statement of the optimal control problem

Let us describe spatial motion about center mass by mathematic apparatus of quaternions (Rodrigues-Hamilton parameters). A motion of body frame E relative to reference frame is given by normalized quaternion Λ (body frame E, or spacecraft coordinate system, is formed by the principal central axis of inertia), $\|\Lambda\|=1$ [12]. We assume that reference frame is inertial. Initial and final spacecraft attitude in inertial frame we specify by quaternions Λ_{in} and Λ_f. Kinematic equation has the form [12]:

$$2\dot{\Lambda} = \Lambda \circ (I^{-1} L) \tag{1}$$

where symbol ∘ is mark for quaternion multiplication. Spacecraft angular momentum (as rigid body) changes according to the equation [24,26]:

$$\dot{L} + (I^{-1}L) \times L = M \tag{2}$$

where L is spacecraft angular momentum, I is inertia tensor, M is control torque (symbol × means a vector product of vectors). Disturbance torques (atmosphere and perturbation caused by external field) are negligibly small, it is very important for spacecraft control during spaceflight. The spacecraft is controlled around center of mass by vector M. The boundary conditions for controlled system Equations (1) and (2) are:

$$\Lambda(0) = \Lambda_{\text{in}}, L(0) = 0 \tag{3}$$

$$\Lambda(T) = \Lambda_f, L(T) = 0 \tag{4}$$

where T is rotation end time; Λ_{in}, and Λ_f specify attitude of a spacecraft at initial and final instant (they must satisfy a requirement $\|\Lambda_{in}\| = \|\Lambda_f\| = 1$). It is set that rotary motion is regulated using control system which creates torques about three main central axis of inertia. For optimization of control program, its efficiency is specified by indicator:

$$G = \int_0^T (M_1^2/J_1 + M_2^2/J_2 + M_3^2/J_3)dt + k_1 \int_0^T (L_1^2/J_1 + L_2^2/J_2 + L_3^2/J_3)dt + k_2 \mathrm{T} \tag{5}$$

where M_i are projections of control torque M on principal central axis of spacecraft's inertia (i = 1, 2, 3); L_i are projections of angular momentum L on axis of spacecraft frame; J_i are principal central moments of inertia; $k_1 > 0$, $k_2 > 0$ are the positive constant coefficients ($k_1 \neq 0$, $k_2 \neq 0$).

We formulate optimal control problem as following: spacecraft needs to be turned from Equation (3) into Equation (4) according to Equations (1) and (2) and minimum sum Equation (5), where $\Lambda_f \neq \pm\Lambda_{in}$. Duration of turn T is unfixed. Solution-function M(t) is found within piecewise-continuous functions of time.

Accepted criteria of optimality Equation (5) distinguishes our problem of optimization from other considered tasks by functional type that must be minimized. Index Equation (5) combines energy costs (including the contributions of control) and time (in its proportion). An adopted criteria allows to estimate an energetically advantageous trajectory from initial orientation Λ_{in} to a required termination attitude Λ_f with minimum costs of the controlling resources and energy, and for determination of control mode corresponding to optimum turn. Energy integral in (2.5) limits kinetic energy during rotation. The required turn may be executed for any values Λ_{in}, Λ_{f} and J_1, J_2, J_3, k_1 и k_2 because the time T is not fixed. Since combination of quadratic performance criterion and time is optimized, optimal duration of a turn T_{opt} exists to be minimum of Equation (5). The optimal rotation problem, when control process quality is estimated by the index Equation (5), is relevant.

Note that angular momentum control for spatial turn minimizing an indicator Equation (5) is useful for spacecraft's attitude system using electric-jet engines (EJE): when controlled using EJE (in particular, with use of ion-engines), in Equation (5) first integral is proportional to electric energy consumed (for EJE, thrust and electric current are directly-proportional [32], and torque of EJE is proportional to an arm of engine installation). We know about a necessity of all-round decrease of electrical consumption for control of motion, a select of functional is clear.

3. Materials and methods

Optimal control problem proposed is dynamical problem of optimum turn [12]; consequently, M_i are the functions that should be found (control by optimal way of spatial motion), but L and Λ are the phase variables. A norm of quaternion Λ is constant, $\|\Lambda\|$ = const [12]. We solve optimum control issue and find optimum law of spacecraft's angular momentum changing during spatial rotation basing on the method of quaternions and Pontryagin's maximum principle [12,33]. They were used by many scientists and researchers, but for other index form [1,12,13–17,21–28]. Quaternions is mathematical tool that were effective applied in another domains of sciences [34–36], also in research process on controled motion of solids. Also, we apply numerical simulation (mathematical modeling) (for proof feasibility in engineering practice). To solve differential equations systems, we made method of successive approximations (shooting algorithm). Method of iteration was applied for solving two-point boundary value problem; other numerical methods have been used also.

The procedure of solving the optimization problem proposed and formulated in section 2 is as follows. In accordance with the Pontryagin's maximum principle [33], conjugate variables ϕ_i corresponding to angular momentum projections on spacecraft axis L_i are introduced. The Hamiltonian H for the problem Equations (1)–(5) is:

$$\begin{aligned} H = {} & -k_2 - k_1(L_1^2/J_1 + L_2^2/J_2 + L_3^2/J_3) - M_1^2/J_1 - M_2^2/J_2 - M_3^2/J_3 + \phi_1(M_1 \\ & + (1/J_3 - 1/J_2)L_2L_3) + \phi_2(M_2 + (1/J_1 - 1/J_3)L_1L_3) + \phi_3(M_3 \\ & + (1/J_2 - 1/J_1)L_1L_2) + L_1r_1/J_1 + L_2r_2/J_2 + L_3r_3/J_3 \end{aligned}$$

where r_i are [19,24]:

$$r_1 = (\lambda_0\psi_1 + \lambda_3\psi_2 - \lambda_1\psi_0 - \lambda_2\psi_3)/2,$$

$$r_2 = (\lambda_0\psi_2 + \lambda_1\psi_3 - \lambda_2\psi_0 - \lambda_3\psi_1)/2,$$

$$r_3 = (\lambda_0\psi_3 + \lambda_2\psi_1 - \lambda_3\psi_0 - \lambda_1\psi_2)/2$$

ψ_j are conjugate variables, corresponding to components of quaternion λ_j (j = 0, 1, 2, 3).

Writing and structure of H does not take into account phase constraint ‖Λ‖=1 due to ‖$\Lambda(0)$‖ = 1. We use universal variables r_i proposed earlier [12,19] because the minimized index (2.5) does not depend on quaternion Λ. The equations for vector **r** formed by variables r_i (optimal functions r_i also) are [24–26]:

$$\dot{r}_1 = L_3 r_2/J_3 - L_2 r_3/J_2,$$

$$\dot{r}_2 = L_1 r_3/J_1 - L_3 r_1/J_3,$$

$$\dot{r}_3 = L_2 r_1/J_2 - L_1 r_2/J_1,$$

$$\dot{r} = r \times (I^{-1}L) \qquad (6)$$

It is known that r turns out to be motionless in inertial frame, $|r|$ = const ≠ 0 [19].

In accordance with the maximum principle, for functions ϕ_i, the equations are [33]:

$$\dot{\phi}_i = -\frac{\partial H}{\partial L_i} \ (i = 1, 2, 3)$$

Conjugate equations system (after differentiation of H) has the form

$$\dot{\phi}_1 = 2k_1 L_1/J_1 + L_3\phi_2(1/J_3 - 1/J_1) + L_2\phi_3(1/J_1 - 1/J_2) - r_1/J_1$$

$$\dot{\phi}_2 = 2k_1 L_2/J_2 + L_1\phi_3(1/J_1 - 1/J_2) + L_3\phi_1(1/J_2 - 1/J_3) - r_2/J_2 \qquad (7)$$

$$\dot{\phi}_3 = 2k_1 L_3/J_3 + L_2\phi_1(1/J_2 - 1/J_3) + L_1\phi_2(1/J_3 - 1/J_1) - r_3/J_3$$

Searching an optimum mode is in writing and solving the equations of motion Equations (1) and (2) and the Equations (6) and (7) under condition that a found control itself is selected by maximization of Hamiltonian. Equation (6) that defines behavior of r in body frame E, will be used, replacing the conjugate equations for ψ_j. Optimum function $r(t)$ and quaternion $\Lambda(t)$ are related [19,24–28]

$$r = \tilde{\Lambda} \circ c_E \circ \Lambda,$$

where $\boldsymbol{c}_E$= const=$\Lambda_{\text{in}} \circ \text{r}(0) \circ \tilde{\Lambda}_{\text{in}}$
where $\tilde{\Lambda}$ is quaternion conjugate to Λ [12, p. 10–20]; and $r(0) \neq 0$ (in another case $r_1 = r_2 = r_3 = 0$ and solution of problem loses sense).

Vector direction c_E is determined by initial and terminal spacecraft attitude: c_E must be defined by solution of Equation (1) and $\Lambda(T) = \Lambda_f$. Differential Equations (6) and (7), together with requirement of maximum for Hamilton function H, are necessary optimality conditions. Conditions of maximum for H determine control function $M(t)$; also, $\Lambda(0)$, $L(0)$, $\Lambda(T)$, $L(T)$ determine solutions $\Lambda(t)$ and $r(t)$, $L(t)$ [24].

A boundary-value problem of maximum principle is in calculating such $r(0)$ for which solving of differential Equations (1) and (2), Equations (6) and (7) together with Hamiltonian maximization, at any time, satisfies the conditions Equations (3) and (4). The restriction $\|\Lambda(t)\|=1$ for phase variable Λ not taken into account because it holds for Equation (1).

4. Principle scheme and algorithm of solving control problem

To specify controlling function $M(t)$ and vector r, maximality conditions for H should be formalized. If $u_i = M_i/\sqrt{J_i}$ and $n_i = \phi_i\sqrt{J_i}$, writing of H gives, using variables u_i and n_i

$$H = u \cdot n - |u|^2 + H_{inv} = |n||u| \cos\delta - |u|^2 + H_{inv}$$

where H_{inv} not explicitly depends on the functions M_i; n and u are two vectors of u_i and n_i; angle between u and n is δ (sign "·" means scalar product of vectors). The Hamiltonian H is quadratic function of functions M_i, H is maximum if only $\delta = 0$. Necessary conditions of extremum are $\partial H/\partial M_i = 0$. After applying them:

$$M_i = J_i\varphi_i/2 \qquad (8)$$

Problem of determination of optimum control is in a solving of Equations (1) and (2), and Equations (6) and (7) under requirement that a sought control M is generated by Equation (8). The problem of optimum control Equations (1)–(5) formulated above is completely solved. Since $|r|$ = const = $|r(0)|\neq 0$, transfer to a normalized vector p: $p = r/|r|$, and $|r(0)| = r_0$ ($|p| = 1$). For p, or elements p_i:

$$\begin{aligned} \dot{p} &= p \times (I^{-1}L) \\ \dot{p}_1 &= L_3p_2/J_3 - L_2p_3/J_2 \\ \dot{p}_2 &= L_1p_3/J_1 - L_3p_1/J_3 \\ \dot{p}_3 &= L_2p_1/J_2 - L_1p_2/J_1 \end{aligned} \qquad (9)$$

Note: $r_i = |r(0)|p_i$. Since $L(0) = L(T) = 0$, we see that our issue Equations (1)–(5) has single and unique solving:

$$\phi_i = a(t)p_i/J_i \qquad (10)$$

$$L_i = b(t)p_i \qquad (11)$$

where $p_i = r_i/r_0$; $a(t)$ and $b(t)$ are scalar time functions (but $b(t) \geq 0$). Respectively, $M_i = a(t)p_i/2$.

Successive substitution of dependences Equation (10) into Equation (7), by taking into account relations Equation (11) with $r_i = r_0\,p_i$, proofs a validity of solution which we specified. i.e., Equations (10) and (11) for the differential equations system Equations (2) and (7), Equations (8) and (9) is truly (relation Equation (11) follows directly from the system Equations (2), (8) and (10). From Equations (7), (10) and (11), we see that optimal functions satisfy the relation.

$$\dot{a}(t) = 2k_1b - r_0 \qquad (12)$$

The Equations (7), (8) and (11) give dependence $\dot{b} = a/2$ for $b(t)$, or

$$b(t) = 0.5\int_0^t a(t)dt$$

Taking into account last dependence and condition Equation (12), we obtain $\ddot{a} = k_1 a$ for $a(t)$, which has analytical form:

$$a(t) = C_1 exp(-t\sqrt{k_1}) + C_2\, exp(t\sqrt{k_1}) \tag{13}$$

where C_1 and C_2 are some constants that will be determined below.

It is seen, $b(0) = b(T) = 0$ and $\dot{a}(0) = \dot{a}(T) = -r_0$, since $L(0) = 0$, $L(T) = 0$. As consequence, $r_0 = \sqrt{k_1}(C_1 - C_2)$. Therefore, for optimal rotation, $b(t)$ is:

$$b(t) = (\dot{a}(t) + r_0)/(2k_1) = [C_2 exp(t\sqrt{k_1}) - C_1 exp(-t\sqrt{k_1}) + C_1 - C_2]/(2\sqrt{k_1}) \tag{14}$$

Hamilton function H not explicitly depends on the time explicitly, and time of rotation finish T is not fixed. Whence, for optimal control H = const = 0 [37]. At ends of trajectory L = L = 0, hence:

$$H(0) = H(T) = -K_2 - \frac{J_1\phi_1^2 + J_2\phi_2^2 + J_3\phi_3^2}{4} + \frac{J_1\phi_1^2 + J_2\phi_2^2 + J_3\phi_3^2}{2} = (J_1\phi_1^2 + J_2\phi_2^2 + J_3\phi_3^2)/4 - k_2$$

or $H(0) = H(T) = M_1^2/J_1 + M_2^2/J_2 + M_3^2/J_3 - k_2 = 0$. Whence $a2(0) = a2(T) = 4k_2/(p_1^2/J_1 + p_2^2/J_2 + p_3^2/J_3)$.

Optimal rotation has specific property: $p_1^2/J_1 + p_2^2/J_2 + p_3^2/J_3 = \text{const}$ for p_i (or ort p). To confirm this feature, left side was differentiated (with accounting for Equations (9) and (11)). After substitution $\dot{p}_i$ by Equation (9) and then L_i by the formulas Equation (11), we show that the resulting derivative is zero. For optimum function $a(t)$, must satisfy the requirements:

$$a(0) = 2\sqrt{k_2}/C\; a(T) = -2\sqrt{k_2}/C\; a(T/2) = 0, \dot{a}(0) = \dot{a}(T) = -r_0 (C = \sqrt{p_{10}^2/J_1 + p_{20}^2/J_2 + p_{30}^2/J_3})$$

Last equality follows from Equation (12), since $b(0) = b(T) = 0$; conditions $L(0) = 0$ and $L(T) = 0$ for optimal turn. The property $a(T) = -a(0)$ follows from the necessary condition of optimality $H(0) = H(T) = 0$ (and Equations (8) and (10)). We can write (on the base Equation (13)):

$$\dot{a}(t) = \sqrt{k_1}(C_2 exp(t\sqrt{k_1}) - C_1 exp(-t\sqrt{k_1}))$$

$$\dot{a}(0) = \sqrt{k_1}(C_2 - C_1) = \dot{a}(T) = \sqrt{k_1}(C_2 exp(T\sqrt{k_1}) - C_1 exp(-T\sqrt{k_1}))$$

Comparation of $\dot{a}(0)$ and $\dot{a}(T)$ gives the equations $C_2(exp(T\sqrt{k_1}) - 1) = C_1(exp(-T\sqrt{k_1}) - 1)$, or $C_1 = -C_2 exp(T\sqrt{k_1})$. From Equation (14), we proof $b(0) = 0$, $b(T) = 0$. Also $a(T) = -a(0)$ and $a(T/2) = 0$, since we have (basing on Equation (13)): $a(0) = C_1 + C_2$, $a(T) = C_1 exp(-T\sqrt{k_1}) + C_2\, exp(T\sqrt{k_1}) = -C2 - C1$,

$$a(T/2) = C_2(exp(T\sqrt{k_1}/2) - exp(T\sqrt{k_1})\, exp(-T\sqrt{k_1}/2))$$

But $r0 = \sqrt{k_1}(C_1 - C_2) = C_1\sqrt{k_1}(exp(-T\sqrt{k_1}) + 1) > 0$, whence $C_1 > 0$, $C2 < 0$ (and $|C1| > |C2|$).

Structure analysis of optimal $a(t)$ shows $\dot{a} < 0$ in every instant $t \in [0, T]$, $\dot{a}$ is minimum at right and left bound points of trajectory: $\dot{a}(0) = \dot{a}(T) = -r_0$. Note see, that $\dot{a}(0) < 0$, $\dot{a}(T) < 0$, and $C1 > 0$, but $C2 < 0$, therefore $a(0)>0$, but $a(T)<0$. If $t<T/2$, then $a>0$ and $\ddot{a}> 0$, but $\dot{a} < 0$; within interval $t > T/2$ we have $a < 0$ and $\ddot{a} < 0$, but $\dot{a} < 0$. At instant $t = T/2$ we see that $\dot{a}$ is maximum (since $a(T/2) = 0$ and b has maximal value). Also, $\dot{a}(T/2) = -2C_1\sqrt{k_1}exp(-T\sqrt{k_1}/2) < 0$. Hence, $\dot{a} < 0$ during time period $t \in [0, T]$, time when $\dot{a}(t) = 0$ is absent. Concrete values of $C1$, $C2$ depend on the coefficients k_1, k_2 and integral.

$$Q = \int_0^T |L(t)|dt = \int_0^T b(t)dt \tag{15}$$

Its value not depends on behavior of function $b(t)$ (for motions according to Equations (9) and (11)); it is defined solely by attitude Λ_{in}, Λ_f, and spacecraft's moments of inertia [18] (Q is computed together with p_0).

Maximum rotary energy Ek and maximum angular momentum achieved at $t = T/2$; $E_{\max} = E_k(T/2)$; $L_{\max} = |\mathbf{L}(T/2)|$. If $k_1 = 0$, $a(t)$ is linear time function $a(t) = 2\sqrt{k_2}(1-2t/T)/C$

(modulus of spacecraft angular momentum is quadratic function of time, respectively), duration of reorientation is $T = \sqrt{6CQ/\sqrt{k_2}}$. Hence, $L\sqrt{3Q\sqrt{k_2}/(8C)}_{max}$ and $E\sqrt{k_2}_{max}$.

Figure 1 shows the form of optimum $b(t)$, $a(t)$ (depending of coefficient k_1 of optimized index (2.5) ($k_1^{(2)} > k_1^{(1)} > 0$, $k_1^{(3)} > k_1^{(2)}$); the dotted lines correspond to a case $k_1 \to 0$. The values $a(0)$ and $a(T)$ are fixed (they do not change if variate value k_1), $a(0) = 2\sqrt{k_2}/C$, $a(T) = -2\sqrt{k_2}/C$, $a(T/2) = 0$.

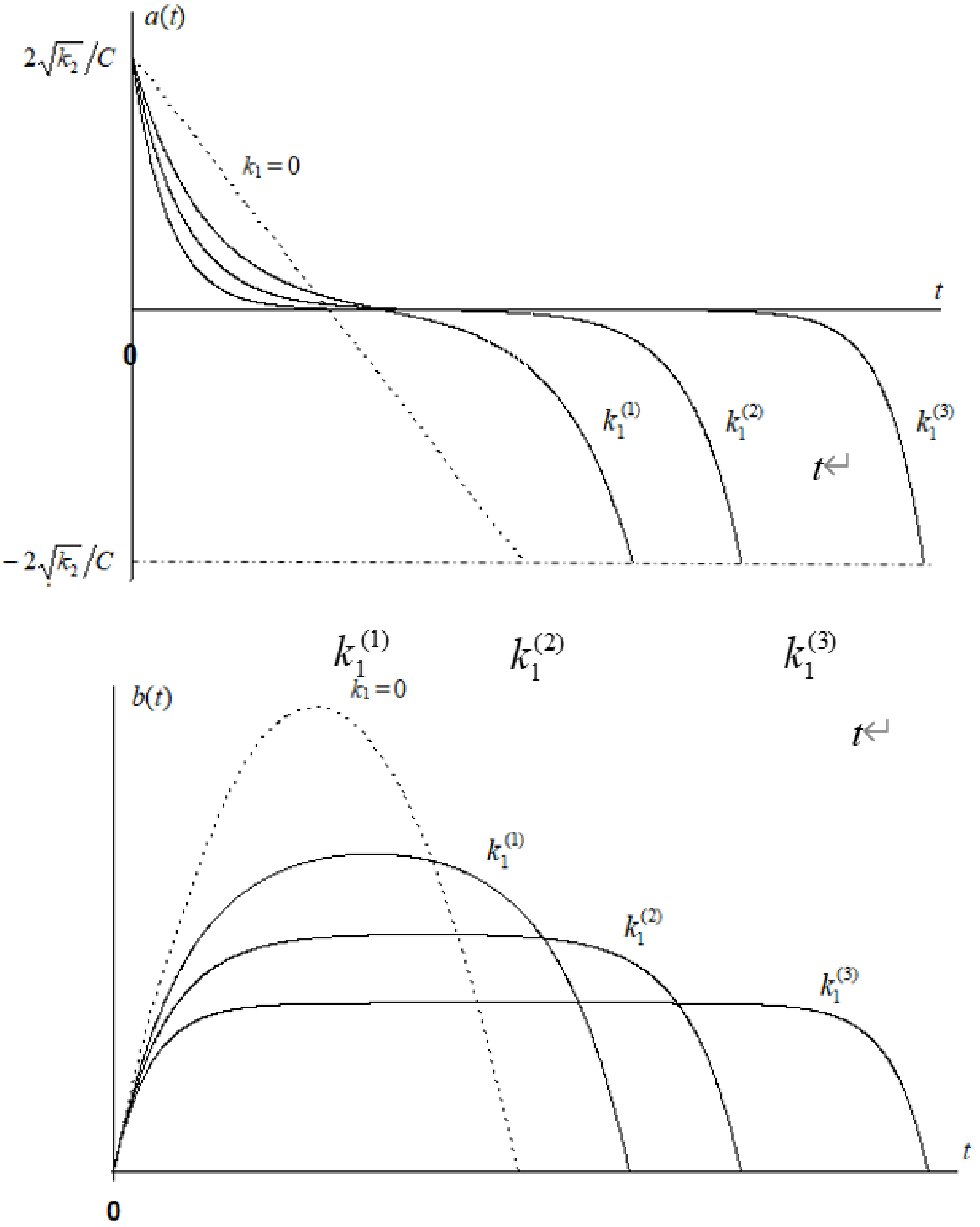

Figure 1. Optimum of $a(t)$ and $b(t)$.

If k_1 more, then function $b(t)$ more fast transfer to segment with $\dot{b} \approx 0$. When $b_{\max}$ decreases, a finish time of rotation maneuver increases, since the value (4.8) is invariable (it does not depend on the coefficients k_1, k_2). Thus, the function $b(t)$ more remotes from quadratic function (parabolic form) and is approximated to piecewise linear dependence when k_1 increases, it can approximate by function included the following segments: time interval with $\dot{b} \approx \sqrt{k_2}/C$, further $b \approx \text{const}$, and then motion with $\dot{b} \approx -\sqrt{k_2}/C$. Under unbounded increasing of coefficients k_1 and k_2, maximal energy of rotation $E_{\max}$ approximates to the level $E_0 = k_2/(2k_1)$.

In optimal solution (when $k_1 \neq 0$), constants C_1, C_2 and time T are calculated by the equations:

$$(exp(T\sqrt{k_1})+1)T=(QC\sqrt{k_1/k_2}+2/\sqrt{k_1})(exp(T\sqrt{k_1})-1) \tag{16}$$

$$C_1=2\sqrt{k_2}/(C(1-exp(-T\sqrt{k_1}))),C_2=2\sqrt{k_2}/C-C_1$$

Time of optimal turn T decreases with increasing of coefficient k_2 (if k_1 is invariable).

Boundary-value problem is to compute p_0 (or, p_{10}, p_{20}, p_{30}), and positive constant r_0, that lead to satisfaction of the terminal condition (2.4) for solution of equations system Equations (1) and (2), Equations (7)–(9) with initial condition (2.3) and dependence $r_i = r_0 p_i$ ($r_0 > 0$).

If take into account Equation (8), Equations (10) and (11) and optimal values of constants C_1 and C_2 for functions a, b, optimum control and optimum motion is described by expressions:

$$M_i=C_1[exp(-t\sqrt{k_1})-exp((t-T)\sqrt{k_1})]\,p_i/2 \tag{17}$$

$$L_i=C_1[1+exp(-T\sqrt{k_1})-exp(-t\sqrt{k_1})-exp((t-T)\sqrt{k_1})]p_i/(2\sqrt{k_1}) \tag{18}$$

p_i satisfy Equation (9) and $p=\tilde{\Lambda}\circ\Lambda_{in}\circ p_0\circ\tilde{\Lambda}_{in}\circ\Lambda$, $C_1=2\sqrt{k_2}/(C(1-exp(-T\sqrt{k_1})))$. Time T is calculated from Equation (16).

Optimum orientation program is determined by the system Equations (5) and (6), Equations (17) and (18); controlling functions M_i and angular momentum projections L_i variate according to Equations (17) and (18). The value p_0 as well as the integral Q, characterizing complexity of a turn, are computed in solution process of boundary-value problem of a turn. Program value of control M relates with attitude Λ

$$M=a(t)\tilde{\Lambda}\circ\Lambda_{in}\circ p_0\circ\tilde{\Lambda}_{in}\circ\Lambda/2$$

at which $a(t)$ changes by the law Equation (13).

Under optimal angular momentum $L(t)$, spacecraft rotation has symmetry properties (for $b(t)$, $a(t)$, primarily) as well as regularities:

$$a(0)=-a(T)>0,\ a(T-t)=-a(t),$$

$$b(t)\geq 0,\quad b(T-t)=b(t)$$

$$\int_0^{T/2}b(t),dt=\int_{T/2}^{T}b(t)dt,\int_0^{T/2}|a(t)|,dt=\int_{T/2}^{T}|a(t)|dt$$

$$\Lambda\circ M(T-t)\circ\tilde{\Lambda}=-\Lambda\circ M(t)\circ\tilde{\Lambda},\ \Lambda\circ L(T-t)\circ\tilde{\Lambda}=\Lambda\circ L(t)\circ\tilde{\Lambda}$$

$$\max_{0\leq t\leq T}|M(t)|=\sqrt{k_2}/C,L_{max}=\max_{0<t<T}\sqrt{L_1^2+L_2^2+L_3^2}=|L(T/2)|$$

$$L_{max}=\frac{r_0+\sqrt{r_0^2-\frac{4k_1k_2}{C^2}}}{(2k_1)\text{или}L_{max}}=(\sqrt{(C_1-C_2)^2/4-k_2/C^2}+(C_1-C_2)/2)/\sqrt{k_1}$$

Angular momentum and optimum control M satisfy the following relationships:

$$\Lambda\circ M(T-t)\circ\tilde{\Lambda}=-\Lambda\circ M(t)\circ\tilde{\Lambda},\ \Lambda\circ L(T-t)\circ\tilde{\Lambda}=\Lambda\circ L(t)\circ\tilde{\Lambda}$$

The conditions Equation (11) show: p is ort for angular momentum; optimum functions $\varphi_i(t)$, $p_i(t)$, $L_i(t)$ meet dependences Equations (10) and (11), where $p_i(t)$ satisfy the system (4.2). Optimal control is determined using (4.10); for any instant $t \in [0, T]$, M and L are collinear. At instant $t = T/2$, direction of torque M variates to an opposite, and modulus $|L|$ has maximal value $|L(T/2)| = L_{\max}$. Control Equation (17) is truly optimum, since this is single function satisfying to Equations (1) and (7), Equations (8) and (9). Optimal rotation (in sense of minimum index Equation (5)) occurs along "trajectory of free motion" [9]. Specify properties of optimum rotation follow from the system Equation (9) with equalities Equations (11) and (14). Original solution is determined by close equations system Equation (1), Equations (9) and (11), and conditions Equations (3) and (4) for function $\Lambda(t)$. Additionally, controlling torque M is smooth time function. Note: during rotation by inertia, body occupies positions Λ that form "trajectory of free motion" [9,24,26].

Ratio of angular momentum and kinetic energy E_k under optimum control is expression:

$$E_k = b^2\,(p_1^2/J_1 + p_2^2/J_2 + p_3^2/J_3)/2$$

Proportion is $E_k/|L|^2 = (p_1^2/J_1 + p_2^2/J_2 + p_3^2/J_3)/2 =$ const for any time within period $0 \le t \le T$. It is key property for spacecraft motion according to criterion Equation (5).

Problem of optimum control synthesis mainly consists in determination of such vector $p(0)$ under which the motion, according to the Equation (1), Equations (9) and (18) with condition Equation (3), satisfies the equality Equation (4). To solve this equations system is difficult in general case: its obtaining to compute $p(0)$, and $p(T)$ by Equations (9) and (11) and formula:

$$\Lambda_f \circ p(T) \circ \tilde{\Lambda}_f = \Lambda_{\text{in}} \circ p(0) \circ \tilde{\Lambda}_{\text{in}} \qquad (19)$$

Significant difference of an offered result is applying of new optimality criterion which combines a contribution of control action (in sense of energy consumption) in motion of a spacecraft during a turn, integral of rotational energy, and maneuver time, with known ratio. Integral of the square form of controlling torques in Equation (5) provides limiting of controlling torques, and secondly, controlling variables are smooth (angular momentum is smooth time function, also). Introduction of time in a minimized indicator reduces duration of turn T. For any turn conditions Equations (3) and (4) (any Λ_{in}, Λ_{f}) and J_1, J_2, J_3, k_1, k_2, kinetic energy of rotation $E(t) \le k_2/(2k_1)$.

5. Particular cases of optimal turn

The determination of optimum rotation mode with minimum index Equation (5) is not trivial issue, $p(0)$ depends on respective attitude Λ_f and Λ_{in}, and characteristics J_1, J_2, J_3. It is non-easy to solve the problem of three-dimensional rotation for an arbitrary moments of inertia $J_1 \neq J_2 \neq J_3$ and attitude in initial and terminal time instants Λ_{in} and Λ_f. Difficulty is to find $p(T)$, $p(0)$ which satisfy Equation (19). Solution of system Equation (1), Equations (9) and (11) (in analytic form) is known for dynamically symmetric and spherical solid only. For body with spherically symmetry ($J_1 = J_2 = J_3$), function $p(t)$ is:

$$p_i(t) = const = p_{i\,0} = \nu_i/\sqrt{\nu_1^2+\nu_2^2+\nu_3^2}$$

$$M_j = C_1[exp(-t\sqrt{k_1}) - exp((t-T)\sqrt{k_1})]p_{i\,0}/2$$

$$L_i(t) = C_1\,[1 + exp(-T\sqrt{k_1}) - exp(-t\sqrt{k_1}) - exp((t-T)\sqrt{k_1})]p_{i0}/(2\sqrt{k_1}), i = \overline{1,3}$$

(ν_0,ν_1,ν_2,ν_3 are the components of quaternion $\Lambda_t = \tilde{\Lambda}_{\text{in}} \circ \Lambda_f$); $Q = 2\ J_1$ accost ν_0.

During optimal reorientation, spherical spacecraft rotates about the Euler axis, optimum trajectory $\Lambda(t)$ (in analytic form) is

$\Lambda(t) = \Lambda_{in} \circ \mathrm{e}^{\boldsymbol{p}_0 s(t)/(2J_1)}$, $s(t)=\int_0^t b(t)dt$

For dynamically symmetric solid body (for example, $J_2 = J_3$), we can solve optimum control problem completely also (in this case p_1 = const = p_{10}): we have conic motion of spacecraft [10] angular momentum modulus is proportional to velocity about longitudinal axis, and angle between longitudinal axis and angular momentum ϑ is constant. Optimal $p(t)$ is:

$$p_1 = p_{10} = \text{const}= cos\,\vartheta,$$

$$p_2 = p_{20}\,cos\,\beta + p_{30}\,sin\,\beta,$$

$$p_3 = -p_{20}\,sin\,\beta + p_{30}\,cos\,\beta,$$

$$\beta = \frac{J_3 - J_1}{J_1 J_2}\int_0^t L_1(t)dt \tag{20}$$

$$\Lambda_f = \Lambda_{in} \circ e^{\boldsymbol{p}_0\beta/2} \circ e^{\boldsymbol{e}_1\alpha/2}$$

where e_1 is unit vector of longitudinal axis of spacecraft; α and β are angles of turns about longitudinal axis, and about p, accordingly ($|\alpha| \le \pi$, $0 \le \beta \le \pi$).

For this case, the relations Equations (17) and (18), Equation (20) are solution for system of Equations (2) and (9) under condition Equation (8); p generates the cone about axis of body's symmetry in body frame (spacecraft coordinate system). To transfer body from attitude Λ_{in} in attitude Λ_f, it rotates simultaneously about its own longitudinal axis, and about c_E, that is constant in inertial coordinate system. Axial-symmetric solid rotates along "conical trajectory". Note, p_0 (corresponding to optimum solution) we can calculate by device [38]. Optimal functions $M_i(t)$ are written in analytical form:

$$M_1 = C_1[exp(-t\sqrt{k_1}) - exp((t-T)\sqrt{k_1})]p_{10}/2$$

$$M_2 = C_1[exp(-t\sqrt{k_1}) - exp((t-T)\sqrt{k_1})]\sqrt{1-p_{10}^2}\,sin(\kappa+\gamma)/2$$

$$M_3 = C_1[exp(-t\sqrt{k_1}) - exp((t-T)\sqrt{k_1})]\sqrt{1-p_{10}^2}\,cos(\kappa+\gamma)/2$$

Programmed values L_i (the components of angular momentum L) are:

$$L_1 = C_1\,[1 + exp(-T\sqrt{k_1}) - exp(-t\sqrt{k_1}) - exp((t-T)\sqrt{k_1})]p_{10}/(2\sqrt{k_1})$$

$$L_2 = C_1 \left[1 + exp(-T\sqrt{k_1}) - exp(-t\sqrt{k_1}) - exp((t-T)\sqrt{k_1})\right]\sqrt{1-p_{10}^2}\, sin(\kappa + \gamma)/(2\sqrt{k_1})$$

$$L_3 = C_1 \left[1 + exp(-T\sqrt{k_1}) - exp(-t\sqrt{k_1}) - exp((t-T)\sqrt{k_1})\right]\sqrt{1-p_{10}^2}\, cos(\kappa + \gamma)/(2J\sqrt{k_1})$$

where $\gamma = arcsin\left(p_{20}/\sqrt{1-p_{10}^2}\right)$, if $p_{30} \geq 0$, or $\gamma = \pi - arcsin\left(p_{20}/\sqrt{1-p_{10}^2}\right)$,если$p_{30} < 0$ ($|p_{10}| \neq 1$); case $|p_{10}| = 1$ corresponds to planar rotation around axis *OX*, and it is not considered.

Optimal trajectory Λ(t) is:

$$\Lambda(t) = \Lambda_{in} \circ e^{\boldsymbol{p}_0\sigma/2} \circ e^{\mu \boldsymbol{e}_1/2}$$

where:

$$\sigma = C_1 \left[(exp(-T\sqrt{k_1}) + 1)t/(2\sqrt{k_1}) + (exp(-t\sqrt{k_1}) + exp(-T\sqrt{k_1}) - exp((t-T)\sqrt{k_1}) - 1)/(2k_1)\right]/J_2$$

$\mu = p_{10}\sigma(J_2 - J_1)/J_1$ (for optimal p_0 and $t = T$, conditions Equations (3) and (4) are satisfied).

For asymmetric body ($J_1 \neq J_2 \neq J_3$), the system Equation (1), Equations (9) and (11) can be solved using only numeric methods (for example, method of successive approximations, or iterations methods). One of such methods has been described in detail in the article [9]. We know that the solution $p(0)$ which satisfies the conditions $\Lambda(0) = \Lambda_{in}$, $\Lambda(T) = \Lambda_f$ and (4.12) for the system of Equation (1), Equations (9) and (11) does not depend on a type of changing the magnitude of angular momentum [18] (therefore, we take b = const ≠ 0 in Equation (11) for search of $p(0)$). To compute the vector $p(0)$, we must solve the boundary problem $\Lambda(0) = \Lambda_{in}$, $\Lambda(T) = \Lambda_f$, taking into account the Equations (1) and (2) in which $M_i = 0$. As a result, vector of angular momentum at initial instant of time L_{cal}, for which a spacecraft rotates with its free motion ($M = 0$) from the state $\Lambda(0) = \Lambda_{in}$, $L(0) = L_{\text{cal}}$ to the state $\Lambda(T) = \Lambda_f$, will be found. The vector $p_0 = p(0)$ relates to L_{cal} as follows:

$$p_{i\,0} = \frac{L_{i\ \text{cal}}}{\sqrt{L_{1\text{cal}}^2 + L_{2\text{cal}}^2 + L_{3\text{cal}}^2}}$$

Other schemes of computing can be successful for some specifical or particular cases [39–41].

6. Example and results of mathematical modeling

Now, we demonstrate numeric example of optimal turn with minimum of Equation (5). Let us take spatial reorientation for 180 degrees from state Λ_{in}, corresponding to spatial position when spacecraft axis are parallel to the axis of inertial frame I, in an assigned attitude Λ_f, if angular rate is absent at instants $t = 0$, and $t=T$ (i.e., $L(0) = L(T) = 0$). The quaternion Λ_f has the following components:

$\lambda_0 = 0$, $\lambda_1 = 0.707107$, $\lambda_2 = 0.5$, $\lambda_3 = 0.5$

It is assumed that spacecraft has characteristics:

$J_1 = 63559$ kg·m², $J_2 = 192218.5$ kg·m², $J_3 = 176809$ kg·m²

Further, after constructing the control program for optimum angular momentum variation during spacecraft rotation from state Equation (3) in the required state Equation (4), result of mathematic simulation of optimum turn are presented for the following coefficients: $k_1 = 0.002\ \mathrm{s}^{-2}$ and $k_2 = 0.04\ \mathrm{J/s}^2$.

Decision of boundary-value problem of the turn from attitude $\Lambda(0) = \Lambda_{in}$ to orientation $\Lambda(T) = \Lambda_f$ give $p_0 = \{0.49535062; –0.11725655; 0.86074309\}$ calculated. The method of iterations has been used, ensuring process of successive-approximation to true p_0 [9] (the method ensures asymptotic approaching in absolute most of cases). Maximum of control torque modulus is $|M(0)| = 70.2$ N m, and $Q = 401.63$ kN m s^2.

7. Result and discussion

Mathematical calculations results and numerical simulation of optimum turn process are shown on **Figures 2–5** (in graphical form). **Figure 2** presents a variating of angular momentum as time function ($L_1(t)$, $L_2(t)$, $L_3(t)$ as projections on the body frame axes). Behavior of spacecraft attitude $\Lambda(t)$ during optimum maneuver is illustrated by **Figure 3** (functions λ_0, λ_1, λ_2, λ_3). Dynamics of p_1, p_2, p_3 for p is reflected on **Figure 4**. Finally, **Figure 5** give behavior of angular momentum modulus. Duration of optimal maneuver is $T = 271.2$ s. The rotational energy during a turn does not exceed $E_{\max} = 9.9$ joules, spacecraft angular momentum has maximum magnitude $L_{\max} = 1562$ N m s at time $t = 135.6$ s. It is seen that p_1 changes lot less than p_2, p_3. For optimum control, all p_i, L_i, λ_j are smooth time functions.

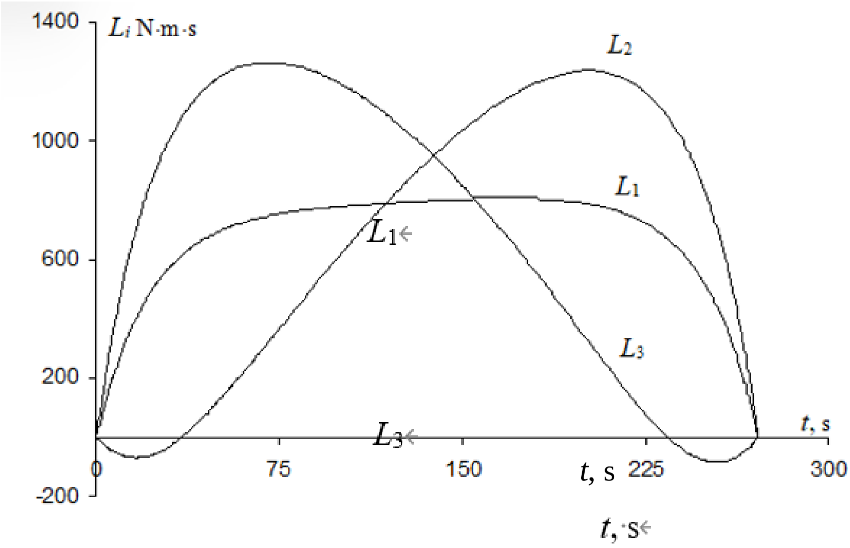

Figure 2. Angular momentum components during optimum turn.

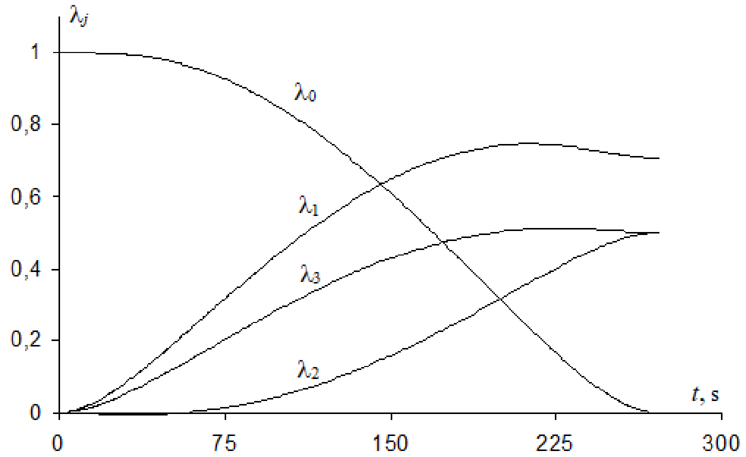

Figure 3. Quaternion (*t*) elements during optimum maneuver.

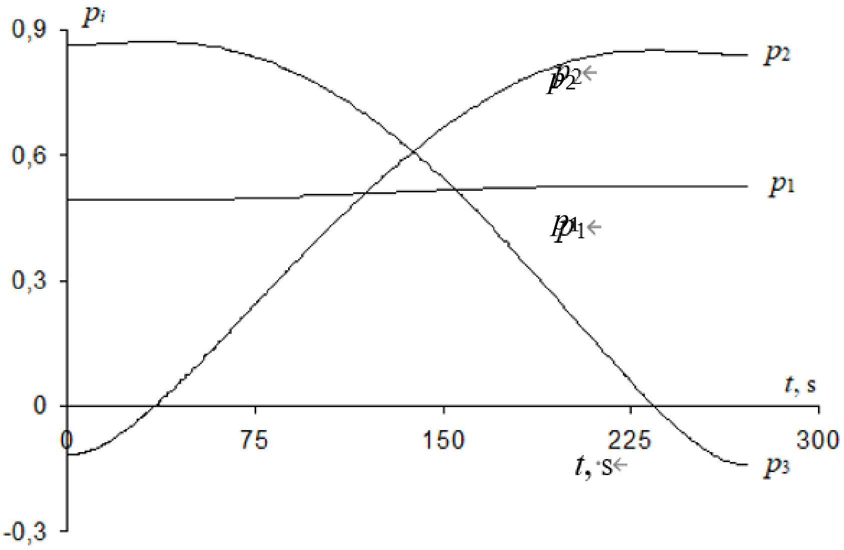

Figure 4. Variation of *p* under optimum control.

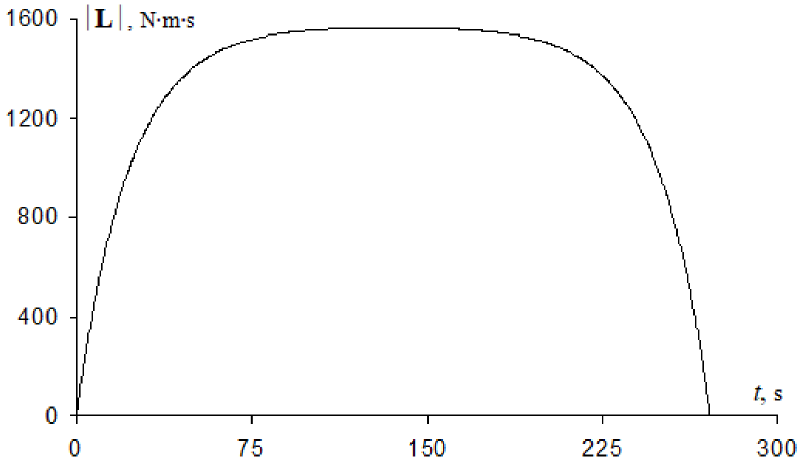

Figure 5. Variation of angular momentum modulus during optimal process.

8. Conclusion

Problem of optimum control of rotation from the initial attitude to the prescribed final attitude was researched in detail. In the considered investigation, new control method of spacecraft was designed; chosen optimality criterion is unique. The developed method for motion control was described in details. For optimization, the selected index of quality combines time, integral of the kinetic energy of rotation and control contribution (as energy consumption), necessary for turn realization. A solved problem is very topical. The issue of economical control of rotation is relevant very march, therefore, a task considered above is very important practically. Importance (implication, or significance) of the made research is that optimization of the adopted quality index minimizes energy costs (for example, electric energy consumption if spacecraft orientation control is performed by EJE-engines).

Main properties of reorientation and trajectory type corresponding to a chosen index of quality Equation (5) have been discovered. The maximum principle and quaternion models were used. As was shown, ratio of kinetic rotary energy to a squared modulus of angular momentum is constant. It was illustrated, mode of control when an angular momentum and a controlling moment are parallel over entire time period of rotation is optimal turn. The Hamilton and the conjugate equations system as well as analytical expressions for optimum controlling functions were written for optimization problem formulated in article. The structure of optimal control was defined, basing on the necessary optimality conditions. Relations for determining a spatial rotation were given, analytical formulas were written. The found optimal solution is unique.

Algorithm for orientation control is an essential element of attitude control system (for spacecrafts, and orbital stations, in particular). Analytical solving of a proposed problem has been presented. Computing expressions (and equations formalized) have been written for optimum program of controlled turn. Formulas to estimate maximum rotational energy and calculate maximum control torque magnitude were written analytically. Expressions of temporal characteristics of optimum process were presented. Implementation of controlled turn was described, also. Presence of calculated formulas given in explicit form, does a made work practically suitable and significant for direct applying in spaceflights practice. Optimum algorithms designed for spacecraft motion control improves a control system efficiency, originating spacecraft performance more economic during orbital flight.

Principal difference of solution, presented in this research, is new quality index used, and control torques cannot be unboundedly large even restrictions in absence for control. It is the original point of this article. Presence of energy integral in Equation (5) limits spacecraft's kinetic energy of rotation. Also, in an obtained mode, controlling torque modulus is not constant. Single admissible version of optimal solution is motion with variable control torque modulus (rotation period with constant control modulus are absent absolutely). How flat change the modulus of an angular momentum modulus, is defined by the coefficient of proportion k_1. The coefficients k_1 and k_2 (the ratio k_2/k_1) specify maximal energy of rotation.

Example of mathematic modeling which demonstrated a behavior of attitude parameters was given. For dynamically symmetric spacecraft (as special particular case), design of optimum control has been completed: the equations system has been written analytically (in direct form) that allows to solve two-point boundary value problem directly (to calculate the constants required for control law). The developed method of spacecraft control differs from all known publications. Its usefulness lies in significantly saving of control resources that will increase possibilities of spacecraft. In particular, interest causes use our method in spacecraft with EJE (or ion engines) because modern EJE has very large value of specific impulse (6000–6500 s approximately [42]) that require less fuel costs, and first integral in Equation (5) estimates electrical consumption. Second integral in Equation (5) limits kinetic energy of rotation (it is important in spaceflight, also). Necessity to reduce energy consumption is relevant problem, therefore research and optimization of optimal turn using on Equation (5) is topical.

Conflict of interest: The author declares no conflict of interest.

References

1. Sinitsin LI, Kramlikh AV. Synthesis of the optimal control law for the reorientation of a nanosatellite using the procedure of analytical construction of optimal regulators. Journal of Physics: Conference Series. 2021; 1745(1): 012053. doi: 10.1088/1742-6596/1745/1/012053
2. Velishchanskii MA, Krishchenko AP, Tkachev SB. Synthesis of spacecraft reorientation algorithms using the concept of the inverse dynamic problem. J. Comput. Syst. Sci. Int. 2003; 42: 811-818.
3. Junkins JL, Turner JD. Optimal spacecraft rotational maneuvers. Elsevier, Amsterdam; 1986.
4. Reshmin SA. Threshold Absolute Value of a Relay Control when Time-Optimally Bringing a Satellite to a Gravitationally Stable Position. Journal of Computer and Systems Sciences International. 2018; 57(5): 713-722. doi: 10.1134/s106423071805012x
5. Scrivener SL, Thompson RC. Survey of time-optimal attitude maneuvers. Journal of Guidance, Control, and Dynamics. 1994; 17(2): 225-233. doi: 10.2514/3.21187
6. Zhou H, Wang D, Wu B, et al. Time-optimal reorientation for rigid satellite with reaction wheels. International Journal of Control. 2012; 85(10): 1452-1463. doi: 10.1080/00207179.2012.688873
7. Reshmin SA. The Threshold Absolute Value of a Relay Control Bringing a Satellite to a Gravitationally Stable Position in Optimal Time. Doklady Physics. 2018; 63(6): 257-261. doi: 10.1134/s1028335818060101
8. Shen H, Tsiotras P. Time-Optimal Control of Axisymmetric Rigid Spacecraft Using Two Controls. Journal of Guidance, Control, and Dynamics. 1999; 22(5): 682-694. doi: 10.2514/2.4436
9. Levskii MV. Pontryagin's maximum principle in optimal control problems of orientation of a spacecraft. Journal of Computer and Systems Sciences International. 2008; 47(6): 974-986. doi: 10.1134/s1064230708060117
10. Molodenkov AV, Sapunkov YaG. Analytical Solution of the Minimum Time Slew Maneuver Problem for an Axially Symmetric Spacecraft in the Class of Conical Motions. Journal of Computer and Systems Sciences International. 2018; 57(2): 302-318. doi: 10.1134/s1064230718020120
11. Branets VN, Chertok MB, Kaznacheev YV. Optimal turn of a rigid body with a single axis of symmetry. Kosm. Issl. 1984; 22(3): 352–360.
12. Branets VN, Shmyglevskii IP. Use of quaternions in problems of orientation of solid bodies. Nauka. 1973.
13. Strelkova NA. On optimal reorientation of a solid, in Problems of Mechanics of Controlled Motion. Nonlinear Dynamical Systems. PGU, Perm; 1990. pp. 115–133.
14. Aipanov ShA, Zhakypov AT. The Method of Separation of Variables and its Application to the Problem of a Spacecraft's Optimal Turn. Cosmic Research. 2020; 58(1): 53-63. doi: 10.1134/s0010952520010013
15. Pankov AA., Chelnokov YuN. Investigation of quaternion laws of kinematic control of solid body orientation in angular velocity. Mechanics of Solids. 1995; 30(6): 3-13.
16. Zelepukina OV, Chelnokov YuN. Construction of optimal laws of variation in the angular momentum vector of a dynamically symmetric rigid body. Mechanics of Solids. 2011; 46(4): 519-533. doi: 10.3103/s0025654411040030

17. Biryukov VG, Chelnokov YuN. Construction of optimal laws of variation of the angular momentum vector of a rigid body. Mechanics of Solids. 2014; 49(5): 479-494. doi: 10.3103/s002565441405001x
18. Levskii MV. Optimal spacecraft terminal attitude control synthesis by the quaternion method. Mechanics of Solids. 2009; 44(2): 169-183. doi: 10.3103/s0025654409020022
19. Levskii MV. Use of universal variables in problems of optimal control concerning spacecrafts orientation. Mekhatron., Avtomatiz., Upravl. 2014; 53-59.
20. Molodenkov AV, Sapunkov YaG. Analytical solution of the optimal slew problem for an axisymmetric spacecraft in the class of conical motions. Journal of Computer and Systems Sciences International. 2016; 55(6): 969-985. doi: 10.1134/s1064230716060095
21. Molodenkov AV, Sapunkov YaG. Analytical Quasi-Optimal Solution of the Slew Problem for an Axially Symmetric Rigid Body with a Combined Performance Index. Journal of Computer and Systems Sciences International. 2020; 59(3): 347-357. doi: 10.1134/s1064230720030107
22. Sapunkov YaG, Molodenkov AV. Analytical Solution of the Problem on an Axisymmetric Spacecraft Attitude Maneuver Optimal with Respect to a Combined Functional. Automation and Remote Control. 2021; 82(7): 1183-1200. doi: 10.1134/s0005117921070043
23. Molodenkov AV, Sapunkov YaG. Analytical approximate solution of the problem of a spacecraft's optimal turn with arbitrary boundary conditions. Journal of Computer and Systems Sciences International. 2015; 54(3): 458-468. doi:10.1134/s1064230715030144
24. Levskii MV. Control of the Rotation of a Solid (Spacecraft) with a Combined Optimality Criterion Based on Quaternions. Mechanics of Solids. 2023; 58(5): 1483-1499. doi: 10.3103/s002565442360040x
25. Molodenkov AV, Sapunkov YaG. Optimal control of rigid body's rotation movement with a combined quality criterion. Journal of Computer and Systems Sciences International. 2019; 58(3): 382-392. doi: 10.1134/S1064230719030122
26. Sapunkov YaG., Molodenkov AV. Quasioptimal spacecraft attitude control constructed according to the poinsot concept. Aerospace 2023; 10(5): 402. doi: 10.3390/aerospace10050402
27. Molodenkov AV, Sapunkov YaG. Analytical quasi-optimal solution for the problem on turn maneuver of an arbitrary solid with arbitrary doundary conditions. Mechanics of Solids. 2019; 54(2): 54(3): 474-485 doi:.10.3103/S0025654419020110
28. Levskii MV. Optimization problem of attitude control of a spacecraft with bounded rotary energy using quaternions. International Robotics & Automation Journal. 2021; 7(2): 63-73. doi: 10.15406/iratj.2021.07.00228
29. Hao Zhou, Danwei Wang, Baolin Wu, EK Poh. Time-optimal reorientation for rigid satellite with reaction wheels. International Journal of Control. 2012; 85(10): 1-12.
30. Levskii MV. Special aspects in attitude control of a spacecraft, equipped with inertial actuators, J. Comp. Sci. Appl. Informat. Technol. 2017; 2: 1-9. https://doi.org/10.15226/2474-9257/2/4/00121
31. Levskii MV. Method of controlling a spacecraft turn. RF Patent for the Invention No. 2093433, 22.03.1994.
32. Gorshkov OA, Muravev VA, Shagayda AA. Holl's and ionic plasma engines for spacecrafts. Mashinostroenie; 2008.
33. Pontryagin LS, Boltyanskii VG, Gamkrelidze RV, et al. The mathematical theory of optimal processes. Springer; 1986.
34. Chanyal BC, Pathak M. Quaternionic Approach to Dual Magnetohydrodynamics of Dyonic Cold Plasma. Advances in High Energy Physics. 2018: 1-13. doi: 10.1155/2018/7843730
35. Chanyal BC. Quaternionic approach on the Dirac–Maxwell, Bernoulli and Navier–Stokes equations for dyonic fluid plasma. International Journal of Modern Physics A. 2019; 34(31): 1950202. doi: 10.1142/s0217751x19502026
36. Chanyal BC, Karnatak S. A comparative study of quaternionic rotational Dirac equation and its interpretation. International Journal of Geometric Methods in Modern Physics. 2020; 17(02): 2050018. doi: 10.1142/s0219887820500188
37. Young LC. Lectures on the calculus of variations and optimal control theory. EA: Saunders, Philadelphia; 1969.
38. Levskii MV. Device for regular rigid body precession parameters formation. RF Patent for the Invention, No. 2146638, 27.02.1996.
39. Lastman GJ. A shooting method for solving two-point boundary-value problems arising from non-singular bang-bang optimal control problems. International Journal of Control. 1978; 27(4): 513-524. doi: 10.1080/00207177808922388
40. Bertolazzi E, Biral F, Da Lio M. Symbolic-numeric efficient solution of optimal control problems for multibody systems. Journal of Computational and Applied Mathematics. 2006; 185(2): 404-421. doi: 10.1016/j.cam.2005.03.019
41. Kumar S, Kanwar V, Singh S. Modified Efficient Families of Two and Three-Step Predictor-Corrector Iterative Methods for Solving Nonlinear Equations. Applied Mathematics. 2010; 01(03): 153-158. doi: 10.4236/am.2010.13020

42. Kulkov VM, Gorshkov VA, Egorov YG, et al. Comparative estimation of efficiency of applying the perspective types of electric-rocket engines on small spacecrafts, Byull. Samara's State Space University; 2012.

Mechanical Engineering Advances 2024, 2(2), 1561.
https://doi.org/10.59400/mea1561

Article

Ocean current turbine power take-off design using fluid dynamics and towing tank experiments

Setare Sadeqi[1,2], Shahab Rouhi[1,2], Nikolaos I. Xiros[1], Erdem Aktosun[3], Lothar Birk[1], Juliette Ioup[2], Miguel Trejos[1,*]

[1] Boysie Bollinger School of Naval Architecture and Marine Engineering, University of New Orleans, Louisiana 70148, USA
[2] Department of Physics, University of New Orleans, Louisiana 70148, USA
[3] Department of Shipbuilding and Ocean Engineering, İzmir Kâtip Çelebi University, Çiğli 35620, Turkey
*** Corresponding author:** Miguel Trejos, matrejos@uno.edu

CITATION

Sadeqi S, Rouhi S, Xiros NI, et al. Ocean current turbine power take-off design using fluid dynamics and towing tank experiments. Mechanical Engineering Advances. 2024; 2(2): 1561. https://doi.org/10.59400/mea1561

ARTICLE INFO

Received: 25 July 2024
Accepted: 30 September 2024
Available online: 13 November 2024

Abstract: This study investigates the performance and power generation capabilities of a small-scale hydrokinetic turbine by comparing numerical simulations with experimental measurements. The key difference between the two models comes from the initial numerical analysis which focused only on the permanent magnet DC motor (PMDC) motor's parameters and did not account for the gear-head reduction that leads to discrepancies in current and torque predictions, especially at lower input voltages. In practice, friction losses within the gear-head increased the required current and torque, highlighting inefficiencies in the motor gear-head system. A modified experimental setup incorporated a magnetic coupling to address leakage issues and enhance system reliability. While the magnetic coupling resulted in a slight reduction in speed, current, and torque, it improved the overall integrity of the system which is essential for marine applications. The comparison between experimental results and Blade Element Momentum (BEM) simulations showed good agreement at lower speeds, but the simulations under-predicted power at higher speeds, likely due to the model's limitations in capturing complex hydrodynamic phenomena. This shows the need for comprehensive analysis, integrating both numerical and experimental approaches to optimize turbine performance. Future research will focus on refining experimental methodologies and further improving turbine design and efficiency for hydrokinetic energy systems.

Keywords: ocean current turbine (OCT); hydrokinetic turbine performance; blade element momentum (BEM) theory; magnetic coupling optimization; dynamometer testing

1. Introduction

In the rapidly advancing field of renewable energy technologies, research into ocean current turbines (OCTs) provides as a promising approach to harness the substantial energy potential of ocean currents. Ocean currents promise a reliable and consistent source of renewable energy, in contrast to the intermittent nature of wind and solar power, making OCTs a critical area of focus in sustainable energy research [1–3]. In addition to this field is the application of Blade Element Momentum (BEM) theory, which plays a crucial role in accurately simulating turbine performance by predicting hydrokinetic forces and optimizing designs for maximum efficiency [4–6]. By using BEM, we can evaluate how OCTs respond to various flow conditions, helping to fine-tune designs for better performance [7–12].

This paper presents a comprehensive study focused on the development and evaluation of a small-scale horizontal axis OCT. It combines advanced BEM simulations with innovative experimental techniques to enhance understanding of turbine behavior and performance. Specifically, BEM is integrated with traditional mathematical models used for propeller blade design, which facilitates more accurate calculations of the forces acting on the turbine blades. This integration allows for a deeper analysis of turbine dynamics under varying operational conditions, providing crucial insights into both turbine efficiency and load distribution [13–17]. The focus of this research is to improve the design of turbine blades by adapting advanced BEM-based simulations into a refined mathematical framework tailored to OCT blade design [18–22]. Through this combination of BEM and mathematical modeling, the study manages highly accurate predictions of hydrokinetic forces, offering a more detail view of turbine behavior in real-world marine environments [23–26].

The methodology of this study is derived from the principles of marine engineering where the combination of simulation and experimentation is critical for validating these models. This combination is essential for fine-tuning the design and ensuring the reliability of OCTs under different operational scenarios [27–30]. A key part of the experimental setup is dynamometer testing which allows precise measurements of the turbine's performance. By closely monitoring the relationship between voltage, power, and rotational speed generated by the Permanent Magnet Direct Current (PMDC) motor, we can obtain detailed performance data during testing [31–35]. This process involves using a 3D-printed turbine model equipped with sensors, enabling accurate monitoring of critical performance parameters in a controlled environment [36–39]. By coupling these dynamometer tests with advanced BEM simulations, the study provides comprehensive insights into the hydrokinetic forces acting on the turbine that shows the complex interactions between blade geometry, fluid dynamics, and turbine efficiency [40–47].

The reliability of BEM simulations is further validated through careful comparisons with other experimental and theoretical models. In this context, the study emphasizes the importance of precise measurements and a comprehensive understanding of hydrodynamic effects to improve the accuracy of BEM predictions. This approach emphasizes the necessity of integrating both simulation and experimentation to achieve a better understanding of OCT behavior under various conditions [48–54]. A significant result in the study was the successful resolution of an issue encountered during earlier OCT tests—minor leakage during prolonged operation. The problem was addressed by redesigning the nacelle and incorporating a magnetic coupling system, which completely eliminated water leakage and extended the testing duration. This innovation is crucial for improving the reliability of OCTs, particularly when operating at different rotational speeds [55]. This achievement not only advances our understanding of small-scale OCT performance but also contributes to the design of more robust and efficient turbines for future applications [56–58].

A defining characteristic of this research is its interdisciplinary approach, which combines mathematical modeling, experimental validation, and innovative engineering design. This multifaceted methodology enhances the study of hydrokinetic energy conversion by providing a deeper understanding of the challenges and opportunities in OCT development. By incorporating state-of-the-art computational techniques, such as those employed in hydrodynamic modeling [59], this research shows a robust framework for optimizing turbine performance and scaling the technology for future energy needs.

In this study, we aim to evaluate and enhance the performance of a small-scale horizontal axis OCT through a combination of numerical simulations and experimental testing. Using BEM theory, this research seeks to accurately model the hydrodynamic forces acting on the turbine and validate these findings with experimental data from a redesigned turbine setup. The study also addresses mechanical inefficiencies caused by gear-head friction and explores the potential of magnetic coupling to prevent water leakage during operation. By improving turbine efficiency, reliability, and design; this research contributes to the optimization of hydrokinetic energy conversion, making the foundation for future advancements in OCT technology.

2. Methods

Numerical method

Before introducing BEM theory for the numerical analysis of OCT performance, it is essential to first establish a foundation with the actuator disc concept which forms a crucial part of turbine analysis. The actuator disc model simplifies a turbine to an idealized, actuator disc that extracts energy from the flow. This concept was first introduced by Froude through classical momentum theory which is built on several key assumptions: the flow is inviscid, incompressible, irrotational and both velocity and pressure are uniform inflow. The actuator disc concept allows for the approximation of the forces exerted by the turbine on the fluid, simplifying the analysis of how energy is extracted from the flow. By applying momentum conservation and energy principles, this model provides insight into how the turbine influences the surrounding flow, both upstream and downstream. This theoretical foundation is instrumental in understanding how OCTs convert kinetic energy from ocean currents into usable mechanical energy. By first examining this simplified model, we can better appreciate the more complex analysis provided by BEM theory, which takes into account the detailed geometry of the blades and other factors that influence the turbine's real-world performance.

To simplify the analysis, we will begin by replacing the OCT with an actuator disc inflow to capture kinetic energy while disregarding any specific turbine design characteristics for now. As shown in **Figure 1**, the downstream section has a larger cross-sectional area than the upstream section, which is smaller than the area of the actuator disc. The flow rate of water through the channel at any given cross-section is represented by AU. Applying the principle of mass conservation, we get:

$$\rho A_\infty U_\infty = \rho A_d U_d = \rho A_w U_w \tag{1}$$

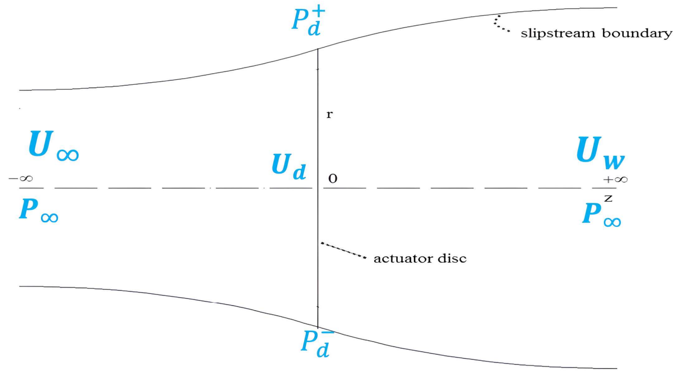

Figure 1. Actuator disc model and stream-tube concept.

The conditions of the upstream (current speed), actuator disc, and downstream are indicated by the subscripts, *d* and *w*. Due to the actuator disc's axial induction factor, a, which causes some variation in the current velocity,

$$U_d = U_\infty(1 - a) \tag{2}$$

We must also take the tangential flow induction factor a' into account by considering tangential velocity in addition to axial velocity. There is zero tangential velocity upstream, $2\Omega ra'$ tangential velocity is present near the actuator disc downstream, and $\Omega ra'$ tangential velocity is present in the wake.

Now let's introduce the BEM numerical analysis. BEM theory is a widely used method for predicting the performance of wind and OCTs. Blade element theory divides each rotor blade into small segments, or blade elements, treating each as a separate hydrofoil to calculate hydrodynamic forces like lift and drag based on factors such as angle of attack, pitch angle, and rotational speed. Momentum theory simplifies the overall rotor analysis by modeling the rotor as a single actuator disc that extracts kinetic energy from the flow, resulting in changes to the fluid's velocity and direction downstream, providing estimates for thrust and power generation. BEM theory integrates these approaches by calculating the forces on each blade element and using momentum theory to determine the total thrust, power, and efficiency, while also accounting for wake effects like induced velocity. Replacing the actuator disc with a 3-blade OCT, as shown in **Figure 2**, the net tangential velocity from blade element theory is $\Omega r\,(1 + a')$, defining the resulting velocity accordingly.

Axial and tangential induction factors are determined by understanding how the aerodynamic lift (C_l) and drag (C_d) coefficients vary with respect to the angle of attack for each cross-section of the blades. **Figure 3** illustrates the application of the laws of conservation of momentum and energy with a single OCT featuring with N blades and varying chord lengths and pitch angles, across 25 distinct cross-sections.

$$\sin\varphi = \frac{U_\infty(1 - a)}{W} \tag{3}$$

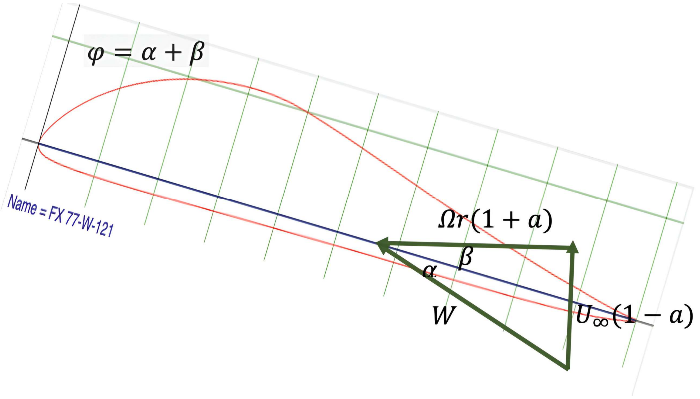

Figure 2. Velocities across the foil cross-section.

$$\cos\varphi = \frac{\Omega_r(1 + a')}{W} \tag{4}$$

where $\varphi = \alpha + \beta$, based on the descriptions of the hydrodynamic forces for each cross-section. **Figure 3** shows the definitions of the cross-sectional lift and drag forces.

$$\delta L = \frac{1}{2}\rho W^2 c C_l \delta r \tag{5}$$

$$\delta D = \frac{1}{2}\rho W^2 c C_d \delta r \tag{6}$$

$$\delta L\cos\varphi + \delta D\sin\varphi = \frac{1}{2} N C \rho W^2 (C_l\cos\varphi + C_d\sin\varphi)\delta r \tag{7}$$

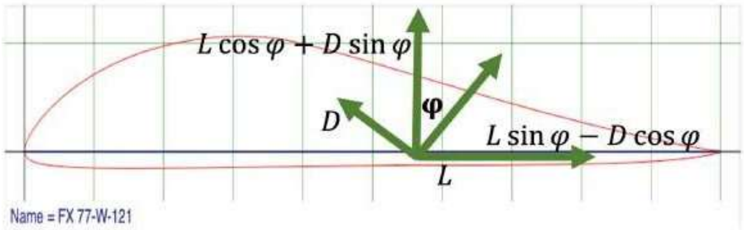

Figure 3. Lift and drag forces on the foil cross-section.

It is practical to use:

$$\mu = \frac{r}{R} \tag{8}$$

$$C_x = C_l\cos\varphi + C_d\sin\varphi \tag{9}$$

$$C_y = C_l\sin\varphi - C_d\cos\varphi \tag{10}$$

$$\frac{a}{a - 1} = \frac{\sigma_r C_x}{4\sin\varphi^2} \tag{11}$$

Because the system is nonlinear, the following equations are used in an iterative process to derive the axial and tangential induction factors based on the two-dimensional hydrofoil characteristics.

$$\frac{a}{1+a'} = \frac{\sigma_r C_v}{4\sin\varphi\cos\varphi} \tag{12}$$

where σ_r is the chord solidity, calculated by dividing the circumferential length at a particular radius by the entire length of the total chord length of the blade. Note that the BEM hypothesis is valid only under the condition of uniform blade rotations.

$$\sigma_r = \frac{Nc}{2\pi r} = \frac{Nc}{2\pi\mu R} \tag{13}$$

When the effect primarily influences the blade tips by reducing the lift force and generating additional torque, it is referred to as tip loss. This phenomenon results in decreased torque that corresponds to a reduction in power. According to Ludwig Prandtl's tip loss factor, we have the following:

$$F = \frac{2}{\pi}\cos^{-1}\left(e^{-f}\right) \tag{14}$$

$$f = \frac{N(R-R)}{2r\sin\varphi} \tag{15}$$

$$\frac{r}{R} = 0.6{:}\, F \approx 1 \& \frac{r}{R} > 0.6{:}\, F < 1 \tag{16}$$

In addition, new equations can be derived to determine the induction factors by incorporating the tip-loss factor into the iterative solutions.

$$a = \frac{1}{\frac{4F\sin\phi^2}{\sigma_x C_x} + 1} \tag{17}$$

$$a' = \frac{1}{\frac{4F\sin\phi\cos\phi}{\sigma_y C_y} - 1} \tag{18}$$

$$\delta Q = 4\pi\rho U_\infty a'(1-a)\Omega r^3 \delta r \tag{19}$$

$$\delta P = \Omega\delta Q = 4\pi\rho U_\infty a'(1-a)\Omega^2 r^3 \delta r \tag{20}$$

Table 1 specifies the machine used to run all codes and obtain the numerical results.

Table 1. Specifications of the machine used to execute the codes and obtain the numerical results.

Component	**Specification**
Processor	12th Gen Intel(R) Core (TM) i5-12400F 2.50 GHz
RAM	32.0 GB (31.9 GB usable)
System Type	64-bit operating system, x64-based processor
Matlab Software	R2013b version

The projected shaft power and torque can be calculated using the designed rotor at its design rotational velocity of 500 RPM with momentum theory. A detailed explanation of the BEM theory is provided in [39] and [60]. These references present a detailed background on the theoretical foundations of BEM simulations. The simulations conducted in this study were carefully aligned with the experimental configurations outlined in these sources, ensuring a high degree of accuracy and consistency between theoretical predictions and experimental results. Also, the in-house developed BEM code iteratively calculates the axial and tangential induction factors and determines the sectional forces for the small-scale OCT. This procedure is given in the algorithmic steps shown in **Figure 4**.

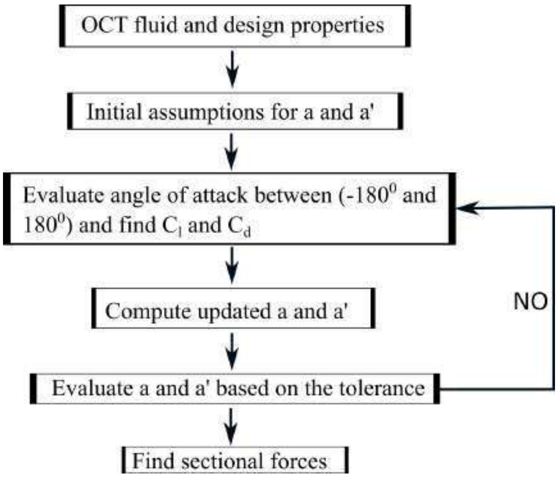

Figure 4. Algorithmic steps for BEM simulation.

3. Experimental methods

3.1. Initial experimental setup

Let's begin with the sizing of the motor/generator, sensors, and circuit components. To achieve this, the BEM theory is a well-established technique for analyzing turbine performance. In this study, an in-house BEM algorithm developed in MATLAB was employed to account for specific fluid conditions and rotor characteristics. The BEM code facilitated the estimation of various parameters, such as differential torque, thrust, and power, for the turbines under investigation. To validate the predictions obtained from the BEM code and conduct proof-of-concept testing, a small-scale, three-bladed horizontal underwater turbine was developed. Using a small-scale turbine is a cost-effective alternative to full-scale testing. This small-scale turbine served as a prototype for both testing and numerical model verification.

For the experimental setup, an electrical system was needed to meet the necessary requirements and measure the generated power. The OCT generates power based on local forces, primarily the lift force acting on the rotor blades. In addition, to prevent any structural damage to a full-scale prototype, the undesirable forces acting on the carriage were taken into account. To estimate the nominal generated power at different carriage speeds and rotor blade rotational speeds, a method was employed. The carriage speed was used to mimic the motion of the water current, which contains kinetic energy. The tip speed ratio was adjusted to achieve optimal power production at a constant carriage speed. This adjustment was accomplished by varying the rotational speed of the rotor blades.

The design of the apparatus system was divided into two subsystems: the motor power supply and the generator power production. The motor drive power supply was responsible for converting the AC line voltage into a DC bus voltage using a switch-mode power supply. By regulating the duty cycle, the output voltage could be controlled, allowing the rotational speed of the DC motor to be varied. Prior to the design process, several considerations needed to be addressed. It was crucial to define the expectations for the entire system and determine the best approach for assembling the system with the required components. Due to the limited carriage speed in University of New Orleans towing tank facility, the DC machine needed to reach steady-state reference rotational speeds before functioning as a generator. Therefore, electricity was supplied to the motor to achieve the desired speed. Additionally, each circuit element within the system had to be carefully selected and sized to ensure proper operation.

By incorporating these considerations and implementing the described methodology, the study aimed to develop an appropriate design and gather the necessary data for further analysis and evaluation of the ocean current turbine's performance. In order to fully understand and analyze the behavior of a motor/generator, it is important to develop a comprehensive electromechanical model that precisely captures its characteristics in both motor mode and generator mode. This model serves as a fundamental requirement for studying the machine's performance and conduct. One approach to determining the characteristics of the motor/generator is through numerical analysis using computer simulation. By creating a numerical model of the machine and simulating its operation under various conditions, we can obtain valuable insights into its electromechanical behavior. Computer simulations enable us to study the machine's performance, efficiency, torque-speed characteristics, and other significant parameters. Additionally, to validate the accuracy of the numerical analysis and simulations, it is crucial to compare the simulation results with experimental data collected from the same motor/generator operating in both modes. This comparison helps in confirming the model's predictive capabilities and ensures that it accurately represents the present behavior of the machine.

By combining numerical investigations, computer simulations, and experimental data, we can develop an extensive comprehension of the machine's electromechanical characteristics. This knowledge is vital for optimizing the machine's performance, designing control strategies, and making informed decisions regarding its practical applications.

The fundamental principle of induction allows DC motors to work as generators. When a DC motor operates as a generator, the movement of a conductor in a magnetic field induces a voltage across the conductor. In this case, the induced voltage is directly proportional to the speed of the motor's shaft. The induced voltage generated by a DC motor used as a generator can be harnessed and utilized. This principle finds practical applications in the regenerative braking of electric vehicles and renewable energy systems, where energy regeneration or recovery is desired. This relationship holds true when the generator is not connected to an external load.

$$V_{ind} = \frac{\omega}{K_s} \tag{21}$$

where V_{ind} is the generated voltage (V), ω is the motor shaft speed (rpm), K_s is the speed constant of the motor, aka, speed equation constant (rpm/V). The speed constant is the inverse of the motor voltage constant (K_e).

$$K_s = 1/K_e \tag{22}$$

When a DC generator is loaded with current, the induced DC voltage at its terminals is reduced due to the presence of motor resistance. The motor resistance causes a voltage drop across the internal components of the generator, which reduces the voltage available at the terminals. Hence, we can rewrite Equation (21) as follows:

$$V_t = \frac{\omega}{K_s} - R_m I_l \tag{23}$$

where V_t is the generated voltage (V), ω is the motor shaft speed (rpm), K_s is the speed constant of the motor (rpm/V), R_m is the motor resistance (Ω), I_l is the current that goes through the wire (A).

To analyze the characteristics of a generator, we can plot a voltage-current curve using an equation that describes the relationship between the generated voltage and the load current. The maximum possible generated voltage is achieved when there is no load current flowing through the generator, which is also known as an open circuit condition. At this point, the generator is not connected to any external load, allowing the maximum voltage to be generated. Conversely, the maximum load current corresponds to the no-voltage induction condition, also known as a short circuit. In this situation, the generator is connected directly to a load with minimal impedance, causing the induced voltage to drop to zero. At this point, the maximum current flows through the generator. By plotting the voltage-current line, we can visualize the generator's behavior and determine its operational limits. The line can help identify the generator's voltage regulation capabilities, efficiency, and optimal operating points for different load conditions. Therefore, the maximum load current is:

$$I_{l_{max}} = \frac{\omega}{K_s} R_m \tag{24}$$

The torque required to drive the generator in order to overcome the generator internal losses and produce the load current is given by Equation (25).

$$\tau = K_t\,(I_l + I_o) \tag{25}$$

where τ is the required driving torque (Nm), I_l is the current through the wire (A), I_0 is the motor no-load current (A) corresponding to the internal torque losses, K_t is the motor torque constant or motor constant (Nm/A). The torque constant is equal to the motor voltage constant (K_e).

$$K_t = K_e \tag{26}$$

The generator power consists of two components, electrical output power and mechanical input power.

The electrical output power can be calculated using Equation (27).

$$P_e = V_t I_l \tag{27}$$

where P_e is the electrical power (W), V_t is the generated voltage (V), I_l is the load current (A). The maximum electrical output power at a given speed can be found from Equation (28).

$$P_{e_{Max}} = \frac{\pi}{30000} \frac{\omega^2}{4} \frac{\Delta\tau}{\Delta\omega} \tag{28}$$

where P_eMax is the maximum electrical output power (W), ω is the motor shaft speed (rpm), $(\frac{\Delta\tau}{})$ is the motor speed-torque gradient (rpm/Nm). Similarly, the mechanical input power can be calculated using Equation (29).

$$P_m = \frac{\pi}{30} \omega\tau \tag{29}$$

where P_m is the mechanical power (W), ω is the motor shaft speed (rpm), and τ is the driving torque (Nm). In general, efficiency is described as the ratio of useful output to total input. Hence, the generator efficiency is measured as the ratio of electrical output power to mechanical input power.

$$\eta_g = \frac{P_e}{P_m} \tag{30}$$

where η_g is the generator efficiency, P_e is the electrical power (W), and P_m is the mechanical power (W).

When a machine operates as a generator, its efficiency corresponds to that of its motor efficiency. Typically, a generator tends to achieve higher efficiency at higher rotational speeds. This implies that when the machine works at a faster rotational speed, it is more proficient in converting mechanical power into electrical power. Higher speeds often result in reduced losses and improved efficiency. Nonetheless, it's critical to note that the maximum efficiency of the generator occurs at a lower load current, while maintaining a given rotational speed. In other words, the generator operates most efficiently when the load associated to it draws a lower current. At lower load currents, the losses within the generator are minimized, allowing for a higher overall efficiency. Designing systems that operate the generator at higher rotational speeds while considering the appropriate load conditions can assist maximize overall efficiency and energy conversion.

In a PMDC motor, the speed of the motor can be constrained by adjusting the input voltage provided to the motor. By varying the motor voltage, we can control its rotational speed. The relationship between the angular speed (rotational speed) of the PMDC motor and the input voltage can be determined by examining the equivalent circuit of the motor. The equivalent circuit provides a simplified representation of the motor's electrical characteristics. The equivalent circuit of a PMDC motor typically consists of a voltage source, an internal resistance, and an inductor. The system equation of a PMDC motor is given by applying Kirchhoff's voltage law:

$$E_a = R_a i_a(t) + L_a \, ia(t) + E_b \tag{31}$$

where E_a is the applied voltage (V), R_a is the terminal resistance (Ω), i_a is the armature current (A), L_a is the terminal inductance (H), and E_b is the back electromotive force

(V). Further system equations are:

$$E_b = K_e\omega(t) \tag{32}$$

where K_e is the back-emf constant ($V/rad/s$), and ω is the angular speed (rad/s).

$$T = K_T i_a(t) = b\omega(t) + J\frac{d\omega(t)}{dt} \tag{33}$$

where T is the generated torque (Nm), K_T is the torque constant (Nm/A), b is the motor friction coefficient (e.g., brushes) (Nm s), and J is the load and armature inertia (kg m^2).

$$\frac{d\theta(t)}{dt} = \omega(t) \tag{34}$$

where θ is the rotor angular position (rad). In the case of a constant operating point, this equation can be simplified as follows:

$$E_a = R_a i_a + E_b \tag{35}$$

Thus, the electrical input power can be calculated by multiplying voltage by current:

$$E_a i_a = R_a i^2 + K_e\omega i_a \tag{36}$$

Mechanical output power is equal to torque times rotational speed:

$$T\omega = K_T\, i_a\omega \tag{37}$$

Electrical losses are caused by the resistance in the circuit:

$$Losses = R_a i_a^2 \tag{38}$$

To develop a model based on these equations, the values of the motor parameters must be defined. Simulations were performed for the PMDC motor using the motor parameters shown in **Table 2**. The models were implemented in a MATLAB environment.

The primary objective of this investigation is to determine the characteristic parameters of a PMDC motor operating in both motor and generator modes. This PMDC motor was selected to be used as a small-scale experimental hydrokinetic turbine. To achieve this objective, an experimental setup was designed. The PMDC motor, chosen as the prime mover, was mechanically connected shaft to shaft to an identical PMDC motor configured as a generator. This mechanical connection allowed for the transfer of mechanical power between the two motors.

Table 2. Key data of PMDC motor.

Motor Data	Units	Values
Nominal Voltage	V	12
No Load Speed	rpm	8130
No Load Current	A	0.32
Speed Constant	rpm/V	699
Torque Constant	Nm/A	0.0137

Table 2. (*Continued*).

Motor Data	Units	Values
Motor Resistance	Ω	0.079
Rotor Inertia	gcm2	99.5
Braking Load Resistance	Ω	1
Load Torque	Nm	0.12

In the experiment, a time-varying input voltage was applied to the prime mover motor, which effectively altered its rotational speed. The speed of the prime mover motor, in turn, forced the generator motor to generate a voltage. This voltage generated by the generator motor varied in amplitude corresponding to the input voltage applied to the prime mover motor.

On the generator side of the circuit, a variable resistor, denoted as "*R*", was manually adjusted. This variable resistor acted as a changeable load within the system. By altering the value of this resistor, the load on the generator motor could be modified, impacting the electrical characteristics of the system.

By manipulating the input voltage applied to the prime mover motor and adjusting the variable resistor on the generator side, the experiment allowed for the collection of data on the generator's performance under different load conditions. This data would enable the determination of important characteristic parameters of the PMDC motor, such as voltage-current relationships, power output, efficiency, and other relevant performance metrics. The equivalent circuit of this setup is illustrated in **Figure 5**.

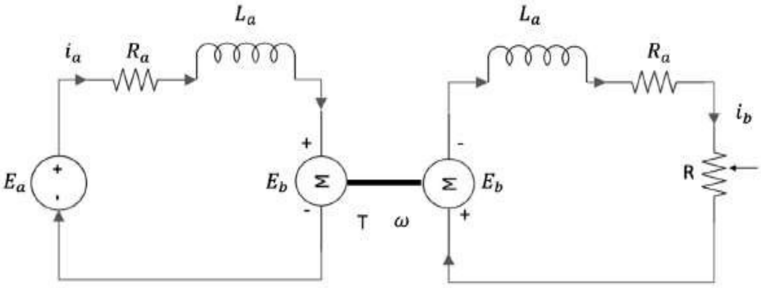

Figure 5. Equivalent circuit of the experimental setup.

The system behavior of the dynamometer is given by applying Kirchhoff's voltage law on both circuits knowing that the armature resistor, armature inductance, angular speed, and the amount of the torque are the same.

Power circuit:

$$E_a = R_a i_a(t) + L_a \frac{di_a(t)}{dt} + K_e \omega(t) \tag{39}$$

Load circuit:

$$E_b = R_a i_b(t) + L_b \frac{di_b(t)}{dt} + K_e i_b(t) \tag{40}$$

where *R* is the variable resistor (**Ω**) and i_b is the generated current (*A*). In the case of a constant operating point, these above equations can be simplified as follows:

Power circuit:

$$E_a = R_a i_a + K_e \omega \tag{41}$$

Load circuit:

$$K_e \omega = (R_a + R) i_b \tag{42}$$

To evaluate the performance and efficiency of the PMDC motor operating in both motor mode and generator mode, certain parameters need to be measured. These parameters include the input voltage, motor parameters, and the shaft angular speed. By utilizing these equations, it becomes possible to estimate the current flowing in both the power circuit and the load circuit. Once the currents in both circuits are estimated using the equations, it becomes possible to calculate the input power and the generated power. By considering the currents and voltages, along with the input power and generated power, it becomes feasible to assess and analyze the performance and efficiency of the PMDC motor. These calculations give valuable insights into how effectively the motor converts electrical power into mechanical power when operating in motor mode and how efficiently it converts mechanical power into electrical power while working as a generator.

To enhance the accuracy of the estimations regarding generated power and input power from numerical analysis, a specific experimental setup was employed including two identical PMDC motors.

- Connection of PMDC Motors: The two PMDC motors were mechanically connected shaft to shaft. This setup allowed us to not just assess the performance of the PMDC motor as a prime mover (when it drives the turbine) yet additionally as a generator (when it produces electrical power).
- Variable DC Voltage Source: A variable DC voltage source was connected to one of the PMDC motors, known as the prime mover motor (type DCX 35 L with a power rating of 80/120 Watts). By changing the input voltage provided to this motor, its rotational speed is adjusted.
- Gearhead for Speed Adjustment: The PMDC motor has a characteristic speed rate of 8130 RPM. However, due to the fact that the turbine was scaled down in size for experimentation, a planetary gearhead (type GPX 37) with a reduction ratio of 16:1 was utilized. This gearhead reduced the motor’s speed to a more suitable level for the scaled-down turbine
- Rotary Torque Sensor: A TRS605 non-contact shaft-to-shaft rotary torque sensor with an encoder was placed between the prime mover and generator shafts. This allowed us to measure the driving torque applied and the rotational speed of the system.
- Servo Motor Driver: To control the speed of the prime mover PMDC motor, an ESCON 50/5 servo controller was utilized as a regulator. This controller allowed us to fix a setpoint value for the motor’s speed, providing precise command over the motor’s rotational speed during testing.

The experimental setup, as described above, is visually depicted in **Figure 6**.

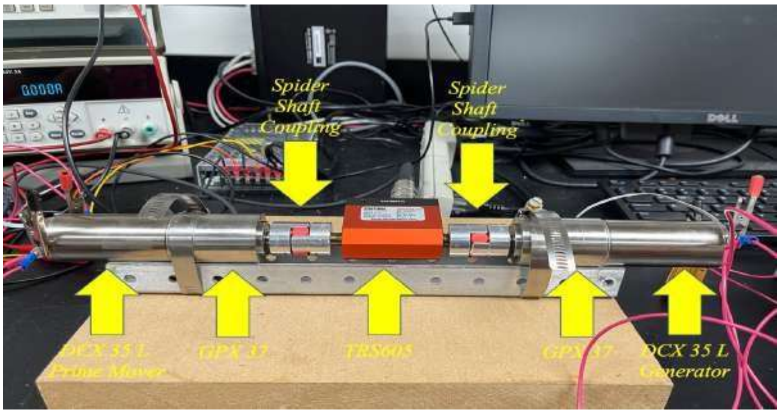

Figure 6. Initial experimental setup.

This setup was carefully intended to provide accurate and reliable data for assessing the performance of the hydrokinetic turbine PMDC motor under various conditions. By measuring torque, speed, and controlling the motor's speed with precision, we can obtain valuable insights into the turbine's PMDC motor behavior and efficiency during experimentation. The data acquisition system incorporates sensors that monitor the electrical current and voltage on both sides of the system, namely the power circuit (supplying electrical power to the prime mover PMDC motor) and the load circuit (where the generated power is utilized). These sensors allow us to measure and analyze the electrical characteristics of the turbine during testing.

To alter the speed of the prime mover, the input voltage is manually adjusted to the motor driver. The generator, mechanically connected to the prime mover, was forced to produce a voltage as a result of this connection. Varied load resistor utilized to assess the system's performance under different conditions. However, there is a restriction on the size of the load resistor. At the point when a smaller load resistor is used, the current flowing through the system increased, resulting in higher power output. This relationship between load resistor size, current, and power is a significant consideration for testing the turbine's efficiency and power generation capabilities. The PMDC motor used in the experiment had the power rating modes: 80 Watts in continuous operation mode and 120 Watts in intermittent operation mode. The decision of the specific motor and its power rating modes were likely based on the requirements and characteristics of the hydrokinetic turbine model.

The reason for using a PMDC motor with a planetary gearhead combination was because of the slow-moving nature of the driving mechanism in ocean current turbines. The turbine model expected a slower rotational speed to match the characteristics of ocean currents. However, this gearing combination presented difficulties when using the motor as a generator. Reversing the motor to function as a generator caused inefficiencies because the two-stage gearhead is not originally intended for such utilization. As a result, the generator mode may not achieve the same level of efficiency as the prime mover mode, impacting the overall performance and power generation capability of the hydrokinetic turbine.

Figure 7 compares two models: one derived from numerical analysis and the other based on actual experimental measurements. The difference between the two models can be attributed to a key factor: the calculations in the numerical analysis were initially based solely on the PMDC motor's parameters, without accounting for the effect of the gearhead reduction. In other words, the numerical analysis focused on the PMDC motor itself, neglecting the influence of the attached gearhead.

In practical experiments, however, the gearhead's reduction effect becomes significant and needs to be accounted for. The figure illustrates that at lower voltage levels, the measured current from experiments is higher than what was initially predicted by the numerical analysis. The reason for this discrepancy is that, at lower voltages, more current is required to compensate for the losses caused by friction within the gearhead. Friction within the gear-head can result in energy losses, making the actual motor-gearhead system less efficient than predicted by the numerical analysis. As a consequence, a higher current is needed to achieve the expected performance level during the experimental measurements.

This observation highlights the importance of considering all components and their interactions in the system when conducting numerical analysis or simulations.

Figure 8 presents a correlation between the rotational speed of the PMDC motor, which was operated as a prime mover, under different input voltage conditions. In the figure, the black solid line represents the rotational speed calculated from numerical analysis, while the square points represent the measured rotational speed obtained from actual experimental testing. The comparison in **Figure 7** reveals that the measured angular speed of the experimental PMDC motor is lower compared to the angular speed predicted by the numerical analysis. The reason for this inconsistency is attributed to the presence of the planetary reduction gearhead.

Figure 9 gives a comparison of the torque delivered by the PMDC motor at different input voltages, alongside the measured torque obtained during experimental testing. In the figure, the black line represents the torque values determined from numerical analysis, while the red line represents the torque values measured during the actual experiment. The comparison in **Figure 6** reveals that the measured torque (squre points) during the experimental testing is different from the torque values estimated by the numerical analysis (black solid line). The reason for this difference is attributed to the presence of the gearhead attached to the PMDC motor. When operating at lower input voltages, the measured torque is higher than the torque values estimated by the numerical analysis. This is because at lower voltages, the motor requires more current to compensate for the friction losses within the gearhead. As mentioned previously, the gearhead introduces mechanical inefficiencies and losses. These losses impact the actual torque output of the motor during experiments, resulting in a higher measured torque compared to what was initially anticipated in the numerical analysis.

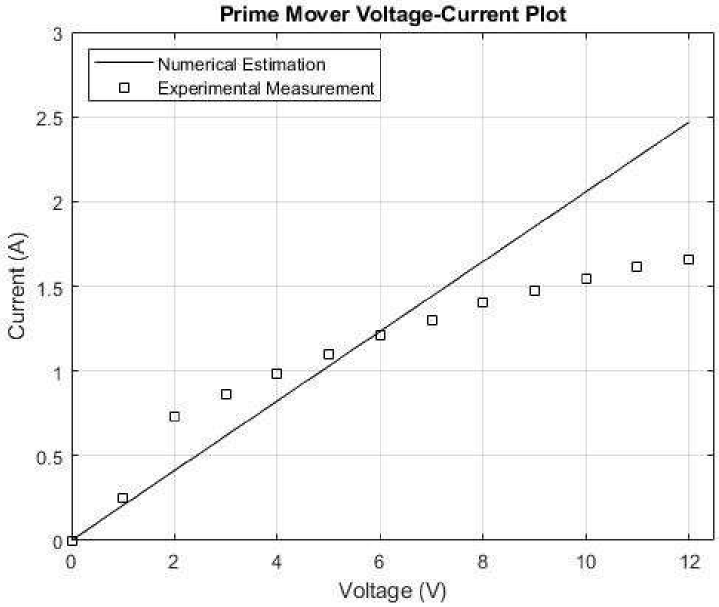

Figure 7. Current comparison at different input voltages between numerical and experimental models.

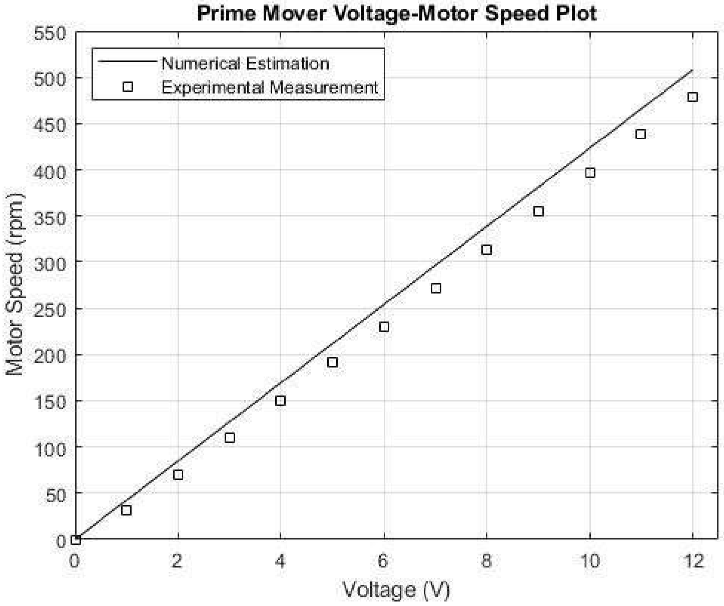

Figure 8. Rotational speed of the PMDC motor under varying input voltages.

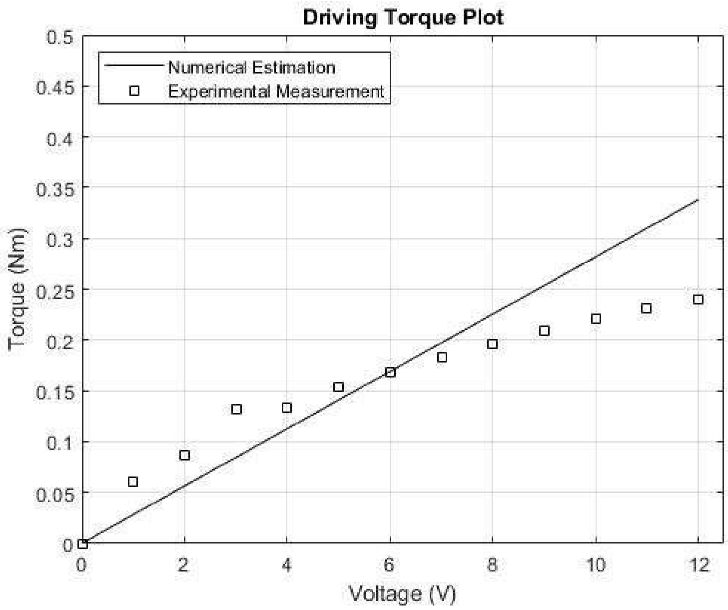

Figure 9. Torque comparison at different input voltages between numerical estimation and experimental measurements.

In summary, as it is represented the influence of the gearhead on the performance of the PMDC motor. The presence of the gearhead leads to discrepancies between the estimated values from numerical analysis and the measurements during experimental testing, especially at lower input voltages. Understanding the impact of the gearhead on PMDC motor output is important for accurately assessing the performance of the hydrokinetic turbine model and optimizing its design and efficiency.

3.2. Modified experimental setup

In this section, we revise the dynamometer characterization testing with a focus on magnetic coupling as shown in **Figure 10**. The primary objective of this revised testing is to determine the characteristic parameters of a PMDC motor configured for use as a small-scale experimental hydrokinetic turbine. Unlike the initial design, the dynamometer now features a redesigned magnetic coupling to address previous issues related to leakage. The fundamental principle remains unchanged, with the PMDC motor serving as a prime mover connected shaft-to-shaft to an identical PMDC motor configured as a generator.

The dynamometer's behavior is governed by Kirchhoff's voltage law, considering identical armature resistors, armature inductances, angular speeds, and torques in both the power and load circuits. The power circuit equation is given by:

Power circuit:

$$E_a = R_a i_a(t) + L_a \frac{di_a(t)}{dt} + K_e \omega(t) \tag{43}$$

Load circuit:

$$E_b = R_a i_b(t) + L_b \frac{di_b(t)}{dt} + K_e i_b(t) \tag{44}$$

where R is the variable resistor (Ω) and i_b is the generated current (A). In the case of a constant operating point, these equations can be simplified as follows:

Power circuit:

$$E_a = R_a i_a + K_e \omega \tag{45}$$

Load circuit:

$$K_e \omega = (R_a + R) i_b \tag{46}$$

To enhance accuracy, a specific experimental setup is employed, incorporating two identical PMDC motors. The connection of PMDC motors, a variable DC voltage source, gearhead for speed adjustment, rotary torque sensor, and a servo motor driver is maintained from the initial design. The key modification is the introduction of a redesigned magnetic coupling to address leakage issues and enhance system reliability.

This setup ensures precise control over the prime mover's speed and allows for comprehensive data collection on torque, speed, and electrical characteristics.

Let's talk about impact of magnetic coupling. The introduction of the magnetic coupling into the system has a subtle impact on the overall performance. One notable effect is a slight reduction in the rotational speed when compared to both the initial dry test and the numerical results as shown in **Figure 11**.

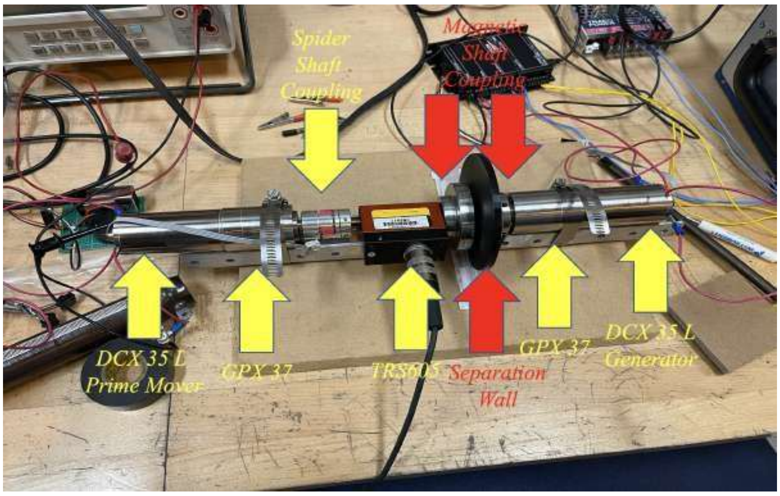

Figure 10. Revised experimental setup.

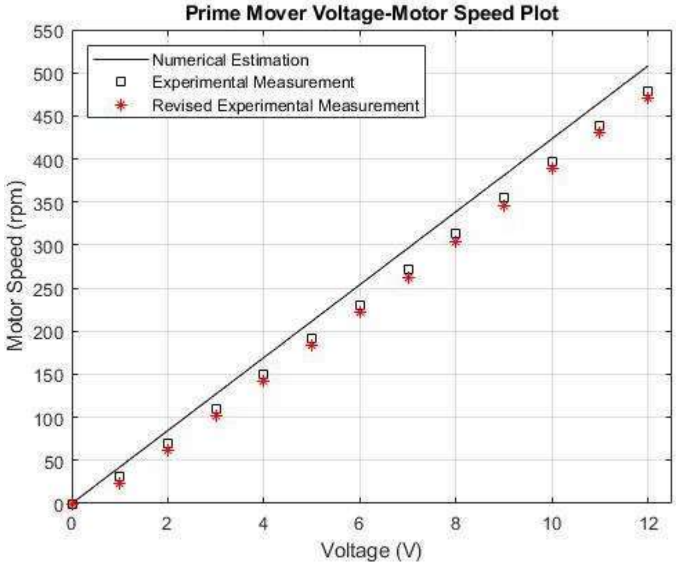

Figure 11. Detailed comparative analysis of revised prime mover voltage-motor speed.

The incorporation of the magnetic coupling into the system has led to a marginal decrease in both the generated current (**Figure 12**) and generated torque (**Figure 13**) in comparison to the initial dry test. This outcome aligns with expectations, considering the observed reduction in rotational speed.

The introduction of a magnetic coupling in the system, while resulting in a minor reduction in overall performance, is deemed essential due to its pivotal role in preventing shaft leakage—a critical issue faced in the initial design. The compromise in performance, evidenced by a slight decrease in rotational speed, generated current, and torque, serves as a trade-off for the enhanced system integrity achieved through the magnetic coupling's ability to seal the shaft. In marine applications, where exposure to corrosive elements is a significant concern, the magnetic coupling proves invaluable by providing a hermetic seal without the need for traditional seals susceptible to wear and corrosion. The technology's benefits include reduced maintenance, enhanced reliability, and resistance to corrosion, positioning magnetic couplings as crucial components in marine systems, aligning with the imperative for robust and durable solutions in challenging environments.

We addressed the nacelle redesign and reconstruction following the initial experiment, as detailed in [37]. During this experiment, a leakage issue was identified around the propeller pipe, indicating that water was escaping from the area surrounding the propeller. This leakage posed a risk to the experiment's integrity and the turbine's functionality for further research. To resolve this issue, a magnetic coupling was implemented through the shaft. A magnetic coupling is a mechanism that transfers torque between two rotating shafts without direct physical contact, making it ideal for applications requiring a water-tight seal. It effectively prevents fluid leakage such that it enhances the system's reliability.

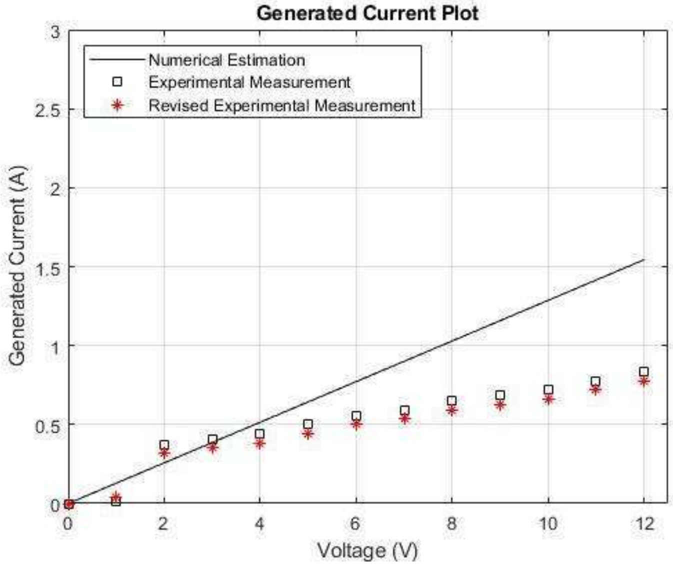

Figure 12. Detailed comparative analysis of revised generated current measurements.

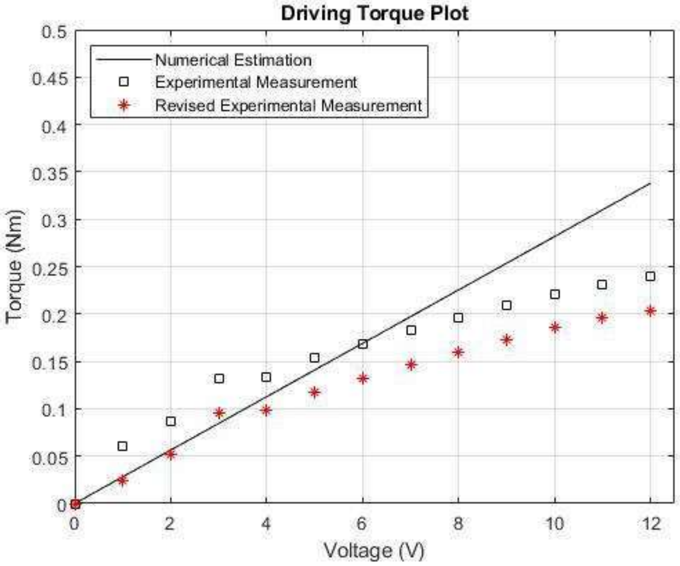

Figure 13. Detailed comparative analysis of revised torque measurements.

The next step involved redesigning the nacelle, specifically the torpedo component, to accommodate this solution and ensure water-tightness. This redesign included dividing the torpedo nacelle into two distinct segments:

- Wet Department: This segment houses the components that are exposed to water, including the propeller and the magnetic coupling mechanism.
- Dry Department: This segment is designed to remain dry and houses components that should not be exposed to water, such as electrical components or sensors.
- Wall Installation: A key feature of this redesign is the installation of a wall between the wet and dry departments of the torpedo nacelle. The magnetic coupling is placed within this wall, between the wet and dry departments. This positioning allows the magnetic coupling to function effectively while preventing any water from entering the dry department.

The wall acts as a barrier, effectively sealing off the wet department from the dry department. **Figure 14 (a)** shows the sketch of the wet part of the torpedo and **Figure 14 (b)** shows the sketch of front wall barrier of the nacelle. It ensures that any leakage from the propeller pipe is contained within the wet department and does not affect the dry components. The redesign was specifically implemented in the front piece of the torpedo nacelle. This piece was split into two parts, and the wall was inserted between them to create the separation between the wet and dry departments.

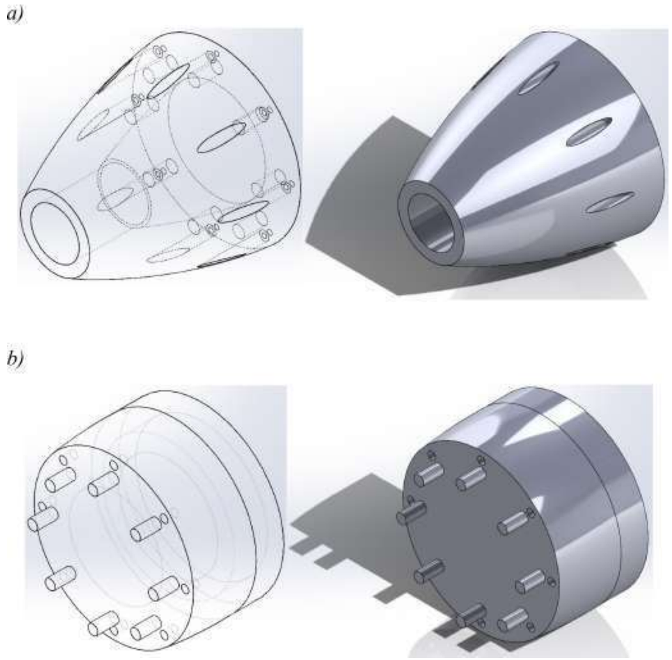

Figure 14. (a) Solidworks sketch of the wet part of the torpedo and; **(b)** solidworks sketch of the wall barrier of the front piece of nacelle.

The modification involved the use of a magnetic coupling and the redesign of the torpedo nacelle to prevent water leakage from the propeller pipe. The installation of a wall between the wet and dry departments, particularly in the front piece of the torpedo, ensures that the magnetic coupling can function as intended while maintaining a water-tight seal, enhancing the overall integrity of the experiment and data collection process. In continuity with our prior work, we implemented identical steps to augment water-tightness and mitigate the risk of leakage in the redesigned model. Employing the same procedural framework as in the previous test, the entire model underwent a thorough coating with epoxy, a robust adhesive and sealant known for its exceptional waterproofing properties as shown in **Figure 15**. This epoxy application, constituting an additional protective layer, substantially reinforces the system against water ingress. The approach mirrors the effective strategy employed during the initial test. The application of epoxy continues to serve as a resilient shield, contributing to the model’s durability and reliability.

Revised printed parts

Revised nacelle coated with epoxy

Figure 15. Revised design of nacelle coated with epoxy and its parts.

4. Results and discussion

For this round of testing, we continued using the same instrumentation as in our previous trials with a key modification in the coupling mechanism. The hydrokinetic turbine model integrates an electric motor capable of functioning as a generator, accompanied by an array of sensors, all housed within the insert. Specifically, we employed a PMDC motor of the DCX 35 L type, boasting a power rating ranging from 80 to 120 Watts, as the motor/generator.

To exert precise control over its operation, the PMDC motor was linked to a driver, facilitating regulation of the motor's speed. A variable DC voltage source, connected to the driver, was employed to adjust the motor speed by varying the input voltage. The motor, with a speed rating of 8130 RPM, was paired with a planetary gearhead (GPX 37) featuring a reduction ratio of 16:1 to accommodate the scaled-down size of the turbine model. This gearhead choice was imperative due to the model's constraint on rotational speed.

In the experimental setup, consistent with our prior work, a range of sensors and equipment was integrated to measure and control various parameters of the hydrokinetic turbine system. Notable instruments included the TRS605 Rotational Force Sensor, serving to precisely gauge driving torque and turbine rotational speed. The ESCON 50/5 Servo Controller, a motor driver, maintained a setpoint rotational speed and adjusted it as required during testing. Current sensors (ACS712) and voltage sensors (DC0-25V) were employed to measure electrical power generation, crucial for computing the generated power. Additionally, temperature and humidity sensors, consisting of SHT30 and DHT22 types, were strategically placed for safety and performance monitoring within the turbine nacelle.

Despite maintaining the consistency of the overall instrumentation from our previous testing, the magnetic coupling replaced the Spyder coupling in the current setup. The integrated sensors and equipment are visually represented in **Figure 16**.

The evaluation of hydrodynamic characteristics for the hydrokinetic turbine involved a systematic process closely mirroring our prior testing methodology. Before initiating experiments, precise positioning of the turbine model within the towing tank ensured optimal alignment and a watertight seal. Subsequently, the turbine underwent towing at a predetermined speed, capturing vital data through installed sensors measuring torque and speed. This approach provided valuable insights into the turbine's performance under varying flow conditions.

Notably, the methodology employed in this testing phase, featuring a magnetic coupling, replicated the exact procedure utilized in previous tests. Emphasizing continuity, we maintained identical numerical values to ensure a meticulous repetition of our prior experiments. **Figure 17** visually illustrates the prototype turbine submerged in the towing tank, showcasing the consistent application of our established testing protocol.

In our nacelle redesign experiments using magnetic coupling, we apply the same protocol as in previous tests. **Figure 18 (a)** compares torque results and **Figure 18 (b)** compares power results by plotting data from three different methods: The solid line represents the numerical method using BEM theory, the black squares denote results from prior testing without magnetic coupling, and the red stars indicate measurements with magnetic coupling. The data reveal a consistent trend where, as carriage speed increases, the generated power also rises, aligning with the expectation that higher fluid speed delivers more energy to the turbine blades. Up to a carriage speed of 1.8 m/s, BEM simulations predicted slightly lower power generation compared to experiments, suggesting a possible underestimation of OCT performance by the simulations. However, beyond 2 m/s, BEM-calculated power exceeded experimental results. Discrepancies between experimental data and BEM simulations can come from several factors. One major issue may be measurement inaccuracies related to the experimental setup or the equipment used, which might not have been sufficiently precise. For instance, errors in sensor calibration or limitations in measurement resolution could contribute to these discrepancies. Also, BEM simulations might not fully capture the complex hydrodynamic effects observed in real OCTs, such as turbulence and three-dimensional flow effects, which are challenging to model accurately. These complex dynamics, particularly at varying flow speeds, might be inadequately represented by the BEM method. To sum up, the simulations may not fully reflect the actual hydrodynamic environment, leading to differences between simulated and experimental results as discussed in [60]. As noted in [60], future work might explore alternative turbine designs, materials, and sensor technologies to enhance hydrokinetic energy systems. Furthermore, measurements with the magnetic coupling exhibited slightly lower values compared to prior experimental measurements that can be attributed to the impact of the coupling on the system.

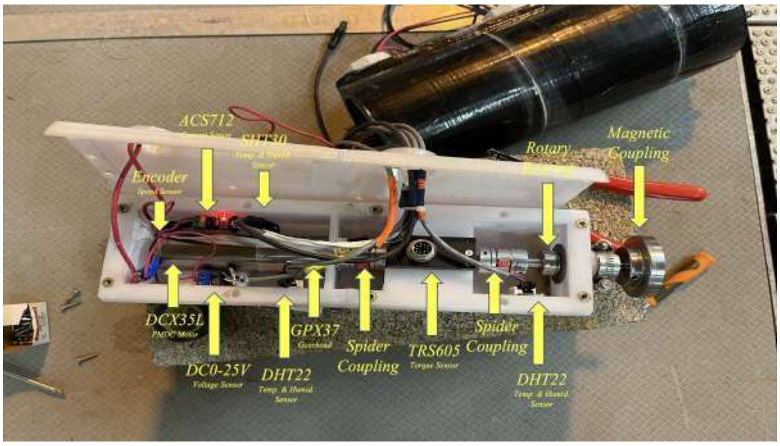

Figure 16. Electric instruments setup.

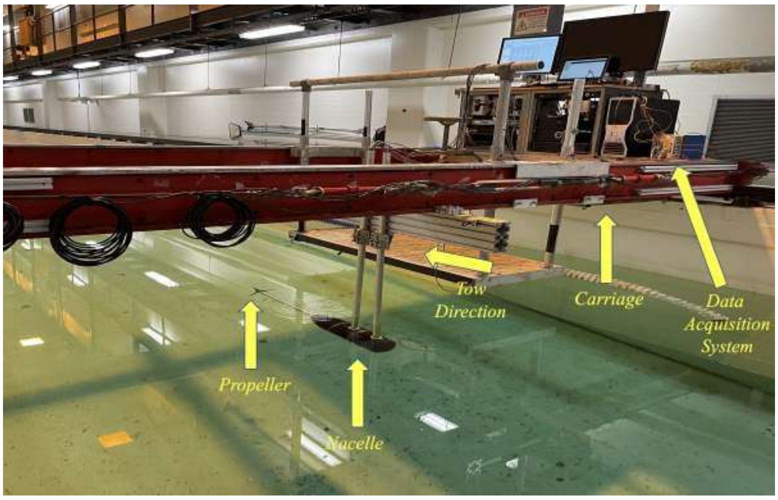

Figure 17. Photograph of the prototype turbine during the towing tank experiment.

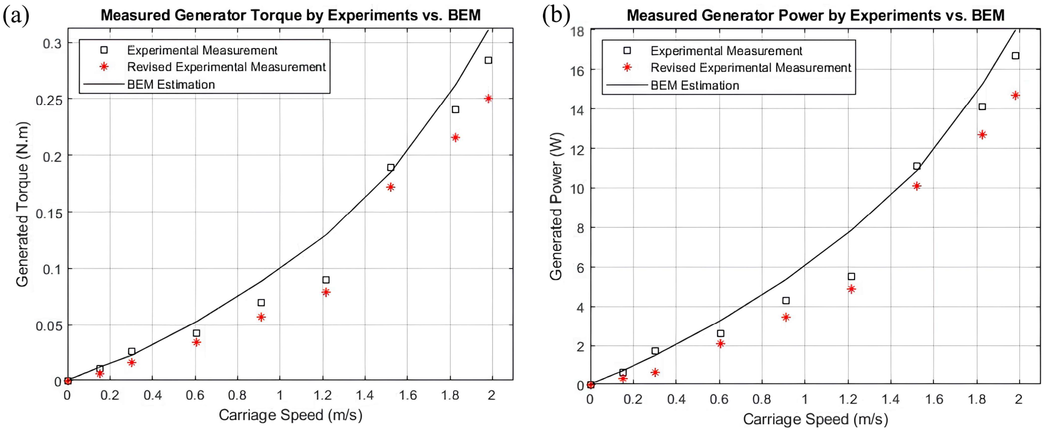

Figure 18. (a) Comparison of generated torque results and; **(b)** comparison of generated power results.

The proposed numerical method based on BEM theory shows the robustness through a strong match with experimental results and adaptability to real-world challenges as shown in [36]. Despite some discrepancies, primarily due to unmodeled hydrodynamic effects and measurement inaccuracies, the method accurately predicts power generation and hydrodynamic forces. It accounts for practical issues, such as the impact of a gear-head on motor speed and torque, and successfully incorporates magnetic couplings to address leakage issues, enhancing system reliability. The method's comprehensive approach that combines advanced simulations with detailed experimental testing, highlights its flexibility and precision. Furthermore, the study identifies areas for future optimization, such as refining simulations to better capture complex flow dynamics, ensuring the model remains robust and capable of continuous improvement in hydrokinetic turbine design.

The study could further explore how its results influence the design and deployment of full-scale OCTs in real-world marine environments. By addressing challenges like hydrodynamic inefficiencies and leakage, the study's insights into torque, speed, and magnetic couplings can optimize larger systems. The use of magnetic couplings enhances OCT durability and reliability in corrosive marine settings. Future research could focus on scaling up turbine designs and refining simulations to improve efficiency in different ocean conditions, advancing sustainable marine energy solutions. Also, we will include additional validation of the results such as comparisons with other established models or larger-scale testing.

5. Conclusions

This study represents a significant advancement in the development and evaluation of a small-scale horizontal OCT through the use of BEM simulations. By integrating a sophisticated mathematical model with practical experimental testing, we achieved precise calculations of hydrokinetic forces and gained a deeper understanding of small-scale turbine performance. The innovative approach of combining detailed simulations with marine-inspired dynamometer testing and a 3D-printed turbine model equipped with sensors enabled comprehensive monitoring of power, force, and rotational speed during towing tank tests. The good agreement between experimental results and BEM simulations highlights the robustness of the model, although some discrepancies were observed due to factors such as measurement accuracy and hydrodynamic effects. The successful redesign, which addressed previous leakage issues by incorporating magnetic coupling, has improved the reliability and longevity of testing, providing valuable insights into turbine performance across different speeds. In the future, we plan to refine our experimental methods, especially with the new nacelle design, and conduct broader studies to further optimize efficiency, applicability, and repeatability. This interdisciplinary research, combining advanced modeling, experimental techniques, and innovative design solutions, fosters future developments in hydrokinetic energy conversion. Also, this study could further explore how its results influence the design and deployment of full-scale OCTs in real-world marine environments. By addressing challenges like hydrodynamic inefficiencies and leakage, the study's insights into torque, speed, and magnetic couplings can optimize larger systems. The use of magnetic couplings enhances OCT durability and reliability in corrosive marine settings. Future research could focus on scaling up turbine designs and refining simulations to improve efficiency in different ocean conditions, advancing sustainable marine energy solutions.

Author contributions: Conceptualization, NIX and EA; methodology, SS, SR, NIX and EA; software, EA; validation, NIX, EA and SS; formal analysis, JI; investigation, SS and SR; resources, NIX and LB; data curation, SS and SR; writing—original draft preparation, NIX, SS and EA; writing—review and editing, NIX, EA and MT; visualization, SS, EA and MT; supervision, NIX, LB and EA; project administration, NIX and LB; funding acquisition, NIX and LB. All authors have read and agreed to the published version of the manuscript.

Funding: This research was funded by the National Science Foundation (NSF) and specifically the Energy, Power, Control and Networks (EPCN) program within the framework of grant ECCS-1809182.

Acknowledgments: The authors would like to thank the National Science Foundation (NSF) and specifically the Energy, Power, Control and Networks (EPCN) program for their valuable ongoing support in this research within the framework of grant ECCS-1809182 'Collaborative Research: Design and Control of Networked Offshore Hydrokinetic Power-Plants with Energy Storage'. We express our deepest thanks to George R. Morrissey and Ryan D. Thiel for their outstanding contributions and the positive impact they have had on our research endeavors. Their invaluable guidance, technical assistance, and collaborative spirit have been integral to the success of our project.

Conflict of interest: The authors declare no conflict of interest.

References

1. Boehlert G, Gill A. Environmental and Ecological Effects of Ocean Renewable Energy Development—A Current Synthesis. Oceanography. 2010; 23(2): 68–81. doi: 10.5670/oceanog.2010.46
2. Majdi Nasab N, Kilby J, Bakhtiaryfard L. The Potential for Integration of Wind and Tidal Power in New Zealand. Sustainability. 2020; 12(5): 1807. doi: 10.3390/su12051807
3. Stevens CL, Smith MJ, Grant B, et al. Tidal energy resource complexity in a large strait: The Karori Rip, Cook Strait. Continental Shelf Research. 2012; 33: 100–109. doi: 10.1016/j.csr.2011.11.012
4. Lewis M, Neill SP, Robins PE, et al. Resource assessment for future generations of tidal-stream energy arrays. Energy. 2015; 83: 403–415. doi: 10.1016/j.energy.2015.02.038
5. Fox CJ, Benjamins S, Masden EA, et al. Challenges and opportunities in monitoring the impacts of tidal-stream energy devices on marine vertebrates. Renewable and Sustainable Energy Reviews. 2018; 81: 1926–1938. doi: 10.1016/j.rser.2017.06.004
6. Brooks DA. The tidal-stream energy resource in Passamaquoddy–Cobscook Bays: A fresh look at an old story. Renewable Energy. 2006; 31(14): 2284–2295. doi: 10.1016/j.renene.2005.10.013
7. El-Shahat SA, Li G, Lai F, et al. Investigation of parameters affecting horizontal axis tidal current turbines modeling by blade element momentum theory. Ocean Engineering. 2020; 202: 107176. doi: 10.1016/j.oceaneng.2020.107176
8. Rahimian M, Walker J, Penesis I. Performance of a horizontal axis marine current turbine– A comprehensive evaluation using experimental, numerical, and theoretical approaches. Energy. 2018; 148: 965–976. doi: 10.1016/j.energy.2018.02.007
9. Dehouck V, Lateb M, Sacheau J, et al. Application of the Blade Element Momentum Theory to Design Horizontal Axis Wind Turbine Blades. Journal of Solar Energy Engineering. 2018; 140(1). doi: 10.1115/1.4038046
10. Bahaj AS, Batten WMJ, McCann G. Experimental verifications of numerical predictions for the hydrodynamic performance of horizontal axis marine current turbines. Renewable Energy. 2007; 32(15): 2479–2490. doi: 10.1016/j.renene.2007.10.001
11. Nachtane M, Tarfaoui M, Goda I, et al. A review on the technologies, design considerations and numerical models of tidal current turbines. Renewable Energy. 2020; 157: 1274–1288. doi: 10.1016/j.renene.2020.04.155

12. Ng KW, Lam WH, Ng KC. 2002–2012: 10 Years of Research Progress in Horizontal-Axis Marine Current Turbines. Energies. 2013; 6(3): 1497–1526. doi: 10.3390/en6031497
13. Vogel CR, Willden RHJ, Houlsby GT. Blade element momentum theory for a tidal turbine. Ocean Engineering. 2018; 169: 215–226. doi: 10.1016/j.oceaneng.2018.09.018
14. Wekesa DW, Wang C, Wei Y, et al. Experimental and numerical study of turbulence effect on aerodynamic performance of a small-scale vertical axis wind turbine. Journal of Wind Engineering and Industrial Aerodynamics. 2016; 157: 1–14. doi: 10.1016/j.jweia.2016.07.018
15. Bottasso CL, Campagnolo F, Petrović V. Wind tunnel testing of scaled wind turbine models: Beyond aerodynamics. Journal of Wind Engineering and Industrial Aerodynamics. 2014; 127: 11–28. doi: 10.1016/j.jweia.2014.01.009
16. Devinant P, Laverne T, Hureau J. Experimental study of wind-turbine airfoil aerody-namics in high turbulence. Journal of Wind Engineering and Industrial Aerodynamics. 2020; 90(6): 689–707.
17. Bayati I, Belloli M, Bernini L, et al. Aerodynamic design methodology for wind tunnel tests of wind turbine rotors. Journal of Wind Engineering and Industrial Aerodynamics. 2017; 167: 217–227. doi: 10.1016/j.jweia.2017.05.004
18. Hansen M. Aerodynamics of Wind Turbines. Routledge; 2015
19. Wilson RE, Lissaman PBS. Applied Aerodynamics of Wind Power Machines. Renewable Energy. 2018: 71–120. doi: 10.4324/9781315793245-89
20. Burton T, Jenkins N, Sharpe D, et al. Wind energy handbook. John Wiley & Sons; 2011.
21. Manwell JF, McGowan JG, Rogers AL. Wind energy explained: theory, design and application. John Wiley & Sons; 2010.
22. Letcher TM. Wind energy engineering: a handbook for onshore and offshore wind turbines. Elsevier; 2023. pp. 3–10.
23. Molland AF, Turnock SR, Hudson DA. Ship resistance and propulsion. Cambridge university press; 2017.
24. Paraschivoiu I. Wind turbine design: with emphasis on Darrieus concept. Presses inter Polytechnique; 2002.
25. Pacheco A, Ferreira Ó. Hydrodynamic changes imposed by tidal energy converters on extracting energy on a real case scenario. Applied Energy. 2016; 180: 369–385. doi: 10.1016/j.apenergy.2016.07.132
26. Atcheson M, MacKinnon P, Elsaesser B. A large scale model experimental study of a tidal turbine in uniform steady flow. Ocean Engineering. 2015; 110: 51–61. doi: 10.1016/j.oceaneng.2015.09.052
27. Malki R, Williams AJ, Croft TN, et al. A coupled blade element momentum—Computational fluid dynamics model for evaluating tidal stream turbine performance. Applied Mathematical Modelling. 2013; 37(5): 3006–3020. doi: 10.1016/j.apm.2012.07.025
28. Mannion B, Leen SB, Nash S. Development and assessment of a blade element momentum theory model for high solidity vertical axis tidal turbines. Ocean Engineering. 2020; 197: 106918. doi: 10.1016/j.oceaneng.2020.106918
29. Faudot C, Dahlhaug OG. Prediction of Wave Loads on Tidal Turbine Blades. Energy Procedia. 2012; 20: 116–133. doi: 10.1016/j.egypro.2012.03.014
30. Zhu FW, Ding L, Huang B, et al. Blade design and optimization of a horizontal axis tidal turbine. Ocean Engineering. 2020; 195: 106652. doi: 10.1016/j.oceaneng.2019.106652
31. Wang L, Liu X, Renevier N, et al. Nonlinear aeroelastic modelling for wind turbine blades based on blade element momentum theory and geometrically exact beam theory. Energy. 2014; 76: 487–501. doi: 10.1016/j.energy.2014.08.046
32. Sun Z, Chen J, Shen WZ, et al. Improved blade element momentum theory for wind turbine aerodynamic computations. Renewable Energy. 2016; 96: 824–831. doi: 10.1016/j.renene.2016.05.035
33. Batten WMJ, Harrison ME, Bahaj AS. Accuracy of the actuator disc-RANS approach for predicting the performance and wake of tidal turbines. Philosophical Transactions of the Royal Society A: Mathematical, Physical and Engineering Sciences. 2013; 371(1985): 20120293. doi: 10.1098/rsta.2012.0293
34. Guillou SS, Thie´bot J, Santa Cruz A, et al. Modelling turbulence with an actuator disk representing a tidal turbine. Renewable Energy. 2016; 97: 625–635. doi: 10.1016/j.renene.2016.06.014
35. Du L, Ingram G, Dominy RG. A review of H-Darrieus wind turbine aerodynamic research. Proceedings of the Institution of Mechanical Engineers, Part C: Journal of Mechanical Engineering Science. 2019; 233(23–24): 7590–7616. doi: 10.1177/0954406219885962
36. Sadeqi S, Xiros N, Aktosun E, et al. Power Estimation of an Experimental Ocean Current Turbine Based on the Conformal Mapping and Blade Element Momentum Theory. American Society of Mechanical Engineers. 2021; 7B. doi: 10.1115/imece2021-71751

37. Rouhi S, Xiros N, Aktosun E, et al. A Small-Scale Experimental Ocean Current Turbine Apparatus for Power Measurement. American Society of Mechanical Engineers. 2021; 7B. doi: 10.1115/imece2021-71754
38. Rouhi S, Sadeqi S, Xiros N, et al. Applying Artificial Intelligence to Optimize Small-Scale Ocean Current Turbine Performance. Volume 5: Dynamics, Vibration, and Control. American Society of Mechanical Engineers. 2022; 7B. doi: 10.1115/imece2022-95804
39. Sadeqi S, Rouhi S, Xiros N, et al. Numerical Investigation of an Experimental Ocean Current Turbine Based on Blade Element Momentum Theory (BEM). American Society of Mechanical Engineers. 2021; 9. doi: 10.1115/omae2021-63010
40. Flickinger KN. Facility development for testing small scale horizontal axis wind turbines. PennState University Libraries; 2013.
41. Burdett TA. Aerodynamic design considerations for small-scale, fixed-pitch, horizontal-axis wind turbines operating in class 2 winds [PhD thesis]. Baylor University; 2012.
42. Musial W, McNiff B. Wind turbine testing in the nrel dynamometer test bed. National Renewable Energy Lab. (NREL), Golden, CO (United States); 2000.
43. Mohanty B, Wang F, A. Stelson K. Design of a Power Regenerative Hydrostatic Wind Turbine Test Platform. JFPS International Journal of Fluid Power System. 2019; 11(3): 130 – 135. doi: 10.5739/jfpsij.11.130
44. Mohanty B, Stelson KA. Dynamics and Control of an Energy-Efficient, Power-Regenerative, Hydrostatic Wind Turbine Dynamometer. Energies. 2022; 15(8): 2868. doi: 10.3390/en15082868
45. Corbus D, Baring-Gould I, Drouilhet S, et al. Small wind turbine testing and applications development. National Renewable Energy Lab. (NREL), Golden, CO (United States); 1999.
46. Bahaj AS, Molland AF, Chaplin JR, et al. Power and thrust measurements of marine current turbines under various hydrodynamic flow conditions in a cavitation tunnel and a towing tank. Renewable Energy. 2007; 32(3): 407 – 426. doi: 10.1016/j.renene.2006.01.012
47. Duhaney J, Khoshgoftaar TM, Sloan JC, et al. A Dynamometer for an Ocean Turbine Prototype: Reliability through Automated Monitoring. In: Proceedings of the 2011 IEEE 13th International Symposium on High-Assurance Systems Engineering; 2011. pp. 244 – 251.
48. Eriksson S, Bernhoff H, Leijon M. Evaluation of different turbine concepts for wind power. Renewable and Sustainable Energy Reviews. 2008; 12(5): 1419 – 1434. doi: 10.1016/j.rser.2006.05.017
49. Hsiao FB, Bai CJ, Chong WT. The Performance Test of Three Different Horizontal Axis Wind Turbine (HAWT) Blade Shapes Using Experimental and Numerical Methods. Energies. 2013; 6(6): 2784 – 2803. doi: 10.3390/en6062784
50. Viterna LA, Janetzke DC. Theoretical and Experimental Power from Large Horizontal-Axis Wind Turbines. Office of Scientific and Technical Information (OSTI); 1982.
51. Bai CJ, Wang WC. Review of computational and experimental approaches to analysis of aerodynamic performance in horizontal-axis wind turbines (HAWTs). Renewable and Sustainable Energy Reviews. 2016; 63: 506 – 519. doi: 10.1016/j.rser.2016.05.078
52. Kishinami K, Taniguchi H, Suzuki J, et al. Theoretical and experimental study on the aerodynamic characteristics of a horizontal axis wind turbine. Energy. 2005; 30(11 – 12): 2089 – 2100. doi: 10.1016/j.energy.2004.08.015
53. Pope K, Dincer I, Naterer GF. Energy and exergy efficiency comparison of horizontal and vertical axis wind turbines. Renewable Energy. 2010; 35(9): 2102 – 2113. doi: 10.1016/j.renene.2010.02.013
54. Lee MH, Shiah YC, Bai CJ. Experiments and numerical simulations of the rotor-blade performance for a small-scale horizontal axis wind turbine. Journal of Wind Engineering and Industrial Aerodynamics. 2016; 149: 17 – 29. doi: 10.1016/j.jweia.2015.12.002
55. Rouhi S, Xiros NI, Sadeqi S, et al. Dynamometer Testing of Hydrokinetic Turbines in a Towing Tank Facility. American Society of Mechanical Engineers. 2023; 6: V006T07A097. doi: 10.1115/imece2023-112837
56. Hasankhani A, VanZwieten J, Tang Y, et al. Modeling and Numerical Simulation of a Buoyancy Controlled Ocean Current Turbine. International Marine Energy Journal. 2021; 4(2): 47 – 58. doi: 10.36688/imej.4.47-58
57. Jackson RS, Amano R. Experimental Study and Simulation of a Small-Scale Horizontal-Axis Wind Turbine. Journal of Energy Resources Technology. 2017; 139(5). doi: 10.1115/1.4036051
58. Encarnacion JI, Johnstone C, Ordonez-Sanchez S. Design of a Horizontal Axis Tidal Turbine for Less Energetic Current Velocity Profiles. Journal of Marine Science and Engineering. 2019; 7(7): 197. doi: 10.3390/jmse7070197

59. Lotfy K, Mahdy AMS, El-Bary AA, et al. Magneto-Photo-Thermoelastic Excitation Rotating Semiconductor Medium Based on Moisture Diffusivity. Computer Modeling in Engineering & Sciences. 2024; 141(1): 107 – 126. doi: 10.32604/cmes.2024.053199
60. Rouhi S, Sadeqi S, Xiros NI, et al. Development of Mathematical Model for Coupled Dynamics of Small-Scale Ocean Current Turbine and Generator to Optimize Hydrokinetic Energy Harvesting Applications. Applied Sciences. 2024; 14(16): 7164. doi: 10.3390/app14167164

Mechanical Engineering Advances 2024, 2(2), 1752.
https://doi.org/10.59400/mea.v2i2.1752

Article

Influence of the new wavy teat liner "Stimulor StressLess" on milk yield performance and its quality in dairy cows: Results of a field study

Shehadeh Kaskous[1,*], Khaled Al-Najjar[2], Michael W. Pfaffl[3]

[1] Department of Research and Development, Siliconform, 86842 Türkheim, Germany
[2] General Commission for Scientific Agricultural Research, GCSAR, Damascus 12573, Syria
[3] Department of Animal Physiology and Immunology, School of Life Sciences, Technical University of Munich, 85354 Freising, Germany
*** Corresponding author:** Shehadeh Kaskous, skaskous@siliconfrom.com

CITATION

Kaskous S, Al-Najjar K, Pfaffl MW. Influence of the new wavy teat liner "Stimulor StressLess" on milk yield performance and its quality in dairy cows: Results of a field study. Mechanical Engineering Advances. 2024; 2(2): 1752. https://doi.org/10.59400/mea.v2i2.1752

ARTICLE INFO

Received: 20 September 2024
Accepted: 31 October 2024
Available online: 21 November 2024

Abstract: The ideal milking system meets the physiological needs of dairy cows to increase milk yield, achieve better milk quality and maintain healthy udders. Therefore, the settings of the milking machine and the properties of the teat cup liners are very important on dairy farms. The aim of the present study was to test a new teat cup liner "Stimulor StressLess" (SSL) in two commercial dairy farms and to investigate its influence on daily milk production and quality having different experimental settings. For this purpose, 40 dairy cows of different breeds in Tirol, Austria (farm 1) were investigated for 6 months, where 3 months represent the control phase (Gr 1) and milked with conventional teat liners, and the second 3 months phase (Gr 2) was the experimental phase and milked with SSL teat cup liners. On the second farm 90 dairy cows of Simmental breed in Baden-Württemberg, Germany (farm 2) were examined for one year equally divided in the first 6 months of control phase and second 6 months of treatment phase. All cows on both farms had the same stage of lactation and lactation number. During the study period, the daily milk production of each cow was recorded and milk samples were collected to determine the ingredients. The results showed that higher daily milk production and better milk quality were observed after using the new SSL teat cup liner in the existing milking machines. However, the use of the new teat cup liner SSL was more efficient in the longer treatment in farm 2 than in farm 1. In addition, after the use of the new SSL teat cup liner, the udders remained healthy throughout the study period, showing lower somatic cell counts (SCC). It can be concluded that high milk yield and better milk quality can be achieved by using SSL teat cup liners, as they are adapted to all teat shapes and dimensions.

Keywords: dairy cows; fat; lactose; liner; protein; SCC; Stimulor StressLess; teat cup; urea

1. Introduction

The aim of the milking machine is to remove the milk completely and quickly from the udder and to keep the cows healthy. To optimally fulfil this task, the characteristics of the milking machine and the milking process play an important role [1]. Many studies have shown that the shape of teat cup liners and milking machine settings have a significant impact on milking performance, milk quality, milking time, and udder health [2–7]. The teat cup liner is the sole component of the milking machine that is in direct contact with the animal [8]. Therefore, it must perfectly match the dimensions and shape of the teats in term of size, fit and material properties to ensure the best possible performance for long-term safe and efficient milking [9]. In addition, the head piece should ensure a good seal with the teat base without restricting the connection between the mammary gland and teat cistern [10]. However, the dimensions of the teat cup liners must be tailored to the size of the teat so that they can be massaged effectively [11]. The most important of these measurements is the depth of the liner mouthpiece. Several pieces of evidence suggest that incorrectly used teat cup liners can lead to the following problems: 1) Adhesion problems of the teat cups, resulting in air slurping and falling off, 2) Increasing restlessness of the animals during milking, 3) Incomplete emptying of the udder, 4) Significant extension of milking time and, 5) Acute disorders of the teat condition after milking [6,9,10,12–14]. In addition, selecting the appropriate teat liner as well as the correct vacuum level and pulsation settings is very important to achieve the basic goals of fast, gentle, and complete milking [11,15]. There is an almost optimal milking machine available that corresponds to the physiological, anatomical, and morphological characteristics of the cow's udder. Its name is MultiLactor (ML) (Siliconform, Germany). ML is a semi-automatic milking system that is technically different from conventional milking machines, based on a quarter-individual milking system compared to conventional milking machines with claw piece [16–19]. In addition, ML is more efficient than conventional milking systems in terms of the positive stimulation effect, because ML has an established stimulation program optimize to the physiological needs of the milking cow [20]. The working vacuum level in the ML is 34 kPa compared to the conventional milking system with 45 kPa [17]. Furthermore, it is noteworthy that ML has an excellent cleaning and disinfection system after milking each cow and after milking all cows, compared to traditional milking machines that are only cleaned after milking all cows [21].

The teats of the cows in a herd have usually different sizes and shapes. Many farmers make a compromise when choosing teat cup liners for their cows. This can mean that teat cup liners seal too tightly on large and wide teats, while allowing air to enter on small and slim teats. Therefore, it is a challenge to find the right one with the best teat fitting [22]. However, there is currently a new teat cup liner on the market for all teat shapes and sizes (Stimulor StressLess, SSL, Siliconform, Germany) [6]. The wave-shaped construction of the SSL features an adaptive lip. This means that different teat sizes can be milked with the same teat liner [23]. This prevents excessive head vacuum, stops the sliding up of the teat cup and reduces stress on the teat tissues [24]. In other words, they are ideal for maintaining teat health during milking for all lactating cows. In this context, the objective of this study was to investigate the influence of liner design "Stimulor StressLess" in routine milking in two commercial dairy farms. We tested the hypothesis whether the new teat liner design affects udder health as well as milking performance and therefore daily milk yield and milk quality.

2. Material and methods

The experiments were carried out on commercial dairy farms in Tirol, Austria (farm 1) and Baden-Württemberg, Germany (farm 2), which is why the requirements of the animal protection laws of both countries were adhered to. The farms owners were informed about experimental procedures and gave informed consent.

2.1. Animals and housing

Farm 1: 40 dairy cows of different breeds (Brown Swiss, Simmental, and Holstein) were examined in two equal phases (called Gr 1 and Gr 2) of 3 months. The first phase of 3 months (Gr 1) was the control phase where animals were milked with MultiLactor milking system (Siliconform, Germany) and normal teat cup liner. The second phase, also 3 months (Gr 2), was the experimental phase, where animals were milked with MultiLactor milking system and SSL teat cup liners (**Figure 1**). Both phases were similar at the start of the experiment in term of milking day, number of lactations and daily milking performance (**Table 1**).

Table 1. Average daily milk yield, average days in milk and, average number of lactations in (Gr 1) and (Gr 2) of the dairy cows examined at baseline in farm 1.

Parameters farm 1	Control phase (Gr 1)	Experimental phase (Gr 2)
Number of animals	40	40
Daily milk yield (kg/day)	21.56	21.61
Days in milk (day)	164.96	162.15
Lactation number	2.60	2.63

The evaluation took place between July and December 2022. Both groups were subjected to the same nutritional and environmental conditions, housed in a free stall system. The supply of diet was grass-and corn-silage, hay, and concentrate, where all nutrients were adapted to the cow's lactation stage and milk yield. The ration mixture consisted of the following feedstuffs: grass silage: 45%, maize silage: 28%, hay: 14%, straw: 4%, rapeseed meal: 6%, grain maize: 2% and minerals: 0.9%. The water was provided ad libitum, and the chemical composition of the diet supplied to dairy cows met the required nutritional standards [25]. The animals were proved to be healthy throughout the course of the experiment.

Farm 2: 90 dairy cows of the Simmental breed were used and examined in two phases (Gr 1, Gr 2), like in farm 1. The first phase (6 months) (Gr 1) was the control phase and the animals were milked with a conventional milking system and normal teat cup liners. The second phase (6 months) (Gr 2) was the experimental phase and the animals were milked with a conventional milking system and SSL teat cup liners. Both animal phases were similar at the start of the experiment in terms of milking day, number of lactations and daily milking performance (**Table 2**).

Table 2. Average daily milk yield, average days in milk and, average number of lactations in Gr 1 and 2 of the dairy cows examined at baseline in farm 2.

Parameters farm 2	Control phase (Gr 1)	Experimental phase (Gr 2)
Number of animals	90	90
Daily milk yield (kg/day)	20.69	20.64
Days in milk (day)	140.02	138.73
Lactation number	3.03	3.05

The experiment took place between September 2022 and August 2023. The cows were kept in a loose housing system. All animals received the same compound feed ration (grass-and corn-silage, hay, and concentrate) depending on performance and maintenance requirements [25]. The ration mixture consisted of the following feedstuffs: grass silage: 38%, maize silage: 35%, hay: 11%, straw: 5%, rapeseed meal: 7%, grain maize: 3% and minerals: 0.9%. Drinking water was administered ad libitum. The animals were proved to be healthy throughout the course of the experiment.

2.2. Milking equipment

2.2.1. Properties of the teat liner "Stimulor StressLess" used in both farms

The new teat liners "Stimulor StressLess" have unique properties that are excellent for maintaining teat health during machine milking in all dairy cows [6]. One of its distinguishing features is the presence of a wave-shaped design of its mouthpiece, which allows it to adapt well to the different teat sizes in a herd, thus ensuring consistent milking of the entire herd. The wave designed of the lip reacts to the pressure difference in the liner and, if necessary, allows the outside air inlet to flow in to compensate. This prevents excessive head vacuum and reduces tissue stress. In addition, with this liner, the head vacuum will be kept stable in the physiological range, and the teats adhere particularly well and do not cause any slurry noise during milking. For dairy cows, this means protection of the sensitive teat tissue and more comfort when milking (**Figure 1**) [1].

Figure 1. Teat cup liners (Stimulor StressLess) used by the two farms for dairy cows.

2.2.2. Milking equipment and milking routine on farm 1

The experimental dairy cows (both phases) were milked twice daily (starting 5 AM and 4 PM) in a tandem milking parlour (2 × 3 places) equipped with MultiLactor (ML) milking system (Siliconform, Germany), based on a quarter-individual milking equipment. This means that teat cups work completely independently of each other (without a claw) (**Figure 2**). The working "vacuum" level was 36 kPa and sequential pulsation (25% offset quarter to quarter) was adopted. The pulsation rate was 60 cycles per minute and the pulsation ratio was 60/40 during the milking time. The milking process took place in both phases according to the usual routine on the farm. At the time of milking with ML the milking routine started with pre-milking preparations, which consisted of fore-stripping of one or two squirts of milk from each teat and then cleaning the udder and teats. After that, the milking unit swing directly in front of the cow's udder. The teats cups were pulled out of the storing individually or in pairs and manually attached to the teats. After this step, the system is started on the control display and the pre-stimulation began. The pre-stimulation is structured to be intensively activated with a normal pulse rate (60 cycles/min) and reduced the milking phase (b-phase) of 10% over a period of 50 s. At the same time, intensive movement of the teats cups is regulated as an additional stimulation by an actuator. This is an arm on which four milk tubes lie. During the pre-stimulation and the milking time, this arm moves up and down. This movement is transferred to the teats cups and vibrate the teats. When the milk flow reaches 250 g/min during milking, then the milking process automatically ends with the detachment of the milking unit and each teat is dipped with a solution containing Chlorhexidin. At the same time teat cups are cleaned and disinfected automatically with water and per acetic acid solution (0.5%) after each cow and milking.


(A) **(B)**

Figure 2. Milking parlor. **(A)** Milking cup with SSL teat liner; **(B)** multiLactor milking machine (Siliconform, Germany).

2.2.3. Milking equipment and milking routine on farm 2

Experimental dairy cows (both phases) were milked twice daily (starting 6:30 AM and 4:30 PM) in a steeply herringbone milking parlour (60 degrees) (2 × 10 places) equipped with conventional milking system. In this milking system, each milking unit consists of four teat cups and a claw piece. The working "vacuum" level was 40 kPa and alternating cyclic pulsation between the front and back were adopted. The pulsation rate was 60 cycles per minute and the pulsation ratio was 60/40 during the milking time. The milking process were performed according to the usual routine of the farm. At the time of milking the milking routine started with pre-milking preparations, which consisted of fore-stripping of one or two squirts of milk from each teat and then cleaning the udder and teats. After that, the teat cups were manually attached to the teats. The milking process was observed and if no milk came, the teat cup was removed and milking stopped. Each teat was then dipped in a chlorhexidine solution. It is noteworthy that in the first phase (Gr 1), in some animals, an additional piece was attached to the teat cup to prevent the teat cup from sliding up.

2.3. Recording of milk yield, taking of milk samples and analysis

Milk yield was recorded and milk samples (50 ml bottle) were collected monthly for qualitative analysis in both farms and groups Gr 1 and Gr 2 from each cow during the study period. The milk samples were preserved and then, they sent to the laboratory. The milk composition was determined by the Tiroler State control association, Innsbruck, Austria (farm 1) and in LKV Baden-Württemberg, Hohenstein, Germany (farm 2). The absolute values of fat (%), protein (%) and lactose (%) in the milk were determined by infrared-spectroscopy (MilkoScan, Foss, Denmark) and the somatic cell count (SCC) was determined by fluorescence optical counting (Fossomatic, Foss, Denmark). An infrared measurement with partial least-squares (PLS) calibration model was used to determine the urea in the milk. It should be mentioned at this point that no lactose was determined in the milk from farm 1.

2.4. Statistical analysis

Program SAS 9.3 was used for statistical evaluation in both farms [26]. GLM was used to determine the effect of the teat liner type on daily milk production, composition of cows according to the following linear models:

Model 1: $Y_{ij} = \mu + G_i + e_{ij}$, where, Y_{ij} =daily milk (kg), fat (%), protein (%), SCC, lactose (%), and urea of ij^{th} record. μ = overall mean. G_i = effect of i^{th} teat liner type coded as $i = 1$ (normal teat liner), and $i = 2$ (SSL teat liner). e_{ij} = random error term associated with Y_{ij} observations with zero mean and variance $I\sigma^2$e.

Model 2: $Y_{ij} = \mu + G_i(Ls)_j + e_{ij}$, where, $(Ls)_j$ = effect of j^{th} stage of lactation within teat liner type coded as $j = 1$ (< 100 days), $j = 2$ (101–200 days), and $j = 3$ (> 200 days).

Model 3: $Y_{ij} = \mu + G_i(Par)_j + e_{ij}$, where, $(Par)_j$= effect of j^{th} parity within teat liner type

coded as $j = 1, 2, ...,$ and 6 for first, second, ... and sixth, respectively.

Model 4: $Y_{ij} = \mu + G_i(scl)_j + e_{ij}$, where, $(scl)_j$ = effect of j^{th} somatic cell counts classes within teat liner type coded as $j = 1$ ($< 50 \times 10^3$), 2 (50×10^3–100×10^3), 3 (101×10^3–150×10^3), 4 (151×10^3–200×10^3), 5 (201×10^3–250×10^3), and 6 ($> 250 \times 10^3$). Since the number of animals on farm 1 was too small, the following somatic cell count classes were carried out. 1 ($< 50 \times 10^3$), 2 (50×10^3–100×10^3), 3 (101×10^3–150×10^3), 4 (151×10^3–300×10^3), 5 ($> 300 \times 10^3$).

To determine significant differences between least square means (LSM) of the group effects, Duncan's multiple range test was used. The results were presented as LSM ± SE.

3. Results

Since different milking systems were used on farm 1 and 2 in this field study, the results were treated separately for each farm.

3.1. Farm 1

3.1.1. General mean values of the examined parameters in Gr 1 and Gr 2

The results in **Table 3** showed that the daily milk yield in Gr 2 increased compared to the milk production in Gr 1 during the study period, but the increase was not significant ($P > 0.05$). Conversely, it was shown that the fat (%) and protein (%) increased significantly ($P < 0.001$) after using the new SSL teat cup liner (Gr 2) in comparison to Gr 1. The values were 4.31 ± 0.06% versus 4.03 ± 0.06% for fat and 3.83 ± 0.04% versus 3.51 ± 0.04% for protein in Gr 2 and Gr 1, respectively. It is noteworthy that after using a new SSL teat cup liner, the SCC in the milk decreased from 126.69 ± 23.24 × 10^3 to 95.06 ± 12.97 × 10^3 in Gr 1 and Gr 2, respectively, but the difference was not significant. According to the urea content in the milk, after using the new SSL teat cup liner (Gr 2), it was in the ideal concentration (15.03 ± 0.54 mg/dl) compared to Gr1 (24.98 ± 0.78 mg/dl).

Table 3. The average (LSM ± SE) of the milk parameters of the examined farm 1 during the investigation period.

Parameters farm 1	**Normal teat liner (Gr 1)**	**StressLess teat liner (Gr 2)**	**Significance (*p*-value)**
Milk yield (kg/day/animal)	21.57 ± 0.66	22.95 ± 0.61	0.1259
Fat (%)	4.03 ± 0.06	4.31 ± 0.06	0.0001
Protein (%)	3.51 ± 0.04	3.83 ± 0.04	0.0001
SCC (× 10^3 cells/ml)	126.69 ± 23.24	95.06 ± 12.97	0.2214
Urea (mg/dL)	24.98 ± 0.78	15.03 ± 0.54	0.0001

Gr 1: Milking the dairy cows with normal teat cup liners. Gr 2: Milking the dairy cows with SSL teat cup liners.

3.1.2. Examined milk parameters in Gr 1 and Gr 2 according to the stage of lactation

Figure 3 shows the tested milk parameters in Gr 1 and Gr 2 based on the lactation stage in farm 1. In all stages of lactation, daily milk production was numerically higher in Gr 2 than in Gr 1 after using the new teat liners (SSL). However, the difference was not significant ($P > 0.05$) (**Figure 3A**). After using a new SSL teat cup liner, a significant increase in milk fat % was observed in Gr 2 compared to Gr 1, in the first and second stages of lactation ($P < 0.05$; $P < 0.01$, respectively) (**Figure 3B**). Similar results were clearly observed for milk Protein (%), which was higher in Gr 2 than in Gr 1 in all lactation stages, and the difference was highly significant ($P < 0.001$) (**Figure 3C**). Regarding the urea content of the milk, it was found that after using the new SSL teat cup liner (Gr 2) a normal urea content (approx. 15 mg/dl) was observed compared to that during Gr 1 (**Figure 3D**). Although the SCC in Gr 2 was lower than in Gr 1 after using the new SSL teat liner, no significant difference was observed ($P > 0.05$) (**Figure 3E**).

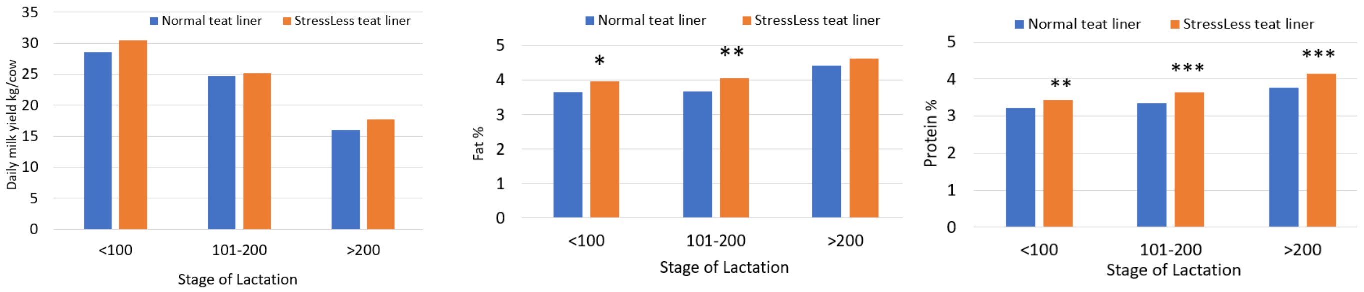

(A) **(B)** **(C)**

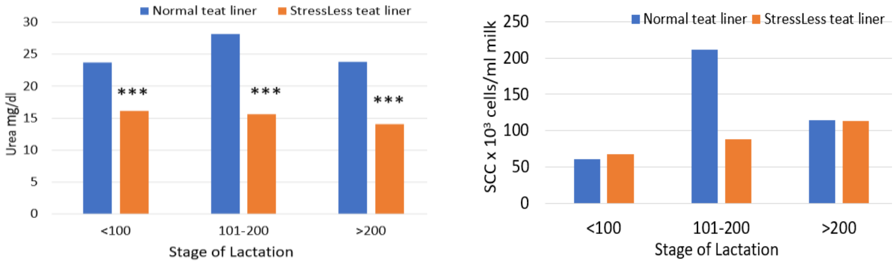

(D) **(E)**

Figure 3. Average (LSM) milk parameters in Gr 1 (normal teat cup liner) and Gr 2 (SSL teat cup liner) with significant differences (*p*-value): * $P < 0.05$, ** $P < 0.01$, *** $P < 0.001$, according to the stage of lactation in farm 1. **(A)** Daily milk yield (kg/cow); **(B)** fat (%); **(C)** protein (%); **(D)** urea (mg/dl); **(E)** somatic cell count (SCC) (× 10^3 cells/ml).

3.1.3. Examined milk parameters in Gr 1 and Gr 2 according to the lactation numbers

Table 4 showed that the daily milk production after using a new teat liner (SSL) in Gr 2 compared to Gr 1 was increased. However, the significant increase was only observed in the sixth lactation and above ($P < 0.05$). Interestingly, the fat content (%) in milk increased significantly in the first, third and fifth lactations in the Gr 2 compared to Gr 1. It is noteworthy that the protein content (%) of milk increased significantly in Gr 2 compared to Gr 1 at all lactation numbers ($P < 0.05$). Current results on the cell count in milk after use of a new teat liner (Gr 2) showed no significant differences ($P > 0.05$) in all lactation numbers compared to (Gr 1). The results for the urea concentrations in the milk showed better values after using new teat cup liner (Gr 2) compared to Gr 1. However, the difference was significant only in the first, second and third lactation numbers.

Table 4. The average (LSM ± SE) milk parameters of the examined farm 1 in the investigation period according to lactation numbers and significances (*p*-values).

Parameters	**Group**	**Lactation number**					
		1 (29)*	**2 (25)**	**3 (21)**	**4 (18)**	**5 (14)**	**≥ 6 (13)**
Milk yield (kg/day/cow)	Gr 1	15.49 ± 0.69	21.44 ± 0.93	25.73 ± 0.93	24.07 ± 0.58	23.80 ± 0.88	22.93 ± 0.82
	Gr 2	16.19 ± 0.48	22.09 ± 0.88	26.40 ± 0.89	25.14 ± 0.57	25.15 ± 0.74	24.45 ± 0.74
significance		0.4155	0.6136	0.6311	0.6592	0.0659	0.0256
Fat (%)	Gr 1	4.16 ± 0.14	4.12 ± 0.09	3.72 ± 0.11	4.07 ± 0.12	4.23 ± 0.22	3.73 ± 0.10
	Gr 2	4.77 ± 0.17	4.28 ± 0.09	4.21 ± 0.09	4.68 ± 0.29	4.71 ± 0.03	4.03 ± 0.16
significance		0.0134	0.2235	0.0009	0.1747	0.0496	0.2145
Protein (%)	Gr 1	3.52 ± 0.52	3.57 ± 0.06	3.37 ± 0.05	3.51 ± 0.10	3.35 ± 0.06	3.52 ± 0.06
	Gr 2	4.11 ± 0.09	3.84 ± 0.07	3.71 ± 0.06	4.06 ± 0.13	4.02 ± 0.03	3.87 ± 0.02
significance		0.0001	0.0048	0.0004	0.0282	0.0001	0.0013
SCC (× 10^3 cells/ml)	Gr 1	92.33 ± 15.31	111.28 ± 31.19	132.04 ± 36.67	126.67 ± 21.73	134.67 ± 22.10	167.67 ± 19.91
	Gr 2	84.33 ± 11.83	78.09 ± 13.42	115.20 ± 32.70	86.00 ± 16.37	90.25 ± 5.34	153.50 ± 16.80
significance		0.7348	0.3277	0.7468	0.1952	0.1721	0.6166

Table 4. (*Continued*).

Parameters	Group	Lactation number					
		1 (29)*	2 (25)	3 (21)	4 (18)	5 (14)	≥ 6 (13)
Urea (mg/dl)	Gr 1	21.22 ± 1.76	25.83 ± 0.10	24.25 ± 1.74	32.67 ± 1.84	26.33 ± 0.38	26.33 ± 0.13
	Gr 2	10.67 ± 2.00	15.12 ± 0.79	15.52 ± 0.90	18.20 ± 2.06	18.00 ± 3.49	11.00 ± 2.65
significance		0.0012	0.0001	0.0001	0.0848	0.1568	0.0718

Gr 1: Milking the dairy cows with normal teat cup liners. Gr 2: Milking the dairy cows with SSL teat cup liners. * The number in brackets indicates the number of milk samples in each group within each lactation number.

3.1.4. Somatic cell classes in Gr1 and Gr2 during the study period

The results of the statistical analysis clearly showed that after using the new teat cup liner, the cell count content of the milk was lower compared to before (**Figure 4**). This means that 80% of the milk samples after using the new teat cup liner (Gr 2) were below 100 × 10^3 cells/ml compared to Gr 1 (69%). Furthermore, it was observed that after using the new teat cup liner, only 12.48% of milk samples were above 150 × 10^3 cells/ml compared to Gr 1 (18.26%) (**Figure 4**).

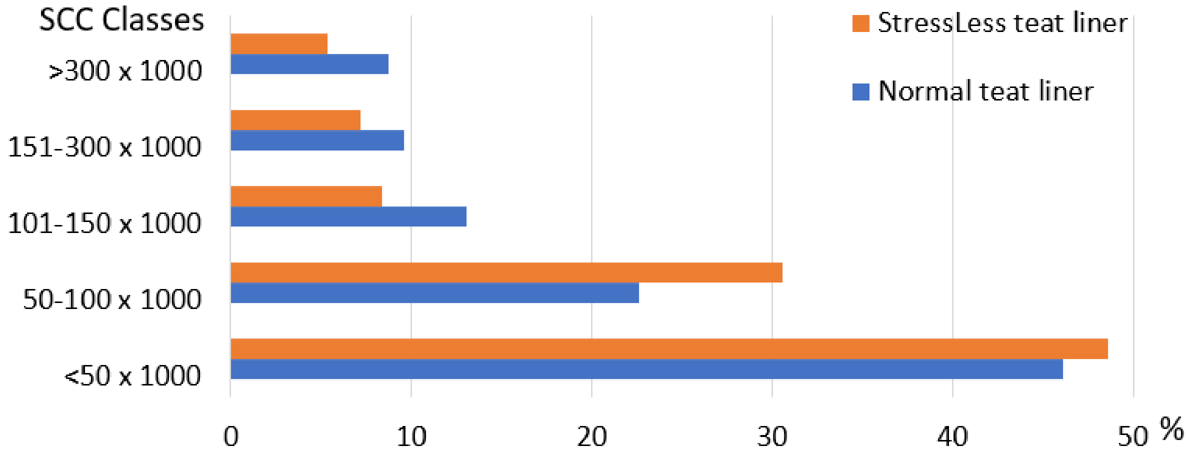

Figure 4. Average somatic cell classes (cells/ml) before and after using the SSL new teat cup liner in all dairy cows examined in farm 1.

3.2. Farm 2

3.2.1. General mean values of the examined parameters in Gr 1 and Gr 2

The results in **Table 5** clearly showed that the daily milk yield in Gr 2 increased significantly ($P < 0.001$) when using the new teat cup liner StressLess and the value has increased by around 2.0 kg per animal. The average fat concentration of dairy cows in Gr 1 was 3.91 ± 0.03% and increased significantly ($P < 0.01$) to 4.04 ± 0.03% in Gr 2. The same trend was observed in protein content and the values increased from 3.22 ± 0.01% in Gr 1 to 3.42 ± 0.02% in Gr 2 and the difference was highly significant ($P < 0.001$). It is noteworthy that the SCC in milk in Gr 2 decreased significantly ($P < 0.001$) compared to Gr 1 and the values were 99.66 ± 3.45 × 10^3 cells/ml and 121.54± 3.39 × 10^3 cells/ml respectively. An interesting aspect was the lactose concentration in dairy cows on this farm and the values increased significantly ($P < 0.001$) from 4.73 ± 0.01% in Gr 1 to 4.81 ± 0.01% in Gr 2. In addition, the urea concentration also increased after using the new teat cup liner and the values were 12.21 ± 0.30 mg/dl and 14.30 ± 0.32 mg/dl in Gr 1 and 2, respectively.

Table 5. The average (LSM ± SE) of the milk parameters of the examined farm 2 during the investigation period.

Parameters farm 2	**Normal teat liner (Gr 1)**	**StressLess teat liner (Gr 2)**	**Significance (*p*-value)**
Milk yield (kg/day/cow)	21.21 ± 0.27	23.30 ± 0.27	0.001
Fat (%)	3.91 ± 0.03	4.04 ± 0.03	0.004
Protein (%)	3.22 ± 0.01	3.42 ± 0.02	0.001
SCC (× 10^3 cell/ml)	121.54 ± 3.39	99.66 ± 3.45	0.001
Lactose (%)	4.73 ± 0.01	4.81 ± 0.01	0.001
Urea (mg/dl)	12.21 ± 0.30	14.30 ± 0.32	0.001

3.2.2. Examined milk parameters in Gr1 and Gr2 according to the stage of lactation

Figure 5 shows the tested milk parameters in Gr 1 and Gr 2 related to the lactation stage. In all lactation stages, daily milk yield was in Gr 2 significantly higher than in Gr 1. The percentage increases in Gr 2 in lactation stages 1, 2 and 3 were 14%, 17% and 14%, respectively (**Figure 5A**). Similar results were shown for protein (%) (**Figure 5C**). Despite an increase in the percentage fat content in Gr 2 compared to Gr 1 after using the SSL teat liner, no significant difference was found ($P > 0.05$) (**Figure 5B**). **Figure 5D** clearly showed an increase in lactose content (%) in the milk of Gr 2 compared to Gr 1 in the second and third stages of lactation ($P < 0.001$). However, the increase in lactose content (%) in the first 100 days of lactation in Gr 2 was not significant compared to Gr 1. Furthermore, it has been shown, that SCC in Gr 2 was numerically lower than in Gr 1 in all lactation stages and the difference was highly significant in the third lactation stage (103.12 ± 6.03 versus 146.85 ± 6.06; $P < 0.001$) (**Figure 5F**). It is noteworthy that urea content in the milk increased significantly after using the new StressLess teat liner in Gr 2 compared to Gr 1 ($P < 0.001$) in lactation stages 1 and 2. The values were 14.91 ± 0.59 compared to 11.46 ± 0.39 and 15.08 ± 0.64 compared to 12.61 ± 0.37 in lactation stages 1 and 2 respectively (**Figure 5E**).

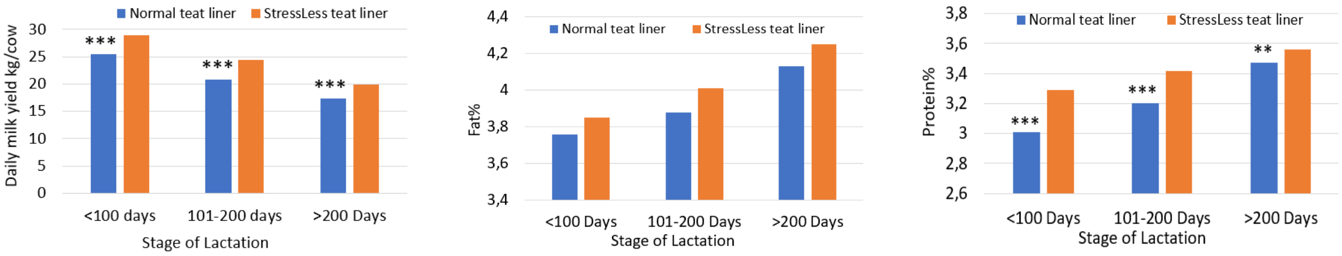

(A) **(B)** **(C)**

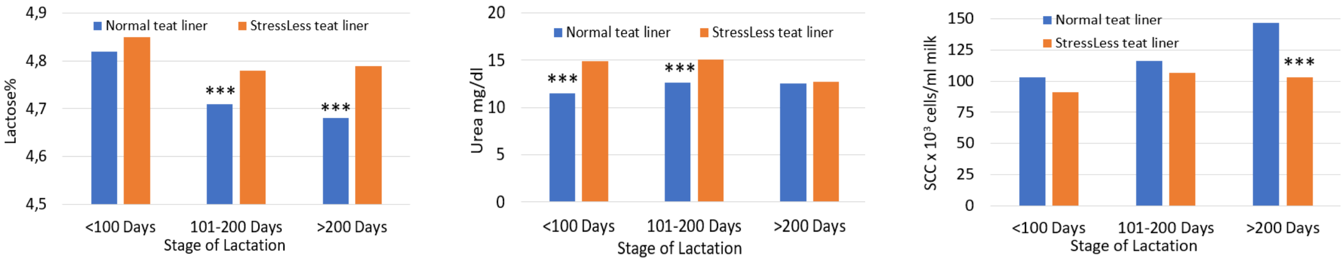

(D) **(E)** **(F)**

Figure 5. Average (LSM) milk parameters in Gr 1 (normal teat cup liner) and Gr 2 (SSL teat cup liner) with significant differences (*p*-value): * $P < 0.05$; ** $P < 0.01$; *** $P < 0.001$, according to the stage of lactation in farm 2. **(A)** Daily milk yield (kg/cow); **(B)** fat (%); **(C)** protein (%); **(D)** lactose (%); **(E)** urea (mg/dl); **(F)** somatic cell count (SCC) (× 10^3 cells/ml).

3.2.3. Examined milk parameters in Gr 1 and Gr 2 according to the lactation numbers

Table 6 shows that all tested parameters were improved after using the SSL teat cup liner in all lactation numbers. Daily milk production was higher in Gr 2 than in Gr 1 at all lactation numbers and the difference was significant except in the fourth lactation. Milk fat content (%) was numerically increased at all lactation numbers after using the new teat cup liner, but it was only significant in the sixth lactation and above. Statistical analysis clearly showed that after using new teat cup liners (Gr 2), the protein content (%) of milk increased significantly at all lactation numbers compared to Gr 1. Similar results were shown for lactose content (%) of milk. Based on the SCC content in milk after using a new teat cup liner (Gr 2), it was lower than Gr 1 for the first and second lactation. The results in **Table 6** also showed that the urea content in milk in Gr 2 was higher than that before using SSL teat cup liners (Gr 1). However, the differences between Gr 1 and Gr 2 were significant only in the first, second, third and sixth and above lactations.

Table 6. The average (LSM ± SE) of the milk parameters of the examined farm 2 in the investigation period according to lactation numbers and significances (*p*-values).

Parameters	**Groups**	**Lactation number**					
		1 (120)*	**2 (110)**	**3 (90)**	**4 (85)**	**5 (80)**	**≥ 6 (55)**
Milk yield (kg/day)	Gr 1	17.81 ± 0.44	20.70 ± 0.46	22.43 ± 0.62	25.13 ± 0.71	23.87 ± 0.75	22.37 ± 0.50
	Gr 2	20.12 ± 0.50	23.38 ± 0.52	24.61 ± 0.71	26.49 ± 0.75	25.06 ± 0.60	24.15 ± 0.64
significance		0.001	0.001	0.004	0.281	0.005	0.001
Fat (%)	Gr 1	3.96 ± 0.06	4.01 ± 0.06	3.93 ± 0.09	3.98 ± 0.09	3.80 ± 0.14	3.65 ± 0.08
	Gr 2	4.02 ± 0.06	4.10 ± 0.06	4.13 ± 0.08	4.21 ± 0.10	3.91 ± 0.10	3.89 ± 0.07
significance		0.456	0.270	0.109	0.094	0.540	0.024
Protein (%)	Gr 1	3.17 ± 0.03	3.23 ± 0.03	3.33 ± 0.04	3.20 ± 0.04	3.20 ± 0.07	3.13 ± 0.04
	Gr 2	3.39 ± 0.03	3.49 ± 0.03	3.48 ± 0.04	3.41 ± 0.05	3.37 ± 0.05	3.37 ± 0.03
significance		0.001	0.001	0.014	0.001	0.012	0.001

Table 6. (*Continued*).

Parameters	Groups	Lactation number					
		1 (120)*	**2 (110)**	**3 (90)**	**4 (85)**	**5 (80)**	**≥ 6 (55)**
SCC (× 10^3 cells/ml)	Gr 1	88.37 ± 6.66	129.32 ± 7.00	133.16 ± 9.45	135.17 ± 10.92	151.40 ± 11.48	128.38 ± 7.58
	Gr 2	69.16 ± 5.85	78.42 ± 6.10	132.35 ± 8.24	132.12 ± 8.70	151.77 ± 13.38	114.18 ± 7.45
significance		0.028	0.001	0.952	0.836	0.982	0.184
Lactose (%)	Gr 1	4.84 ± 0.02	4.74 ± 0.02	4.68 ± 0.03	4.70 ± 0.03	4.67 ± 0.03	4.69 ± 0.02
	Gr 2	4.90 ± 0.01	4.80 ± 0.01	4.79 ± 0.02	4.74 ± 0.02	4.76 ± 0.03	4.75 ± 0.02
significance		0.006	0.009	0.001	0.234	0.031	0.060
Urea (mg/dl)	Gr 1	12.68 ± 0.44	12.10 ± 0.46	12.02 ± 0.62	11.83 ± 0.72	13.66 ± 0.75	11.39 ± 0.50
	Gr 2	14.57 ± 0.70	14.42 ± 0.73	14.60 ± 0.10	13.71 ± 1.04	13.55 ± 1.60	14.10 ± 0.89
significance		0.030	0.005	0.025	0.121	0.947	0.009

Gr 1: Milking the dairy cows with normal teat cup liners. Gr 2: Milking the dairy cows with SSL teat cup liners. * The number in brackets indicates the number of milk samples in each group within each lactation number.

3.2.4. Somatic cell classes in Gr 1 and Gr 2 during the study period

It was found that 60% of SCC in milk after using a new teat cup liner had less than 100 × 10^3 cells/ml, compared to only 45% for Gr1 (**Figure 6**). An interesting aspect is that after using the new teat cup liner, only 4.25% of milk samples were above 250 × 10^3 cells/ml, compared to 7.76% in Gr 1.

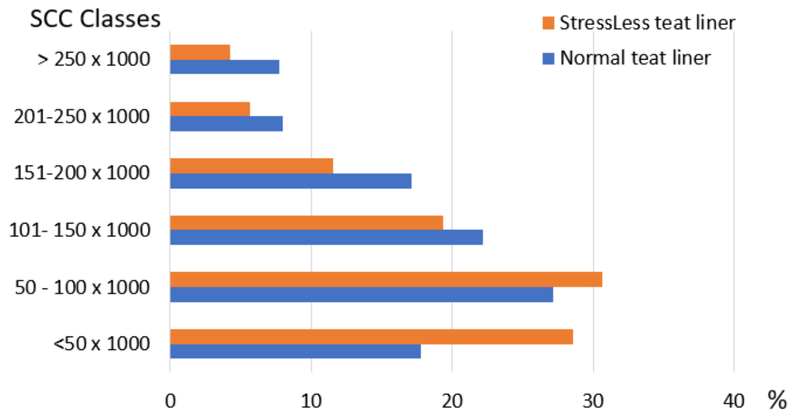

Figure 6. Average somatic cell classes (cells/ml) before and after using the SSL new teat cup liner in all dairy cows examined.

4. Discussion

This study in the two commercial dairy farms clearly showed that higher daily milk production, better milk quality and less SCC were observed after using the new SSL teat cup liner in the existing milking machines. In any case, it has been shown that the SSL teat cup liner plays an important role in optimal milk removal during the milking process. It was observed that a well-designed milking machine harvests milk quickly, gently, and maintains the health of the animals' udders and is easy to clean and disinfect [7,13]. Thus, for optimal milk removal, the continuous availability of milk from the cluster attachment to the point of extraction is crucial. Based on that, the liner plays an important and central role in this as its movement provides continuous stimulation during milking, resulting in oxytocin release from the pituitary gland and continuous milk ejection until the teat cups are removed [27,28]. This process works well and optimally if, in addition to the properties of the milking machine, the teat cup liner used is tailored to the dimensions of the udder teats [1]. Notably, if the dimensions between the teat and teat cup liner are different, the teat cups can climb up, which can lead to an obstruction of the milk flow by disability the connection between the gland cistern and the teat cistern [8]. It should be noted that the shape of the teats and teat dimensions vary greatly within different dairy cows of the same herd, since dairy cows have been primarily are selected for their higher milking speed and for their milking parlour throughput [29,30]. This is exactly what we found during our experiment, particularly on farm 2, very different shapes, lengths, and diameters of udder teats (**Figure 7**).

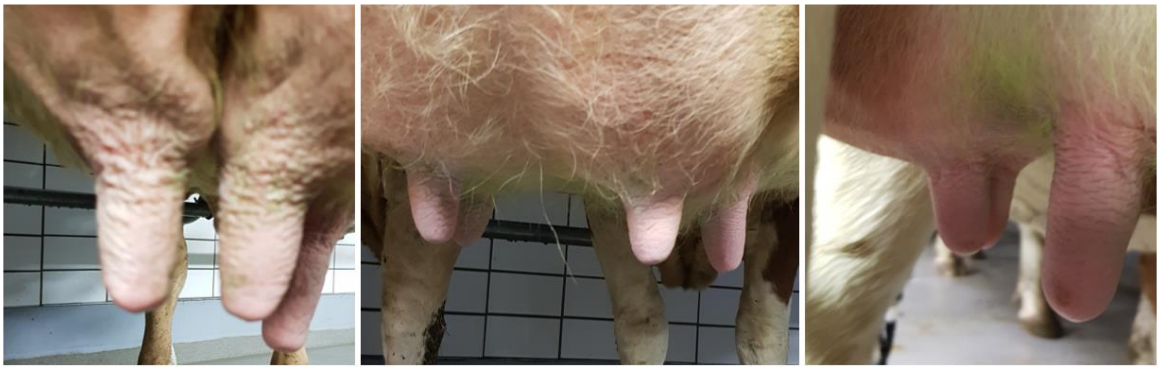

Figure 7. Some teats with different shapes, lengths, and diameters in farm 2.

From a practical point of view, every cow owner uses one type of teat cup liner for all lactating cows and he cannot use additional teat cup liners for each lactating cow with different teat sizes on the farm. Hence individual dairy cows suffered from unsuitable fitting teat liners. Normally, the selected teat cup liner size only fits optimally for around 80% of the lactating cows in a herd [31]. This means that the remaining 20% of cows have more or less problems with this chosen teat cup liner. The properties of the new SSL teat liner (presence of mouthpiece with wavy construction design) were therefore particularly noticeable in the farms examined and had a very good effect because they fit all teat shapes. With large or wide teats, the teat cup liners often fit tightly to the teats and the negative pressure of the milking machine hinders blood and lymph circulation, which puts a lot of strain on the teat tissue. This causes pain and induces mammary immune reactions by increased SCC in the milk produced, as observed in this study before using the SSL teat cup liner. These changes in the circulatory system damage the teat ends, reduce the effectiveness of the udder defense, and can cause in the long-range severe mastitis [15,32,33]. Hillerton [34] found that teat liners had a significant impact on milking performance, cow behaviour during milking, udder health and teat immune reaction. In addition, if the teats are small, air gets into the teat cup and the cluster falls off. In such situations, there may be problems with the attachment of the teat cup or poor adhesion to the teat during milking. The wave-shaped construction of the new liner used (Stimulor StressLess) has an adaptive lip. This means that with the integrated adaptive lip, different teat sizes can be milked with the same liner [6]. These new teat cup liners do not only improve milking performance, but also positively support the well-being of dairy cows. One explanation for the increased milk yield after using the new SSL teat cup liner in our experiment is the complete emptying of the udder. It has long been known that complete emptying of the udder promotes milk synthesis and secretion, hence the milk yield increases [6]. An earlier study indicated that poor teat cup design results in cows not being fully milked [9]. Studies on the physiological relationships between complete milking and milk secretion rate show that milk secretion is controlled via local mechanisms in the udder tissue [34]. Based on the relationships described by Wilde and Peaker [35], it can be assumed that the epithelial cells in the alveoli will reach their genetically determined secretion maximum again, after the inhibitor has been completely removed. This inhibitor is a component of whey protein that acts quickly- and concentration-dependently. In any case, complete udder emptying keeps the content of effective inhibitors in the udder low, and thus stimulates milk secretion.

Milk ingredients are an indicator of the success of the milking process and allow identifying some important management errors. Therefore, in many countries the determination of fat, protein, lactose, urea, and SCC is routinely carried out on each individual cow. Milk fat content is influenced by composition of the feed ration and physical structure of the ration [36–39]. The milking machine, the teat liner fitting and the milking process have also a significant influence on the milk fat content, as this study has shown. After using the SSL teat cup liner on both farms, the udder is completely empty after milking. As a result, the fat content in the milk increased significantly on both farms. It has long been known that the fat content of milk increases continuously during the course of milking and the last portions of milk are of the highest fat content which improves the quality of the final product [38,40,41].

For the protein content of the milk, the results of the test farms showed that it increased after using the new teat cup liner. This increase in milk protein proves that the milking process after using the new teat liner was better than that of the normal teat liner. At this point, udder health and fitness plays “the central role” in the level of milk protein content and their fraction in lactating cows [42]. Many studies have shown that a negative relationship has been demonstrated between the SCC in the milk and the protein content of milk [42,43]. This condition was clearly visible in our study after using the new teat cup liner. It means that the SCC has decreased and the protein content of the milk has increased. This could be explained by the fact that decrease in protein synthesis and DNA in epithelial cells in the udder is due to the increase in SCC in milk [43,44]. Milk from mastitis udders has been observed to have greatly increased proteolytic activity [45–47]. However, plasmin is the main protease in the milk of diseased udders with increased SCC, because the enzyme plasmin is produced by leucocytes [48,49]. It is noteworthy that casein hydrolysis in the udder begins between milking times when subclinical or clinical mastitis is present [50]. The research clearly showed that higher SCC reduces the proportion of β-Casein (β-CN) and αS1-Casein (αS1-CN), which is due to the increased activity of proteolysis [43,51].

Referring to the SCC in the milk of both farms examined clearly showed that the SCC in the milk fell below 100×10^3 cells/ml after using the new teat cup liner SSL.

However, the influence of teat cup liners on teat condition, udder health, and thus on the level of SCC is well known [1]. It should be noted that the somatic cell count in milk is the most important inflammatory parameter of the cow udder [52,53]. Many studies have shown that with prolonged use of an unsuitable milking machine or improperly fitting teat cup liners, the milking machine attacks the teat tip tissue and forms a callus ring around the teat opening, resulting in hyperkeratosis [54–57]. In addition, it has been observed that the proper functioning of the milking machine and milking hygiene are necessary for reducing the risks of mastitis, and thus reducing SCC in milk [53].

The significant increase in lactose content in milk (4.81 ± 0.01 versus 4.73 ± 0.01, $P < 0.001$, **Table 5**) after using the new SSL teat liner showed that the udders of all cows tested were healthy. This means that lactose synthesis in the udder was going well since there were no secretion disorders. It is known that in clinical or subclinical mastitis, the lactose content of the milk decreases and new synthesis is reduced [58]. However, lactose is osmotically active; it is in osmotic equilibrium with sodium and chloride ions in milk. When there is an inflammation of the udder, lactose is transported back into the blood and appears in the urine. At the same time, increased amounts of sodium and chloride ions pass from blood into the milk. Therefore, lactose is very important in maintaining the osmotic pressure of milk.

Urea is the major metabolite formed from dietary proteins and tissue protein turnover and is excreted from the liver into the bloodstream and then into milk in a stable form [59]. The results of this study showed that the urea content of milk was optimized after using the new teat liner. This means that after using the new teat liner in farm 1, the urea content fell from 24.98 ± 0.78 mg/dl to 15.03 ± 0.54 mg/dl and in farm 2, the urea content increased from 12.21 ± 0.30 mg/dl to 14.30 ± 032 mg/dl. Since the situation on farm 1 was the same before and after the use of the new teat liner, it is difficult to determine which factor other than the liner influenced the urea content of the milk. This is also the case on farm 2. whether this contradiction in the results (decrease in urea concentration in milk on farm 1 and increase in urea concentration in milk on farm 2) that occurred after the use of new teat liners was coincidental or whether there were other factors that influenced these results. Nowadays, it is not yet known whether the teat liner has an influence on the urea content of the milk or not, as urea is strongly influenced by husbandry and feeding conditions, such as the lack of rumen-degradable proteins and changes in dry matter intake or energy in the feed ration [60]. Therefore, the milk urea content may serve as an on-farm indicator to guide nutritional strategies [61–65]. Further studies are needed to clearly demonstrate the influence of the use of teat liners on urea in milk. However, it has been observed that a reduction in the amount of urea in the milk of cows is associated with IMI and increased SCC [66,67]. This is exactly what was observed in farm 2, that the urea content increased after the use of new teat cup liners and the reduction of SCC in the milk. The mechanisms behind this relationship are not yet fully understood and therefore require further investigation.

5. Conclusion

- The SSL teat cup liner has a significant influence on the degree of udder emptying, the maintenance of the udder health and the quality of raw milk.
- After using the new SSL teat cup liner, the udders remained healthy throughout the study period, showing lower somatic cell counts (SCC).
- High milk yield and better milk quality can be achieved by using SSL teat cup liner as it is adapted to all teat shapes.
- Finally, the SSL teat cup liner prevents injuries, and thus makes a decisive contribution to greater animal welfare and improved animal health.

Author contributions: Conceptualization, SK; methodology, SK; software, KAN; validation, SK, KAN and MWP; formal analysis, KAN; investigation, SK; resources, SK; data curation, SK, KAN; writing—original draft preparation, SK; writing—review and editing, MWP; visualization, SK; supervision, MWP; project administration, SK; All authors have read and agreed to the published version of the manuscript.

Conflict of interest: The authors declare no conflict of interest.

References

1. Kaskous S, Pfaffl, MW. Milking machine settings and liner design are important to improve milking efficiency and lactating animal welfare-technical note. AgriEngineering. 2023; 5: 1314–1326.
2. Parilova M, Stadnik L, Jezkova A, Stolc L. Effect of milking vacuum level and overmilking on cow's teat characteristics. Acta Univ. Agric. Et Silvic. Aemendelianae Brun. 2011; 59: 193–202.
3. Edwards JP, O'Brien B, Lopez-Villalobos N, et al. Overmilking causes deterioration in teat-end condition of dairy cows in late lactation. J. Dairy Res. 2013; 80: 344–348.
4. Ferneborg S, Svennersten-Sjaunja K. The effect of pulsation ratio on teat condition, milk somatic cell count and productivity in dairy cows in automatic milking. J. Dairy Res. 2015; 82: 453–459.
5. Gasparik M, Duchacek J, Stadnik L, et al. Impact of milking settings optimization on milk quality, milking time, and milk yield in Holstein cows. IOP Conf. Ser. Mater. Sci. Eng. 2018; 420: 012073.
6. Kaskous S. Importance of the new silicone liner "Stimulor Stressless" for optimal milking performance and welfare of the lactating animals-technical report. Applied Veterinary Research. 2023; 2(3): 2023011. doi: 10.31893/avr.2023011
7. Reinemann DJ. Milking machines and milking parlours. In: Handbook of farm, dairy and food machinery Engineering, 3rd Edition. Academic Press; 2019. pp. 225–243.
8. Cesna J, Medvedskyi O, Postol Y, et al. Simulation of design parameters of a milking cup with an extended service life. Agricultural Engineering. 2022; 26(1): 243–252.
9. Walker M. Choosing the best teat cup liner for optimal milking performance. International Dairy Topics. 2018; 17(3): 9–11.
10. Krömker V. Melken. In: Krömker V (editor). Short textbook on dairy science and milk hygiene. Parey in MVS Medizinverlage Stuttgart: Stuttgart; 2007. pp. 23–46.
11. Reinemann DJ. The smart position on teat condition. In: Proceedings of the New Zealand milk quality conference; 18–19 June 2012; Hamilton, New Zealand. pp. 124–131.
12. Gleeson DE, Ocallaghan EJ, Rath MV. Effect of liner design, pulsator setting, and vacuum level on bovine teat tissue changes and milking characteristics as measured by ultrasonography. Irish Veterinary Journal. 2004; 57(5): 289–296.
13. Vermaak P, Petzer IM, Karzis J. Effects of milking machine settings and teat liners on bovine udder health. South African Journal of Animal Science. 2022; 52(4): 421–432.
14. Wieland M, Sipka A. Prospective cohort study of the relationship between milking machine liner slip, milking performance, and cow characteristics. J. Dairy Sci. 2023; 106: 2044–2053.

15. Reinemann DJ, Mein GA. Unravelling the mysteries of liner compression. In: Proceedings of the Countdown Symposium, Tackling Strep Uberis; 8 June 2011; Melbourne, Australia. p. 10.
16. Kaskous S. The effect of using quarter individual milking system “MultiLactor” on improvement of milk performance and milk quality of different dairy cow’s breeds in different farms. Emir. J. Food Agric. 2018; 30: 57–64.
17. Kaskous S, Fadlelmoula A. Adaptability of dairy cows to individual quarter milking system after changing from tying to loose housing system. Advances in Animal and Veterinary Sciences. 2015; 3(4): 225–232.
18. Kaskous S. Optimization of milk performance and quality in dairy farms by using a quarter individual milking system “MultiLactor”. Int. J. Environ. Agric Biotechnol. 2020; 5: 943–952.
19. Kaskous S. Influence of the quarter-individual milking system “MultiLactor” on the milk yield and quality in dairy cows: Results of a field study. In: Proceedings of International Conference on research on food security, natural resource management and rural development-Tropentag, Humboldt-Universität zu Berlin; 20–22 September 2023; Germany. p. 384.
20. Müller AB, Rose-Meierhöfer S, Ammon C, et al. Comparison of the effects of quarter-individual and conventional milking system on milkability traits. Archiv Tierzucht. 2011; 54(4): 360–373.
21. Kaskous, S. MultiLactor Melksystem, eine Revolution in der Melktechnik. In: Forschungsbericht, Abteilung der Forschung und Entwicklung; Siliconform: Türkheim, Germany, 2016; pp. 1–40.
22. Holst GE, Adrion F, Umstätter C, et al. Type of teat cup liner and cluster ventilation affect vacuum conditions in the liner and milking performance in dairy cows. J. Dairy Sci. 2021; 104 (4): 4775–4786.
23. EuroTier Special. These are the novelties 2022. Silicone mold: corrugated liners adapt (German). Agriculture. 2022; 20(16): 31.
24. EuroTier. Innovation is rewarded, Stimulor StressLess, Siliconform Vertriebs GmbH und Co. KG (German). Allgäuer Bauernblatt. 2022; 44(3): 50.
25. NRC. Nutrient Requirement of Dairy Cattle, 8th ed. National Academies Press; 2021. pp. 1–502.
26. SAS Institute. SAS User’s Guide, Release version 9.3. SAS Institute INC; 2012.
27. Bruckmaier RM, Schams D, Blum JW. Continuously elevated concentrations of oxytocin during milking are necessary for complete milk removal in dairy cows. J. Dairy Res. 1994; 61: 323–334.
28. Bruckmaier RM, Blum JW. Oxytocin release and milk removal in ruminants. J. Dairy Sci. 1998; 81: 939–949.
29. Nazar M, Lu X, Abdalla IM, et al. Genome-Wide Association Study Candidate Genes on Mammary System-Related Teat-Shape Conformation Traits in Chinese Holstein Cattle. Genes. 2021; 12(12): 2020.
30. Ruegg PL, Erskine RJ. Mammary gland health. In: Smith BP, Van Metre DC, Pusterla N (editors). Large Animal Internal Medicine, 5th ed. Elsevier Mosby; 2014, pp. 1015–1043.
31. Upper Austrian Cattle Production Advice Center, Chamber of Agriculture, Upper Austria. The right liner, which liner suits my cows (German)? Upper Austrian Cattle Production Advice Center, Chamber of Agriculture, Upper Austria. 2015. pp. 1–8.
32. Penry JF, Upton J, Mein GA, et al. Estimating teat canal cross-sectional area to determine the effects of teat-end and mouthpiece chamber vacuum on teat congestion. J. Dairy Sci. 2017; 100(1): 821–827.
33. Maier J, Kaskous S. Multi-Lactor die R-Evolution in der Melktechnik. 6. Fachtagung Automatisierung in der Milcherzeugung, Bauernscheune Bösleben der AGRAR Genossenschaft, Thüringen, Germany; May 12. pp. 1-9.
34. Hillerton JE. Do liners differ? In Natl. Mastitis Counc. Reg. Mtg. Proc. Orlando, FL. National Mastitis Council, Madison, WL. 2005. pp. 133–138
35. Wilde CJ, Peaker M. Autocrine control in milk secretion. J. Agric. Sci. 1990; 114: 235–238.
36. Zebeli Q, Tafaj M, Steingass H, et al. Effects of physically effective fiber on digestive processes and milk fat content in early lactating dairy cows fed total mixed rations. J. Dairy Sci. 2006; 89(2): 651–668.
37. Caccamo M, Veerkamp RF, Licitra G, et al. Association of total-mixed-ration chemical composition with milk, fat, and protein yield lactation curves at the individual level. J. Dairy Sci. 2012; 95(10): 6171–6138.
38. Rico DE, Marshall ER, Choi J, et al. Within-milking variation in milk composition and fatty acid profile of Holstein dairy cows. J. Dairy Sci. 2014; 97: 4259–4268.
39. Bostanova S, Aitmukhanbetov D, Bayazitova K, et al. Indicators of full value feeding rations for dairy cows. Brazilian J. Biology. 2022; 82: e254111.
40. Whittlestone WG. Variation in the fat content of milk throughout the milking process. J. Dairy Sci. 1953; 20: 146–153.

41. Upton J, Penry J, Rasmussen M, et al. Effect of pulsation rest phase duration on teat end congestion. J. Dairy Sci. 2016; 99: 3958–3965.
42. Urech E, Puhan Z, Schällibaum M. Changes in milk protein fraction as affected by subclinical mastitis. J. Dairy Sci. 1999; 82: 2402–2411.
43. Bisutti V, Vanzin A, Pegolo S, et al. Effect of intramammary infection and inflammation on milk protein profile assessed at (the quarter level in Holstein cows. J. Dairy Sci. 2024; 107(3): 1413–1426. doi: 10.3168/jds.2023-23818
44. Zhang L, Boeren S, Van Hooijdonk ACM, et al. Proteomic perspective on the changes in milk proteins due to high somatic cell count. J. Dairy Sci. 2015; 98: 5339–5351.
45. Schaar J. Plasmin activity and proteose-peptone content of individual milks. J. Dairy Res. 1985; 52: 369–378.
46. Le Roux Y, Colin O, Laurent F. Proteolysis in samples of quarter milk with varying somatic cell counts: 1. Comparison of some indicators of endogenous proteolysis in milk. J. Dairy Sci. 1995; 78: 1289–1297.
47. Auldist MJ, Coats S, Sutherland BJ, et al. Effects of somatic cell count and stage of lactation on raw milk composition and the yield and quality of cheddar cheese. J. Dairy Res. 1996; 63: 269–280.
48. Le Roux Y, Laurent F, Moussaoui F. Polymorphonuclear proteolytic activity and milk composition change. Vet. Res. 2003; 34: 629–645.
49. Forsback L, Lindmark-Mansson H, Andren A, et al. Evaluation of quality changes in udder quarter milk from cows with low-to-moderate somatic cell counts. Animal. 2010; 4: 617–626.
50. Caggiano N, Lorenzo SA, Bottini JM, et al. Protease activity and protein profile in milk from healthy dairy cows and cows with different types of mastitis. Int. Dairy J. 2019; 89: 1–5.
51. Rogers SA, Slattery SL, Mitchell GE, et al. The relationship between somatic cell count, composition, and manufacturing properties of bulk milk. Aust. J. Dairy Technol. 1989; 44: 49–52.
52. Ruegg PL. A 100-Year Review: Mastitis detection, management, and prevention. J. Dairy Sci. 2017; 100: 10381–10397.
53. Tesin N, Radinovic M, Tomanic D, et al. Analysis of the somatic cell pattern in mastitis-affected cows on three dairy farms in Vojvodina. Contemporary Agriculture. 2023; 72(4): 175–180.
54. Neijenhuis F, de Koning K, Barkema H, et al. The effect of machine milking on teat condition. In: Proceedings of Conference on Physiological and technical aspects of machine milking, ICAR Technical Series. 2001. pp. 33–40.
55. Hamann J, Burvenich C, Mayntz M, et al. Machine induced changes in the status of the bovine teat tissue with respect to new infection risk. Bul. IDF. 1994; 2: 13–22.
56. Neijenhuis F, Barkhema HW, Hogeveen H, Noordhuizen JPTM. Classification and longitudinal examination of callused teat ends in dairy cows. J. Dairy Sci. 2000; 83: 2795–2804.
57. Dairy NZ. Correct teat cup liners will keep cows healthy and happy. Available online: www.ruralnewsgroup.co.nz/dairy-management (accessed on 7 September 2024).
58. Schulz J. Structure of the mammary gland and physiology of lactation. In: Fahr RD, von Lengergen G (editors). Milk production. German specialized publisher; 2003. pp. 45–79.
59. Hayton A, Husband J, Vecqueray R. Nutritional management of herd health. In: Dairy HH, Green MJ, Bradley AJ (editors). Dairy herd health, 1st ed. CABI North American Office; 2012. pp. 227–278.
60. Rezamand P, Hoagland TA, Moyes KM, et al. Energy status, lipid-soluble vitamins, and acute phase proteins in periparturient Holstein and Jersey dairy cows with or without subclinical mastitis. J. Dairy Sci. 2007; 90: 5097–5107.
61. Eicher R, Bouchard E, Bigras-Poulin M. Factors affecting milk urea nitrogen and protein concentrations in Quebec dairy cows. Prev. Vet. Med. 1999; 39: 53–63.
62. Olmos Colmenero JJ, Broderick GA. Effect of dietary crude protein concentration on milk production and nitrogen utilization in lactating dairy cows. J. Dairy Sci. 2006; 89(5): 1704–1712.
63. Borucki Castro SI, Phillip LE, Lapierre H, et al. The relative merit of ruminal undegradable protein from soybean meal or soluble fibre from beet pulp to improve nitrogen utilization in dairy cows. J. Dairy Sci. 2008; 91: 3947–3957.
64. Spek JW, Dijkstra J, Van Duinkerken G, et al. A review of factors influencing milk urea concentration and its relationship with urinary urea excretion in lactating dairy cattle. Journal of Agricultural Science. 2013; 151: 407–423.
65. Siachos N, Panousis N, Arsenos G, et al. Investigation of milk urea nitrogen concentration and factors affecting its variation in Greek Holstein herds. J. Hell Vet. Med. Soc. 2017; 68: 423–432.
66. Nyman AK, Persson Waller K, Bennedsgaard TW, et al. Associations of udder-health indicators with cow factors and with intramammary infection in dairy cows. J. Dairy Sci. 2014; 97: 5459–5473.

67. Timonen AAE, Katholm J, Petersen A, et al. Within-herd prevalence of intramammary infection caused by Mycoplasma bovis and associations between cow udder health, milk yield, and composition. J. Dairy Sci. 2017; 100: 6554–6561.

Mechanical Engineering Advances 2024, 2(2), 1223.
https://doi.org/10.59400/mea.v2i2.1223

Review

Prelithiation of electrodes in lithium-ion capacitors: A review

Aston Sam D'Silva[1], **M. P. Eldho**[1], **K. Lekha**[1], **J. Anushree**[1], **Vinayambika S. Bhat**[1], **Raghavendra Sagar**[2,*]

[1] Department of Electronics & Communication Engineering, Mangalore Institute of Technology & Engineering, Badaga Mijar, Mangaluru 574225, India
[2] Department of Physics, Mangalore Institute of Technology & Engineering, Badaga Mijar Moodabidri, Mangaluru 574225, India
*** Corresponding author:** Raghavendra Sagar, raghav_sagar@rediffmail.com

CITATION

D'Silva AS, Eldho MP, Lekha K, et al. Prelithiation of electrodes in lithium-ion capacitors: A review. Mechanical Engineering Advances. 2024; 2(2): 1223. https://doi.org/10.59400/mea.v2i2.1223

ARTICLE INFO

Received: 5 January 2024
Accepted: 19 March 2024
Available online: 27 March 2024

Abstract: Lithium-ion capacitors (LICs) are one of the modern state-of-the-art hybrid capacitors, comprising a high potential window and imparting a higher energy density than supercapacitors (SCs). These LICs encompass elevated power density and a longer life span than lithium-ion batteries (LIBs). Preparation of high-performance electrode materials with electrochemically active microstructure and prelithiation are two efficient approaches to fabricate highly efficient LICs. But it comes across as a real dilemma of low initial Columbic efficiency if only microstructure is considered as an efficient way to enhance the performance. Nevertheless, prelithiation plays a crucial role in the manufacturing of LICs, improving the initial Coulombic efficiency and enlarging the voltage window. This paper reviews the recent lithiation approaches for lithium-ion capacitors by providing their methods and discussing their results concerning their energy and power density.

Keywords: electrodes; columbic efficiency; prelithiation; LIC; energy density

1. Introduction

An increase in the market size of EVs and consumer electronic goods like computer systems and mobiles has swayed the research attention towards high-density energy storage systems [1]. These energy storage systems should be capable of generating fair output power and safe operational characteristics to be used in both vehicles and consumer electronic applications [2]. Among all types of energy storage devices, lithium-based materials are the most commonly used commercial systems to store energy from renewable energy sources. Among most lithium-based energy storage systems, LIBs have become the most widely used electrochemical energy storage device due to their superior energy density values, much needed for modern-day EVs and consumer electronics [3,4]. Nonetheless, both LIB's and SCs exhibit a notable discrepancy in performance due to their inability to meet the demands of fast charging and slow discharging. Thus, to overcome such discrepancy, an electrochemical energy storage device needs to be able to have both a high energy density and a high power density in order to achieve these requirements [5].

LICs are hybrid energy storage systems where SC's type cathode and LIB's type anode are used to derive high power and energy densities simultaneously. Conventionally activated carbon is used as a cathode material, which imparts greater power density, and compositions like $LiTi_5O_{12}$ are used as anode materials, which result in higher energy density. This asymmetric device construction makes these devices appropriate for both consumer electronics as well as automotive mobility. It is well known that the electrochemical properties of LICs can be easily tuned using prelithiation, where anions move from or towards the cathode, where intercalation occurs [6]. Thus, prelithiation is one of the preferred strategies adopted to compensate for the intercalation. However, the commercialization of LIC increased traction some time ago when graphite was started to be probed as a potential negative electrode material, anticipating its capability to improve energy density and potential window [7].

2. Need for prelithiation

In LIC's, prelithiation is expected to compensate for the loss of Li-ions that occurred due to the formation of solid electrolyte interphase towards the anode terminal since a higher proportion of activated carbon is expected to facilitate higher Li-ion loss [8,9]. Hence, selection and preparation of appropriate cathode and anode materials is one of the useful approaches to make possible LICs to attain high energy density at high power density. However, despite the recent developments in electrode materials, we come across the problem of low initial columbic efficiency in LICs. For example, let us consider $LiCoO_2$//graphite cell where Li-ions de-intercalated from $LiCoO_2$ and intercalated towards graphite at the time of charging. The reaction corresponding to the movement of Li-ions is as follows:

$$LiCoO_2 \leftrightarrow Li_{1-x}CoO_2 + xLi^{+}xe^{-} \tag{1}$$

$$C + xLi^{+} + xe- \leftrightarrow LixC \tag{2}$$

$$LiCoO_2 + C \leftrightarrow Li_{1-x}CoO_2 + Li_xC \tag{3}$$

The above equations represent the reaction of entire cells, i.e., on the anode's and cathode's, respectively. When the anode potential falls below 1V versus Li^{+}/Li, parasitic processes on the anode surface cause the organic electrolyte to be simultaneously reduced to create the solid electrolyte interphase (SEI) layer during the intercalation of Li-ion. While it is widely known that this SEI layer is essential in preventing electrolyte ions from co-intercalating into the electrode bulk, some lithium ions may be permanently caught in the electrode during lithiation, which causes a rapid shift in the concentration of the electrolyte and the consumption of lithium ions, resulting in low initial coulombic efficiency and high initial capacity loss [10,11]. **Figure 1** shows the formation of SEI in $LiCoO_2$//graphite lithium ion batteries. A significant challenge for LICs is the absence of a lithium source in the cathode, which limits energy density. Here, prelithiation plays a crucial role in the manufacturing of LICs to improve the initial columbic efficiency and boost energy density [12]. It also provides the extra Li-ions to make up the initial loss in the capacitor [13–16].

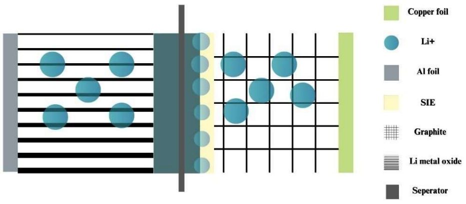

Figure 1. Formation of SEI in $LiCoO_2$//graphite LIBs.

3. Prelithiation approaches

Prelithiation is a strategy to preemptively lithiate pre-doping of extra Li-ions into electrodes before battery/capacitor assembly for active Li^+ loss compensation [17–22]. Currently, numerous prelithiation processes are applied for recovering initial irrevocable capacitance compensation [23–27]. The prelithiation approaches for LICs can be broadly classified into two types, namely the anode prelithiation and cathode prelithiation. Herein all the prelithiation approaches mentioned are expected to enhance the LICs performance.

3.1. Anode prelithiation

In In order to enhance the initial columbic efficiency and improve the life span of LIC's, prelithiation of the anode is one of the most effective strategies. Here the anode can be prelithiated by various processes like chemical prelithiation, electrochemical prelithiation, additive prelithiation, and metal lithium foil/powder prelithiation [28,29]. But they were mainly fabricated through electrochemical prelithiation and direct contact with a Li source [30]. These prelithiation approaches are discussed in detail.

3.1.1. Chemical prelithiation

In chemical prelithiation, organic molecules are used as the mediator for lithium transfer [31,32]. The first method deals with the prelithiation of anode with the chemical prelithiation method for SiO_x/Graphite composite anode. In this, lithium ararene (LiA) was used as a prelithiation reagent for the composite anode. Anaryl lithium impregnation method with 2 min of prelithiation resulted in the increased ICE from 88% to 98%. They found that the ICE can be easily tuned using impregnation time and LiA reagent concentration. The study was limited to half-cell testing and did not assess the performance of the prelithiated anode in a complete battery system [33]. Another chemical prelithiation method deals with the use of 2-methyltetrahydrofuran (MTHF) as prelithiation solvent. MTHF solvent was used to prelithiate soft carbon (SC), where the time for prelithiation was set to be ~5 min, which resulted in the display of a small potential of 0.21 V vs. Li/Li^+. As prelithiated SC was found to be chemically stable and deployed as cathode, excellent capacitance retention was observed even after 5000 charging and discharging cycles. Also, the energy density was computed at ~69.4 Wh/kg, and the power density was 5.7 kW/kg in the fabricated LIC made up of prelithiated SCs [34].

3.1.2. Sacrificial prelithiation material

In order to prevent the use of a metallic lithium electrode during the initial charging phase, provide lithium ions into the anode. It is to be noted that Li_3N is one of the best salts that could be used as a sacrificial source and can be easily produced by reacting lithium with nitrogen gas. Li_3N is investigated as a novel sacrificial material that offers a number of special benefits over existing prelithiation materials. **Figure 2** shows the configuration of LIC with an

AC/Li_3N electrode.

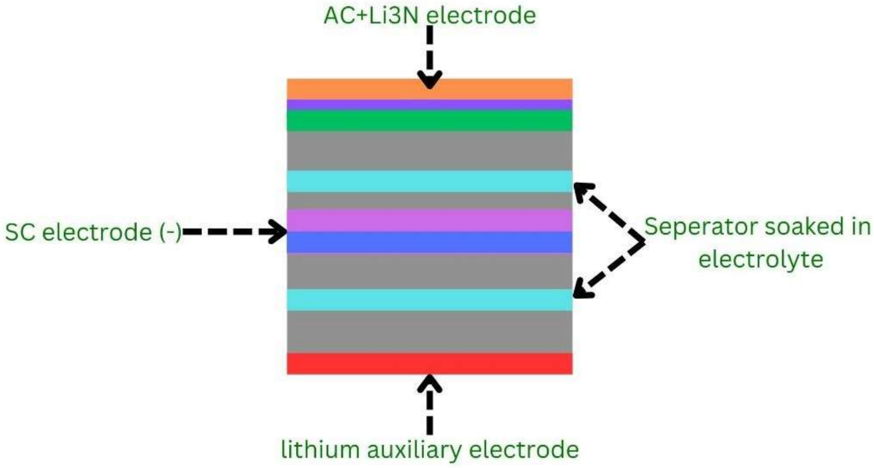

Figure 2. The configuration of LIC with AC/Li_3N electrode, SC electrode and lithium auxiliary electrode.

Here, the LIC was constructed using AC/Li_3N cathode and SC as anode, which showed a high energy density of 214.7 Wh kg^{-1} at 0.18 kW kg^{-1} and 65.0 Wh kg^{-1} at a high power density of 19.5 kW kg^{-1} with excellent cycling stability (75.1% retention after 5000 cycles at 3.2 kW kg^{-1}). Overall, the approach of using Li_3N as prelithiation material offers several advantages, including avoiding electrolyte decomposition, reducing the amount of prelithiation material needed, and simplifying the construction of pouch LICs. The results obtained in this work revealed the difficulties in obtaining high energy and power densities owing to the divergence of electrode kinetics.

Anaiz et al. reported about the use of sacrificial salts as a prelithiation tactic to get efficient LIB and SCs. The prelithiation procedure includes the usage of sacrificial salts, especially dilithium squarate ($Li_2C_4O_4$), in a LIC prototype fabricated in a pilot line. This process gets done during the first ten cycles, and after the needed gas exhaust, the electrochemical performance of prototypes was found to be satisfactory [35].

Veluri et al. proposed the construction of a LIC with a long life span (85% capacity retention after 10,000 charge-discharge cycles at 1A/g and a high energy density of 80 Wh/kg and a high power density of 8.4 kW/kg) utilizing carbon materials obtained entirely from petroleum coke. No additional prelithiation was done; instead, the suggested LIC was prelithiated by keeping a small amount of Li metal foil (ratio of Li to disordered carbon, 1:7) on the anode surface to supply lithium during the initial charging stage. High-surface-area activated carbon made from petroleum coke served as the cathode, and low-surface-area disorder carbon served as the anode. **Figure 3** demonstrates the capacitance retention of petroleum coke-based LIC vs. the petroleum coke-based supercapacitor [36].

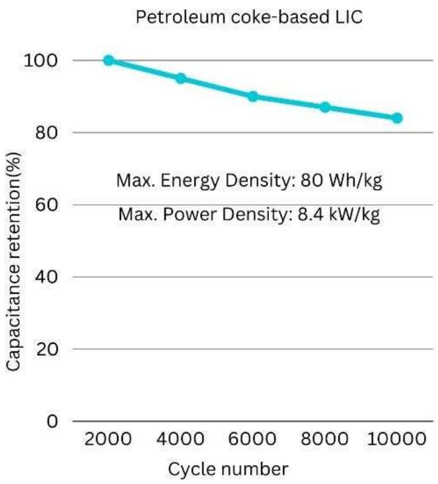

Figure 3. Petroleum coke-based LIC vs the petroleum coke-based supercapacitor.

Kong et al. reported the LICs with anode compositions of high-content P and N co-doped porous carbon nanomaterials (X-PNC) and cathode made using pyrrolic-N-doped porous carbon nanomaterials (X-NC). The working electrodes in the half-cells were X-PNC and X-NC electrodes, whereas the counter electrode was lithium metal foil. With great cycling stability (75.1% retention after 5000 cycles at 3.2 kW kg^{-1}), the built-in LIC demonstrated a high energy density of 214.7 Wh kg^{-1} at 0.18 kW kg^{-1} and 65.0 Wh kg^{-1} at a high power density of 19.5 kW kg^{-1} [37].

Han et al. reported the fabrication of LIC built utilizing pre-lithiated nitrogen-doped porous carbon (NPC) anodes and hierarchical porous carbon (CHPC) cathode electrodes generated from coal. It has a gravimetric capacitance of 139 mAh g^{-1} cathode at 0.5 A g^{-1}. In this work, the NPC electrode was in contact with Li metal foils for 45 minutes for prelithiation without any use of a polypropylene membrane. The CR2032 button cells fabricated in this work demonstrated a specific capacity of 139 mAh g^{-1} with 99% retention after 1000 cycles of charging and discharging at 1 A g^{-1}. The energy density was estimated to be 220 Wh kg^{-1} at a specific power of 805 W kg^{-1}. **Figure 4** shows the schematic representation of pre-lithiated cells prepared using NPC and CHPC [38].

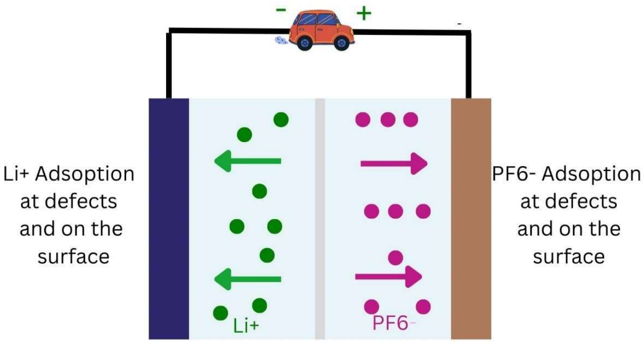

Figure 4. The diagram illustrating charge-storage mechanisms (gray ball: carbon atoms; blue ball: oxygen atoms; red ball: nitrogen atoms; yellow ball: sulfur atoms; purple ball: PF_6^- anion; green ball: Li^+ cation).

3.1.3. Prelithiation by charging/discharging a half cell

Tan et al. reported the fabrication of LIC by means of hollow porous α-Fe_2O_3 nanoparticles and carbon nanospheres derived from glucose as anodes and cathodes, where excellent electrochemical characteristics were observed. Half cell prepared using hollow porous α-Fe_2O_3 nanoparticles was prelithiated using charging/discharging at 0.2 A g^{-1}, resulting in 107 Wh kg^{-1} energy density at 0.24 W kg^{-1} and an energy density of 86 Wh kg^{-1} at a power density of 9.68 kW kg^{-1}. **Figure 5** shows typical LIC comprising important parts like cathode, anode, and electrolyte layers. Besides, it displayed towering-capacity retention ~84% after 2000 CV cycles ~1 Ag^{-1} [39].

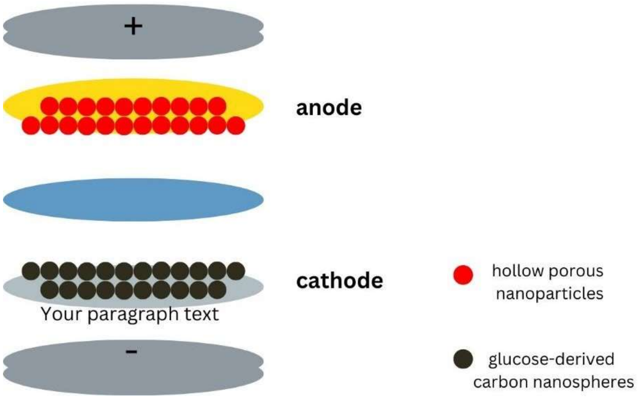

Figure 5. Graphical representation of approach for the Lithium-ion capacitor in coin cell.

An additional step in the prelithiation process is used to activate a graphite half-cell by charging and discharging it five times before assembling it into a full-cell configuration. New peaks were observed in the XPS spectra, and atomic percentages change as the graphite electrode is exposed to particular electrolytes. These changes in elemental composition and chemical bonding occur during this process. These alterations show that during the prelithiation phase, an artificial solid electrolyte interphase (SEI) is formed on the graphite surface [40].

Among the other techniques is the use of lignin, the second most common natural polymer, which is also the primary waste byproduct from the pulp and paper industry and is used as an electrode material for lithium-ion batteries. Here, lignin is transformed into two types of functional carbons that act as the electrode materials in LICs by controlling the porous framework and graphitic degree with the goal of building high-performance LICs. In a manufactured capacitor, lignin-derived hierarchical porous carbon (LPC-3) served as the anode and lignin-derived graphitic carbon (LGC-1500) as the anode. The assembled LGC-1500//LPC-3 LIC delivered a high-energy density of 97W h kg^{-1}, a high-power density of 11.4 kW kg^{-1}, and a superior cyclic stability of 92.3% after 5000 cycles at 1 Ag^{-1} [41].

The "in-situ electrolyte" is a sustainable alternative for the realization of high-power devices [42,43]. These devices, including electric double-layer and metal-ion capacitors prepared using waste products for carbon synthesis, enable the realization of Li- and Na-based EDLCs containing aqueous, water in salt, and organic electrolytes, as well as an alternative for Li-ion capacitors. The prelithiation process involves generating a lithium inventory to ensure the formation of a SEI on the anode and to avoid concentration gradients within the electrolyte solution. This is achieved by utilizing activated carbon (AC) loaded with a selected lithium salt to create a LIC with a high and tunable lithium inventory directly during the assembly process. A mixture of carbonaceous materials, including hard carbon and graphite, serves as the anode material. The study does highlight some of the difficulties in determining the ideal concentration of activating agents for carbon porosity. The fabricated LIC displayed a power density of 10 kW kg^{-1} and a specific capacitance of ~21 Fg^{-1} [44].

The developed hybrid LICs with a prelithiated graphite anode and two cathodes exhibit superior electrochemical performance, including high energy density, power density, and capacity retention. The prelithiation process was conducted by lithiating the graphite anode using a perforated $LiCO_2$ electrode. The anode material was composed of graphite, carbon black, carboxymethyl cellulose (CMC), and styrene butadiene rubber (SBR), and the cathode material was prepared using active carbon, carbon black, CMC, SBR, and $LiCO_2$. Within a voltage range of 2.2 V to 3.8 V, the hybrid LICs showed excellent discharge and charge performance, together with high energy and power densities. After 300 cycles, the hybrid LICs capacitance dropped by less than 1%, demonstrating exceptional cycling performance and capacity retention of up to 99% [45].

The potential for easy and low-cost fabrication of LICs and the feasibility of adopting new technologies such as sodium ion and potassium ion capacitors are extensively reported. Arnaiz et al. reported in-house synthesized olive pit-derived hard carbon (HC) as anode and AC as cathode material. In this report, 1 M $LiPF_6$ in ethylene carbonate (EC) and dimethyl carbonate (DMC) with 3 wt% of vinylene carbonate (VC) was used as an electrolyte. The energy density of LICs, with a 2- to 3-fold enhanced performance, was observed compared to EDLCs in terms of power density and specific capacitance [46].

Anothumakkool et al. reported the development of prelithiated electrodes in LIC, which could help overcome a significant scientific obstacle in the field. The prelithiation process in this paper involves a cascade-type mechanism with two consecutive irreversible reactions within the positive electrode, where oxidative electro-polymerization of pyrene moieties releases electrons and protons. These protons are captured by Li_3PO_4 and exchanged for a stoichiometric amount of Li^+ into the electrolyte, aiming to compensate for the loss of active lithium and electrons during cycling and reach full utilization of the active materials. Carbon black and activated carbon are used as anodes in the construction of LIC, whereas pyrene and Li_3PO_4 additives are used as cathodes. The prelithiation process used in the construction of the LIC revealed an energy density of 63 $WhKg^{-1}$. However, challenges in commercialization and inability to achieve long-term stability, instability in ambient air, and low electron conductivity limit its applications [47].

Park et al. [48] reported the feasibility and advantages of using prelithiated Si/SiO_x nanospheres as an advanced negative electrode. This LIC shows improved cycle performance and excellent energy density compared to conventional graphite electrodes. When compared to traditional graphite LICs, prelithiated C-coated Si/SiO_x nanospheres have better reversible capacity and rate capability. Traditional LICs employing prelithiated C-coated Si/SiO_x nanospheres exhibit significantly better cycle performance and rate capability. The as reported LIC achieves an energy density that is more than twice as high as conventional LICs.

Sugiawati et al. [49] reported another prelithiation technique that is suggested with Li^+ to reduce its potential, which would bring the insertion voltage of anodes closer to 0.1 V. LICs can function within a broader voltage window, which increases the voltage gap between the anode and cathode. When repeating Li^+ insertion/desorption procedures, the extra Li^+ can also restore the consumption of lithium-ion sources. A half-cell containing anode and Li-foil without separators can be assembled, and the anode can be prelithiated for several hours by allowing the anode to have a lower Li^+ insertion plateau. This chemical reaction between metal oxides and lithium sources results in an energy density of around 200 Wh kg^{-1}.

3.2. Cathode prelithiation

The energy density of lithium-ion batteries is greatly reduced by the irreversible loss of lithium during the first cycle. Although anode prelithiation is a popular solution to this issue, it has drawbacks of its own, including strong chemical reactivity and instability in battery production and environmental conditions. Therefore, cathode prelithiation is far less complicated in contrast [50]. Many cathode prelithiation additions have been created to date. Sacrificial Li salt additives, for instance (Li_2C_2, Li_3N, Li_2O, etc.), can effectively offset the ICL. However, undesirable gaseous N_2, CO, or CO_2 will inevitably evolve. On the other hand, ternary compounds (such as Li_5FeO_4, Li_6CoO_4, and Li_2NiO_2) don’t raise issues with gaseous evolution when used as cathode prelithiation additives. We will talk about various cathode prelithiation techniques in the following section [51–55].

3.2.1. Cathode prelithiation approaches

Sacrificial Li-rich additives have recently been considered a promising approach for cathode prelithiation. Due to their irreversible specific capacities during the initial charging process to provide an additional Li^+ source for anode prelithiation, a number of Li-rich additives, such as inorganic binary Li compounds (e.g., Li_3N and Li_2S), inorganic ternary Li compounds (e.g., Li_5Re

and Li_6CoO), and organic Li salts (e.g., Li_2DHBN and $Li_2C_2O_4$), have been investigated as cathode prelithiation additives. However, gas escape is typically associated with the delithiation of cathode prelithiation additives and must be eliminated using a secondary sealing method. A workable and economical prelithiation strategy has been proposed, along with a compatible modification that involves the introduction of Li_2S as a cathode prelithiation additive and lithium difluoro (oxalato) borate (LiDFOB) as an electrolyte additive. The built LICs demonstrated an exceptional capacity retention of 92% after 10,000 cycles at a current density of 1 A g^{-1}, along with a high energy density of 155 Wh kg^{-1} at a power density of 210 Wkg^{-1} and retaining 32 Wh kg^{-1} at an ultrahigh power density of 105 kW kg^{-1} [56].

3.2.2. Capacitive adsorption approach

Using capacitive adsorption, lithium ions are pre-stored in the cathode in this method [57]. Additionally, in the initial cycles, they serve as the supply of lithium to accomplish prelithiation. In the mean time, the capacitive adsorption's charge voltage can be altered to control the prelithiation level. The complete LIC device prelithiated using this technique has a specific capacity of 31.4 mAh g^{-1}.

Figure 6 shows the graphical representation of prelithiation by capacitive absorption. LICs experience capacity loss during their initial charge and discharge cycles due to irreversible lithium intercalation behaviors. Even though prelithiation frequently uses lithium metal, there are concerns about safety and operational complexity. As an alternative, cathode sacrificial lithium salts (CSLSs) present a feasible option because of their affordability, ease of use, and safety. This review compares several prelithiation techniques and thoroughly examines the function of prelithiation in LICs. In particular, it explores the use of CSLSs for prelithiation methods, going over the mechanisms of lithium extraction from them as well as the effects of doping levels and intrinsic properties on LIC performance.

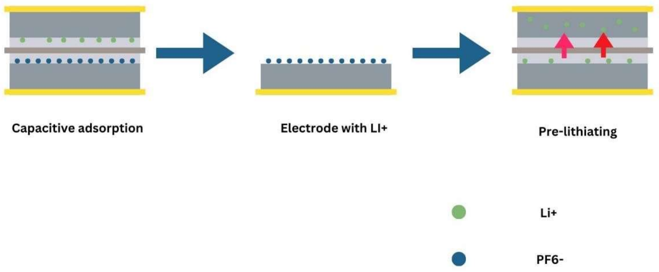

Figure 6. The prelithiation method by capacitive absorption.

The prelithiation procedure begins with the identification of sacrificial lithium salts that have a high capacity, a high degree of irreversibility in the first cycle, a low voltage for lithium extraction, and no "dead" materials left over after the initial charge. Additionally, it makes use of a number of prelithiation technologies, including the in-situ chemical (ISC) and in-situ electrochemical (ISEC) methods. CSLSs, which are used for prelithiation in LICs, are essential to the process, which attempts to make up for the irreversible capacity loss in LICs and is critical to their electrochemical performance [58]. **Table 1** shows the example of LICs using various prelithiation methods and their energy and power densities.

Table 1. Examples of LICs prepared using various prelithiation methods.

Prelithiationmaterials	Cathode	Anode	Energydensity (Wh/kg)	Powerdensity (kW/kg)	Cyclicstability	Ref.
Li		Soft Carbon (SC)	69.4	5.7	96.7 % after5000 cycles	[34]
Li_3N	AC/Li_3N	SC	214.7	19.5	75.1% retention after 5000 cycles at 3.2 $kWkg^{-1}$	[8]
Li	activatedcarbon	low surface area disordered carbon	80	8.4	85% capacity retention after 10,000 cycles	[36]
Li	X-NC	X-PNC	214.7	19.5	75.1% retention after 5000 cycles	[37]
Li	CHPC	NPC	220	0.805	90% capacity retained	[38]
Li	GCNS	HPNP	86	9.68	84% after 2500 cycle	[39]
Li	LGC-1500	LPC-3	197	11.4	92.3% retention after 5000 cycles	[41]
Li_2S	NPCNF	MNCNF	155	0.210	92% after 10,000 cycles	[12]

Basically, Li metal, Li_3N, and Li_2S are extensively used as lithium sources for prelithiation, and it is observed from **Table 1** that, among all prelithiation sources, Li metal is observed to be the best source, notably improving the energy and power densities of devices. Also, it is understood that AC/Li_3N is the best cathode material when used with SC as an anode material, where retention ration was observed to be around 75% after 5000 cycles.

4. Conclusion

A review of prelithiation processes on LICs reveals its significant potential to enhance the performance and efficiency of these devices. The various methods have been discussed with respect to prelithiation, such as chemical prelithiation, lithiation by direct contact of lithium foil, and prelithiation by half cell assembly. Further advancements in prelithiation techniques and materials expected to drive the continued improvement of LICs are discussed. In conclusion, electrochemical prelithiation holds great promise for enhancing the performance and efficiency of LICs. Continued research and development in this area is essential to unlocking the full potential of prelithiation and advancing the field of energy storage technologies.

Conflict of interest: The authors declare no conflict of interest.

References

1. Li F, Wang G, Zheng D, et al. Controlled prelithiation of SnO_2/C nanocomposite anodes for building full lithium-ion batteries. ACS Applied Materials & Interfaces. 2020; 12(17): 19423-19430. doi: 10.1021/acsami.0c00729
2. Mao Z, Song Y, Zhen AG, et al. Recycling of electrolyte from spent lithium-ion batteries. Next Sustainability. 2024; 3: 100015. doi: 10.1016/j.nxsust.2023.100015
3. Wang G, Li F, Liu D, et al. Chemical prelithiation of negative electrodes in ambient air for advanced lithium-ion batteries. ACS Applied Materials & Interfaces. 2019; 11(9): 8699-8703. doi: 10.1021/acsami.8b19416
4. Esen E, Mohrhardt M, Lennartz P, et al. Effect of prelithiation with passivated lithium metal powder on passivation films on high-energy NMC-811 and SiC_x electrodes. Materials Today Chemistry. 2023; 30: 101587. doi: 10.1016/j.mtchem.2023.101587
5. Sun C, Zhang X, Li C, et al. Recent advances in prelithiation materials and approaches for lithium-ion batteries and capacitors. Energy Storage Materials. 2020; 32: 497-516. doi: 10.1016/j.ensm.2020.07.009
6. Cementon C, Ramireddy T, Dewar D, et al. We may be underestimating the power capabilities of lithium-ion capacitors. Journal of Power Sources. 2024; 591: 233857. doi: 10.1016/j.jpowsour.2023.233857
7. Jin L, Shen C, Shellikeri A, et al. Progress and perspectives on pre-lithiation technologies for lithium ion capacitors. Energy & Environmental Science. 2020; 13(8): 2341-2362. doi: 10.1039/d0ee00807a
8. Sun C, Zhang X, Li C, et al. High-efficiency sacrificial prelithiation of lithium-ion capacitors with superior energy-storage performance. Energy Storage Materials. 2020; 24: 160-166. doi: 10.1016/j.ensm.2019.08.023
9. Xu J, Gao B, Huo KF, et al. Recent progress in electrode materials for nonaqueous lithium-ion capacitors. Journal of Nanoscience and Nanotechnology. 2020; 20(5): 2652-2667. doi: 10.1166/jnn.2020.17475
10. Meng Q, Li G, Yue J, et al. High-performance lithiated SiO_x anode obtained by a controllable and efficient prelithiation strategy. ACS Applied Materials & Interfaces. 2019; 11(35): 32062-32068. doi: 10.1021/acsami.9b12086
11. Zou Y, Zhang Z, Chen P, et al. Improving the cycle performance of porous schiff-base polymer electrode materials in lithium-ion batteries by prelithiation. ACS Applied Energy Materials. 2023; 6(21): 11322-11330. doi: 10.1021/acsaem.3c02197
12. Chen M, Huang X, Yang C, et al. Simultaneous prelithiation and compatible modification toward ultrafast and ultrastable lithium-ion capacitors. ACS Applied Energy Materials. 2022; 5(8): 9684-9691. doi: 10.1021/acsaem.2c01339
13. Jang J, Ki H, Kang Y, et al. Chemically prelithiated graphene for anodes of li-ion batteries. Energy & Fuels. 2020; 34(10): 13048-13055. doi: 10.1021/acs.energyfuels.0c01854
14. Shen Y, Zhang J, Pu Y, et al. Effective chemical prelithiation strategy for building a silicon/sulfur li-ion battery. ACS Energy Letters. 2019; 4(7): 1717-1724. doi: 10.1021/acsenergylett.9b00889
15. Yan MY, Li G, Zhang J, et al. Enabling SiO_x/C anode with high initial coulombic efficiency through a chemical pre-lithiation strategy for high-energy-density lithium-ion batteries. ACS Applied Materials & Interfaces. 2020; 12(24): 27202-27209. doi: 10.1021/acsami.0c05153
16. He X, Mu X, Wang Y, et al. Fast and scalable complete chemical prelithiation strategy for Si/C anodes enabling high-performance Li_xSi–S full cells. ACS Applied Energy Materials. 2023; 6(12): 6790-6796. doi: 10.1021/acsaem.3c00980
17. Yang Y, Wang J, Kim SC, et al. In Situ prelithiation by direct integration of lithium mesh into battery cells. Nano Letters. 2023; 23(11): 5042-5047. doi: 10.1021/acs.nanolett.3c00859
18. Choi J, Jeong H, Jang J, et al. Weakly solvating solution enables chemical prelithiation of Graphite–SiO_x anodes for high-energy li-ion batteries. Journal of the American Chemical Society. 2021; 143(24): 9169-9176. doi: 10.1021/jacs.1c03648
19. Wang Y, Lu J, Qiao Y, et al. The efficient solid electrochemical corrosion prelithiation of graphite and SiO_x/C anodes for longer-lasting lithium ion batteries. Journal of Power Sources. 2023; 580: 233402. doi: 10.1016/j.jpowsour.2023.233402
20. Johnson R, Baji DS, Nair S, et al. Spent-graphite anode from failed batteries: Regeneration and chemical prelithiation for sustainable fresh Li-ion batteries. Journal of Industrial and Engineering Chemistry. 2024; 133: 473-481. doi: 10.1016/j.jiec.2023.12.024
21. Wang H, Wu W, Jia Q, et al. Scalable layer-by-layer stacking of the Silicon-Graphite composite: Prelithiation strategy of the high-capacity anode for energy/power-dense li batteries. Industrial & Engineering Chemistry Research. 2022; 61(22): 7442-

7450. doi: 10.1021/acs.iecr.1c04702

22. Ying K C, Ping H H, C, W. Lan. Scalable chemical prelithiation of SiO/C anode material for lithium-ion batteries. Journal of Power Sources. 2023; 558: 232599. doi: 10.1016/j.jpowsour.2022.232599
23. Wang F, Wang B, Li J, et al. Prelithiation: A crucial strategy for boosting the practical application of next-generation lithium ion battery. ACS Nano. 2021; 15(2): 2197-2218. doi: 10.1021/acsnano.0c10664
24. Jia T, Zhong G, Lv Y, et al. Prelithiation strategies for silicon-based anode in high energy density lithium-ion battery. Green Energy & Environment. 2023; 8(5): 1325-1340. doi: 10.1016/j.gee.2022.08.005
25. Berhaut CL, Dominguez DZ, Tomasi D, et al. Prelithiation of silicon/graphite composite anodes: Benefits and mechanisms for long-lasting Li-Ion batteries. Energy Storage Materials. 2020; 29: 190-197. doi: 10.1016/j.ensm.2020.04.008
26. Shi J, Su CC, Amine R, et al. Prelithiation of lithium peroxide for silicon anode: achieving a high activation rate. ACS Applied Materials & Interfaces. 2023; 15(22): 26710-26717. doi: 10.1021/acsami.3c03312
27. Huang B, Huang T, Wan L, et al. Pre-lithiating SiO anodes for lithium-ion batteries by a simple, effective, and controllable strategy using stabilized lithium metal powder. ACS Sustainable Chemistry & Engineering. 2021; 9(2): 648-657. doi: 10.1021/acssuschemeng.0c05851
28. Lai P, Liu C, Sun Z, et al. A highly effective and controllable chemical prelithiation of Silicon/Carbon/Graphite composite anodes for lithium-ion batteries. Solid State Ionics. 2023; 403: 116415. doi: 10.1016/j.ssi.2023.116415
29. Zhang X, Qu H, Ji W, et al. Fast and Controllable Prelithiation of Hard Carbon Anodes for Lithium-Ion Batteries. ACS Applied Materials & Interfaces. 2020; 12(10): 11589-11599. doi: 10.1021/acsami.9b21417
30. Huang YE, Huang PW, Zhong Y, et al. Achieving high initial coulombic efficiencies and cycle stability of free-standing anodes by chemical prelithiation of carbon matrix. Applied Surface Science. 2023; 612: 155691. doi: 10.1016/j.apsusc.2022.155691
31. Yue H, Zhang S, Feng T, et al. Understanding of the Mechanism Enables Controllable Chemical Prelithiation of Anode Materials for Lithium-Ion Batteries. ACS Applied Materials & Interfaces. 2021; 13(45): 53996-54004. doi: 10.1021/acsami.1c16842
32. Divya ML, Aravindan V. Electrochemically generated γ-$Li_xV_2O_5$ as insertion host for high-energy Li-ion capacitors. Chemistry – An Asian Journal. 2019; 14(24): 4665-4672. doi: 10.1002/asia.201900946.
33. Zhang X, Hou X, Hou Y, et al. Insights into chemical prelithiation of SiO_x/Graphite composite anodes through scanning electron microscope imaging. ACS Applied Energy Materials. 2023; 6(15): 7996-8005. doi: 10.1021/acsaem.3c01077
34. Sun C, Zhang X, An Y, et al. Molecularly chemical prelithiation of soft carbon towards high-performance lithium-ion capacitors. Journal of Energy Storage. 2022; 56: 106009. doi: 10.1016/j.est.2022.106009
35. Arnaiz M, Canal-Rodríguez M, Martin-Fuentes S, et al. Roll-to-roll double side electrode processing for the development of pre-lithiated 80 F lithium-ion capacitor prototypes. Journal of Physics: Energy. 2023; 6(1): 015001. doi: 10.1088/2515-7655/ad064e
36. Veluri PS, Katchala N, Anandan S, et al. Petroleum coke as an efficient single carbon source for high-energy and high-power lithium-ion capacitors. Energy & Fuels. 2021; 35(10): 9010-9016. doi: 10.1021/acs.energyfuels.1c00665
37. Kong L, Xu X, Hou L, et al. Phosphorus and nitrogen co-doped carbon nanoparticles as both anode and cathode materials with enhanced Li^+/PF_6^- storage for high energy density lithium-ion capacitors. ACS Sustainable Chemistry & Engineering. 2023; 11(34): 12583-12594. doi: 10.1021/acssuschemeng.3c02068
38. Han L, Kang S, Zhu X, et al. High-performance lithium-ion capacitors produced by atom-thick carbon cathode and nitrogen-doped porous carbon anode. Energy & Fuels. 2021; 35(20): 16894-16902. doi: 10.1021/acs.energyfuels.1c02509
39. Tan JY, Su JT, Wu YJ, et al. Hollow porous α-Fe_2O_3 nanoparticles as anode materials for high-performance lithium-ion capacitors. ACS Sustainable Chemistry & Engineering. 2021; 9(3): 1180-1192. doi: 10.1021/acssuschemeng.0c06650
40. Ahn S, Fukushima M, Nara H, et al. Effect of fluoroethylene carbonate and vinylene carbonate additives on full-cell optimization of Li-ion capacitors. Electrochemistry Communications. 2021; 122: 106905. doi: 10.1016/j.elecom.2020.106905
41. Yang Z, Guo H, Yan G, et al. High-value utilization of lignin to prepare functional carbons toward advanced lithium-ion capacitors. ACS Sustainable Chemistry & Engineering. 2020; 8(31): 11522-11531. doi: 10.1021/acssuschemeng.0c01949
42. Fan Z, Ding B, Li Z, et al. In-situ prelithiation of electrolyte-free silicon anode for sulfide all-solid-state batteries. eTransportation. 2023; 18: 100277. doi: 10.1016/j.etran.2023.100277
43. Wang YK, Yang SY, Yang Y, et al. In-situ synthesized cathode prelithiation additive to compensate initial capacity loss for

lithium ion batteries. Journal of Electroanalytical Chemistry. 2022; 919: 116567. doi: 10.1016/j.jelechem.2022.116567

44. Sander M, Magar SD, Etter M, et al. The "In situ electrolyte" as a sustainable alternative for the realization of high-power devices. Chem. Sus. Chem. 2024; 17(5): e202301746. doi: 10.1002/cssc.202301746
45. Ren Y, Li J, Guo J. Perforated active carbon and pre-lithiated graphite electrodes for high performance hybrid lithium-ion capacitors. International Journal of Electrochemical Science. 2020; 15(3): 2659-2666. doi: 10.20964/2020.03.03
46. Arnaiz M, Shanmukaraj D, Carriazo D, et al. A transversal low-cost pre-metallation strategy enabling ultrafast and stable metal ion capacitor technologies. Energy & Environmental Science. 2020; 13(8): 2441-2449. doi: 10.1039/d0ee00351d
47. Anothumakkool B, Wiemers-Meyer S, Guyomard D, et al. Cascade-type prelithiation approach for Li-ion capacitors. Advanced Energy Materials. 2019; 9(27). doi: 10.1002/aenm.201900078
48. Park E, Chung DJ, Park MS, et al. Pre-lithiated carbon-coated Si/SiO nanospheres as a negative electrode material for advanced lithium ion capacitors. Journal of Power Sources. 2019; 440: 227094. doi: 10.1016/j.jpowsour.2019.227094
49. Sugiawati VA, Vacandio F, Yitzhack N, et al. Direct pre-lithiation of electropolymerized carbon nanotubes for enhanced cycling performance of flexible Li-ion micro-batteries. Polymers. 2020; 12(2): 406. doi: 10.3390/polym12020406
50. Ding R, Tian S, Zhang K, et al. Recent advances in cathode prelithiation additives and their use in lithium–ion batteries. Journal of Electroanalytical Chemistry. 2021; 893: 115325. doi: 10.1016/j.jelechem.2021.115325
51. Wu Y, Zhang W, Li S, et al. $Li_2Cu_{0.1}Ni_{0.9}O_2$ with Copper Substitution: A new cathode prelithiation additive for lithium-ion batteries. ACS Sustainable Chemistry & Engineering. 2023; 11(3): 1044-1053. doi: 10.1021/acssuschemeng.2c05779
52. Pan Y, Qi X, Du H, et al. Li_2Se as a cathode prelithiation additive for lithium-ion batteries. ACS Applied Materials & Interfaces. 2023; 15(15): 18763-18770. doi: 10.1021/acsami.2c21312
53. Watanabe T, Tsuda T, Ando N, et al. An improved pre-lithiation of graphite anodes using through-holed cathode and anode electrodes in a laminated lithiumion battery. Electrochimica Acta. 2019; 324: 134848. doi: 10.1016/j.electacta.2019.134848
54. Huo X, Gong X, Liu Y, et al. Conformal 3D Li/$Li_{13}Sn_5$ scaffolds anodes for high-areal energy density flexible lithium metal batteries. Advanced Science. 2024; 11(14). doi: 10.1002/advs.202309254
55. Shen C, Ye D, Jin L, et al. A simple and scalable prelithiation approach for high energy and low cost lithium ion sulfur batteries. Journal of The Electrochemical Society. 2020; 167(6): 060517. doi: 10.1149/1945-7111/ab8408
56. Betz J, Nowak L, Winter M, et al. An approach for pre-lithiation of $Li_{1+x}Ni_{0.5}Mn_{1.5}O_4$ cathodes mitigating active lithium loss. Journal of The Electrochemical Society. 2019; 166(15): A3531-A3538. doi: 10.1149/2.1221914jes
57. Zhu H, Li J, Wu D, et al. A novel pre-lithiation strategy achieved by the capacitive adsorption in the cathode for lithium-ion capacitors. Renewable Energy. 2023; 217: 119163. doi: 10.1016/j.renene.2023.119163
58. Su K, Wang Y, Yang B, et al. A Review: Pre-lithiation strategies based on cathode sacrificial lithium salts for lithium-ion capacitors. Energy & Environmental Materials. 2023; 6(6). doi: 10.1002/eem2.12506

Mechanical Engineering Advances 2024, 2(2), 1746.
https://doi.org/10.59400/mea.v2i2.1746

Review

The development of machine vision and its applications in different industries: A review

Lili Zhang[1], Xiaowei Jia[1], Qing Chang[1], Xin Liu[1], Zhicheng Zhang[1,*], Yanghao Cao[1], Junjie Liu[2], Yizhao Yang[1]

[1] Machinery and Electronics Engineering College, Shandong Agriculture and Engineering University, Zibo 255300, China
[2] Ocean University of China, Qingdao 266100, China
*** Corresponding author:** Zhicheng Zhang, z2022046@sdaeu.edu.cn

CITATION

Zhang L, Jia X, Chang Q, et al. The development of machine vision and its applications in different industries: A review. Mechanical Engineering Advances. 2024; 2(2): 1746. https://doi.org/10.59400/mea.v2i2.1746

ARTICLE INFO

Received: 20 September 2024
Accepted: 12 November 2024
Available online: 22 November 2024

Abstract: In recent years, the development of machine vision research is rapid in several areas. In order to promote the better development of machine vision research, it is necessary to clarify its development and application direction. At present, there are few reviews on the application direction of machine vision. This paper sorts out the application of machine vision in various fields, and summarizes the current application status of machine vision from four main functions: recognition, measurement, classification and detection. This paper mainly introduces the improvement of different algorithms of machine vision and its application in medical, agriculture, manufacturing and other industries, providing guidance for the selection of machine vision research direction.

Keywords: machine vision; algorithm; applications; manufactruing

1. Introduction

Machine Vision (MV), also known as Computer Vision (CV), is an important section of Artificial Intelligence. As shown in **Figure 1**, it mainly helps people make decisions from four aspects: recognition, measurement, classification and detection to reduce workload. It helps human beings in measuring, deciding, and judging by using machines. **Figure 2** shows the evolution of machine vision. Since the concept of machine recognition was proposed in 1950, MV has experienced a long development process, with MV developing, it has plenty of applications in image processing, robotics, industry automation, optics, and so on. The versatility and flexibility of MV applications have been significantly improved. In this paper, the research group reviewed the MV applications released from 2018 to 2022 in these areas. **Figure 1** is a simple sketch of the mainly application areas of MV. And **Figure 2** shows a brief history of MV. The idea of MV was proposed in 1950s, but most applications were used in 2000s, because of the rapid development of computer science in 1990s.

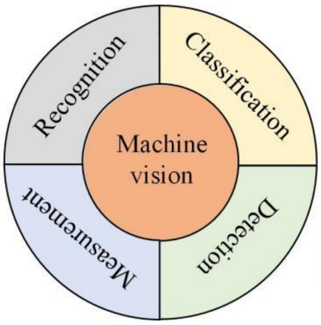

Figure 1. The main function of machine vision.

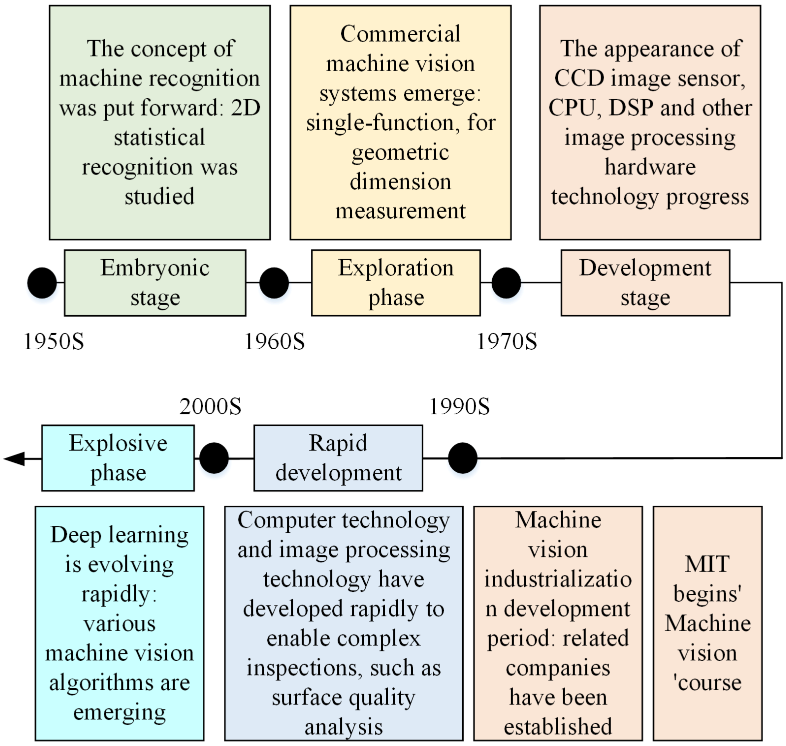

Figure 2. The main development process of machine vision.

2. Algorithm of machine vision

From the year of 2018, MV has been widely used in different areas because the development of algorithms and some research groups have summarized it. For example, In the paper of WU, Li, and Yao, the methods, applications, and challenges of Deep Learning in MV tasks have been reviewed. Also, they introduced some basic knowledge of algorithms in this area [1]. And Katti et al. studied the MV benefits from human contextual expectations [2]. This research group evaluate some MV algorithms with car/person classification. In Gorodokin's research, MV has been applied in traffic area [3]. By using MV algorithm, the congestion has been relieved, the drivers do not waste lots of time on waiting. Panagakis et al. summarized the application of tensor methods in Deep Learning, especially on visual data analysis and MV applications [4]. Besides, Zhang et al. reviewed adversarial network applications in MV [5]. They pointed out that applications have been more and more extensive, but they also came up with several challenges in this area. Also, Gustafsson et al. evaluate scalable Bayesian Deep Learning methods for robust MV [6]. The results show that ensembling consistently provides more reliable and practically useful uncertainty estimates. The research group of Whatmough et al. proposed a new CNN framework in MV area [7]. And the experimental results show that it can achieve very high energy efficiencies. Shu, Xiong, and Fan developed an interactive design of intelligent MV based on human-computer interaction mode [8]. They used several matrices to evaluate this mode. Wu et al. developed a MV algorithm to detect electrical connector defects. The accuracy of this work is 93.5% [9]. Wu et al. summarized the progress and challenges of applying 2D material photodetectors in sense-memory-computational integration and biomimetic image sensors for MV [10]. In underwater tasks, MV has a lot of applications to aid operators. And this area has been reviewed by Reggiannini [11].

These researches reviewed the development of MV algorithms before 2022. From the above works, it could be concluded that MV algorithm is an important topic and people would like to use MV as a tool in manufacturing, medicine, agriculture, and so on.

In the area of MV, Machine Learning is the most widely used tool. There are many researches to improve the accuracy and speed of MV by changing the Machine Learning algorithms. Akhtar et al. reviewed several works on it [12]. Deep Neural Networks behave well in many MV tasks. However, it requires a lot of parameters and operations. Goel et al. [13] surveyed the low-power MV methods to finish the same tasks with less memory requirement. O'Mahony et al. [14] compares the benefits and drawbacks of Deep Learning and traditional MV. The aim of this work is to improve the performance of MV algorithms and help operators get accurate results. Based on the analysis of Yang et al. [15], the research group proposed a GPU scheduler for MV applications. In real applications, the speed of operating MV is important. The operation cannot occupy a lot of time.

In the area of MV, recognizing images is important. Baygin et al. pointed out that MV is widely used in production lines because of it is low-cost and high-precision on image recolonization [16]. Talebi and Peyman's learned image resizer is jointly trained with a baseline vision model. In this paper, a method of resetting the image size is proposed and applied to the existing classification algorithm shown in **Figures 3** and **4**. It is found that the image quality is improved after resetting, and the **Figure 5** shows the effect of resetting the image size [17]. Several researchers focus on the integration of MV and national language processing. El-Komy et al. [18] generated a Faster Region Convolutional Neural Network based central server to detect the objects in the image to inform the blind person to avoid obstacles in their way. Li et al. [19] generated a new framework of machine learning algorithm for recognizing complex SEM image automatedly. Their framework detected the position of each molecule and labeled the chirality accurately. Besides, this framework does not require plenty of data, which is an important advantage. After summarizing the coding in both human and machine vision, Hu et al. [20] believed that the signal fidelity-driven coding pipeline design limits the capability of the existing image/video coding frameworks to fulfill the needs of both machine and human vision. Thus, they generated a new image coding framework to support both MV and human perception tasks together. In the work of Roggi et al. [21], an UAV-based automatic inspection method for photovoltaic plants analyzing has been proposed. Besides, testing a vision-based guidance method has been developed to finish this task. When autonomous vehicles driving into sun, the direct sunlight is a significant influence. Thus, Paul et al. [22] apply high dynamic range imaging algorithms to the MV system and measured the accuracy of performance in direct sunlight. In MV area, RGB images are usually used to train the algorithm. Datta et al. [23] developed a new algorithm to use raw images and the accuracy is acceptable. In the work of Rebecq et al. [24], they take a different view and propose to apply existing, mature MV techniques to video reconstructed from event data. They improve the quality of image by using their algorithm. Mennel et al. [25] show that an image sensor could constitute an ANN by itself. Besides, this framework can simultaneously sense and process optical images without latency. In real-time application, it is difficult for MV to implement at the edge. In order to solve this problem, Gamanayake et al. [26] developed a novel MV algorithm, which is named cluster pruning. The above mentioned works help people to detect objects with the assistant of MV.

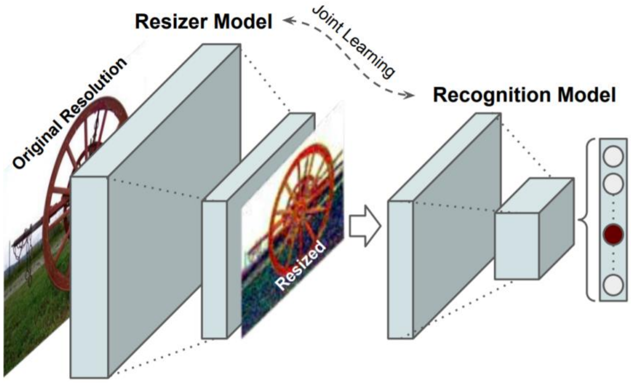

Figure 3. Proposed framework for joint learning of the image. Resizer and recognition models [17].

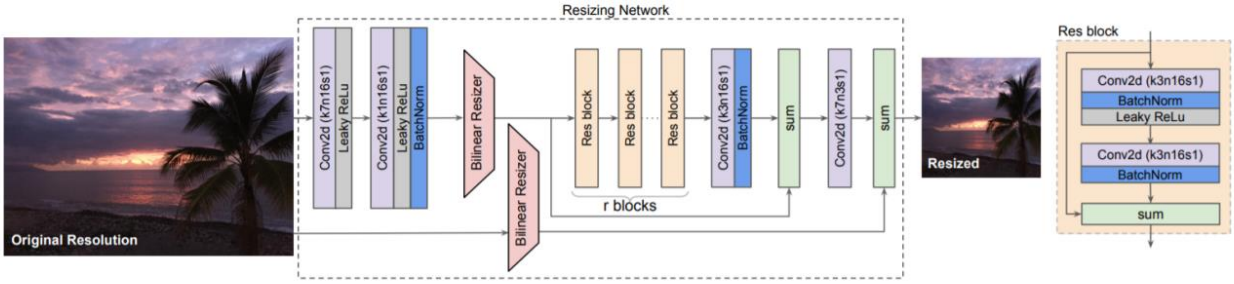

Figure 4. Proposed CNN model for resizing images [17].

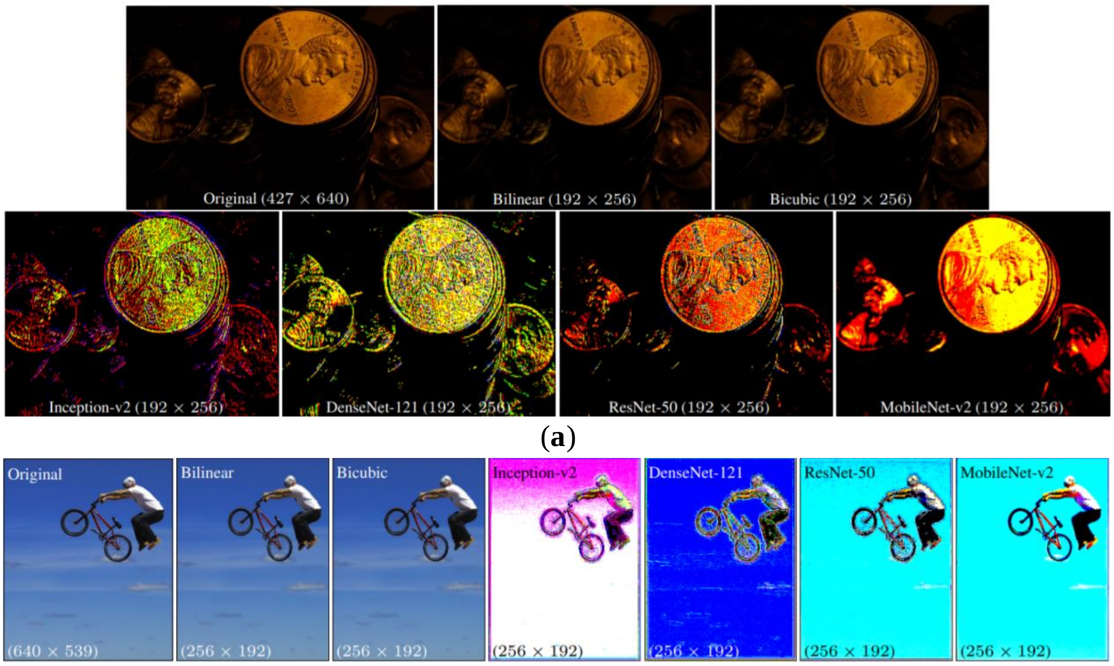

(**a**)

(**b**)

Figure 5. Examples of the proposed learned resizer trained with various classification models. **(a)** Improved recognition performance of coins; **(b)** improved recognition performance of bicycle rider.

Besides recognizing stationary objects, MV can also be used to detect moving 3D objects. MV is a good tool for object classification in production line. Cong et al. designed a MV system of two robot arms to do classification based on the shape and size of the objects [27]. In Gubbi's research, with the help of MV, the performance of predicting target tracking has improved significantly [28]. Wang et al. proposed a prototype neuromorphic vision system by networking retinomorphic sensor with a memristive crossbar [29]. This system is developed for fast letter recognition and object tracking. There was a paper published in the 2021 British Machine Vision Conference. In this work, multi-person activity recognition problem is tackled. They developed a new multi-branch CNN to increase the accuracy. This algorithm is trained end-to-end by using a multi-task learning framework [30]. In today's world, 3D object detection and tracking is an essential constituent in several applications. In the research of Shreyas et al., various 3D object detection and tracking methods are explained detailly for plenty of CV applications [31]. Ding et al. believed that moving object detection in image is a crucial point in CV research [32]. They developed a moving object detection algorithm based on robust image feature threshold segmentation with improved optical flow estimation. Two different optical flow methods has been presented in this paper. Autonomous driving in complex scenes is a challenge in auto industry. Fang's group improved the Mask R-CNN by replacing the backbone network ResNet with ResNeXt. In order to more intuitively evaluate the target detection and segmentation effects of the improved Mask R-CNN algorithm in different complex scenes, cityscape test dataset was selected for testing, and the experimental results were shown in **Figures 6** and **7**. The target detection and segmentation accuracy increased by 4.73% and 3.96% separately. In the manufacturing of gears, quality control has become a priority [33]. The aim of Moru and Borro's work is to deploy an improved MV application to determine the precise measurement of industrial gears [34]. Li et al. developed a Deep Learning algorithm to classify objects [35]. This MV framework can also be extended to other spectral-domain measurement systems. In the research of Yin's group, they proposed a novel method to count vehicles based on MV algorithm [36]. In bridge monitoring, it is important to identify moving loads accurately. Based on MV, Dan's group generated a novel method to tackle this problem [37].

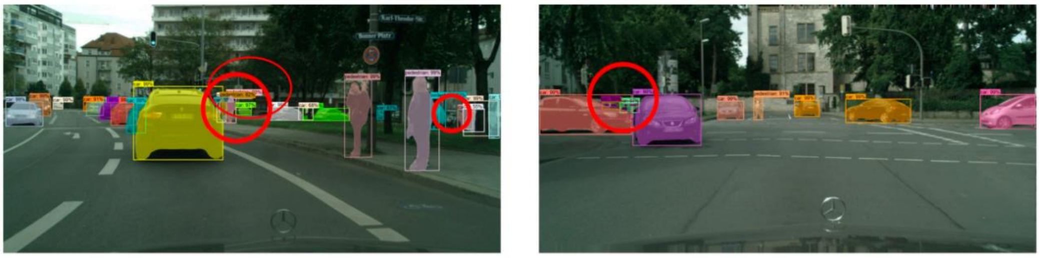

Figure 6. Test results of Mask R-CNN on cityscapes test dataset [33].

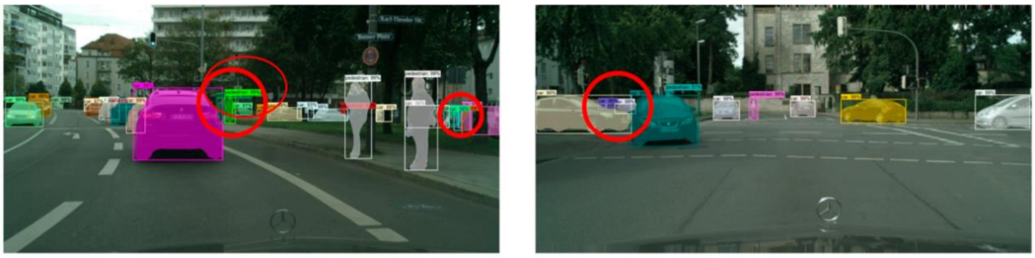

Figure 7. Test results of Improved Mask R-CNN on cityscapes test dataset [33].

Besides, some other MV algorithms are generated to help human beings to finish some work. In order to suppress impulse noise in MV, median filter is one of the predominant filters. Appiah et al. improve the output and running time of median filter. this research gives a discussion on pros and cons of several different median filters [38]. In the research of Kaushal's group, they found that if diversity-based subset selection done in the right way, the accuracy of the algorithm will increase by 5–10% [39]. And Zhang et al. present an effective method to improve the fine-level retrieval performance [40]. This method is based on a multi-level Gaussian loss function, and it takes the advantages of class-level similarity learning and full-level hierarchy labels in training. Semitsu et al. proposed a new method to measure the contributions of multiple datasets [41]. Contributions are calculated in a fair way that each trial are evaluated not by its improvements of accuracy, but by the number of data needed to make the improvements. Riba et al. introduced Kornia, which is an open-source MV library [42]. This library is used in MV to improve performance using hardware acceleration. In the area of big data, image and video coding techniques have developed rapidly in these years [43]. In order to fulfill the needs of both machine and human vision, Yang et al. developed a novel face image coding framework by considering both the compressive and generative models. Suma reviewed the applications of computer vision that is helpful in the interaction between the human and the machines [44]. The following **Table 1** and **Figure 8** are visual summary of this chapter.

Table 1 briefly describes the work done on the functional application of different algorithms.

Table 1. Functions and applications of different algorithms.

Authors	Function	Application	Research outcome
Katti [2]	Detection	Traffic	Katti et al. studied the CV benefits from human contextual expectations.
Gorodokin [3]	Detection	Traffic	By using CV algorithm, the congestion has been relieved, the drivers do not waste lots of time on waiting.
Cong [27]	Detection	3D object detection	This work designed a MV system of two robot arms to do classification based on the shape and size of the objects
Shreyas [31]	Detection	3D object detection	In this research, various 3D object detection and tracking methods are explained detailly for plenty of CV applications.
Yin [36]	Detection	vehicle detection	This work proposed a novel method to count vehicles based on MV algorithm.
Wu [10]	Measurement	2D material photodetectors	This work summarized the progress and challenges of applying 2D material photodetectors in sense-memory-computational integration and biomimetic image sensors for MV

Table 1. (*Continued*).

Authors	Function	Application	Research outcome
Moru [35]	Measurement	measurement	This work deploys an improved CV application to determine the precise measurement of industrial gears.
Baygin [16]	Recognition	Image recognization	This work pointed out that MV is widely used in production lines because of it is low-cost and high-precision on image recolonization.
El-Komy [18]	Recognition	Image recognization	This work generated a Faster Region Convolutional Neural Network based central server to detect the objects in the image to inform the blind person to avoid obstacles in their way

The research group generated a topology diagram of this section and it is shown in **Figure 8**. This chapter introduces different algorithms of MV, such as Neural Network and Deep Learning. Also, MV could be used to detect both 3D and 2D objects or images.

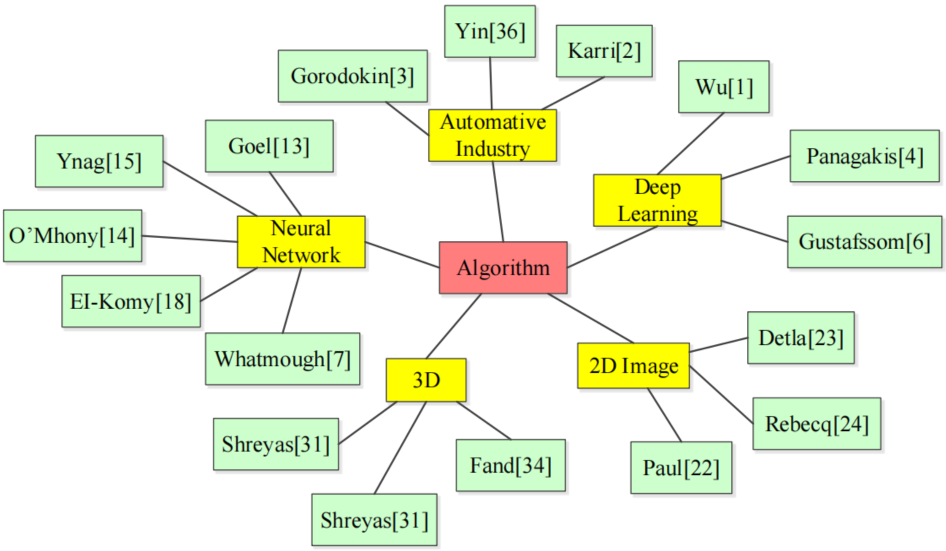

Figure 8. Topology Diagram of Algorithm of Machine Vision.

3. Agricultural applications of machine vision

In recent years, the application of MV technology in agriculture has become quite extensive and significantly promoted the development of intelligent agriculture. Many scholars did research on the application of MV technology in the agricultural field and this section summarized these results.

Nowadays, MV technology has been widely used in seed selection achieved a good classification effect yet. TU Ke-ling et al. [45] used MV technology to study the classification of high-quality and low-quality pepper seeds. They collected and processed the images and feature data, established a multi-layer perceptron neural network model with 15 features as variate. The experiment of pepper seed germination was also carried out. Nadia Ansari et al. [46] produced a total of 375 rice seed images from 3 varieties, extracted 20 important features, and then used relevant algorithms to establish a classification model to achieve the purity detection of rice seeds. Similarly, in the paper of Keling Tu and Peng Xu, the detection of corn seed purity was studied. Keling Tu et al. [47] scanned the images of both the germ and non-germ surfaces of the seeds and used them as data set. Then they used the fine-tuned transfer learning of VGG16 network to identify and classify the seed images. **Figure 9** shows that Peng Xu et al. [48] combined MV with deep learning algorithms and used the Convolutional Neural Networks (CNN) model to automatically classify five kinds of corn seeds.

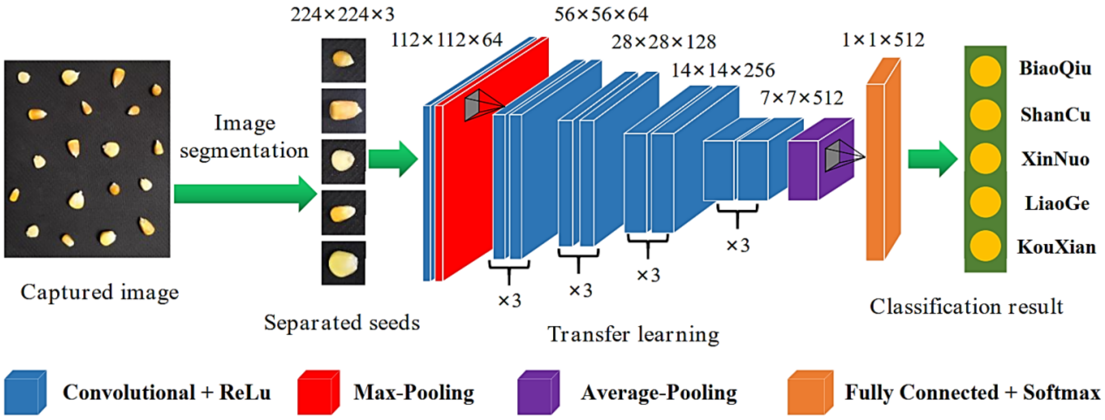

Figure 9. Process of transfer learning and classification of maize seeds [48].

There are plenty of MV applications on fruit classification. Mohammad Saber Iraji, S. Dhakshina Kumard and Li Liu all studied tomato grading with MV technology. Mohammad Saber Iraji's research proposed a deep stacked sparse auto-encoders (DSSAEs) method for tomato quality grading using image data directly based on MV and soft computing techniques [49]. The classification system of S. Dhakshina Kumar et al. performs classifications of tomatoes in three stages i.e. Tomato/Non-Tomato, Good/Defective and the type of defect, with digital images of samples captured in an experimental setup deployed using microcontroller [50]. Liu et al. [51] built a comprehensive tomato classifier based on the color, shape and size diameters. A grading platform was set up to verify the effect of the classifier [51]. MV application in beans is another important area and their classification has been getting attention. Belan et al. [52] proposed computational approaches for segmentation, classification, and detection of three of the main defects founded in beans (broken, bored, and moldy). In this way, grains can be located in the analyzed image, even if they are glued to each other. Then appropriate software together with the equipment were developed. Besides, Zhou et al [53]. developed a real-time computer-aided potato inspection system which can be used to sort out the good and bad potatoes. It can handle up to 50 potato images. Thinh et al [54]. created a system that can classify mangoes in terms of color, volume, size, shape and fruit density. This study also described the method and terminology of several tools that are used for image processing and analysis in sorting and classification of mangoes based on Artificial Intelligence. Ismail et al. [55] proposed and designed a low-cost MV system for grading the fruits based on their outer appearance and freshness. This system uses an end-to-end approach and can work both in offline and real time mode.

In addition, MV can also be used to estimate the volume of each crop fruit, so as to estimate global production Uluişik et al. [56] researched volume estimation of tomato. Five different images of a tomato are captured using high resolution digital cameras. Volume of the fruit is computed by estimating horizontal and vertical distance of captured images and the results are validated with experimental results. Innocent Nyalala et al. [57] developed a novel tomato weight and volume prediction method for tomatoes with no and partial occlusions. Polygon approximation for concave and convex point extraction algorithms were used to segment the occluded tomatoes. Furthermore, they developed seven models for regression using single-tomato image features and the seven models were compared. Besides, Concha-Meyer et al. [58] used MV technique to determine the volume of raw agricultural products with an irregular shape, such as tomato, white button mushroom and strawberry. In this study, the volume of each fruit was measured in less than five seconds.

Ripeness estimation of fruits and vegetables is a key factor for the optimization of field management and the harvesting of the desired product quality. Vrochidou et al. [59] investigated the most recent applications of MV techniques for ripeness estimation related to grapes, and provided an overview of the grape ripening estimation work. The paper also highlighted challenges and limitations of different estimation methods. In the paper of [60], a nondestructive approach was developed to estimate the physicochemical properties and ripeness levels of apples in orchard environments. They recorded videos of apples at four levels of ripeness and extracted color and texture features from these samples. Then five physicochemical properties were estimated and measured using neural network and corresponding algorithm. Anindita Septiarini et al. [61] proposed a classification method for the maturity level of oil palm fresh fruit bunch. The proposed method can distinguish three levels of maturity (raw, ripe, and half-ripe) according to color and texture features.

In the process of agricultural production, machine vision technology can be used to find the disease situation of crops in time, so as to facilitate the treatment of diseases and avoid production reduction. Different rice diseases and insect pests have similar symptoms shown in **Figure 10**. It takes experienced workers and huge time to distinguish them artificially, and machine vision can capture small differences between different diseases, at the same time can reduce the use of separate time. Mahadi Hasan Kamrul et al. developed a model which can recognize six main rice disease that is commonly seen in the paddy fields of Bangladesh [62]. This research builds on authentic data set and the accuracy rate of the model is high. Mahmud et al. [63] established an artificial cloud lighting condition system for detecting strawberry powdery mildew leaf disease. Texture analysis based on color co-occurrence matrix was used to extract image features and discriminant analysis (quadratic) for classification. Kim et al. [64] developed an onion downy mildew detection system for large-scale automatic monitoring. Symptom identification is realized based on the images periodically captured through automatic detection, and the crop disease region can be positioned. Palei et al. [65] overviewed the papers related to citrus diseases and fruit grading between 2010 and 2021. Symptomatic information about citrus diseases is provided, and the related techniques (image processing, machine learning and deep learning) are analyzed. In the paper of [66], a simple and inexpensive detection system of ochre spot disease was studied, and the images used in the system were captured from a low-cost RGB camera which is placed on board a drone. And the algorithm which could process limited-quality images from a low-cost camera has been developed else. Jiang et al. [67] proposed a method for detecting the infected apples using convolution neural network and it can timely prevent further infections caused by environmental factors.

Figure 10. A little portion of dataset [62].

Pest identification and classification based on MV is a prerequisite for accurate and real-time pesticide spraying of precision agriculture. Lins et al. [68] presented a method to automate the counting and classification of aphids using image processing, MV, and deep learning. A software named AphidCV was developed for implementing the proposed method. The disadvantage of this method is that the overlapping insects are classified as one. Liu et al. [69] developed a multispectral MV system to detect common invertebrate pests on green leaves in natural environment.

For intelligent agriculture, identifying weeds based on MV is a prerequisite for accurate weed removal. In the research of [70], an efficient automated weed detection system was developed. Besides, two kinds of feature extraction techniques, two classification algorithms and two data sets were touched on, and their influence on recognition accuracy was analyzed. Abouzahir et al. [71] proposed a new method of weed detection. **Figure 11** shows that a histogram based on color indices is used to discriminate between three classes: soil, soybean and weeds. However, a major drawback of this method is that color indices can be sometimes sensitive to outdoor illumination changes, which will affect the performance of the system. In the paper of [72], two main challenges (dealing with changing light and crop/weed discrimination) are firstly listed, followed by the detailed review of methods for dealing with those challenges. Wu et al. [73] analyzed the advantages and disadvantages of several existing methods, and introduced several related plant leaves, weed data sets, and weeding machinery. Lastly, the problems and difficulties of the existing weed detection methods are analyzed, and the development trend of future research is prospected.

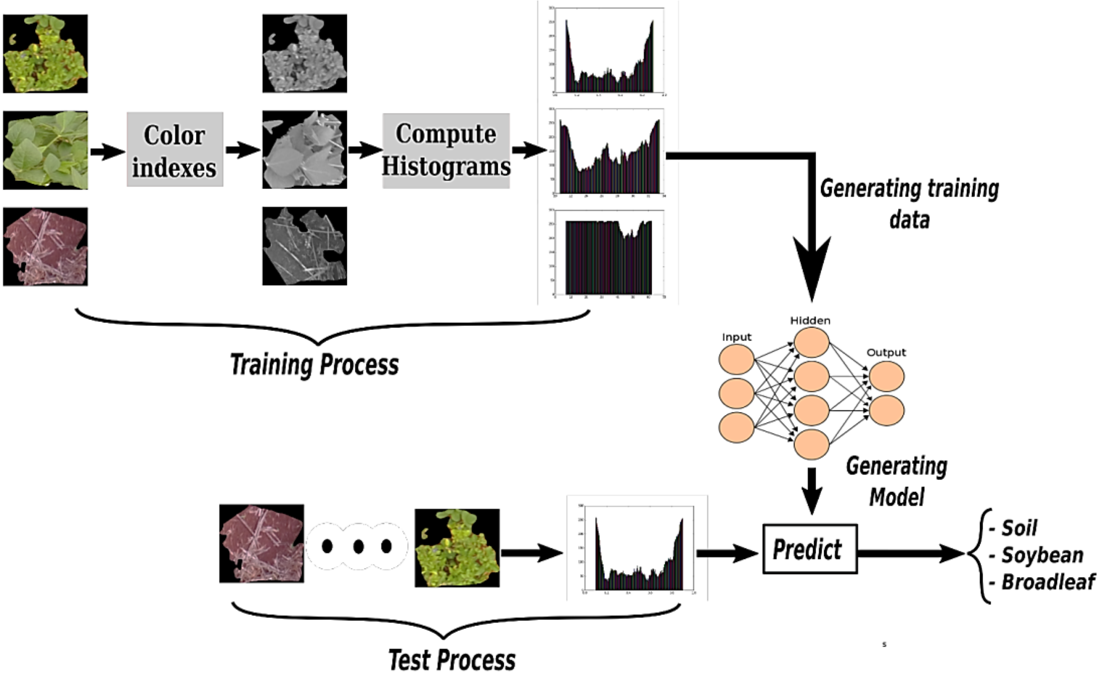

Figure 11. Classification system based on the color indices to predict plants types as well as soil and residues [72].

In recent years, MV-based methods have been applied to monitor animal behaviors worldwide. In the study of [74], a new deep learning method (i.e., an integration of background-subtraction and inter-frame difference) was developed for automatically recognizing dairy calf scene-interactive behaviors based on MV-based technology. Besides, Guo et al. [75] also developed and tested a method to identify the floor distributions of broiler chicken, including the total number of chickens on the house floor and their distribution in drinking and feeding zones. Zhang et al. [76] proposed an automated fish population counting method based on a hybrid neural network model to estimate the number of farmed Atlantic salmon. In this method, convolution kernels of different sizes are used to adapt to the changes in angle, shape, and size caused by the motion of fish, so the counting is real-time, accurate, objective and lossless.

MV technology is also widely integrated into various agricultural equipment, acting as their eyes, and plays a key role. In the article of [77], an automatic sorting device for agricultural products was designed. The sorting test platform based on a visual servo was built, and the target classification, positioning and sorting tests were carried out using tomatoes and oranges as the test objects. Kanagasingham et al. [78] attempted to integrate GNSS, compass and MV into a rice field weeding robot to achieve fully autonomous navigation for the weeding operation. Terra et al. [79] proposed a low-cost modular robotic system to automate agricultural sprayers using MV and individual nozzle control. In the early process of plug seedlings culture, sweet corn seed misses are inevitable. Bai et al. [80] developed an automatic supplemental seeding device using MV technique for corrections of seeding errors of plug seeder, and replacement of the manual reseeding. The paper of Henry Williams et al. [81] presents a kiwifruit harvesting robot. The robot consists of four harvesting arms, end effectors designed specifically for kiwifruit detachment, and a MV system employing convolution neural networks. By using MV, the harvest of different crops could be increased because MV could help farmers to irrigate and spread manure more scientific.

Table 2 briefly describes the work done on the functional application in agriculture.

Table 2. Functions and applications in agriculture.

Authors	Method	Function	Material	Research outcome
TU [45]	MLP	Detection	Pepper Seeds	This method was effective in predicting the germination of pepper seeds based on their seed color and size.
Mohammad [49]	Deep Stacked Sparse Auto-Encoders (DSSAEs)	Classification	Tomatoes	The system can directly classify tomato image data without using image processing technology to extract features, and the accuracy rate can reach 95.5%.
Selman [56]	Thresholding	Classification Detection	Tomatoes	Five different images of each fruit were used and the estimation error is under 20%.
S. Sabzi [60]	Hybrid Multilayer Perceptron	Recognization Detection	Apples	1356 apples in natural orchard environments were examined and the correct classification rate is 97.86%.
Mahadi [62]	Convolutional Neural Network, Inception-v3, MobileNet-v1, Resnet50	Detection	Rice	The validation accuracy rate of disease detection is about 98%.
Elison [68]	Inception-v3	Classification Recognization	Aphids	A software named AphidCV was developed for identifying aphids and the AphidCV can saves time during the processes of counting and sorting.
Saad [71]	BPNN, SVM	Recognization	Soil, Soybean and Weeds	An overall accuracy of 96.601% for BPNN, and 95.078% SVM.
Guo [74]	Integrated Background Model	Measurement	Dairy Calf	The scene-interactive behaviors of entering or leaving the resting area, turning around, and stationary were identified automatically and the success rate is between 93% and 97%.

Figure 12 is a topology diagram generated by this research group. In the area of agriculture, MV could apply in several fields, such as seed selection, fruit classification, pest identification, and so on.

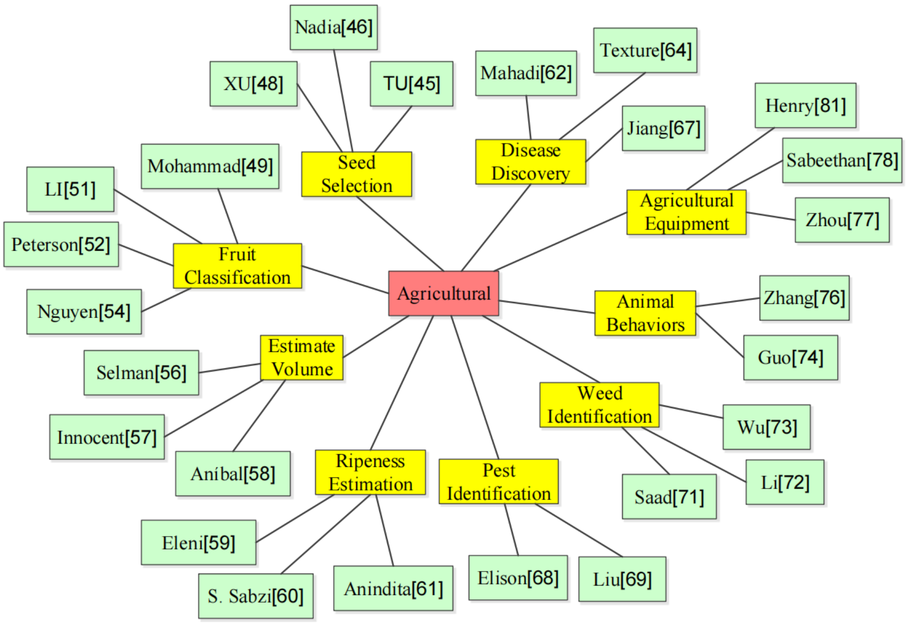

Figure 12. Topology diagram of agricultural applications of machine vision.

4. Medical applications of machine vision

MV also has plenty of applications in medical area, such as processing medical images; realizing automatic detection of tumors; analyzing case characteristics to help doctors diagnose diseases, and so on. MV has improved the efficiency and accuracy of medical detection and treatment.

Wood et al. [82] built a deep learning model, which analyzed the neuroradiology report, obtained the report features and give corresponding checks. This model breaks through the bottleneck of CV model development. In the paper of [83], a CV system was built for detection of missing tablet in the pharmaceutical industry. Assembly line camera captures images of packages. The RGB format images are converted to HSI color format for images. Then, by comparing the position and quantity of the circles, the pills are identified, and informations such as whether the pills are lost or where they are lost are obtained. The CV system increases productivity and safeguards consumer safety. Sethy et al. [84] developed an application of image processing, Machine Learning (ML) and Deep Learning (DL) techniques in breast cancer diagnosis. The authors also proposed a computer vision-based method on diagnosis of breast cancer, it can find the exact location of breast abnormalities, which can help in breast-conserving surgery or partial mastectomy. Compared with the existing methods, the proposed method is highly accurate. Alkadi's [85] group trained a deep convolutional encoder-decoder architecture to address prostate lesions in magnetic resonance (MR) images. They proposed a 3D sliding window approach, an experiment conducted on 19 patient data, which outperfoms traditional pattern recognition and machine learning methods. Gu et al. [86] built a user-friendly CV interactive system based on Exercise Check. The research of [87]. enhanced a Convolutional Neural Network (CNN) model and proposed an integrated acceleration method, which detects COVID-19 symptoms from CT (Computed Tomography) chest scan images. In order to increase the computing speed, they implemented a hardware-based acceleration method on a re-configurable platform (FPGA). It involves reducing the number of vectors that need to be processed in classification tasks, the method is a unique advantage for particular application.

The paper of Kollias [88] introduced a baseline method consisting of DL methods based on CNN-RNN networks applied to the second Covid-19 competition. They splited the database to training, verifying and testing. The first two datasets are used for training and validation of machine learning models, while the latter will be used to evaluate the developed models. Ismael et al. [89] proposed a method which uses Residual Networks in the field of artificial intelligence to improve the accuracy of recognizing brain cancer. They adopted a computer-aided diagnosis (CAD) system assisting doctors and radiologists in diagnosing and classifying brain tumors. The method achieves the highest accuracy rate of 99% by training brain tumor model containing 3064 MRI images of 3 types. Therefore, the method enables doctors to make correct treatment choices and helping save lives. Gu and Yang [90] established an automated method for diagnosing breast cancer by using CV, artificial intelligence technology and DL to observe cancer from B-ultrasound images. This method can quickly enhance the correct diagnosis rate and reduce the difference in the operation level of urban and rural doctors. Khemasuwan's [91] group provided information of artificial intelligence in pulmonary medicine for pulmonary experts, described the concept of artificial intelligence and some necessary needs of ML and DL, and reviewed some literature of CV too. The main content of the literature is the application of CV in medical imaging. They finally concluded with a discussion of the limitations and challenges in incorporating artificial intelligence into clinical pulmonary practice. The paper of [92]. presented a novel strategy combining bounding box annotations from multiple clinicians, and took advantage of deep neural networks for building an automated system in which complex patterns are derived to address this difficult task. Two deep learning-based CV methods were evaluated by the initial data collected in this study, automatic detection and classification of oral lesions detect oral cancer early.

In the work of [93], self-supervised learning is used to improve the effectiveness of medical image classification. There are two main classifications: classification of dermatological conditions from digital camera images and classification of multi-label chest X-rays, while a novel Multiple Instance Contrastive Learning (MICLe) method is introduced. Top-1 accuracy increases by 6.7% on dermatology and chest X-ray classification, which outperforms strongly supervised baselines pretrained on ImageNet. The paper of [94]. discussed CV and artificial intelligence. From the perspective of application, it describes the application of artificial intelligence and machine vision in patient care in details, and how to achieve satisfactory results of artificial intelligence through different model to help driving cars. To predict cancer, pathologists evaluated the microscopic appearance of biopsy tissue samples based on morphological characteristics that correlate with patient outcome. Aksac et al.'s [95] article used 162 kinds of breast cancer histopathological tissue images to form a database, and the task is to automatically divide them into 6 types that are required in medicine. Zhou et al. [96] introduced Adaptive GraphSage which is a graph convolution technology that combines multi-level features in a data-driven manner. A deep neural network model is trained in the paper of Chao's research, it simplified the classification of genome-wide cancer types and can accurately classify 17 cancer types across the genome. Treating each cancer type as an associated task using a meta-learning approach outperforms traditional neural network classifiers [97].

Image segmentation is important in medical image processing. It has been extensively researched and developed in order to refine clinical analysis and application. In the paper of Chen et al. [98], a new DL model was proposed to solve this limitation. The new model considers the internal area as a deep learning-based model, and inside and outside the area of interest and the size of the boundary were considered during the learning process. Convolutional Neural Network (CNN) methods were used in many biomedical segmentation tasks. Shah et al. [99] proposed another CNN-based method that uses dilated convolutions and residual connections for training and inference based on traditional filters. They increased the use of dilated convolutions and residual connections, training and inference are performed using an efficient patch-based method, reducing unnecessary calculations. CV has been successful used in solving various complex healthcare problems. Ulhaq et al. [100] aimed to conduct a preliminary review of the existing literature on CV to combat COVID-19, collected information about available research and pointed out future research directions, and provided them to CV researchers to save their precious time. In the work of Rehman et al. [101], a computer vision-based FC-DSCNN CAD system was proposed to detect micro-calcification clusters in mammograms and classified them as malignant and benign. This research results showed that the performance of this method was higher than traditional methods. Abdelrahman et al. [102] discussed structured convolutional neural network (CNN) databases for mammography. It began with an introduction to computer-aided detection (CAD) and CNN-based CV models for mammography. Then, the literature of mammography training dataset was discussed. Rakhlin et al. [103] reviewed deep convolutional neural network computational methods for breast cancer histology image classification. For the 4-class classification task, the classification accuracy is 87.2%, and for the 2-class classification task, the classification accuracy is 97.3%. This method outperforms other common methods in automatic pathology classification, and the source code has been released.

Since the birth of deep learning, medical imaging community has developed deep learning-based methods for many applications including image recognition. The research of Haskins provided an overview of DL for medical images, introduced the evolution and research challenges of DL for medicine in the past few years, and also highlighted future research directions and possible new levels in this field [104]. Esteva et al. [105] investigated recent advances in the application of modern CV techniques in medicine. Especially in medical imaging and clinical diagnostic applications. In the work of Zheng et al. [106], an efficient Adaboost algorithm (DLA-EABA) was established using DL to detect breast cancer. A tumor classification method was developed by using a deep convolutional neural network (CNN) to traditional CV methods. In the paper of Amiri et al. [107], keratoconus disease was first introduced and then 33 images were used. In the research of Wu et al. [108], two-dimensional (2D) fractional convolutions were used on ARFI-VTI images to accurately predict lesions in ROIs. A multilayer MV classifier was used to screen tumors. The paper of Gupta and Bhavsar [109] mentioned that DL methods were applied in CV and had also been applied to medical image analysis. However, existing methods are unsatisfactory for multi-layer feature classification. Specifically, this work focused on building a framework that considered both layers and inter-layer dependencies. Therefore, they selected the best subset of layers according to the information theory measurement (ITS), conducted experiments on the BreaKHis dataset, and verified that the multi-layer feature fusion performance is better.

In recent years, DL has been widely used in histopathology image analysis. Gupta and Bhavsar [110] believed that multi-layer features were important because different regions of the image contain different levels of information. They proposed a DenseNet sequence framework to extract multi-layer deep features. Experiments on the BreaKHis dataset show that the proposed framework achieves good performance in most cases. Working with histopathology images is time-consuming when analyzing images of different levels. CV and ML methods automate the diagnosis of pathology, reducing analysis time. In the paper of Sheikh et al. [111], a multi-feature network (MSI-MFNet) model was proposed, which can learn the overall structure and texture features. Their proposed model outperforms existing models in terms of accuracy, sensitivity and specificity. Liu et al. [112] used DNN segmentation to design a 3D image compression framework for MV. This method was to extract and retain important image features. Harned et al. [113] summarized the capabilities of artificial intelligence and MV, and the advances in MV that have changed technical regulations for manufacturers. In the work of Mok and Chung [114], an algorithm was presented for 3D affine medical image registration. The method used a convolutional visual transformer to learn global affine registration, which outperforms CNN-based affine registration methods in terms of registration accuracy and generalization, while retaining the operational advantages of learning-based methods. In Wu's [115] research, a multi-layer MV classifier was proposed to automatically identify lung disease categories from chest X-ray images. For digital image texture analysis, convolution operations were used to enhance symptom features and remove noise. Yoo et al. [116] developed an automated CNN-based pipeline for the detection of prostate cancer (PCa) in patients. To test the automated pipeline, DWI images of 427 patients were used as a dataset, which received good test results. The paper of Hassan et al. [117] provided a brief overview of AI, CV, and CT medical images for the diagnosis of COVID-19. The authors analyzed previous reviews, and after an in-depth analysis, 114 studies were collected. According to the analysis, AI and MV have potential in the rapid diagnosis of COVID-19, and further research is needed to bring accurate and effective models to clinics.

The utilization of image processing and MV in medicine has increased in recent years. In the paper of Zhang et al. [118], a new method of image processing was proposed for early detection of skin cancer. Deniz et al. [119] introduced transfer learning and deep feature extraction methods, and pre-train CNN models. AlexNet and Vgg16 models are adopted in feature extraction, and then the obtained features were classified by support vector machine (SVM) [119]. Experiments were carried out on the breast cancer dataset and the accuracy was evaluated. Evaluation results show that transfer learning produces better results than deep feature extraction and SVM classification. Zhao et al. [120] mentioned the development of a DL model that can diagnose the severity of acne based on images, and its diagnosis results were as accurate as dermatologists.

Table 3. briefly describes the work done on the functional application in medical field.

Table 3. Application of machine vision in medical field.

Authors	**Method**	**Function**	**Material**	**Research outcome**
Zhao [83]	vision	Detection	Tablets	The obtained RGB format images are transformed into HSI color format. The tablets could be identified and determined by carrying out of the image segmentation.
Dimitrios [88]	CNN-RNN	Recognition Classification	CT images	Detection of COVID-19 from COV19-CT-DB database. The basic of model diagnoses COVID-19
Sarah [89]	CNN Networks	Detection Classification	Brain MRI images	The accuracy of outperforming is 99% higher than others on the same dataset.
Shekoofeh [93]	MICLe	Detection Classification	Chest X-ray Dermatology	The accuracy improvement is 6.7% and 1.1% in mean AUC.
Zhou [96]	GCN CNC-Net	Detection Classification	Colorectal cancer histology images	Outperforming current methods on a large scale colorectal cancer grading
Khalil [101]	CNN	Detection Classification	Mammograms	The method obtains a score of 0.97 with a 2.35 and 0.99 true positive ratio with 2.45 false positive per image.
Alexander [103]	CNN CAD	Detection Classification	Breast cancer histology image	The 4-class accuracy is 87.2% and the 2-class accuracy is 93.8%.
Wu [109]	2D convolution	Detection Classification	ARFI-VTI images	Dimensions of feature patterns from 32 × 32 to 16 × 16 size.
Taimoor [114]	BN-ReLU convolution CNN	Classification	Breast cancer images	The accuracy reaches 90% and 98% without data argumentation and with data augmentation scenarios.
Wu [119]	2D convolution vision	Detection Classification	Digital chest X-ray images	The mean recall is 98.68%, the mean precision is 82.42%, the mean accuracy is 83.57%.
Zhao [120]	CNN	Detection Recognition	Magnetic resonance imaging	The receiver operating characteristic curve of 0.87 and 0.84 at slice level and patient level.

Based on different model, the applications of MV are classified and showed in the following topology diagram **Figure 13**.

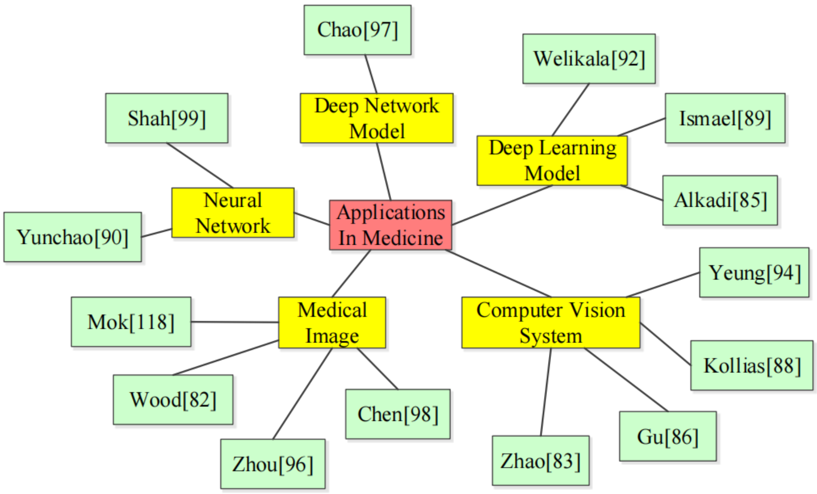

Figure 13. Topology diagram of medical applications of machine vision.

5. Manufacturing applications of machine vision

With the development of technology, MV technology has been widely used in manufacturing, most of which are used in work-piece classification, defect detection, and work-piece processing degree prediction. MV tools would help to improve the quality of the fabricated parts.

The obvious features of simple classification used for scenes, common MV algorithms can achieve the function of simple classification. Yu et al. [121] investigated a fusion of near infrared spectroscopy (NIR) and MV for improving the accuracy of recognizing surface defects in wood. It was found that the combination of NIR and Back Propagation Neural Network (BPNN) showed better discrimination accuracy with 92.7% for the training set and 92.0% for the test set. Chen et al. proposed a missing-pin chip detection system based on the YOLOv4-tiny algorithm and a small-size AXU2CGB platform, which has a two-layer ping-pong optimization as well as an FPGA gas pedal structure with multiple parallel convolutional kernels, and achieves a detection speed of 0.468 seconds per image, 89.33% mean average precision (mAP), and 100% missing-pin recognition rate [122]. The detection efficiency is greatly improved and the power consumption is reduced. Lin et al. [123] proposed an intelligent hybrid strategy for edge-inconsistent feature detection using machine vision, and a feature classification model based on deep CNN was established using K-Means clustering strategy. In order to reduce the error between the regression output of the network and the labeled values, a hidden layer of -1 neuron was introduced. The results showed that the combined model was able to classify different types of geometric contour edge features with 100% correctness, and the average dice similarity index between the model results and the actual edges was 0.84, and the maximum error of HO shape was less than 0.06 mm for a work-piece with a size of 142 × 119 mm. Liong et al. [124] developed an automatic mechanism to classify leather defects in order to control leather quality in combination with machine vision. Manual feature extractors (edge detectors and statistical methods) and data-driven (artificial neural network) methods were utilized to represent leather patches. A variety of classifiers (decision trees, support vector machines, nearest neighbor classifiers, and ensemble classifiers) were then utilized to determine whether a test sample patch contains a defective segment. The classification accuracy was found to be 84%, which can be further improved by subsequently substituting the CNN for the artificial neural network and tuning the classifier parameters.

Compared with the simple classification, the image features corresponding to the complex classification are similar, and the different characteristics are difficult to find, so more accurate algorithm parameters and the application of new algorithms are needed. Lin et al. [125] used MV technology to detect defects in products processed using selective laser melting. Multi-layer Perceptron (MLP) is mainly used to classify stripe defects generated during processing. The number of neurons in the input layer was set to 4, and the number of neurons in the output layer was 2. The defect recognition accuracy of MLP reaches 98.33%, and the time consumption was faster than that of SVM. Ryu et al. [126] generated a new method for segmentation using the ability of a line scan camera in order to identify fine scratchings on the edge of a steel plate. Focusing on using Gabor filter had a scratch on the boundary of the error, to identify a particular area has a defect, then according to the extracted features using SVM classifier to classify. Through the experimental verification of 2061 frames of images collected from real samples, the true detection rate of the method is 97.26%, and the false detection rate is 1.66%. Masinaei et al. [127] used MV technology for coal detection to recover fine coal particles and found that SVM classifier with linear kernel had the highest accuracy and generalization ability. Wang et al. [128] proposed a CNN-based MV method to improve the quality of image data and assist in improving the accuracy of defect recognition. This method was mainly used for single-camera CNN based MV grayscale images, and can greatly improve the accuracy of image classification and target detection when training the data of industrial image enhancement. The research of Jain et al. [129] significantly improved the performance of CNN for classifying surface defects with a GAN-based enhancement scheme. The results showed that the sensitivity and specificity of the classical enhanced CNN are 90.28% and 98.06%, respectively. In contrast, the comprehensive enhanced CNN obtained better results, with a sensitivity and specificity of 95.33% and 99.16%, respectively. Hao's [130] group developed a method for real-time classification and location of steel defects. An industrial inspection robot scanned the steel surface to generate an image, and the surface defect detection algorithm recognized the image. The deformable convolution enhanced backbone network is used to extract complex features of multi-shape steel surface defects. Then, the feature fusion network of the balanced feature pyramid is used to generate high-quality multi-resolution feature maps for detecting multi-size defects. The results show that the model achieves 0.805 mAP and shows high efficiency. Zhang et al. [131] proposed a CP-YOLOv3-dense neural network for fast and effective detection of rigid band defects. The model used YOLOv3 as the basic network to prioritize the image, and then replaced the two residual network modules with two dense network modules. The results showed that the CP-YOLOv3 dense network had a detection accuracy of 85.7%, a recall rate of 82.3%, an average detection accuracy of 82.73%, and a detection time of 9.68 ms per image. Boikov et al. [132] changed the method of using a single data to train the model and proposed a method of training neural networks for vision tasks based on comprehensive data. The generated symmetric distributed billet defect data set was used as the comprehensive data training set to train two neural networks, Unet and Xception. Under the training of the comprehensive training set, the two neural networks have achieved good results in the classification and segmentation of steel work-piece surface defects in images. The Dice score and accuracy on synthetic data are 0.62 and 0.81, respectively.

Real-time quality detection in the process of work-piece processing can reduce the defect rate of the work-piece, and can adjust the work-piece processing according to the real-time status, which is also the development trend of machine vision application in the manufacturing industry, but it also puts forward higher requirements for the improvement of the algorithm. Dynamic testing the quality of the work-piece is the purpose of most of the MV applications. Penumuru et al. [133] developed a based on SVM method of classification for typical machining environment accurate identification and classification was the plane of the material. Quadratic programming was used to minimize the plane boundary. Through the mapping function, the linearly non-separable data can be projected into the high-dimensional space to become linearly separable. Kernel-Svm was used for linearly non-separable data. The number of samples in the training set was 2491, and the number of samples in the test set was 1068. **Figure 14** shows that the surface images of different materials under different lighting conditions. The training results showed that the SVM did not overfit and the accuracy was 100%, which was verified by ten-fold cross validation. But this 100% accuracy was limited by the same lighting conditions. Benbarrad et al. [134] proposed a product quality control inspection model based on MV for classification and process prediction of product inspection. Inception v3 was found to be the most suitable model for classification and recognition, which can reach 95% accuracy in a faster time. Decision tree was more suitable for process prediction and achieve a very high R2 score (0.99), achieving high accuracy predictions. Machining tool wear condition has a direct relationship between the work-piece machining quality, so the real-time processing tool condition is also very important. Peng et al. [135] set up a tool wear monitoring platform based on MV. The structural similarity algorithm and Harris Angle detection algorithm were used to solve the problem of automatic shooting of the tool and realize the automation of the monitoring. At the same time, the binary morphology method was used to improve the image quality, and the gray co-occurrence matrix method was used to detect the tool wear value. It was found that the error rate between the calculated wear value of the monitoring system and the actual wear value was less than 5.73%, which met the requirements of industrial precision. With the development of manufacturing industry, many of the artifacts is developing toward miniaturization, it also calls for machine vision can carry on the detection of small objects. Dai et al. [136] proposed a small object detection network model to detect the position and quality of spot welding of automobile body. They proposed a recognition method based on yolov3, the network architecture is shown in the **Figure 15**, and compared the proposed method with other existing methods, the effect is shown in the **Figure 16**. In **Figure 17**, the green bounding box represents the good spot welds detected from the image, while red box denotes the bad spot welds. The number represents the confidence that there are spot welds in the bounding box. Zhang et al. [137] used ML method to collect coal photos in real time and detect multi-parameter information of coal online. Finite Erosion and Precise Expansion (FEED) algorithm and particle edge region segmentation algorithm were used to segment the overlapping particles, and 29 features were extracted and optimized. The total ash content error was found to be 2.54%. The method will likely be widely used in the coal processing industry.

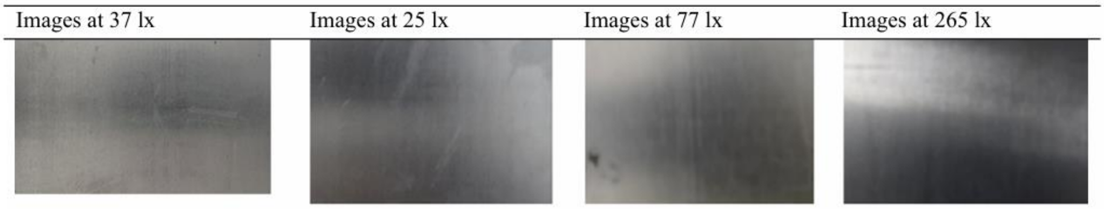

(**a**)

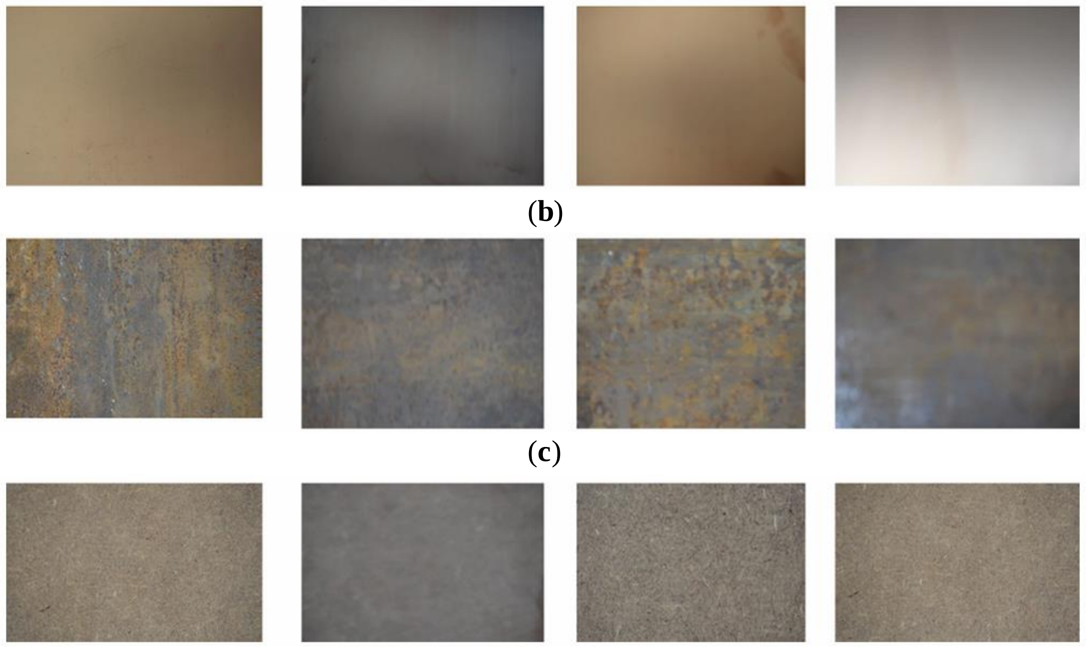

(b)

(c)

(d)

Figure 14. Surface images under different lighting conditions: (**a**) aluminium; (**b**) copper; (**c**) mild steel-rusted; (**d**) MDF [133].

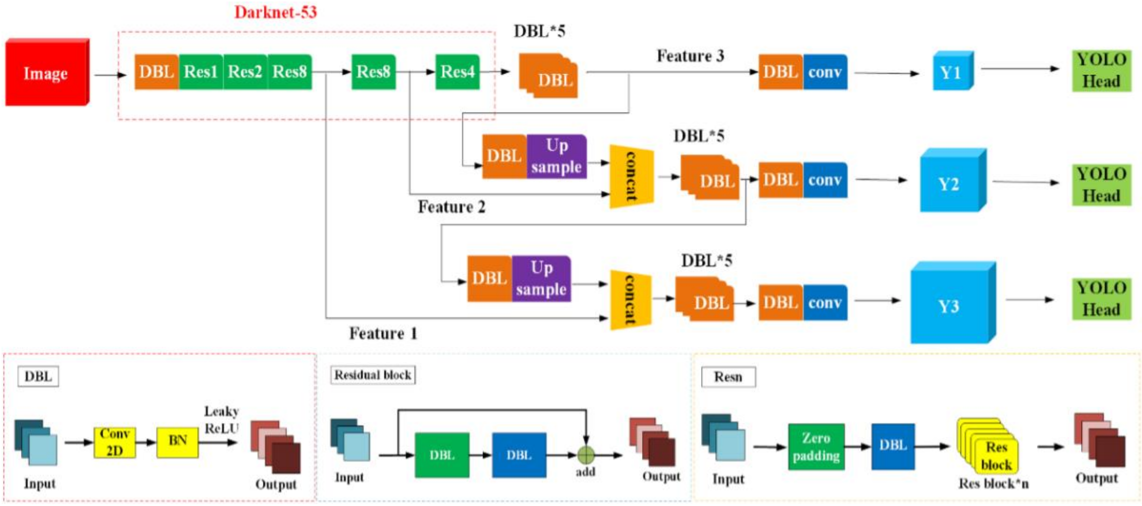

Figure 15. YOLOv3 architecture for object detection [136].

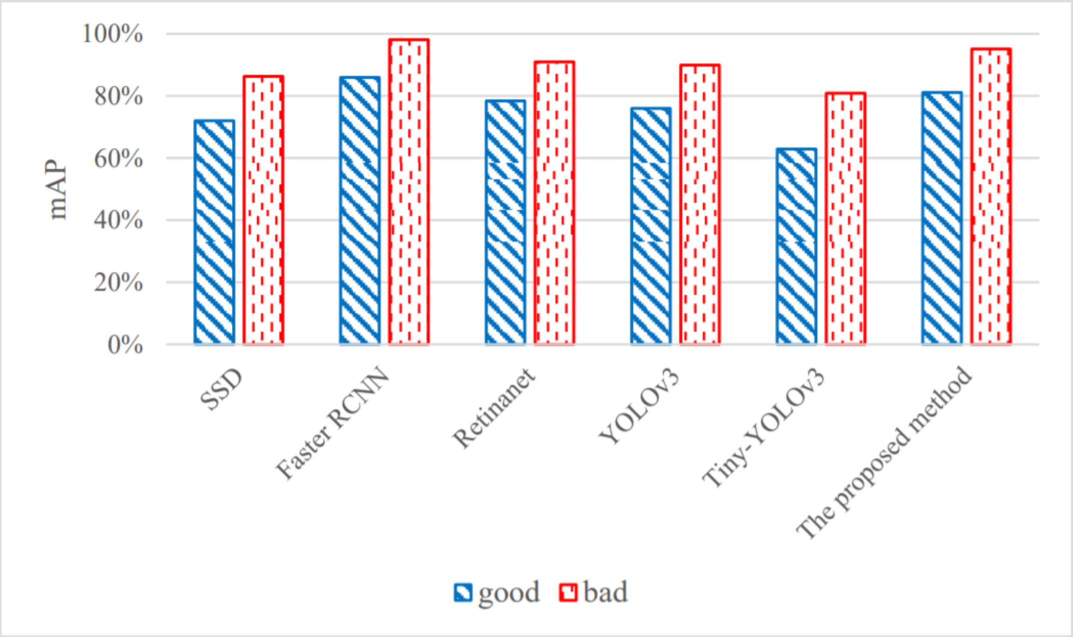

Figure 16. Comparisons between the proposed model and typical object detection algorithm on the spot welds dataset [136].

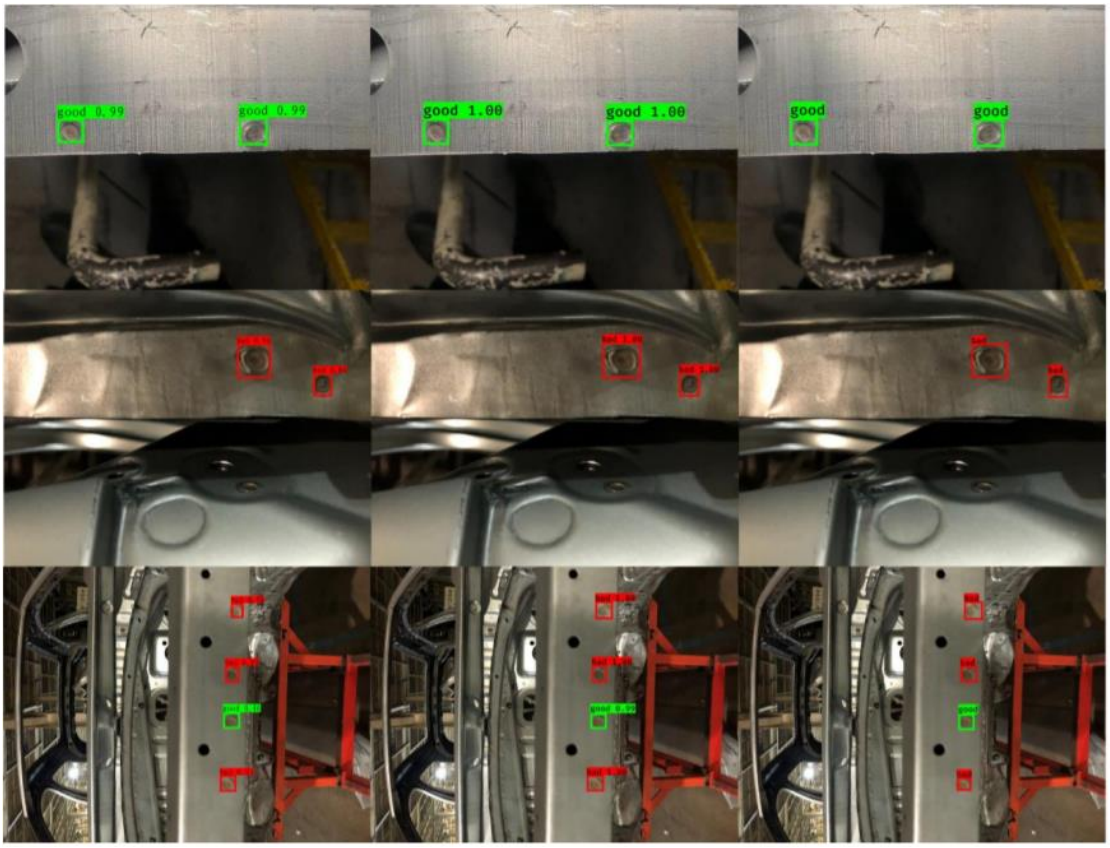

Figure 17. Some examples of spot welds detection results. YOLOv3(left), the proposed model (middle) and the ground truth (right) [136].

The research group generated a topology diagram of MV applications in the area of manufacturing and it is shown in **Figure 18**:

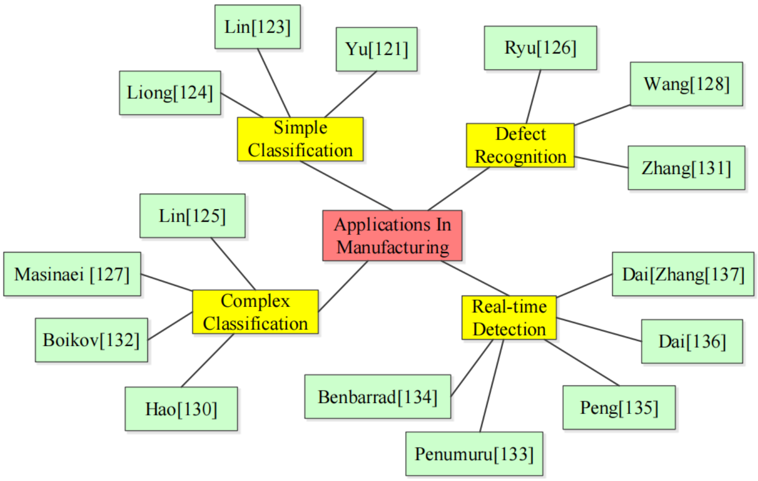

Figure 18. Topology diagram of manufacturing applications of machine vision.

Table 4 briefly describes the work done on the functional application in manufacturing.

Table 4. Application of machine vision in manufacturing.

Authors	Method	Function	Material	Research outcome
Massinaei [127]	SVM	Measurement Detection	Coal powder	The quality of the powder in the collection pipe can effectively predict the appropriate parameters of metallurgy.
Penumuru [133]	SVM	Classification Recognition	Metal Fiberboard	Training set 2491, verification set 1068, through the ten-fold cross-verification method, the accuracy of 100%.
Liong [124]	ANN CNN	Detection Classification	Leather	The classification accuracy rate was 84% in approximately 2,500 samples of 400 × 400 leather patches.
Wang [128]	CNN YoloV4	Classification Detection	Metal	Image enhancement using CNN can effectively improve the accuracy of surface defect recognition and detection by YoloV4.
Dai [136]	YoloV3 + MobileNetV3	Detection	Welded part	When the detection time is within 0.506s, the accuracy rate is 89.32%, which effectively balances the detection time and accuracy.
Lin [125]	MLP	Detection Classification	Metal of SLM	The recognition accuracy is 98.33%, but it will increase the print molding time.
Benbarrad [134]	Inception v3	Detection	Metal Ore	Can achieve 95% accuracy in the allowed time
Yu [121]	NIR + BPNN	Recognition	wood	The backpropagation neural network model showed better discrimination accuracy of 92.7% for the training set and 92.0% for the test set.
Peng [135]	GLCM	Detection	Metal cutter	The binary morphology method improves the image quality, and the error rate between the predicted and actual tool wear values is less than 5.73%.
Lin [123]	K-Means	Classification Detection	Metal	The accuracy rate is 100%, and the proposed method can recognize geometric shapes less than 0.06 mm well.
Zhang [137]	Finite-Erosion-and-Exact-Dilation	Detection	Coal	Various parameters of coal were predicted, and it was found that the comprehensive error remained within 2.54%.

6. Other applications of machine vision

In the previous sections, the applications of MV in agriculture, medicine, and manufacturing have been reviewed. Besides, MV also has other applications in human recognition, traffic, research assistance, and so on. In this chapter, these applications are introduced.

Compared with traffic accidents caused by violating traffic rules, fatigue driving can lead to accidents with higher mortality and public hazards. Sikander and Anwar [138] studied a new method based on machine vision to predict driver fatigue based on driver's facial movements. The **Figure 19** shows the framework details of the proposed 3D machine vision-based fatigue detection method for facial motion unit recognition. The technology reconstructs the driver's facial movements based on photo-metric stereo and identifies fatigue-related facial movements. Compared with other methods, this method improved the accuracy of driver fatigue identification by 95%. Zhao et al. [139] studied a method of human flow detection in crowded places by MV. The measurement of human body parameters is of great significance in sports, clothing and medical treatment. Traditional human body parameter measurement is complicated and requires a lot of human input. Arellano-González et al. [140] generated a new technique for measuring anthropocentric parameters based on a MV system. The results of the study showed that this technique had advantages in shortening sampling time, improving measurement accuracy and reducing equipment requirements compared with traditional measurement methods. Falling seriously affects the life safety of the elderly. Based on Microsoft Kinect® camera and Open CV library, Panahi et al. [141] developed a human fall recognition method based on machine vision. For human fall recognition, this method can achieve the recognition effect of the acceleration sensor.

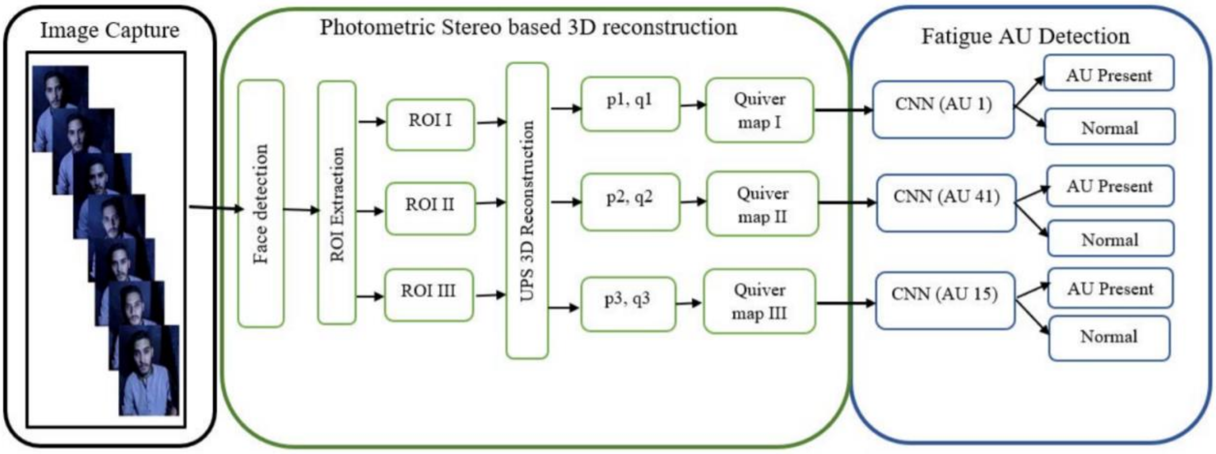

Figure 19. Framework of 3D facial action unit identification for fatigue detection [138].

Traffic plays an important role in the normal operation of human society. Road conditions, traffic facility management conditions, and vehicle driving technology have an important impact on traffic. Research on applying machine vision to these aspects has been widely carried out. Huang et al. [142] used MV to judge the degradation of ballast using the permeability of ballast as an index, and proposed a ballast inspection and maintenance method. The flowchart of the entire imaging-based ballast degradation analysis, including several preprocessing image enhancement techniques such as gamma adjustment, histogram equalization, and bilateral filtering is shown in **Figure 20**. Burghardt et al. [143] studied the impact of traffic signs of different materials and colors on machine vision recognition under different weather conditions in the laboratory. Yang et al. [144] proposed a new algorithm, which can eliminate the influence of oil and rust pollution on the track surface image recognition through denoising, and significantly improve the accuracy and processing speed of MV with an average accuracy of 97.11%, an average recall of 96.10%, and an average frame rate of 0.0064 s. Bridges play an important role in traffic. In order to ensure traffic safety, it is very important to detect the condition of bridges. Because it can simulate and reproduce the real scene, digital twin technology can be used to detect the condition of the bridge body. Dan et al. [145] studied a bridge parameter acquisition technology based on stress detection and machine vision, and relied on the acquired data for modeling to realize the digital twin detection of bridge conditions. Bridge cracks can be observed through drone photography and machine vision. Because there are problems in the clarity and other aspects of the photos taken by drones, traditional algorithms cannot analyze and judge them. Dan and Dan [146] have studied a new algorithm that can analyze the pictures taken by drones, and carried out experimental verification. Liu et al. [147] studied the impact of fog on the machine vision assisted driving system, determined the impact of fog and other adverse weather conditions on machine vision, and provided support for improving the safety of the machine vision assisted driving system.

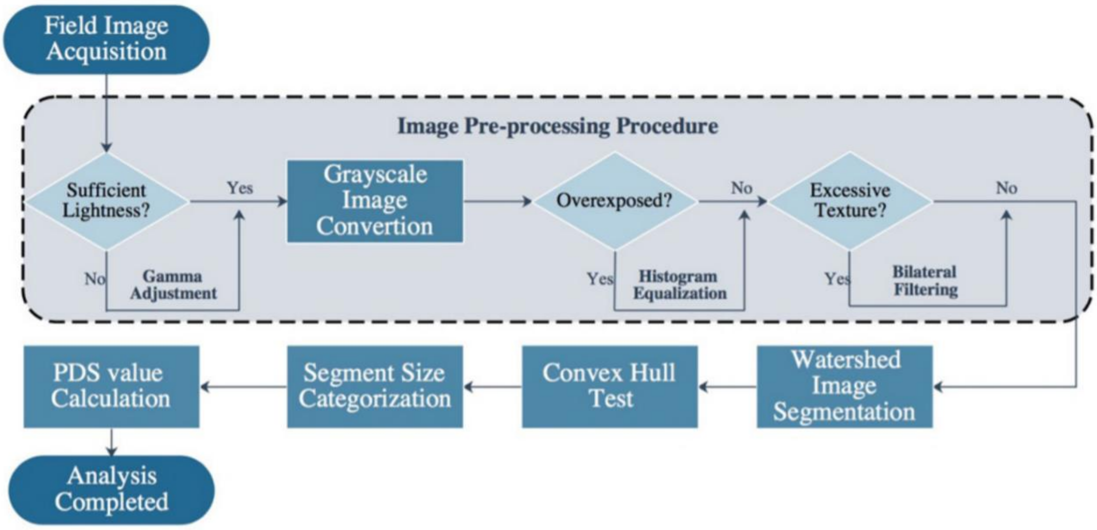

Figure 20. Flowchart of the imaging-based degradation analysis including preprocessing procedure [142].

There are a lot of time-consuming mechanical work in scientific research, such as Scanning Electron Microscopy (SEM) image analysis. The existence of these tasks has caused a lot of burden to scientific researchers and increased the cost of scientific research. Machine vision is used to analyze this type of image, which can reduce the workload of scientific researchers, reduce scientific research costs, and improve scientific research efficiency. Kim et al [148] studied the analysis method of SEM images based on machine vision and machine learning. The method has a good performance in determining particle size, particle size distribution and microscopic morphology of objects. Natova et al. [149] studied the application of machine vision and deep learning to identify transmission electron microscopy (TEM). This technology greatly improves the speed of TEM identification, and the identification time is about 2% of manual identification. Hendel et al. [150] applied machine vision to astronomical research, used machine vision and related algorithms to analyze space debris, and studied the evolution history of galaxies.

Table 5 briefly describes the work done on the functional application in other industries.

Table 5. Applications of machine vision in other industries.

Research direction	**Authors**	**Method**	**Function**	**Research outcome**
Human recognition	Sikander [138]	Photo-metric stereo	Predict driver fatigue	Improved the accuracy of driver fatigue identification by 95%
	Arellano [140]	Machine Vision	The measurement of human body parameters	Shorten sampling time, improve measurement accuracy and reduce equipment requirements
	Panahi [141]	Microsoft Kinect® camera and Open CV library	Human fall recognition	Achieve the recognition effect of the acceleration sensor
Traffic	Huang [142]	Machine Vision	Judge the degradation of ballast	Proposed a ballast inspection and maintenance method
	Yang [144]	New algorithm	Eliminate the influence of oil and rust pollution	Improve the accuracy and processing speed of MV
	D. Dan [145]	stress detection and machine vision	Bridge parameter acquisition	Realize the digital twin detection of bridge conditions
Research assistance	Kim [148]	machine vision and machine learning	Analyze SEM images	Perform good in determining particle size, particle size distribution and microscopic morphology of objects
	Natova [149]	machine vision and machine learning	Identify transmission electron microscopy (TEM)	improves the speed of TEM identification, the identification time is about 2% of manual identification
	Hendel [150]	machine vision	Analyze space debris	study the evolution history of galaxies

The research group generated a topology diagram, **Figure 21**, of this section and it is shown below:

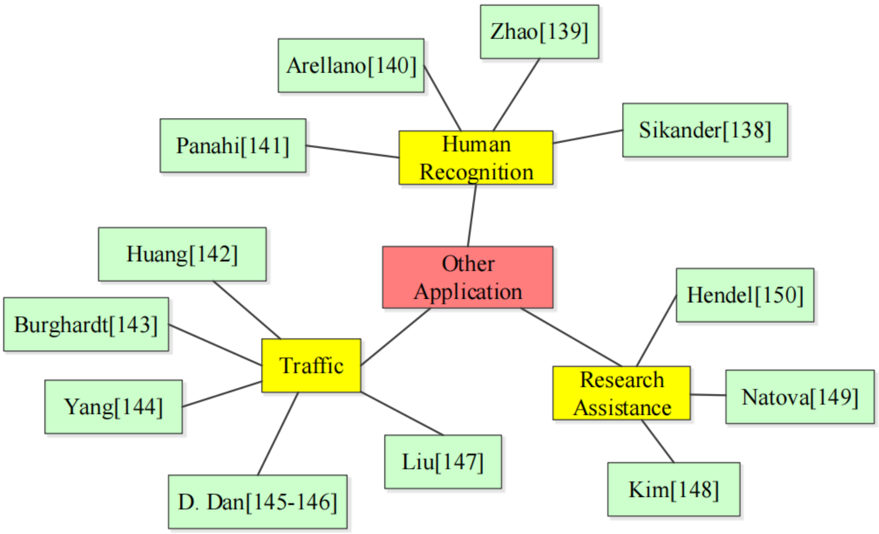

Figure 21. Topology diagram of other applications of machine vision.

7. Results

In this research, firstly, the group introduced the development of MV algorithm. Then the authors review the applications of MV in several areas, including agriculture, medicine, manufacturing, and so on. There are plenty of results are founded in this work:

- As the algorithm developed, MV could afford some work to reduce workload of human beings.
- Since MV is good at image classification, it has plenty of applications in the area of agriculture, especially in seed selection, fruit classification, pest identification, and so on.
- With the help of MV, the workload of doctors is reduced since the algorithm could do detection tasks and improve the accuracy of medical decision and treatment.
- In the field of manufacturing, MV is used in work-piece classification, defect detection, work-piece processing degree prediction, and so on.
- Besides, MV also has several applications in different areas. For example, it could be used in traffic to reduce the happen of accident. And MV can be used to analyze SEM images to help doing research. Moreover, MV could help to study the evolution history of galaxies.

8. Conclusion

Advancements in the MV field have been growing in every aspect of daily life, from research to manufacturing. Many organizations and academia continuously create a high number of unique solutions for refining high-quality and low-cost MV applications. And the applications of MV is growing sharply since the ability of image detection, classification, and processing. After summarizing the above articles, this team summarized the relevant applications of MV in agriculture, medicine, manufacturing, traffic, and so on. The research did a brief analysis based on the number of published paper, MV has more applications in medicine than other fields. But in agriculture, the number of MV applications develops fast. Thus, in future work, the group plan to focus on agriculture, because in this area, MV could do detection of the crop, then help farmers to irrigate or spread manure. MV is a useful tool to increase the harvest of crop. Today, MV has a profound impact on the daily life of everyone. This team completed this article to make a phased summary of the application of MV. It is evident that the current trends in the growth of MV technology will positively impact several utilizations in the mentioned areas in this research.

Funding: This work is supported by the Funding for Visiting Scholar project of ordinary undergraduate universities in Shandong Province in 2024 and Youth Fund of Shandong Agriculture and Engineering University (QNKJZ202301).

Conflict of interest: The authors declare no conflict of interest.

References

1. Wu Mingfei, Chen Li, Zehuan Yao. Deep Active Learning for Computer Vision Tasks: Methodologies, Applications, and Challenges. Applied Sciences. 2022; 12(16): 8103.
2. Katti H, Marius VP, Arun SP. Machine vision benefits from human contextual expectations. Scientific Reports. 2019; 9(1): 2112.
3. Gorodokin V, Zhankaziev S, Shepeleva E, et al. Optimization of adaptive traffic light control modes based on machine vision. Transportation research procedia. 2021; 57: 241–249.
4. Panagakis Y, Kossaifi J, Chrysos GG, et al. Tensor methods in computer vision and deep learning. Proceedings of the IEEE. 2021; 109(5): 863–890.
5. Zhang D, Dongru H, Kang L, et al. The generative adversarial networks and its application in machine vision. Enterprise Information Systems. 2022; 16(2): 326–346.
6. Gustafsson FK, Danelljan M, Schon TB. Evaluating scalable bayesian deep learning methods for robust computer vision. In: Proceedings of the IEEE/CVF conference on computer vision and pattern recognition workshops; 14–19 June 2020; Seattle, WA, USA.
7. Whatmough PN., Zhou C, Hansen P, et al. Fixynn: Efficient hardware for mobile computer vision via transfer learning. Available online: https://doi.org/10.48550/arXiv.1902.11128 (accessed on 10 September 2024).
8. Shu Y, Xiong C, Fan S. Interactive design of intelligent machine vision based on human–computer interaction mode. Microprocessors and microsystems. 2020; 75: 103059.
9. Wu W, Li Q. Machine vision inspection of electrical connectors based on improved Yolo v3. IEEE Access. 2020; 8: 166184–166196.
10. Wu P, He T, Zhu H, et al. Next-generation machine vision systems incorporating two-dimensional materials: progress and perspectives. InfoMat. 2022; 4(1): e12275.
11. Reggiannini M, Moroni D. The use of saliency in underwater computer vision: A review. Remote Sensing. 2020; 13(1): 22.
12. Akhtar N, Mian A, Kardan N, et al. Advances in adversarial attacks and defenses in computer vision: A survey. IEEE Access. 2021; 9: 155161–155196.
13. Goel A, Tung C, Lu Y-H, et al. A survey of methods for low-power deep learning and computer vision. In: Proceedings of the 2020 IEEE 6th World Forum on Internet of Things (WF-IoT); 02–16 June 2020; New Orleans, LA, USA.
14. O'Mahony N, Campbell S, Carvalho A, et al. Deep learning vs. traditional computer vision. In: Proceedings of the 2019 Computer Vision Conference (CVC); 25–26 April 2020; Las Vegas, Nevada, USA.
15. Yang Z, Nahrstedt K, Guo H, et al. Deeprt: A soft real time scheduler for computer vision applications on the edge. In: Proceedings of the 2021 IEEE/ACM Symposium on Edge Computing (SEC); 14–17 December 2021; San Jose, CA, USA.
16. Baygin M, Karakose M, Sarimaden A, et al. An image processing based object counting approach for machine vision application. Available online: https://doi.org/10.48550/arXiv.1802.05911 (accessed on 10 September 2024).
17. Talebi Hossein, Milanfar P. Learning to resize images for computer vision tasks. In: Proceedings of the IEEE/CVF international conference on computer vision; 10–17 October 2021; Montreal, QC, Canada.
18. El-Komy, A, Shahin OR, El-Aziz RM, et al. Integration of computer vision and natural language processing in multimedia robotics application. Inf. Sci. 2022; 11(3): 765–775.
19. Li Jiali, Telychko M, Yin J, et al. Machine vision automated chiral molecule detection and classification in molecular imaging. Journal of the American Chemical Society. 2021; 143(27): 10177–10188.
20. Hu Y, Yang S, Yang W, et al. Towards coding for human and machine vision: A scalable image coding approach. In: Proceedings of the 2020 IEEE International Conference on Multimedia and Expo (ICME); 6–10 July 2020; London, United Kingdom.
21. Roggi G, Niccolai A, Grimaccia F, et al. A computer vision line-tracking algorithm for automatic UAV photovoltaic plants monitoring applications. Energies. 2020; 13(4): 838.
22. Paul N, Chung C. Application of HDR algorithms to solve direct sunlight problems when autonomous vehicles using machine vision systems are driving into sun. Computers in Industry. 2018; 98: 192–196.
23. Datta G, Liu Z, Yin Z, et al. Enabling ISPless Low-Power Computer Vision. In: Proceedings of the IEEE/CVF Winter Conference on Applications of Computer Vision; 2–7 January 2023; Waikoloa, HI, USA.

24. Rebecq H, Ranftl R, Koltun V, et al. Events-to-video: Bringing modern computer vision to event cameras. In: Proceedings of the IEEE/CVF Conference on Computer Vision and Pattern Recognition; 7–11 January 2019; Waikoloa, HI, USA.
25. Mennel L, Symonowicz J, Wachter S, et al. Ultrafast machine vision with 2D material neural network image sensors. Nature. 2020; 579(7797): 62–66.
26. Gamanayake C, Jayasinghe L, Ng B, et al. Cluster pruning: An efficient filter pruning method for edge AI vision applications. IEEE Journal of Selected Topics in Signal Processing. 2020; 14(4): 802–816.
27. Cong VD, Hanh LD, Phuong LH, et al. Design and development of robot arm system for classification and sorting using machine vision. FME Transactions. 2022; 50(1): 181–181.
28. Gubbi MR, Gonzalez EA, Lediju Bell MA. Theoretical framework to predict generalized contrast-to-noise ratios of photoacoustic images with applications to computer vision. IEEE Transactions on Ultrasonics, Ferroelectrics, and Frequency Control. 2022; 69(6): 2098–2114.
29. Wang S, Wang C-Y, Wang P, et al. Networking retinomorphic sensor with memristive crossbar for brain-inspired visual perception. National science review. 2021; 8(2): nwaa172.
30. Tarashima S, Center I. One-Shot Deep Model for End-to-End Multi-Person Activity Recognition. British Machine Vision Conference. 2021.
31. Shreyas E, Sheth MH, Mohana. 3D Object Detection and Tracking Methods using Deep Learning for Computer Vision Applications. In: Proceedings of the 2021 International Conference on Recent Trends on Electronics, Information, Communication & Technology (RTEICT); 27–28 August 2021; Bangalore, India.
32. Ding J, Zhang Z, Yu X, et al. A Novel Moving Object Detection Algorithm Based on Robust Image Feature Threshold Segmentation with Improved Optical Flow Estimation. Applied Sciences. 2023; 13(8): 4854.
33. Fang S, Zhang B, Hu J. Improved mask R-CNN multi-target detection and segmentation for autonomous driving in complex scenes. Sensors. 2023; 23(8): 3853.
34. Moru DK, Borro D. A machine vision algorithm for quality control inspection of gears. The International Journal of Advanced Manufacturing Technology. 2020; 106: 105–123.
35. Li J, Mengu D, Yardimci NT, et al. Spectrally encoded single-pixel machine vision using diffractive networks. Science Advances. 2021; 7(13): eabd7690.
36. Yin K, Wang L, Zhang J. ST-CSNN: a novel method for vehicle counting. Machine Vision and Applications. 2021; 32(5): 108.
37. Dan D, Ge L, Yan X. Identification of moving loads based on the information fusion of weigh-in-motion system and multiple camera machine vision. Measurement. 2019; 144: 155–166.
38. Appiah O, Asante M, Hayfron-Acquah BJ. Improved approximated median filter algorithm for real-time computer vision applications. Journal of King Saud University-Computer and Information Sciences. 2022; 34(3): 782–792.
39. Kaushal V, Iyer R, Kothawade S, et al. Learning from less data: A unified data subset selection and active learning framework for computer vision. In: Proceedings of the 2019 IEEE Winter Conference on Applications of Computer Vision (WACV); 7–11 January 2019; Waikoloa, HI, USA.
40. Zhang M, Zhe X, Ou-Yang L, et al. Semantic hierarchy preserving deep hashing for large-scale image retrieval. In: Proceedings of the 2021 17th International Conference on Machine Vision and Applications (MVA); 25–27 July 2021; Aichi, Japan.
41. Semitsu T, Nakamura M, Ishigami S, et al. Estimating Contribution of Training Datasets using Shapley Values in Data-scale for Visual Recognition. In: Proceedings of the 2021 17th International Conference on Machine Vision and Applications (MVA); 25–27 July 2021; Aichi, Japan.
42. Riba E, Mishkin D, Ponsa D, et al. Kornia: An open source differentiable computer vision library for pytorch. In: Proceedings of the IEEE/CVF Winter Conference on Applications of Computer Vision; 13–19 June 2020; Seattle, WA, USA.
43. Yang S, Hu Y, Yang W, et al. Towards coding for human and machine vision: Scalable face image coding. IEEE Transactions on Multimedia. 2021; 23: 2957–2971.
44. Suma V. Computer vision for human-machine interaction-review. Journal of trends in Computer Science and Smart technology (TCSST). 2019; 1(02): 131–139.
45. Tu K, Li L, Yang L, et al. Selection for high quality pepper seeds by machine vision and classifiers. Journal of Integrative Agriculture. 2018; 17(9): 1999–2006.

46. Ansari N, Ratri SS, Jahan A, et al. Inspection of paddy seed varietal purity using machine vision and multivariate analysis. Journal of Agriculture and Food Research. 2021; 3: 100109.
47. Tu K, Wen S, Cheng Y, et al. A non-destructive and highly efficient model for detecting the genuineness of maize variety 'JINGKE 968' using machine vision combined with deep learning. Computers and Electronics in Agriculture. 2021; 182: 106002.
48. Xu P, Tan Q, Zhang Y, et al. Research on maize seed classification and recognition based on machine vision and deep learning. Agriculture. 2022; 12(2): 232.
49. Iraji M. Comparison between soft computing methods for tomato quality grading using machine vision. Journal of Food Measurement and Characterization. 2019; 13(1): 1–15.
50. Kumar SD, Esakkirajan S, Bama S, et al. A microcontroller based machine vision approach for tomato grading and sorting using SVM classifier. Microprocessors and Microsystems. 2020; 76: 103090.
51. Liu L, Li Z, Shi Y, et al. Design of a tomato classifier based on machine vision. PloS one. 2019; 14(7): e0219803.
52. Belan PA, de Macedo RAG, Luz Alves WA, et al. Machine vision system for quality inspection of beans. The International Journal of Advanced Manufacturing Technology. 2020; 111: 3421–3435.
53. Zhou L, Chalana V, Kim Y. PC-based machine vision system for real-time computer-aided potato inspection. International journal of imaging systems and technology. 1998; 9(6): 423–433.
54. Thinh NT, Duc Thong N, Cong HT, et al. Mango classification system based on machine vision and artificial intelligence. In: Proceedings of the 2019 7th International Conference on Control, Mechatronics and Automation (ICCMA); 6–8 November 2019; Delft, Netherlands.
55. Ismail N, Malik OA. Real-time visual inspection system for grading fruits using computer vision and deep learning techniques. Information Processing in Agriculture. 2022; 9(1): 24–37.
56. Uluişik S, Yildiz F, Özdemİr AT. Image processing based machine vision system for tomato volume estimation. In: Proceedings of the 2018 Electric Electronics, Computer Science, Biomedical Engineerings' Meeting (EBBT); 18–19 April 2018; Istanbul, Turkey.
57. Nyalala I, Okinda C, Chao Q, et al. Weight and volume estimation of single and occluded tomatoes using machine vision. International Journal of Food Properties. 2021; 24(1): 818–832.
58. Concha-Meyer A, Eifert J, Wang H, et al. Volume estimation of strawberries, mushrooms, and tomatoes with a machine vision system. International Journal of Food Properties. 2018; 21(1): 1867–1874.
59. Vrochidou E, Banzinas C, Manios M, et al. Machine vision for ripeness estimation in viticulture automation. Horticulturae. 2021; 7(9): 282.
60. Sabzi S, Nadimi M, Abbaspour-Gilandeh Y, et al. Non-destructive estimation of physicochemical properties and detection of ripeness level of apples using machine vision. International Journal of Fruit Science. 2022; 22(1): 628–645.
61. Septiarini A, Sunyoto A, Hamdani H, et al. Machine vision for the maturity classification of oil palm fresh fruit bunches based on color and texture features. Scientia Horticulturae. 2021; 286: 110245.
62. Kamrul MH, Paul P, Rahman M. Machine vision based rice disease recognition by deep learning. 2019 22nd International Conference on Computer and Information Technology (ICCIT). IEEE, 2019.
63. Mahmud MS, Zaman QU, Esau TJ, et al. Development of an artificial cloud lighting condition system using machine vision for strawberry powdery mildew disease detection. Computers and Electronics in Agriculture. 2019; 158: 219–225.
64. Kim W-S, Lee D-H, Kim Y-J. Machine vision-based automatic disease symptom detection of onion downy mildew. Computers and Electronics in Agriculture. 2020; 168: 105099.
65. Palei S, Behera SK, Sethy PK. A Systematic Review of Citrus Disease Perceptions and Fruit Grading Using Machine Vision. Procedia Computer Science. 2023; 218: 2504–2519.
66. Martínez-Heredia JM, Gálvez AI, Colodro F, et al. Feasibility Study of Detection of Ochre Spot on Almonds Aimed at Very Low-Cost Cameras Onboard a Drone. Drones. 2023; 7(3): 186.
67. Jiang H, Li X, Safara F. IoT-based agriculture: Deep learning in detecting apple fruit diseases. Microprocessors and Microsystems. 2021; 104321.
68. Lins EA, Mazuco Rodriguez JP, Scoloski SI, et al. A method for counting and classifying aphids using computer vision. Computers and electronics in agriculture. 2020; 169: 105200.
69. Liu H, Chahl JS. A multispectral machine vision system for invertebrate detection on green leaves. Computers and Electronics in Agriculture. 2018; 150: 279–288.

70. Rani SVJ, Kumar PS, Priyadharsini R, et al. Automated weed detection system in smart farming for developing sustainable agriculture. International Journal of Environmental Science and Technology. 2022; 19(9): 9083–9094.
71. Abouzahir S, Sadik M, Sabir E. Enhanced approach for weeds species detection using machine vision. In: Proceedings of the 2018 International Conference on Electronics, Control, Optimization and Computer Science (ICECOCS); 5–6 December 2018; Kenitra, Morocco.
72. Li N, Zhang X, Zhang C, et al. Review of machine-vision-based plant detection technologies for robotic weeding. In: Proceedings of the 2019 IEEE International Conference on Robotics and Biomimetics (ROBIO); 6–8 December 2019; Dali, China.
73. Wu Z, Chen Y, Zhao B, et al. Review of weed detection methods based on computer vision. Sensors. 2021; 21(11): 3647.
74. Guo Y, He D, Chai L. A machine vision-based method for monitoring scene-interactive behaviors of dairy calf. Animals. 2020; 10(2): 190.
75. Guo Y, Chai L, Aggrey SE, et al. A machine vision-based method for monitoring broiler chicken floor distribution. Sensors. 2020; 20(11): 3179.
76. Zhang S, Yang X, Wang Y, et al. Automatic fish population counting by machine vision and a hybrid deep neural network model. Animals. 2020; 10(2): 364.
77. Zhou K, Meng Z, He M, et al. Design and test of a sorting device based on machine vision. IEEE Access. 2020; 8: 27178–27187.
78. Kanagasingham S, Ekpanyapong M, Chaihan R. Integrating machine vision-based row guidance with GPS and compass-based routing to achieve autonomous navigation for a rice field weeding robot. Precision Agriculture. 2020; 21(4): 831–855.
79. Terra FP, do Nascimento GH, Duarte GA, et al. Autonomous agricultural sprayer using machine vision and nozzle control. Journal of Intelligent & Robotic Systems. 2021; 102(2): 38.
80. Bai J, Hao F, Cheng G, et al. Machine vision-based supplemental seeding device for plug seedling of sweet corn. Computers and Electronics in Agriculture. 2021; 188: 106345.
81. Williams HAM, Jone MH, Nejati M, et al. Robotic kiwifruit harvesting using machine vision, convolutional neural networks, and robotic arms. Biosystems Engineering. 2019; 181: 140–156.
82. Wood DA., Kafiabadi S, Busaidi AA, et al. Deep learning to automate the labelling of head MRI datasets for computer vision applications. European radiology. 2022; 32: 725–736.
83. Zhao X. A Computer Vision System for Missing Tablets Detection. Journal of Physics: Conference Series. 2021; 1827(1).
84. Sethy PK, Pandey C, Khan MR, et al. A cost-effective computer-vision based breast cancer diagnosis. Journal of Intelligent & Fuzzy Systems. 2021; 41(5): 5253–5263.
85. Alkadi R, Taher F, El-Baz A, et al. A deep learning-based approach for the detection and localization of prostate cancer in T2 magnetic resonance images. Journal of digital imaging. 2019; 32: 793–807.
86. Gu Y, Pandit S, Saraee E, et al. Home-based physical therapy with an interactive computer vision system. In: Proceedings of the IEEE/CVF International Conference on Computer Vision Workshops; 27–28 October 2019; Seoul, Korea (South).
87. Ghani A, Aina A, See CH, et al. Accelerated diagnosis of novel Coronavirus (COVID-19)—Computer vision with convolutional neural networks (CNNs). Electronics. 2022; 11(7): 1148.
88. Kollias D, Arsenos A, Kollias S. Ai-mia: Covid-19 detection and severity analysis through medical imaging. In: Proceedings of the European Conference on Computer Vision; 23–27 October 2022; Tel Aviv, Israel.
89. Ismael SAA, Mohammed A, Hefny H. An enhanced deep learning approach for brain cancer MRI images classification using residual networks. Artificial intelligence in medicine. 2020; 102: 101779.
90. Gu Y, Yang J. Application of computer vision and deep learning in breast cancer assisted diagnosis. In: Proceedings of the 3rd International Conference on Machine Learning and Soft Computing; 25–28 January 2019; Da Lat, Viet Nam.
91. Khemasuwan D, Sorensen JS, Colt HG. Artificial intelligence in pulmonary medicine: Computer vision, predictive model and COVID-19. European respiratory review. 2020; 29(157).
92. Welikala RA, Remagnino P, Lim JH, et al. Automated detection and classification of oral lesions using deep learning for early detection of oral cancer. IEEE Access. 2020; 8: 132677–132693.
93. Azizi S, Mustafa B, Ryan F, et al. Big self-supervised models advance medical image classification. In: Proceedings of the IEEE/CVF international conference on computer vision; 10–17 October 2021; Montreal, QC, Canada.
94. Yeung S, Downing NL, Fei-Fei L, et al. Bedside computer vision-moving artificial intelligence from driver assistance to patient safety. N Engl J Med. 2018; 378(14): 1271–1273.

95. Aksac A, Demetrick DJ, Ozyer T, Alhajj R. BreCaHAD: A dataset for breast cancer histopathological annotation and diagnosis. BMC research notes. 2019; 12(1): 1–3.
96. Zhou Y, Graham S, Koohbanani NA, et al. Cgc-net: Cell graph convolutional network for grading of colorectal cancer histology images. In: Proceedings of the IEEE/CVF international conference on computer vision workshops; 27–28 October 2019; Seoul, Korea (South).
97. Chao S, Belanger D. Generalizing Few-Shot Classification of Whole-Genome Doubling Across Cancer Types. In: Proceedings of the IEEE/CVF International Conference on Computer Vision; 10–17 October 2021; Montreal, QC, Canada.
98. Chen X, Williams BM, Vallabhaneni SR, et al. Learning active contour models for medical image segmentation. In: Proceedings of the IEEE/CVF conference on computer vision and pattern recognition; 15–20 June 2019; Long Beach, CA, USA.
99. Shah NA, Gupta D, Lodaya R, et al. Colorectal cancer segmentation using atrous convolution and residual enhanced unet. In: Proceedings of the Computer Vision and Image Processing: 5th International Conference, CVIP 2020; 4–6 December 2020; Prayagraj, India.
100. Ulhaq A, Khan A, Gomes D, et al. Computer vision for COVID-19 control: A survey. Available online: https://doi.org/10.48550/arXiv.2004.09420 (accessed on 10 September 2024).
101. Rehman KU, Li J, Pei Y, et al. Computer vision-based microcalcification detection in digital mammograms using fully connected depthwise separable convolutional neural network. Sensors. 2021; 21(14): 4854.
102. Abdelrahman L, Ghamdi MA, Collado-Mesa F, et al. Convolutional neural networks for breast cancer detection in mammography: A survey. Computers in biology and medicine. 2021; 131: 104248.
103. Rakhlin A, Shvets A, Iglovikov V, et al. Deep convolutional neural networks for breast cancer histology image analysis. In: Proceedings of the Image Analysis and Recognition: 15th International Conference, ICIAR 2018; 27–29 June 2018; Póvoa de Varzim, Portugal.
104. Haskins G, Kruger U, Yan P. Deep learning in medical image registration: a survey. Machine Vision and Applications. 2020; 31: 1–18.
105. Esteva A, Chou K, Yeung S, et al. Deep learning-enabled medical computer vision. NPJ digital medicine. 2021; 4(1): 5. 25–1
106. Zheng J, Lin D, Gao Z, et al. Deep learning assisted efficient AdaBoost algorithm for breast cancer detection and early diagnosis. IEEE Access. 2020; 8: 96946–96954.
107. Amiri E, Roozbakhsh Z, Amiri S, et al. Detection of topographic images of keratoconus disease using machine vision. International Journal of Engineering Science and Application. 2020; 4(4): 145–150.
108. Wu J-X, Liu H-C, Chen P-Y, et al. Enhancement of ARFI-VTI elastography images in order to preliminary rapid screening of benign and malignant breast tumors using multilayer fractional-order machine vision classifier. IEEE access. 2020; 8: 164222–164237.
109. Gupta V, Bhavsar A. Partially-independent framework for breast cancer histopathological image classification. In: Proceedings of the IEEE/CVF Conference on Computer Vision and Pattern Recognition Workshops; 15–20 June 2019; Long Beach, CA, USA.
110. Gupta V, Bhavsar A. Sequential modeling of deep features for breast cancer histopathological image classification. In: Proceedings of the IEEE Conference on Computer Vision and Pattern Recognition Workshops; 18–22 June 2018; Salt Lake City, UT, USA.
111. Sheikh TS, Lee Y, Cho M. Histopathological classification of breast cancer images using a multi-scale input and multi-feature network. Cancers. 2020; 12(8): 2031.
112. Liu Z, Xu X, Liu T, et al. Machine vision guided 3d medical image compression for efficient transmission and accurate segmentation in the clouds. In: Proceedings of the IEEE/CVF conference on computer vision and pattern recognition; 15–20 June 2019; Long Beach, CA, USA.
113. Harned Z, Lungren MP, Rajpurkar P. Machine vision, medical AI, and malpractice. JL & Tech. Dig. 2019.
114. Mok TCW, Chung A. Affine medical image registration with coarse-to-fine vision transformer. In: Proceedings of the IEEE/CVF Conference on Computer Vision and Pattern Recognition; 16–22 June 2024; New Orleans, LA, USA.
115. Wu J-X, Chen P-Y, Chen P-Y, et al. Multilayer fractional-order machine vision classifier for rapid typical lung diseases screening on digital chest X-ray images. IEEE Access. 2020; 8: 105886–105902.

116. Yoo S, Gujrathi I, Haider MA, et al. Prostate cancer detection using deep convolutional neural networks. Scientific reports. 2019; 9(1): 19518.
117. Hassan H, Ren Z, Zhao H, et al. Review and classification of AI-enabled COVID-19 CT imaging models based on computer vision tasks. Computers in biology and medicine. 2022; 141: 105123.
118. Zhang Ni, Cai Y-X, Wang Y-Y, et al. Skin cancer diagnosis based on optimized convolutional neural network. Artificial intelligence in medicine. 2020; 102: 101756.
119. Deniz E, Şengür A, Kadiroğlu Z, et al. Transfer learning based histopathologic image classification for breast cancer detection. Health information science and systems. 2018; 6: 1–7.
120. Zhao T, Zhang H, Spoelstra J. A computer vision application for assessing facial acne severity from selfie images. Available online: https://doi.org/10.48550/arXiv.1907.07901 (accessed on 10 September 2024).
121. Yu H, Liang Y, Liang H, et al. Recognition of wood surface defects with near infrared spectroscopy and machine vision. Journal of Forestry Research. 2019; 30(6): 2379–2386.
122. Chen S, Lai W, Ye J, et al. A Fast and Low-Power Detection System for the Missing Pin Chip Based on YOLOv4-Tiny Algorithm. Sensors. 2023; 23(8): 3918.
123. Lin X, Wang X, Li L. Intelligent detection of edge inconsistency for mechanical workpiece by machine vision with deep learning and variable geometry model. Applied Intelligence. 2020; 50: 2105–2119.
124. Liong S-T, Gan YS, Huang Y-C, et al. Integrated neural network and machine vision approach for leather defect classification. Available online: https://doi.org/10.48550/arXiv.1905.11731 (accessed on 10 September 2024).
125. Lin Z, Lai Y, Pan T, et al. A new method for automatic detection of defects in selective laser melting based on machine vision. Materials. 2021; 14(15): 4175.
126. Ryu S-G, Kim SW, Yun JP, et al. Detection of scarfing faults on the edges of slabs. ISIJ international. 2014; 54(1): 112–118.
127. Massinaei M, Jahedsaravani A, Taheri E, et al. Machine vision based monitoring and analysis of a coal column flotation circuit. Powder Technology. 2019; 343: 330–341.
128. Wang J, Lee S. Data augmentation methods applying grayscale images for convolutional neural networks in machine vision. Applied Sciences. 2021; 11(15): 6721.
129. Jain S, Seth G, Paruthi A. Synthetic data augmentation for surface defect detection and classification using deep learning. Journal of Intelligent Manufacturing. 2022; 1–14.
130. Hao R, Lu B, Cheng Y, et al. A steel surface defect inspection approach towards smart industrial monitoring. Journal of Intelligent Manufacturing. 2021; 32: 1833–1843.
131. Zhang J, Kang X, Ni H, et al. Surface defect detection of steel strips based on classification priority YOLOv3-dense network. Ironmaking & Steelmaking. 2021; 48(5): 547–558.
132. Boikov A, Payor V, Savelev R, et al. Synthetic data generation for steel defect detection and classification using deep learning. Symmetry. 2021; 13(7): 1176.
133. Penumuru DP, Muthuswamy S, Karumbu P. Identification and classification of materials using machine vision and machine learning in the context of industry 4.0. Journal of Intelligent Manufacturing. 2020; 31(5): 1229–1241.
134. Benbarrad T, Salhaoui M, Kenitar SB, et al. Intelligent machine vision model for defective product inspection based on machine learning. Journal of Sensor and Actuator Networks. 2021; 10(1): 7.
135. Peng R, Liu J, Fu X, et al. Application of machine vision method in tool wear monitoring. The International Journal of Advanced Manufacturing Technology 116.3-4. 2021; 1357–1372.
136. Dai W, Li D, Tang D, et al. Deep learning assisted vision inspection of resistance spot welds. Journal of Manufacturing Processes. 2021; 62: 262–274.
137. Zhang Z, Liu Y, Hu Q, et al. Multi-information online detection of coal quality based on machine vision. Powder Technology. 2020; 374: 250–262.
138. Sikander G, Anwar S. A novel machine vision-based 3d facial action unit identification for fatigue detection. IEEE Transactions on Intelligent Transportation Systems. 2020; 22(5): 2730–2740.
139. Zhao R, Jia P, Wang Y, et al. Dynamic model of crowd flow in multi-angle cross passages based on machine vision. In: Proceedings of the 2021 IEEE 5th Advanced Information Technology, Electronic and Automation Control Conference (IAEAC); 12–14 March 2021; Chongqing, China.
140. Arellano-González JC, Medellín-Castillo HI, Hernández-Molina RI, et al. Determination of Anthropometric Lengths of Body Segments Using Machine Vision Systems. Machines. 2023; 11(3): 369.

141. Panahi L, Ghods V. Human fall detection using machine vision techniques on RGB–D images. Biomedical Signal Processing and Control. 2018; 44: 146–153.
142. Huang H, Moaveni M, Schmidt S, et al. Evaluation of Railway Ballast Permeability Using Machine Vision–Based Degradation Analysis. Transportation Research Record. 2018; 2672(10): 62–73.
143. Burghardt TE, Popp R, Helmreich B, et al. Visibility of various road markings for machine vision. Case Studies in Construction Materials. 2021; 15: e00579.
144. Yang H, Wang Y, Hu J, et al. Deep learning and machine vision-based inspection of rail surface defects. IEEE Transactions on Instrumentation and Measurement. 2021; 71: 1–14.
145. Dan D, Ying Y, Ge L. Digital Twin System of Bridges Group Based on Machine Vision Fusion Monitoring of Bridge Traffic Load. IEEE transactions on intelligent transportation systems. 2021; 23.
146. Dan D, Dan Q. Automatic recognition of surface cracks in bridges based on 2D-APES and mobile machine vision. Measurement. 2021; 168.
147. Liu Z, He Y, Wang C, et al. Analysis of the influence of foggy weather environment on the detection effect of machine vision obstacles. Sensors. 2020; 20(2): 349.
148. Kim H, Han J, Han TY-J. Machine vision-driven automatic recognition of particle size and morphology in SEM images. Nanoscale. 2020; 12(37): 19461–19469.
149. Nartova AV., Mashukov MY, Astakhov RR, et al. Particle recognition on transmission electron microscopy images using computer vision and deep learning for catalytic applications. Catalysts. 2022; 12(2): 135.
150. Hendel D, Johnston KV, Patra RK, et al. A machine-vision method for automatic classification of stellar halo substructure. Monthly Notices of the Royal Astronomical Society. 2019; 486(3): 3604–3616.

ACADEMIC
ACADEMIC PUBLISHING PTE LTD

Academic Publishing Pte. Ltd.

Add: 73 Upper Paya Lebar Road, #07-02B-01, Centro Bianco, Singapore 534818
Tel: +65 83184869
E-mail: editorial_office@acad-pub.com
Web: http://ojs.acad-pub.com/